

University of Southampton Research Repository
ePrints Soton

Copyright © and Moral Rights for this thesis are retained by the author and/or other copyright owners. A copy can be downloaded for personal non-commercial research or study, without prior permission or charge. This thesis cannot be reproduced or quoted extensively from without first obtaining permission in writing from the copyright holder/s. The content must not be changed in any way or sold commercially in any format or medium without the formal permission of the copyright holders.

When referring to this work, full bibliographic details including the author, title, awarding institution and date of the thesis must be given e.g.

AUTHOR (year of submission) "Full thesis title", University of Southampton, name of the University School or Department, PhD Thesis, pagination

UNIVERSITY OF SOUTHAMPTON

FACULTY OF SOCIAL AND HUMAN SCIENCES

School of Mathematics

**The Mathematical Modelling of Flow
and Deformation in the Human Eye**

by

Zuhaila Ismail

Thesis for the degree of Doctor of Philosophy

April 2013

UNIVERSITY OF SOUTHAMPTON

ABSTRACT

FACULTY OF SOCIAL AND HUMAN SCIENCES

SCHOOL OF MATHEMATICS

Doctor of Philosophy

THE MATHEMATICAL MODELLING OF FLOW AND DEFORMATION IN
THE HUMAN EYE

by Zuhaila Ismail

Modelling the human eye provides a great challenge in both the field of mathematical medicine and in engineering. Four different problems regarding flow and deformation in the eyeball are considered, showing how changes in both the fluid and solid mechanics of the human eye contribute to the development of pathological states. Firstly, a mathematical model is presented for the flow of aqueous humour through the trabecular meshwork and into the Schlemm canal. This predicts the intraocular pressure and investigates how this influences primary open angle glaucoma. Secondly, paradigm problems concerning the development of rhegmatogenous retinal detachment are presented. A two-dimensional model of pressure driven fluid flow between rigid walls, and between one rigid and one moving wall is presented and followed by a three-dimensional model concerning liquefied vitreous humour flow induced by saccadic eye motion. The purpose of these models is to examine the flow behaviour and the deformation of the detached retina. Thirdly, a mathematical model of aqueous humour flow, driven by buoyancy effects through the detached descemet membrane in the anterior chamber, has been developed to analyse the fluid mechanics concerning the progression of descemet membrane detachment. Lastly, mathematical models studying the effects of a tonometer and a scleral buckle on the shape of the eyeball membrane are presented. The modelling of fluid flow in these studies is based on the lubrication theory limit of the Navier-Stokes equations. However, the full Navier-Stokes equations have been used in the development of a three-dimensional model of retinal detachment. In the modelling of the tonometry and scleral buckling the membrane theory of spherical shells has been used. The results of these models predict changes in the intraocular pressure as well as examining the fluid flow behaviour and the deformation of the detached retina. The modelling of descemet membrane detachment is shown to explain the progress of the spontaneous reattachment and redetachment of descemet membrane may be controlled under the correct conditions. The results of the modelling of the tonometer cast doubt on the Imbert-Fick law, but the results of the scleral buckle may prove useful to predict changes in the focal length of the eye when a scleral buckle is present.

Contents

DECLARATION OF AUTHORSHIP	xxi
List of Publications	xxiii
Acknowledgements	xxv
1 Introduction and Problem Formulation	1
1.1 Introduction	1
1.2 The Human Eye	1
1.3 Common Causes of Vision Loss	3
1.3.1 Primary Open Angle Glaucoma (POAG)	3
1.3.2 Rhegmatogenous Retinal Detachment (RRD)	5
1.3.3 Descemet Membrane Detachment (DMD)	6
1.4 Contributions of the Thesis	7
1.5 Mathematical Framework of this Thesis	8
2 Flow in the Schlemm Canal and its Influence on POAG	11
2.1 Introduction	11
2.2 Anatomy and Physiology of the Trabecular Meshwork, and Aqueous Humour Dynamics	12
2.2.1 POAG in Human Eyes	15
2.2.2 Diagnosis and Treatment of POAG	16
2.3 Motivation for the Mathematical Model	18
2.4 Modelling of Aqueous Humour Flow through the Trabecular Meshwork and into the Canal of Schlemm	19
2.4.1 The Governing Equations	19
2.4.2 Friedenwald's Law	20
2.4.3 Solution Procedures	21
2.5 Mathematical Analysis of the Results and Discussion	22
2.5.1 Aqueous Humour Flow through the Trabecular Meshwork determined by Darcy's Law	22
2.5.2 Model of the Trabecular Meshwork by Applying the Beam Bending Theory	35
2.6 Conclusions	58
3 The Flow of Liquefied Vitreous Humour and Its Contribution to RRD	61
3.1 Introduction	61
3.2 The Retina	62

3.2.1	RRD in the Human Eye	63
3.2.2	Scleral Buckling in the Treatment of RRD	64
3.3	Liquefied Vitreous Humour Flow driven by Saccadic Eye Motion	65
3.4	Motivation for the Mathematical Model	67
3.5	Modelling of Paradigm Problem: Flow in a Channel with Rigid Walls	68
3.5.1	Mathematical Model	68
3.5.2	Solution Procedures	69
3.5.3	Analytical Results	71
3.6	Modelling of Paradigm Problem: Flow in a Channel with One Stationary and One Moving Wall	77
3.6.1	Mathematical Model	78
3.6.2	Solution Procedures	79
3.6.3	Analytical Results	82
3.7	Conclusion for Retinal Detachment	84
3.8	Modelling of the Liquefied Vitreous Humour Flow during Retinal Detachment	85
3.8.1	The Governing Equations	86
3.8.2	Solution Procedures	88
3.8.3	Mathematical Analysis and Discussion	92
3.9	Conclusions and Further Work	107
4	Flow in the Anterior Chamber during DMD	111
4.1	Introduction	111
4.2	Corneal Structure	112
4.3	Descemet Membrane Detachment (DMD) in Human Eyes	113
4.3.1	Causes and Management of DMD	114
4.4	Motivation for the Mathematical Model	115
4.5	Aqueous Humour Flow in the Anterior Chamber	116
4.6	Modelling of Paradigm Problem: Flow in the Rectangular-shaped region	119
4.6.1	Mathematical Model	120
4.6.2	Solution Procedures	121
4.6.3	Analytical Results and Simulations	126
4.7	Modelling of Aqueous Humour Flow during Descemet Membrane Detachment	131
4.7.1	Mathematical Model	131
4.7.2	Solution Procedures	133
4.7.3	Analytical Results and Simulations	136
4.7.4	DMD Equations	138
4.8	Conclusions and Further Work	139
5	Modelling of Tonometry and Scleral Buckling	143
5.1	Introduction	143
5.2	Anatomy and Physiology of the Eyeball	143
5.3	Measurement of the Intraocular Pressure (IOP)	148
5.3.1	The Indentation (Schiotz) Tonometer	149
5.3.2	The Goldmann Applanation Tonometer	149
5.3.3	The iCare Rebound Tonometer	152

5.4 Motivation for Mathematical Modelling	153
5.5 The Membrane Theory of Shells	153
5.5.1 Derivation of the Membrane equations of Equilibrium for Ax-isymmetric Spherical Shells	154
5.6 Mathematical Analysis of the Eyeball Membrane when undergoing Tonometry and Scleral Buckling	161
5.6.1 A Mathematical Model of the Eyeball Membrane	162
5.6.2 The Governing Equations	163
5.6.3 The General Solution Procedures	164
5.6.4 Boundary Conditions	165
5.6.5 Numerical Analysis of Tonometry and Scleral Buckling	165
5.6.5.1 Tonometry	166
5.6.5.2 Scleral Buckling	170
5.7 Conclusions and Further Work	180
6 Conclusions	183
A Linearization of Friedenwald's law	189
A.1 Introduction	189
A.2 The Governing Equations	189
A.3 Boundary Conditions	191
A.4 Linearization	192
A.5 Numerical Results	193
B Proof of Completeness	197
C Flow Map	199

List of Figures

1.1	Schematic Diagram of the Human Eye. This figure was extracted from [134].	2
1.2	Mechanism for Intraocular Pressure (IOP) increases in Human Eyes. This figure was reproduced from [135].	4
1.3	Retinal Detachments. This figure was extracted from [141] and [142].	6
1.4	DMD after cataract surgery. This figure was extracted from [147].	7
2.1	Cross section of the eye showing how the aqueous humour flow continuously in and out of the anterior chamber. This figure was extracted from [150].	12
2.2	Schematic diagram of eye structures involved in aqueous humour dynamics. This figure was extracted from [151].	13
2.3	The structure of the Trabecular Meshwork.	14
2.4	Healthy and Glaucomatous Optic Nerve. This figure was extracted from [152].	17
2.5	Schematic diagram of flow through the trabecular meshwork into the Schlemm canal.	19
2.6	The changes in intraocular pressure, $p_i(t)$ in ten seconds given in equation (2.16), when the permeability, k in Darcy's law is constant. The standard parameter values, Table 2.1, have been imposed to calculate and plot this figure. The changes in intraocular pressure start from normal intraocular pressure which is equal to 14mmHg ($\cong 1867\text{Pa}$).	24
2.7	The changes in intraocular pressure, $p_i(t)$ in ten seconds by solving equation (2.33) numerically and using the typical parameter values such as listed in Table 2.1. In this case, the permeability, k in Darcy's law is assumed to be proportional to the pressure different through the trabecular meshwork for different values of ϑ	28
2.8	The changes in intraocular pressure, $p_i(t)$ given in equation (2.38), when the permeability, k in Darcy's law is inversely related to the pressure difference through the trabecular meshwork, $\frac{1}{p_i-p}$. The standard parameter values given in Table 2.1 have been employed in this calculation, whereas the total amount of fluid flowing out of the eye, V_{out} is assumed to be zero.	29
2.9	The changes in intraocular pressure, $p_i(t)$ given in equation (2.38), when the permeability, k in Darcy's law is inversely proportional to the pressure difference through the trabecular meshwork, $\frac{1}{p_i-p}$ for different values of ζ . The straight, the dotted and the dashed lines represent the values of ζ corresponding to $\zeta = 10^3$, $\zeta = 10^5$ and $\zeta = 10^6$. The parameter values inherent to these calculations are given in Table 2.1.	30

2.17 The deformation of the trabecular meshwork for different values of λ by solving numerically equation (2.122) subject to the boundary conditions given in equation (2.123). In this case, the permeability, k in Darcy's law is inversely related to the pressure difference through the trabecular meshwork, $\frac{1}{(p_i-p)}$. The solid red line denotes the trabecular meshwork associated with $\lambda = 2$, whereas the dashed-dotted green, the dashed blue and the dotted magenta lines represent the corresponding trabecular meshwork for λ equal to 5, 15 and 23 respectively.	55
2.18 The deformation of the trabecular meshwork when λ is large by solving numerically equation (2.138) subject to the boundary conditions given in equation (2.139). In this case, the permeability, k in Darcy's law is inversely related to the square of pressure difference, $\frac{1}{(p_i-p)^2}$ and the value of ψ inherent to these calculations is equal to order one. Each graph corresponds to a different value of λ . The solid red, the dashed-dotted green, the dashed blue and the dotted magenta lines associated with $\lambda = 2$, $\lambda = 5$, $\lambda = 15$ and $\lambda = 23$ respectively.	58
3.1 Diagram of a human eye and a structure of the retina.	62
3.2 The retinal detachment and the scleral buckle. This figure was taken from [154].	64
3.3 Schematic diagram of liquefied vitreous humour flow through the detached retina.	68
3.4 The deformation of detached retina, $h(x)$ given in equation (3.36) for different values of α . The solid magenta line represents the detached retina associated with an α equal to 0.01, whereas the dotted-dashed green line and the dashed blue line denote the corresponding detached retina for α equal to 0.1 and 0.5.	74
3.5 The volume flux in Region (2), $Q_2(x)$ given in equation (3.38) versus the pressure different, $p_o - p_L$. Each graph corresponds to a different value of α . The solid blue line, the dotted magenta line and the dashed green line represent the corresponding detached retina for α equal to 0.5, 0.1, and 0.05.	75
3.6 Bending moment, $M(x)$ at the end of the detached retina, $x = L$ given in equation (3.40) versus pressure different, $p_o - p_L$ for different values of $\beta = \frac{L^7}{6H}$ where $\varepsilon = \frac{1}{\beta}$. The dashed blue line represents the bending moment associated with β equal to $\frac{1}{5}$, whereas the dotted magenta line and the solid green line denote the corresponding bending moment for β equal to $\frac{1}{10}$ and $\frac{1}{15}$	76
3.7 Bending moment, $M(x)$ versus length of the detached retina, L given in equation (3.40). The value chosen for the L is 10mm. Each graph corresponds to a different value of ε . The dashed blue line, the dotted magenta line and the solid green line denote the corresponding bending moment for ε equal to 0.5, 0.1 and 0.05.	77
3.8 Schematic diagram of flow with One Moving and One Stationary Plate.	78
3.9 The deformation of the detached retina, $h(x)$ for different value of small β . The dashed blue line represents the detached retina associated with β equal to -100 whereas the dotted green line, the solid red line, the dashed dotted yellow line and the long dashed magenta line denote the corresponding detached retina for β equal to -75, -50, -25 and 0.	84

3.10 The deformation of the detached retina $h(x)$. Each graph corresponds to different value of β from 0 to 100. The dashed blue line, the dotted green line, the solid red line, the dashed dotted yellow line and the long dashed magenta line represent the corresponding detached retina for β equal to 0, 25, 50, 75 and 100.	85
3.11 Spherical coordinate system which illustrates the model of saccadic eye motion.	86
3.12 Schematic diagram of the human eye presenting a two dimensional cross section of retinal detachment for illustrating the detached retina, $h(\theta)$	86
3.13 The $ALiC$ series approximation for the function, $f(\theta) = \theta(\pi - \theta)\sin(\theta)$ that satisfies the odd part of the hypergeometric function over the interval $[0, \pi]$ and its given by the solid red line. The dashed magenta line represents the $ALiC$ series approximation of degree 1 ($m = 1$) whereas the long dashed green line and the dashed-dotted blue line denote the $ALiC$ series approximation for m equal to 5 and 9. In this case when $m = 9$, the $ALiC$ series approximation is equivalent to the original function.	100
3.14 The $ALiC$ series approximation for the piecewise function, $f(\theta) = \theta \cdot \sin(\theta)$ over the interval $[0, \frac{\pi}{2}]$ and $f(\theta) = (\pi - \theta)\sin(\theta)$ in between $\frac{\pi}{2}$ and π . The solid red line denotes the piecewise function. Each graph corresponds to a different degree of approximation. The dashed magenta line, the long dashed green line and the dashed-dotted blue line represent the corresponding $ALiC$ series approximation for m equal to 1, 5 and 9. As the degree of $ALiC$ series approximation rises to 9, it approaches a close approximation to $f(\theta)$	101
3.15 Approximation to the function, $f(\theta) = \sin(\theta)$ over the interval $[0, \pi]$ by $ALiC$ series. The solid red line represents the function $f(\theta) = \sin(\theta)$ and the dashed blue line shows the $ALiC$ series approximation of degree 1. The $ALiC$ series obtained when $m = 1$ is algebraically equivalent to the original function.	101
3.16 The $ALiC$ series approximation for the function, $f(\theta) = \sin^2(\theta)$ over the interval $[0, \pi]$ that represented by the solid red line. The dashed magenta line denotes the $ALiC$ series approximation of degree 1 ($m = 1$) whereas the long dashed green line and the dashed-dotted blue line represent the $ALiC$ series approximation of degree 5 and 9. As the degree of $ALiC$ series approximation equal to 9, it approaches the correct function.	102
3.17 Approximation to the function, $f(\theta) = \sin^3(\theta)$ over the interval $[0, \pi]$ by $ALiC$ series. The solid red line denotes $f(\theta)$ and, the dashed magenta line and the long dashed blue line represent the $ALiC$ series approximation of degree 1 and 3. The $ALiC$ series obtained when $m = 3$ is algebraically equivalent to the function, $f(\theta) = \sin^3(\theta)$	102
3.18 The $ALiC$ series approximation for the function, $f(\theta) = \sin(2\theta)$ that satisfies the even part of the hypergeometric function over the interval $[0, \pi]$ and its given by the solid red line. The long dashed blue line represents the $ALiC$ series approximation of degree 2. When $m = 2$ the $ALiC$ series approximation look a good representation of $f(\theta)$	103

3.19 Approximation to the function, $f(\theta) = \sin(3\theta)$ that satisfies the odd part of the hypergeometric function over the interval $[0, \pi]$ by <i>ALiC</i> series. The function $f(\theta) = \sin(3\theta)$ is shown in solid red line. The dashed magenta line and the long dashed blue line denote the <i>ALiC</i> series approximation of degree 1 and 3. As the degree of <i>ALiC</i> series approximation equal to 3, it approaches the correct function.	103
3.20 Approximation to the function, $f(\theta) = \sin(4\theta)$ that satisfies the even part of the hypergeometric function over the interval $[0, \pi]$ by <i>ALiC</i> series. The original function is given by solid red line. The dashed magenta line and the dotted blue line represent the <i>ALiC</i> series approximation of degree 2 and 4. The <i>ALiC</i> series obtained when $m = 4$ is algebraically equivalent to the original function.	104
3.21 The <i>ALiC</i> series approximation for the function, $f(\theta) = \sin(5\theta)$. The solid red line denotes the original function. Each graph corresponds to a different degree of approximation. The dashed magenta line, the long dashed purple line and the dashed-dotted blue line represent the corresponding <i>ALiC</i> series approximation for m equal to 1, 3 and 5. As the degree of <i>ALiC</i> series approximation rises to 5, it appoaches a close approximation to $f(\theta)$	104
3.22 Approximation to the function, $f(\theta) = \sin(6\theta)$ that satisfies the even part of the hypergeometric function in between $[0, \pi]$ by <i>ALiC</i> series. The original function, $f(\theta) = \sin(6\theta)$ is shown in solid red line. The dashed magenta line, the dotted purple line and the long dashed blue line represent the <i>ALiC</i> series approximation of degree 2, 4 and 6. The <i>ALiC</i> series obtained when $m = 6$ is equivalent to the original function.	105
3.23 The <i>ALiC</i> series approximation for the function, $f(\theta) = \sin(2\theta) \sin(\theta)$ over the interval $[0, \pi]$ that represented by the solid red line. The dashed magenta line denotes the <i>ALiC</i> series approximation of degree 4 ($m = 4$) whereas the dotted purple line and the long dashed blue line represent the <i>ALiC</i> series approximation of degree 8 and 10. As the degree of <i>ALiC</i> series approximation approximation rises to 10, it approaches the correct function.	105
3.24 Approximation to the function, $f(\theta) = \sin(3\theta) \sin(\theta)$ that satisfies the odd part of the hypergeometric function over the interval $[0, \pi]$ by <i>ALiC</i> series. The solid red line denotes the function, $f(\theta) = \sin(3\theta) \sin(\theta)$. Each graph corresponds to a different degree of approximation. The dashed magenta line, the long dashed purple line and the dashed-dotted blue line denote the <i>ALiC</i> series approximation of degree 3, 7 and 11. The <i>ALiC</i> series obtained when $m = 11$ is algebraically equivalent to the function, $f(\theta)$	106
4.1 The Cornea. This figure was extracted from [155].	112
4.2 The structure of the Cornea. This figure was extracted from [156].	113
4.3 DMD. This figure was taken from [76] with permission.	114
4.4 Mechanism of spontaneous Descemet membrane reattachment. This figure was reproduced from [76] with permission.	115

- 4.5 Schematic diagram of a three-dimensional of the anterior chamber. The function selected for $h_o \left(1 - \frac{x^2}{a^2} - \frac{y^2}{a^2}\right)^{\frac{1}{2}}$, whereas the temperature difference between the cornea, T_c and the circular plane formed by the pupil aperture and the iris, T_p with the radius, $r = a$, is given by $T = T_p - T_c$. 116
- 4.6 Streamlines for buoyancy-driven flow in the plane $y = 0$. Gravity, g is assumed to be acting horizontally to the right and the function, $h(x) = h_0 \left(1 - \frac{x^2}{a^2}\right)$ represents the cornea. The typical values of a human eye given in equation (4.9) are employed in this numerical simulation using COMSOL [72], Figure 4.6(b), in order to compare with the result that produced by [75], Figure 4.6(a). This figure was taken from [75] with permission. 119
- 4.7 Schematic diagram of fluid flow through a small flap in a rectangular shaped region. 120
- 4.8 Streamlines for buoyancy-driven flow in the rectangular shaped region when gravity is acting horizontally to the right. The function selected for the flap, $d(x)$ is $d(x) = -0.15x + 0.00015$ over the interval $x \in [-0.001, 0.001]$ and the temperature gradient between the top and the bottom plates is equivalent to 2. (a) Streamlines in all regions given in equations (4.31), (4.36), (4.42) and (4.44) are plotted using Maple [8]. (b) Numerical simulation for streamline plots are carried out using COMSOL Multiphysics [72] in the purpose of comparison with the analytical calculation. Both figures are plotted using the standard parameter values of a human eye given in equation (4.9). 127
- 4.9 The deformation of the flap given in equation (4.57) for different positive values of $\beta = \frac{g\rho_o\alpha\eta h_o b}{2EI}$. The solid red line represents the flap when β is equal to zero, whereas the dashed blue line, the dotted green line, the dashed-dotted magenta line and the dotted brown line denote the corresponding flap for β equal to 0.1, 0.25, 0.5 and 0.75. 129
- 4.10 The deformation of the flap given in equation (4.57). Each graph corresponds to a different negative values of β . The solid red, the dashed blue, the dotted green, the dashed-dotted magenta and the dotted brown lines denote the corresponding flap for β equal to 0, -0.1, -0.25, -0.5 and -0.75. 130
- 4.11 Schematic diagram of the detached Descemet membrane in the anterior chamber in the plane $y = 0$ when gravity is acting horizontally to the right. The function, $h(x) = h_o \left(1 - \frac{x^2}{a^2}\right)^{\frac{1}{2}}$ represents the cornea and the function selected for the DMD, $d(x)$ is given by $0.2x + 0.002455$ over the interval $[-b, b]$ 131

4.12 Streamlines for buoyancy-driven flow in the anterior chamber around a DMD in the plane $y = 0$. Gravity is assumed to be acting horizontally to the right. The function selected for the detached Descemet membrane is considered to be $d(x) = 0.2x + 0.002455$ over the interval $[-0.001, 0.001]$, whereas the function for the corneal shape is assumed to be $h(x) = h_0 \left(1 - \frac{x^2}{a^2}\right)^{\frac{1}{2}}$. The temperature gradient between the cornea, T_c and the plane formed by pupil aperture and the iris, T_p is given by $T_p - T_c = 2$. The typical values for a human eye given in equation (4.9) are employed in these graph: (a) Streamlines given in equations (4.74), (4.78), (4.80) and (4.82) are combined in one plot using Maple [8]; (b) Numerical simulation for streamlines, arrow and surface velocity field are carried out using COMSOL Multiphysics [72].	137
4.13 Streamlines for buoyancy-driven flow in the anterior chamber around a DMD in the plane $y = 0$, when gravity is pointing from left to right. The same conditions and parameter values applied in Figure 4.12 have been employed in the production of this comparison figure. The DMD equation is given by $d(x) = -0.2x + 0.002455$ over the interval $[-0.001, 0.001]$	138
4.14 Magnification of numerical predictions for the flow in the region between the cornea surface and the DMD presenting Moffatt vortices.	139
4.15 The deformation of the detached Descemet membrane given in equation (4.86) for different negative values of $\beta = \frac{g\rho_0\alpha\eta h_0 b^7}{2EIa^2d_0}$. The solid red line denotes the DMD when β is equal to zero, whereas the dashed blue line, the dotted green line, the dashed-dotted magenta line and the dotted brown line represent the corresponding DMD for β equal to -0.1, -0.25, -0.5 and -0.75.	140
4.16 The deformation of the detached Descemet membrane given in equation (4.86) at different positive values of β . The solid red line represents the detached Descemet membrane at $\beta = 0$, whereas the dashed blue, the dotted green, the dashed-dotted magenta and the dotted brown lines are associated with $\beta = 0.1$, $\beta = 0.25$, $\beta = 0.5$ and $\beta = 0.75$ respectively.	140
5.1 The diagram of the eyeball.	144
5.2 The eyeball thickness distribution.	145
5.3 The structure of the sclera.	145
5.4 The indentation (Schiotz) tonometer in 1905. This figure was extracted from [158].	149
5.5 The Goldmann Applanation tonometer. This figure was extracted from [157].	150
5.6 Schematic represent a variety of appearances of the meniscus semicircles through the Goldmann applanation prism.	150
5.7 The ICare rebound tonometer. This figure was extracted from [159] . . .	152
5.8 Geometry of Spherical Shell.	154
5.9 Stress Resultants in a Spherical Shell Element.	155
5.10 Line elements before and after deformation (a) meridian (b) parallel circle.	159
5.11 Schematic diagram of the cross section of the eyeball in the plane $\phi = 0$.	162

- 5.12 The axial force, N_θ distribution at the outer surface of the eyeball when the pressure exerted by the tonometer is equal to the intraocular pressure, P_{IOP} , 15mmHg. The remaining parameter values have been established in Table 5.2. 167
- 5.13 Qualitative behaviour of the shape of the eyeball presented by the displacements due to the pressure exerted by the tonometer, P_T . The values of the tonometer pressure are taken to be equal to the intraocular pressure, P_{IOP} which are 15mmHg, 30mmHg, 45mmHg and 60mmHg. Standard parameter values required for these numerical calculation are given in Table 5.2. 169
- 5.14 Qualitative behaviour of the displacements produced by the tonometer when the intraocular pressure, P_{IOP} equals the tonometer pressure, P_T at 15mmHg, 30mHg, 45mmHg and 60mmHg. This figure is the same as Figure 5.13, however these graphs only show the displacements in the quadrant between $\theta \in [0, \frac{\pi}{2}]$ 170
- 5.15 Numerical calculation of the tonometer pressure, P_T and comparison between the Imber-Fick law and the current model. The solid black line represents the Imbert-Fick law and the long dashed black line denotes the current numerical model. Both are fitted curves to the data given in Table 5.4. 172
- 5.16 The axial force, N_θ distribution at the outer surface of the eyeball when the pressure exerted by the scleral buckle around the equator of the eyeball, P_S is equal to the intraocular pressure, P_{IOP} , 15mmHg. Again, the standard parameter values given in Table 5.2 were employed. 172
- 5.17 Qualitative behaviour given by the displacements due to the pressure exerted by the scleral buckle, P_S , at the equator of the eyeball. The values of the scleral buckle pressure are taken to be equal to 10mmHg, 20mmHg, 30mmHg, 40mmHg, 50mmHg and 60mmHg and the intraocular pressure, P_{IOP} is taken to be 15mmHg for each value of P_S . The parameter values required for these numerical calculation are the same as given in Table 5.2. 174
- 5.18 The deformation of the eyeball given by the displacements under the action of the scleral buckle for different values of the scleral and corneal Young's modulus. The value of the intraocular pressure, P_{IOP} has been taken to be equal to 15mmHg, the pressure provoked by the scleral buckle, P_S is equal to twice the P_{IOP} whereas the rest of the parameter values are given in Table 5.2. 174
- 5.19 Numerical calculation of the changes in the focal length around the equator of the eyeball under the pressure exerted by the scleral buckle. The points show the measurement data of the changes in focal length against the indentation whereas the solid lines are fitted curves to the points. The intraocular pressure, P_{IOP} is given by 15mmHg and the pressure exerted by the scleral buckle are taken to be equal to 10mmHg, 20mmHg, 30mmHg, 40mmHg, 50mmHg and 60mmHg. Each graph corresponds to different values of the scleral and corneal Young's modulus, E_s and E_c . The remaining parameters are given in Table 5.2. 176

5.20	The axial force, N_θ distribution at the outer surface of the eyeball under the action of the scleral buckle near the equator of the eyeball. The pressure exerted by the scleral buckle, P_S is assumed to be equal to the intraocular pressure, P_{IOP} , 15mmHg, whereas the remaining parameter required for these numerical calculations have been given in Table 5.2.	177
5.21	Qualitative behaviour of the shape of the eyeball presented by the displacements due to the pressure exerted by the scleral buckle, P_S , near the equator. The value of the the intraocular pressure, P_{IOP} is taken to be equal to 15mmHg for each different corresponding values of the pressure exerted by the scleral buckle which are equal to 10mmHg, 20mmHg, 30mmHg, 40mmHg, 50mmHg and 60mmHg. The parameter values inherent to these numerical calculation are given in Table 5.2.	178
5.22	The deformation of the eyeball near the equator presented by the displacements due to the pressure exerted by the scleral buckle, P_S which is equal to two times the intraocular pressure, P_{IOP} for different values of the Young's modulus of the sclera and the cornea.	178
5.23	Numerical calculation of the modified focal length of the eyeball near the equator for different material values of the Young's modulus of the sclera and the cornea. The standard parameters given in Table 5.2 are employed in these graph. The intraocular pressure, P_{IOP} is taken to be 15mmHg and the pressure provoked the indentation at $\phi = \frac{\pi}{3}$ are taken to be varied between 10mmHg to 60mmHg. The points show the measurement data of the modified focal length versus the indentation, whereas the solid lines are fitted curves that coresspond to the measurement data.	179
A.1	Schematic diagram of the sclera presenting the outer and the inner radius, R , pressure, P and volume, V	191
A.2	The graph of volume, V versus intraocular pressure, P for linear elastic theory given in equation (A.15). The standard parameter values given in section (A.1 - A.4).	193
A.3	The comparison graph of volume, V versus intraocular pressure, P between linear elastic theory such as given in Figure A.2 and Friedenwald's law given in equation (A.2). The solid line represents the volume changes for linear elastic theory whereas the line with the square marker denotes the Friedenwald's law. The parameter values are given in section (A.1 - A.4) are employed in this calculation.	194
A.4	The comparison between linear elastic theory and Friedenwald's law given in equations (A.15) and (A.2). The solid line represents the volume changes for linear elastic theory whereas the line with square marker denotes the volume changes for Friedenwald's law. The modulus of elasticity, E is considered to be 11×10^6 and the other parameter values given in section (A.1 - A.4) are employed in this graph.	194
A.5	The comparison between linear elastic theory and Friedenwald's law given in equations (A.15) and (A.2). The line with square marker and the solid line represent the corresponding volume, V versus intraocular pressure, P for Friedenwald's law and linear elastic theory. The modulus of elasticity, E and the Poisson's ratio, σ are considered to be 11×10^6 and 0.48. Both curves are plotted using typical values given in section (A.1 - A.4).	195

-
- A.6 The comparison graph of volume, V versus intraocular pressure, P between linear elastic theory and Friedenwald's law using the typical parameter values given in section (A.1 - A.4) together with the Poisson's ratio, σ which is assumed to be equal to 0.47). The solid line represents the volume, V changes for linear elastic theory whereas the square marker line denotes the volume, V changes for Friedenwald's law. 195
 - A.7 The comparison between linear elastic theory and Friedenwald's law given in equations (A.15) and (A.2). The solid and the square marker lines denote the corresponding volume, V versus intraocular pressure, P for linear elastic theory and Friedenwald's law. The Poisson's ratio, σ is considered to be 0.45 and the rest of parameter values given in section (A.1 - A.4). 196

List of Tables

2.1	Standard data used for calculations.	22
5.1	Summary of material parameters values for the cornea and the sclera from the previous studies showing: radius of the human eye (a), central corneal radius of curvature (a_c), radius of curvature of the equatorial sclera (a_s), cornea thickness (α_c), scleral thickness (α_s), corneal Young's modulus (E_c), scleral Young's modulus (E_s), Poisson's ratio of the cornea (ν_c) and Poisson's ratio of the sclera (ν_s).	147
5.2	The parameter values of the membrane eyeball model used in numerical calculations.	167
5.3	Pressure conversion units from 1mmHg to 60mmHg.	171
5.4	The measurement data of the tonometer pressure, P_T as predicted by the current numerical model and the Imbert-Fick law that corresponding to the given values of the intraocular pressure, P_{IOP} between 10mmHg and 45mmHg.	171

DECLARATION OF AUTHORSHIP

I, **Zuhaila Ismail**, declare that the thesis entitled **The Mathematical Modelling of Flow and Deformation in the Human Eye** and the work presented in the thesis are both my own, and have been generated by me as the result of my own research. I confirm that:

- this work was done wholly or mainly while in candidature for a research degree at this University;
- any part if this thesis has previously been submitted for a degree or any other qualification at this University or any other institution, this has been clearly stated;
- where I have consulted the published work of others, this is always clearly attributed;
- where I have quoted from the work of others, the source is always given. With the exception of such quotations this thesis entirely my own work;
- I have acknowledged all main sources of help;
- where the thesis is based on work done by myself jointly with others, I have made clear exactly what was done by others and what I have contributed myself;
- parts of this work have been published.

Signed:

Date:

List of Publications

1. Ismail, Z. and Fitt, A.D. (2008). **Mathematical Modelling of Flow in Schlemm's Canal and Its Influence on Primary Open Angle Glaucoma.** *International Conference on Science and Technology (ICSTIE): Applications in Industry and Education.* 1967 - 1973.
2. Ismail, Z., Fitt, A.D. and Please, C.P. **A Fluid Mechanical Explanation of the Spontaneous Reattachment of a previously Detached Descemet.** (Accepted for publication, to appear in IMA Journal of Mathematical Medicine and Biology)

Acknowledgements

Thanks to Almighty Allah S.W.T. for graciously bestowing me the perseverance to undertake this research. Special thanks are due to University of Southampton for the opportunity to carry out research and to Universiti Teknologi Malaysia (UTM) for the financial support.

Warmest thanks and a deepest gratitude to Professor Alistair Fitt and Professor Colin Please, my academic fathers, for their invaluable advice and patient guidance, for the encouragement and useful critiques of this research work.

I would like to express my appreciation to the staff of Department of Mathematical Sciences, UTM, for all their help and support in completing my thesis writing.

I wish to express my heartfelt gratitude, appreciation and thanks to my beloved parents, my dear husband and my family, for a lifetime of love, concern, support and strength all these years; none of this would have been possible without them.

Last but not least, thanks to my friends, for all their support and for sharing me so often with my problems.

To my beloved parents, my dear husband and my family... .

Chapter 1

Introduction and Problem Formulation

1.1 Introduction

The human eye is one of the most important and sensitive organs in the human body. The eye is complex organ consisting of many parts, each essential for clear vision. The eye is a highly specialized organ regarding photoreception, the process by which light energy from the environment passes through the vitreous humour and is then focused directly onto the retina. This process produces changes in specialized nerve cells in the retina, which convert the light energy into electrical signals that are transmitted to the brain through the optic nerve. The brain then translates the electrical signals into images and this complex process is known as visual processing.

This chapter contains a basic description of the human eye in order to understand the relationship between the structure of the eye and how it functions. A general introduction about the causes of vision disorder that relate to the problems in the following chapters is given. In this chapter we also state the contributions of the thesis.

1.2 The Human Eye

The human eye is an incredibly complicated structure. Each part of the eye has its own special function and if just one of these parts is damaged or injured this may lead to blindness. Figure 1.1 shows the most important components of the human eye. There are three different layers within the eye. These are; (i) the outer layer, formed by the sclera and cornea; (ii) the middle layer, consisting of the anterior chamber, between the cornea and the iris and the posterior chamber, between the iris, the pupil and the ciliary muscle; bounded by the lens; and (iii) the internal layer, formed by the retina.

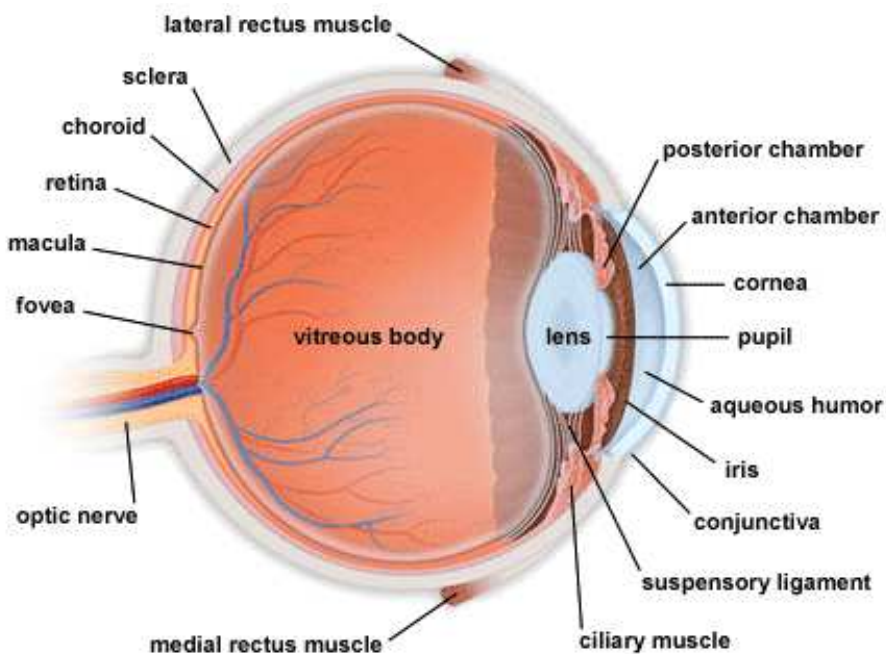


FIGURE 1.1: Schematic Diagram of the Human Eye. This figure was extracted from [134].

The **sclera** is the white tough outer wall of the eye. It is covered by the episclera, a fibrous layer between the conjunctiva and sclera and **conjunctiva**, a thin and transparent membrane that protects the eye. The **cornea** is a transparent membrane on the front of the eye. It allows light to pass through the eye and together with the lens. The cornea is responsible for seventy percent of the total focusing and the directing of light onto the retina.

The **anterior chamber** is shaped like a half moon and is situated in the front part of the eye between the lens and cornea. The diameter is typically between 12mm to 14mm [1], and it is a region filled with **aqueous humour**; a clear and colourless fluid. The aqueous humour is produced by the **ciliary body** which comprises of the ciliary process and the ciliary muscles, the latter which causes the lens to change shape.

The **posterior chamber** is the space behind the iris and in front of the lens. This chamber also contains aqueous humour. The **iris** is the coloured part of the eye that controls the size of the **pupil** - the black area in the centre of the iris dilates and contracts to regulate the quantity of light that reaches the retina. The **lens** is located between the anterior and posterior poles, and is a transparent and flexible structure that changes shape so that it can focus on objects at different distances.

The **vitreous humour**, also known as the vitreous body, is a colourless, transparent gel with a high water content that fills the back portion of the eye behind the lens. This fluid helps the eye keep its spherical shape, as well as helping to support the retina. The **choroid**, a membrane found between the sclera and the retina, lines the back of

the eyes containing many blood vessels. The choroid supplies the eyes with nutrients and oxygen.

The **retina** is the innermost layer, and is the light-sensitive part of the eye. The retina contains millions of cells known as photoreceptors, and each photoreceptor is linked to a nerve fibre. It converts light rays into electrical signals and sends the signals to the brain through the **optic nerve**. The head of the optic nerve, known as the optic disc, corresponds with the blind spot of the eye whilst the fovea is the most sensitive area of the retina, providing the sharpest vision. For further detailed information, refer to [1, 98, 99].

1.3 Common Causes of Vision Loss

1.3.1 Primary Open Angle Glaucoma (POAG)

Glaucoma is a group of eye diseases that is one of the most common causes of preventable blindness, [136]. Glaucoma often begins unnoticed and damages the eye without showing any sign or symptom till very late. [137], reported that about 1 in 50 people over 40 have glaucoma in the UK and it becomes more common with increasing age. Glaucoma can affect anyone, but there is a particular risk in people with a family history of glaucoma, short sightedness, diabetes or people from African or Afro-Caribbean origin.

No one knows exactly what the cause of glaucoma is. In most cases glaucoma is an eye condition where the optic nerve is damaged. The damage to the optic nerve is due to an increase in pressure within the eye, see Figure 1.2. In a healthy eye, the intraocular pressure is maintained at a constant level when the aqueous humour is produced consistently and is allowed to flow out of the eye [1]. The aqueous humour flows into the anterior chamber and exits via the trabecular meshwork into the Schlemm canal, which is a circular, irregular canal within the scleral tissues, and eventually exits at the collector channels. For further information, see Section 2.2. In many cases of glaucoma, the ‘draining system’ becomes clogged so that aqueous humour cannot leave the eye as fast as it is produced [136]. This causes the intraocular pressure to build up in the eye, causing damage to the optic nerve and leading to loss of vision.

Primary open angle glaucoma (POAG), acute angle closure glaucoma (AACG), secondary glaucoma and congenital glaucoma are examples of different types of glaucoma, of which POAG or chronic glaucoma is the most common [138]. The term ‘open angle’ refers to the angle between the iris and sclera. In AACG this angle has narrowed. AACG is uncommon but can cause a sudden increase in intraocular pressure. This can cause the eye to become painful and the patient may exhibit redness in the eye or blurred vision. Secondary glaucoma occurs as a result of an external disease, for

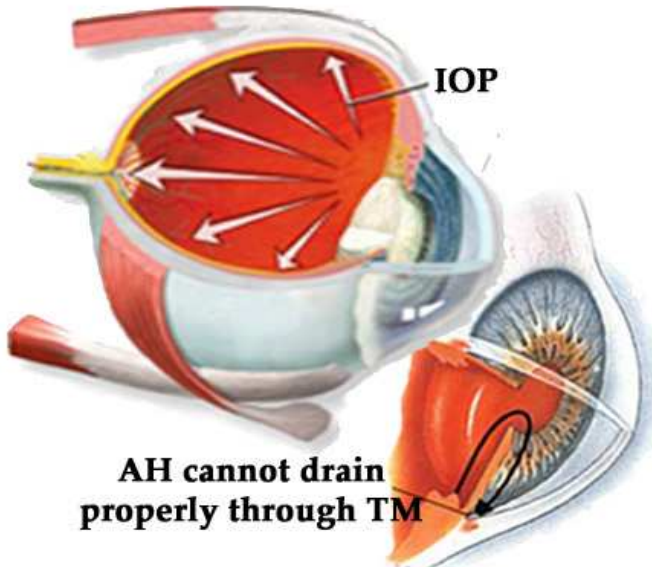


FIGURE 1.2: Mechanism for Intraocular Pressure (IOP) increases in Human Eyes.
This figure was reproduced from [135].

example, inflammation, trauma, previous surgery, diabetes or a tumour [138]. It can also be caused by certain drugs such as steroids. Congenital glaucoma, also called childhood glaucoma, is where the glaucoma is present from birth [139]. Early symptoms of childhood glaucoma are poor vision, light sensitivity, tearing, and blinking. Permanent loss of vision can occur if congenital glaucoma is not recognized and treated quickly.

In this thesis we focus on POAG. POAG most often occurs when the intraocular pressure increases. The cause of this high pressure is generally accepted to be an imbalance in the production and drainage of aqueous humour in the eye [23]. The trabecular meshwork that normally allows the aqueous humour to drain from inside the eye does not function properly. The amount of fluid inside the eye therefore increases, thereby raising the intraocular pressure.

We have seen that POAG occurs due to an increased intraocular pressure. The average pressure in the healthy population is 14mmHg - 16mmHg and one can find values ranging between 10.50mmHg and 20.50mmHg [1]. Elevated intraocular pressure is usually defined to be an eye pressure of greater than 21mmHg. People can have optic nerve damage without having elevated intraocular pressure. This condition is known as normal pressure glaucoma [140]. In contrast, some people can also have elevated IOP without signs of optic nerve damage or vision loss. However, generally, if the intraocular pressure is high then there is a much increased risk of developing glaucoma and eventual vision loss.

POAG is a major health concern throughout the world because of the lack of symptoms and progressive nature. Most people with POAG do not notice problems until

substantial visual loss has occurred. Untreated POAG may cause blindness but can be prevented if POAG is diagnosed and treated early [140]. With appropriate screening and treatment by an ophthalmologist, a specialist in eye care and surgery, POAG can be controlled before significant visual loss occurs. The aim of the treatment is to decrease the level of intraocular pressure, which is measured with an instrument called a tonometer.

Tonometers are classified according to how the eyeball is deformed which is either indented or flattened [97]. The most widely used indentation tonometer is the Schiotz tonometer, while the tonometer that measures intraocular pressure by flattening the cornea is known as an applanation tonometer; the most accurate of which is the Goldmann tonometer. Applanation tonometers are normally based on the principle of Imbert-Fick's law [100]. This law states the relationship between the external applied forces and the internal pressure of the flattened sphere. Intraocular pressure is important in the diagnosis of glaucoma and in monitoring the effectiveness of medication used to control intraocular pressure.

1.3.2 Rhegmatogenous Retinal Detachment (RRD)

Retinal Detachment is another major cause of vision loss. The retina is a thin layer of nerve tissue that lines the back inside wall of the eye. Retinal detachment is a disorder of the eye in which the retina peels away or tears from its underlying layer of support tissue, see Figure 1.3. Occasionally, posterior vitreous detachment, or injury to the head or eye may cause a small tear in the retina. When this happens, the liquefied vitreous humour can flow through the tear and push the retina away from the eye wall. Thus, the retina becomes separated from the back wall of the eye and is removed from its blood supply and source of nutrition [2]. If a small part of the retina becomes detached, it will often cause the remainder to detach the entire retina and the retina will lose its ability to function. Then all vision will be lost.

There are three main types of RD: Rhegmatogenous Retinal Detachment (RRD), Exudative Retinal Detachment (ERD) and Tractional Retinal Detachment (TRD). RRD is due to a tear or break in the retina that allows the liquefied vitreous humour to pass through the tear and detach the retina. An ERD most often occurs due to inflammatory disorders or the presence of a tumour which can lead to fluid accumulating underneath the retina without the presence of a hole or tear. Finally, TRD results from the pull of fibro-vascular tissues within the vitreous cavity. A common cause of TRD is proliferative diabetic retinopathy [143].

RRD is the most common type of retinal detachment [4]. It usually occurs when a tear in the retina allows liquefied vitreous humour to accumulate with a separation of the neurosensory retina from the underlying retinal pigment epithelium [3]. Most cases of

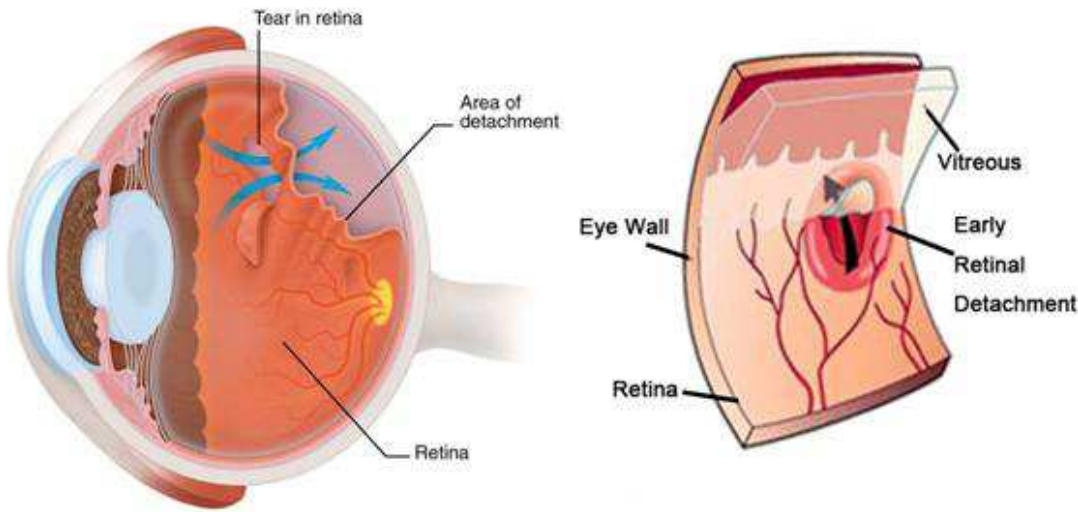


FIGURE 1.3: Retinal Detachments. This figure was extracted from [141] and [142].

RRD are associated with posterior vitreous detachment. Posterior vitreous detachment is a normal event occurring in most middle aged people [143]. The vitreous humour, a gel-like substance inside the eye, changes with age. The central part of the vitreous humour becomes more liquid and the outer part, the cortex, peels away from the retina, this can cause the symptoms of posterior vitreous detachment [144]. Awareness of the symptoms of posterior vitreous detachment is one of the first steps in preventing RRD.

Treatment options for RRD include scleral buckling surgery, vitrectomy and pneumatic retinopexy [145]. The traditional surgery for RRD is scleral buckling surgery. The surgery is usually performed under a general anaesthetic and treats the retinal tear with cryotherapy [146]. Cryotherapy is used to freeze the retina to the wall of the eye. This surgery involves using a buckle, a piece of silicone sponge or solid silicone which is secured around the eyeball. The buckle will push the sclera toward the retinal tear and effectively repairs the tear. Usually the scleral buckle is permanently left on the eye.

1.3.3 Descemet Membrane Detachment (DMD)

The cornea is a transparent tissue that covers the front of the eye. It is important for the focusing ability of the eye, and even a small change in the structure of the cornea can result in a large change in the quality of the focus. The cornea consists of five layers of membranes. The stroma provides the cornea with its strength, whilst the endothelium maintains the health and the clarity of the stroma, [5]. However in this study we are interested in the descemet membrane which lies between the stroma and the endothelium. The descemet membrane is a thin layer of tissue that gradually becomes thicker with age [6]. The descemet membrane plays an important role in the

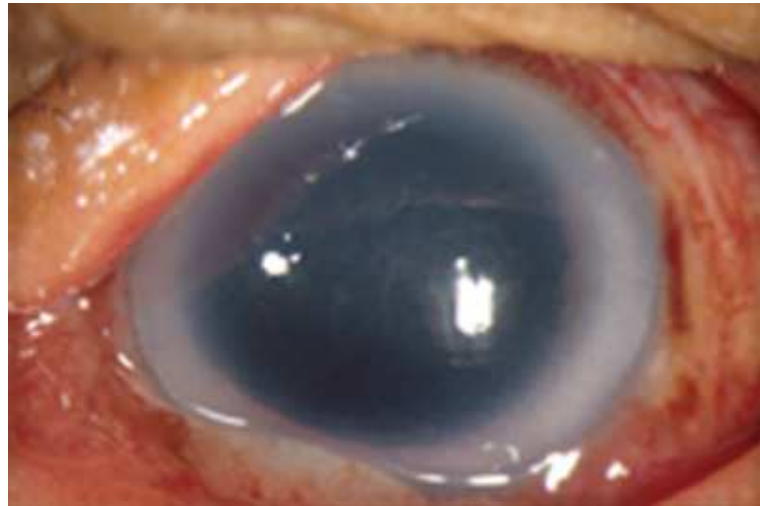


FIGURE 1.4: DMD after cataract surgery. This figure was extracted from [147].

corneal hydration and in the maintenance of the endothelium after surgery [6].

Descemet membrane detachment (DMD) allows aqueous humour to flow underneath the detached descemet membrane and causes the membrane to separate from the stroma. Detachments can be classified as planar or nonplanar, see Section 4.3 for a detailed explanation. Classification of both the type and severity of the detachment can determine whether medical, surgical or nonsurgical treatments are used in attempts to manage the DMD [82]. Appropriate management may prevent the patients from suffering vision loss. Most detachments are small and have little effect on the patients vision. Large detachments are rare but can lead to blindness [7]. Therefore DMD should not be taken lightly. Although uncommon, DMD can also arise as a surgical complication, most often during cataract surgery, see Figure 1.4.

1.4 Contributions of the Thesis

Based on the common causes of vision loss described above, we address these problems and develop four different mathematical models. Firstly, we present a mathematical model regarding the flow of aqueous humour through the trabecular meshwork into the Schlemm canal. The aim of doing this is to predict the intraocular pressure and investigate how this influences primary open angle glaucoma (POAG). In this research we extend the study of [23] and we examine several different cases relating aqueous humour flow to changes in intraocular pressure for various submodels.

Secondly, we propose three mathematical models relating to the development of rhegmatogenous retinal detachment (RRD), caused by the flow of liquefied vitreous humour driven by the saccadic rotations of the human eye. The first and second models concern

the fluid flow between rigid walls, and between one rigid and one moving wall. Then, the third model is a model of liquefied vitreous humour flow driven by saccadic eye motion. The third model is the extension on the studies of [56, 69, 70] and several cases have been classified and examined. The purpose of consider these models is to calculate and analyse the flow behaviour and the deformation of the detached retina.

Thirdly, we build on the work presented in [75] to develop a mathematical model of the flow of aqueous humour in the anterior chamber with the presence of a detached descemet membrane. This model is able to explain how this can cause the spontaneous reattachment or worsening of the descemet membrane detachment as noted in [76]. Lastly, we develop the eyeball membrane model to calculate and examine the elastic membrane shells of the human eye under the effect of the tonometer and the sclera buckle.

This research concerns a number of human eye problems as stated above. The fluid flow models are based on the Navier-Stokes equations and the solid mechanics models are governed by the general equations of equilibrium and axisymmetric spherical shells. The analytical and numerical calculations are carried out to analyse the flow behaviour and the deformation of the human eye. Neither experiment nor clinical tests on human or animal eyes are involved in this research.

1.5 Mathematical Framework of this Thesis

Chapter 1 explains the background of the research, a general description of the main components of the human eye is given as well as a description of the function of each part. A brief explanation regarding disorders of the eye brought on by POAG, RRD and DMD is given. A detailed discussion of the anatomy and physiology of parts of the human eye and their influence on POAG, RRD and DMD will be given later in the following chapters. Each relevant part of the anatomy will be explained in the appropriate chapter. This information is important in order to gain a better understanding of the nature and physiological effects of each problem. From the relevant information we can develop mathematical models of the problems.

Chapter 2 presents mathematical analysis of aqueous humour flow through the trabecular meshwork and into the Schlemm canal in order to predict changes in intraocular pressure. In this chapter, we discuss the anatomy and physiology of the trabecular meshwork and aqueous humour dynamics and give a detailed explanation regarding POAG in human eyes and its diagnosis and treatment. Using the Navier-Stokes equations and considering lubrication theory flow and Friedenwalds law the governing equations are derived and solutions given. Then, we examine a large number of different cases relating aqueous humour flow to changes in intraocular pressure for various sub-cases. A number of analytical approaches have been considered in this analysis such as

the regular perturbation method and the singular perturbation method - Van Dyke's matching principle has been used. We examine high level analytical cases by using MAPLE [8], and finally we discuss and summarize the results in terms of physical conditions.

The following chapter presents some paradigm problems of retinal detachment. We start by looking at a simple model by considering the fluid driven by a pressure gradient flow between rigid walls. We assume that a thin flap, the detached retina which is kept in contact with the plane wall, the retina is elastic and deformable so that the general theory of beams under axial loading is applicable. In this study, we use an asymptotic series solution in order to calculate and analyse the flow behaviour and the deformation of the detached retina, as well as the fluxes of fluid and the bending moment. Next, we examine and consider the fluid flow between one rigid and one moving wall. We then propose another realistic model of retinal detachment, which concerns the manner in which liquefied vitreous humour flows during saccadic rotations of the eyeball. We model the saccadic rotations as oscillations of frequency, ω and amplitude, ε about a vertical axis and we consider the Navier-Stokes equations in spherical coordinates in order to govern the problem. In particular, asymptotic series solutions have been used in order to find the azimuthal fluid velocities at leading and second order and also to find the pressure.

Chapter 4 concerns a fluid mechanical model of aqueous humour flow in the anterior chamber around a DMD. The model is developed to explain how either spontaneous reattachment or worsening of the detached descemet membrane may occur. The aqueous humour flow is governed by the lubrication theory limit of the Navier-Stokes equations and the equation of DMD motion is determined using the theory of beams under axial loading. In this chapter, the anatomy and physiology of the cornea and DMD and also the causes and management of DMD will be presented. We start by analysing the aqueous humour flow driven by buoyancy effects when no detachment is present. Then we apply the analogy of buoyancy effects to a paradigm problem of flow through the flap in the rectangular-shaped region. We then propose a more realistic shaped model in order to examine the aqueous humour flow in the anterior chamber with a DMD.

Chapter 5 presents a mathematical analysis of membrane shells when undergoing tonometry and scleral buckling. Two mathematical models will be presented in this chapter: a mathematical model for tonometry and a mathematical model for a scleral buckle. In this chapter, we will discuss the anatomy and physiology of the eyeball, the measurement of the intraocular pressure and several instruments that are used to measure the intraocular pressure. Next we will present the derivation of the governing equations of the membrane theory for equilibrium and axisymmetric spherical shells. Then we will develop the two mathematical models by using the theory of membrane shells. Goldmann tonometry is performed to measure the intraocular pressure. Goldmann tonometry is based on the Imbert-Fick principle which relates external forces directly

to the internal pressure of a sphere times the area flattened by the force. A mathematical analysis of Goldmann tonometry will be carried out in order to determine the relationship between the external forces and the internal pressure. Scleral buckling surgery is probably the most commonly required procedure for RRD. The buckle is placed around the eyeball so that it pushes against the detached retina and forces the retina back into contact with the choroid. A mathematical description of a scleral buckle will be proposed to examine how the focal length of the eye is affected under the action of the external force.

Finally, in Chapter 6 we will summarize the work done for each problem in this thesis. Several suggestions for the modelling of the human eye will be stated for future research.

Chapter 2

Flow in the Schlemm Canal and its Influence on POAG

2.1 Introduction

Primary Open Angle Glaucoma (POAG) is the second leading cause of blindness worldwide after cataracts. It is also known as chronic glaucoma or “the silent thief of sight” because of the lack of early symptoms. Most patients with POAG are not aware that they have the disease until significant vision loss has occurred. POAG is essentially caused by an increase in the intraocular pressure due to an imbalance in the production and drainage of aqueous humour in the eye. Aqueous humour is continually being produced by the ciliary body but sometimes cannot be properly drained due to a blockage of the trabecular meshwork. Thereby the intraocular pressure within the eye builds up. In this chapter a mathematical model is presented for the flow of aqueous humour through the trabecular meshwork and into the Schlemm canal in order to predict changes in intraocular pressure. The governing equations have been developed using the Navier-Stokes equations and lubrication theory. To predict changes in intraocular pressure Friedenwald’s law has been applied. Several different cases have been examined in the model relating aqueous humour flow to changes in intraocular pressure for various submodels: (i) the permeability, k in Darcy’s law being constant or varying with a pressure difference; (ii) the trabecular meshwork being deformable so that the general theory of a beam under axial load is applicable. This chapter includes a brief introduction to the anatomy and physiology of the trabecular meshwork and the fluid dynamics of the aqueous humour inflow and outflow, along with a review of possible methods to diagnosis and treat POAG. A mathematical model of aqueous humour flow through the trabecular meshwork and into the Schlemm canal will be presented. This is followed by analysis of a large number of different cases and the results of each of these cases are discussed in terms of POAG.

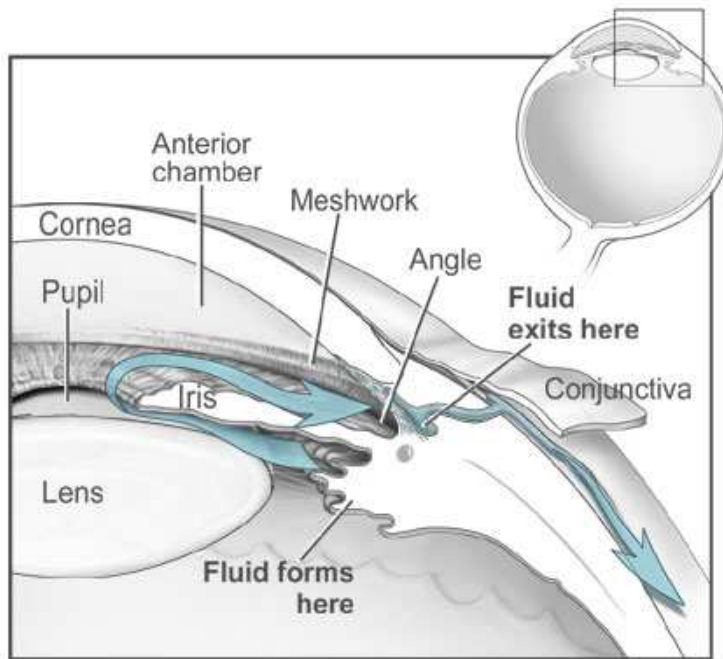


FIGURE 2.1: Cross section of the eye showing how the aqueous humour flow continuously in and out of the anterior chamber. This figure was extracted from [150].

2.2 Anatomy and Physiology of the Trabecular Meshwork, and Aqueous Humour Dynamics

Figure 2.1 shows the area of the human eye that is responsible for producing the aqueous humour that circulates at the front of the eye. The anterior chamber is positioned at the front of the eye and is an empty region surrounded by the cornea, pupil and iris. The aqueous humour is produced through ciliary processes by the ciliary body and flows into the posterior chamber of the eye. This process is known as aqueous humour inflow [30]. Note that the ciliary processes and the ciliary muscles are part of the ciliary body. The ciliary muscles are responsible for holding and changing the shape of the lens by suspensory ligaments called zonular ligaments.

The aqueous humour enters the anterior chamber and flows between the iris and the lens through the pupil. It provides the lens and the cornea with nutrients and oxygen, and carries away excess protein, blood and other waste products, [1]. Furthermore, the aqueous humour also contributes to maintaining the shape of the eye and governs the intraocular pressure. The aqueous humour is then recycled by exiting the anterior chamber at the open angle of the eye between the cornea and the iris junction and returning to systemic circulation, see Figure 2.1. This process is known as aqueous humour outflow, [30, 31]. There are two different exit routes for aqueous humour outflow. The main route is the conventional or trabecular pathway, where the aqueous

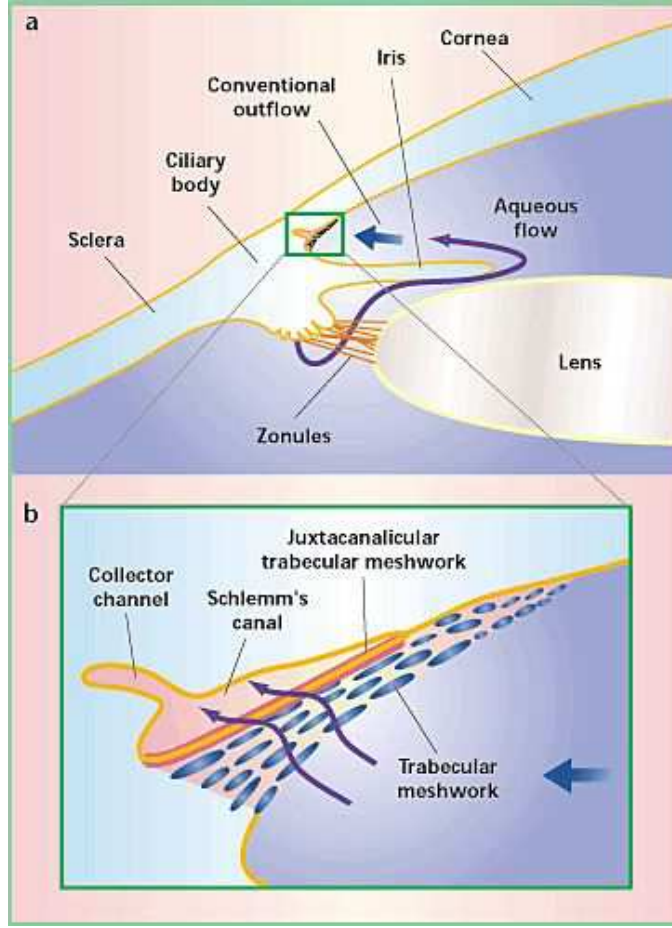


FIGURE 2.2: Schematic diagram of eye structures involved in aqueous humour dynamics. This figure was extracted from [151].

humour travels through the trabecular meshwork into the drainage angle. The aqueous humour leaves through a passageway known as the Schlemm canal and exits at collector channels, see Figure 2.2. The second route for aqueous humour exit occurs when aqueous humour passes through the uveoscleral or nonconventional pathway via the intercellular spaces between the iris root and the ciliary muscle fibres. For further details see [1, 30, 31, 32]. In human eyes, the flow of aqueous humour exits the eye via the trabecular meshwork (conventional or trabecular pathway) is much stronger and more dominant compared to the other pathway of aqueous humour outflow [30]. Thus in this study we consider the effect of the trabecular pathway and neglected the effects of uveoscleral outflow.

The conventional pathway consists of the trabecular meshwork and the Schlemm canal. The trabecular meshwork is a filter and contains three main layers; the inner uveal meshwork, the corneoscleral meshwork and the juxtacanalicular meshwork, see Figure 2.3. The aqueous humour outflow, via the trabecular pathway and through the different regions has been explained in detail in [30, 31, 32]. According to studies in [30, 31, 32], the aqueous humour travels through the trabecular meshwork moving from the inner

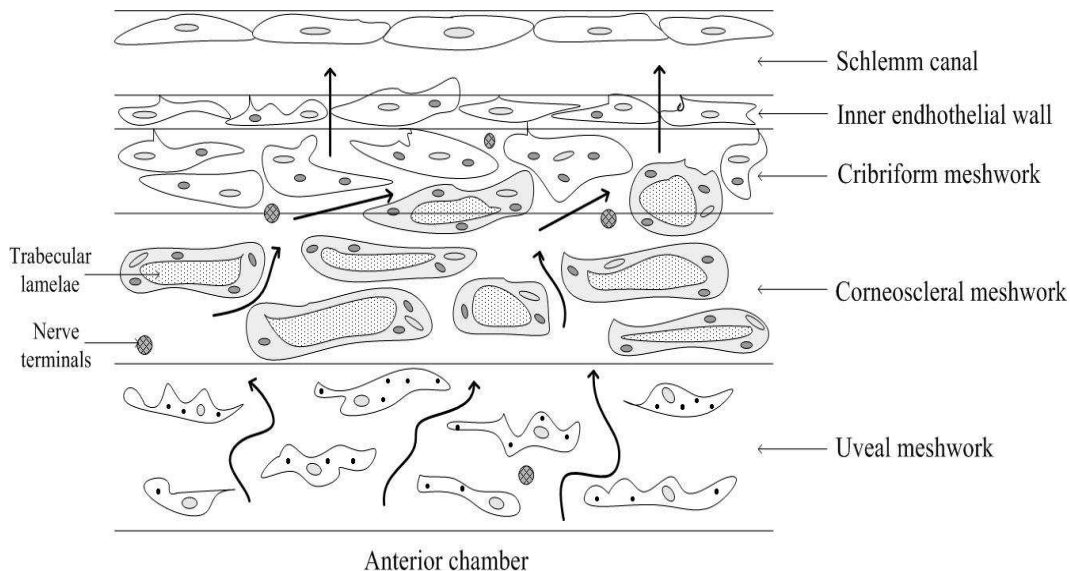


FIGURE 2.3: The structure of the Trabecular Meshwork.

uveal meshwork and into the anterior chamber angle. The inner uveal meshwork contains slender cord-like trabeculae, where the trabeculae spaces are larger than the corneoscleral meshwork, Figure 2.3. This layer does not cause much resistance to the aqueous humour outflow. The aqueous humour then flows into the middle layer; the corneoscleral meshwork. The corneoscleral meshwork consists of large amount of trabecular lamellae which are formed by glycoproteins, collagen, hyaluronic acid and elastin, [30]. The intercellular spaces in this layer become narrower and this increases the resistance to the flow of aqueous humour. Finally the aqueous humour moves to the outermost part, the juxtaganular meshwork, otherwise known as the cribriform meshwork. At this stage, the porosity of the trabecular meshwork decreases. The aqueous fluid then crosses the last barrier, which is the inner endothelium wall of the Schlemm canal, that is in direct contact with the juxtaganular meshwork, before exiting at a collector channel. Studies in [30, 31, 32] have agreed that the highest resistance to the outflow of aqueous humour is generated in or near the inner endothelium wall of the Schlemm canal either in normal eyes or in glaucomatous eyes. [32], noted that the function of the inner endothelium wall of the Schlemm canal is to control the flow of aqueous humour through this region, by changing the position of the giant vacuoles and pores that are found in cells in the inner endothelium wall.

Aqueous humour volume is produced constantly to maintain a constant intraocular pressure level. The intraocular pressure in the eye is determined by the volume of aqueous humour that enters and exits the eye through the trabecular meshwork and into the Schlemm canal before exiting at a collector channel. It has long been assumed that the volume of aqueous humour and the intraocular pressure in the eye are related by Friedenwald's law. Due to this relation this study attempted to examine volume changes of aqueous humour and to convert volume changes of aqueous humour to intraocular

pressure changes. In healthy eyes, the intraocular pressure values range between 10 to 21mmHg. Chronic open angle glaucoma is thought to be caused when the aqueous humour passes too slowly through the trabecular meshwork. As the aqueous humour builds up, the intraocular pressure inside the eye rises to a level that may damage the optic nerve which may result in vision loss.

2.2.1 POAG in Human Eyes

The most common type of glaucoma is Primary Open Angle Glaucoma (POAG). POAG leads to progressive optic nerve damage, see Figure 2.4, at the back of the eye [10, 11]. A number of studies [10, 12, 13] have reported POAG as a major cause of vision loss. POAG affects approximately one percent of the population over 40 years old and more than ten percent over the age of 80 [10]. This relates to 70 million individuals worldwide in the year 2000 with 6.7 million people suffering from bilateral blindness [13]. [14] projected the prevalence of POAG in 2020. In 2020 [14] estimated that 11.1 million people will be blind from POAG. Based on blindness prevalence surveys, [12, 13, 14] show that the most treatable disease that causes blindness is POAG.

POAG can affect anyone, but commonly it will affect people who have a family history of glaucoma, short sightedness, or diabetes [149]. [15] presents data showing that the patients at the highest risk on contracting POAG include black people around 40 years old and above, white people over 65 years old and either people with a family history of glaucoma or people with a history of diabetes. According to [16], POAG is an age-related disease because the variations in the normal aging processes could change the balance towards the initiation of glaucoma and its progression. Several theories have been analysed in order to postulate what types of aging processes are most common for triggering the onset of POAG.

A number of researchers have studied the problem of POAG, [17, 18, 19, 20, 21]. It is agreed that POAG occurs when the amount of aqueous humour inside the eye rises due to the trabecular meshwork not functioning properly, thereby the intraocular pressure increases. Although [15] agrees that high intraocular pressure is a strong influence on whether or not the patient has POAG, they also point out that some patients with glaucoma have normal intraocular pressure and several patients with higher intraocular pressure do not have glaucoma. Many previous studies, [17, 18, 19, 20, 21] have given us an understanding of the nature of the flow of aqueous humour, through the trabecular meshwork into the Schlemm canal, that produces a pressure drop in the eye. Studies in [17, 18, 19, 20, 21] show that the relationship between pressure and flow is linear, with flow resistance increasing slowly with pressure. From these studies, one can formulate and develop relevant mathematical models.

According to studies in [17, 18, 19, 20, 21], if the intraocular pressure increases, then

the wall of the Schlemm canal collapses dramatically. “The collapse of the canal caused by elevated intraocular pressure offers resistance to the aqueous flow through it”, [20]. [21] modelled aqueous humour flow in the Schlemm canal and assumed the inner wall of the canal to be rigid. [17] improved the model by treating the inner wall of the canal as a porous elastic wall, and proposed that “the trabecular meshwork is a series of linear springs that allow the inner wall of canal to deform in proportion to the local pressure drop across it”. [18] developed a mathematical model of aqueous humour flow through the trabecular meshwork and into the Schlemm canal by observing the effects that influenced the collapse of the wall. They show the modelling equations may be reduced to a second order problem for the fluid pressure and then solve the problem using an approximate iterative scheme. [19] has shown how the full problem for a collapsible inner wall, which is developed by [18], can be reduced to a linear first order equation that can be solved exactly in terms of a definite integral. [20] extended the study of [18] by considering the inner wall of canal to be both resilient and elastic.

2.2.2 Diagnosis and Treatment of POAG

Early diagnosis of glaucoma is important to prevent the structure of the eye from being permanently damaged and to avoid inevitable blindness. A variety of diagnostic tools have been developed for glaucoma detection and management. Several common tests for glaucoma are tonometry, ophthalmoscopy and perimetry, [97, 33]. The intraocular measurements are essential in diagnosis and follow-up treatment of glaucoma. Thus tonometry is used to measure the intraocular pressure in the eye. There are two types of tonometry for measuring the intraocular pressure which are, tonometers that in contact with the eye, *e.g.* Goldmann type applanation tonometer, or non contact tonometers, *e.g.* the ocular response analyser [97].

Ophthalmoscopy is a technique that has been used to examine inside the eye by directly looking at the optic nerve through the pupil. [33] stated that ophthalmoscopy helps to look at colour and shape of the optic nerve and thus determine if glaucoma is present and how serious it is. A perimetry test, also known as a visual field test, is conducted to check the field of vision and to evaluate the function of the optic nerve, [33]. Glaucoma is usually a very slow, progressive disease. Patients normally have to be regularly checked and watched carefully before the final diagnosis is made and treatment is initiated. Treatment for each glaucomatous patient is different depending on the conditions of the patient and the type of glaucoma. However the objective of the treatment of POAG is to reduce the intraocular pressure to the normal range, either by reducing the production of aqueous humour or by increasing the aqueous humour outflow through the trabecular meshwork drainage system, [35].

There are three basic options for treatment of glaucoma. Initial treatment often involves medications, *i.e.* eye drops and tablets. If medication is not effective and not tolerable,

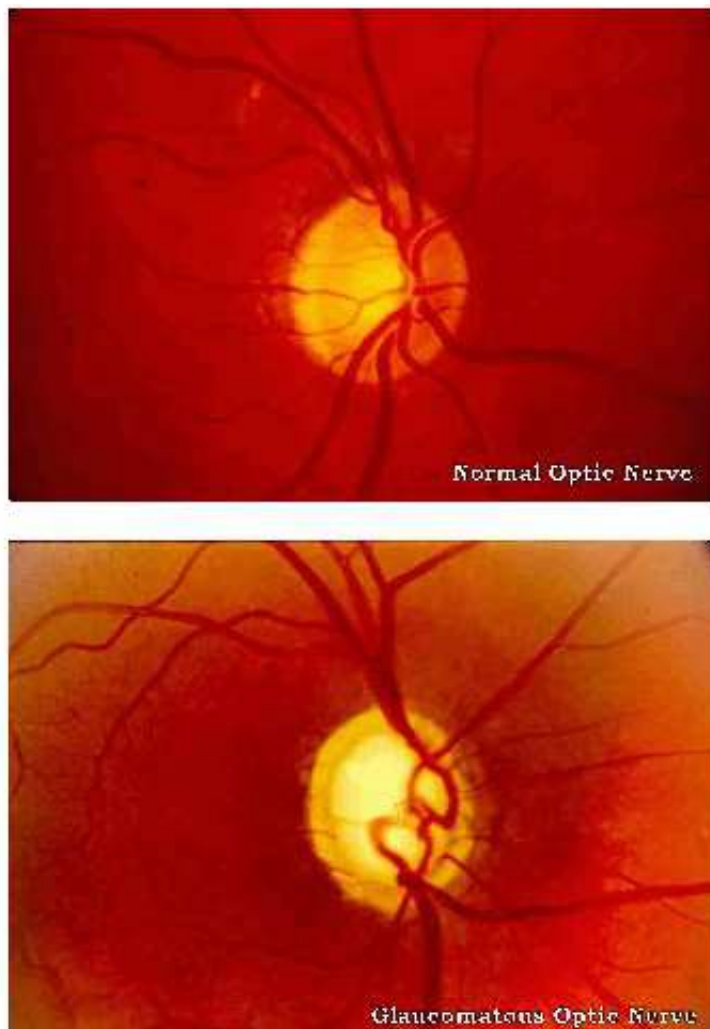


FIGURE 2.4: Healthy and Glaucomatous Optic Nerve. This figure was extracted from [152].

then laser treatments are considered. An example of laser treatment is laser trabeculoplasty. Laser trabeculoplasty delivers laser energy to the trabecular meshwork. The aims of this treatment is to assist the progress of aqueous humour outflow from the eye in order to decrease intraocular pressure in patients with POAG [34]. There are two types of laser trabeculoplasty which are argon laser trabeculoplasty and selective laser trabeculoplasty. The argon laser trabeculoplasty uses an argon laser to open up the drainage angle of the eye and provides a significant reduction of intraocular pressure in the eye with POAG, pigmentary glaucoma, and exfoliative glaucoma [39]. [39] stated that the argon laser trabeculoplasty is likely to be most suitable treatment to treat older patients which the medical treatment no longer can control the glaucoma and patients with early diagnosed POAG. However, the argon laser trabeculoplasty produces coagulation damage to the trabecular meshwork and contributes to the limited effectiveness of retreatment. The selective laser trabeculoplasty is recently developed in order to treat POAG and other forms of glaucoma, and to overcome the problem

of the argon laser trabeculoplasty. This technique has the advantages compared to the argon laser trabeculoplasty which are less collateral tissue damage and allows to repeat the laser surgery over the same area of the angle [40].

Sometimes medications are still needed after laser treatments because these treatments can cause inflammation and irritation of the eye. When both medications and laser treatments are no longer effective in reducing the intraocular pressure inside the eye, the final treatment option is glaucoma drainage surgery. The most common surgery is called a trabeculectomy, where a surgical drain is created to allow the aqueous humour to flow through the clogged trabecular meshwork, [35]. There are several other glaucoma drainage treatments available that provide alternatives to trabeculectomy procedures, such as a tube shunt or a glaucoma drainage device, [36, 37]. However each treatment has its own risks and complications. Therefore early diagnosis and treatment is important before the disease becomes difficult to control.

2.3 Motivation for the Mathematical Model

Studies in [17, 18, 19, 20, 21] have focused on the flow of aqueous humour through the trabecular meshwork and into the Schlemm canal before the aqueous humour exits at a collector channel. However these studies did not consider that the flows involved can be interpreted to be lubrication theory flows [22]. Despite the final fluid dynamics equations that are given in Section 2.4 being very similar to those in [20], extra coupling is now added to determine the intraocular pressure. This contrasts with [20], where the fluid flow was assumed to be through a narrow elliptical and circular channel. A previous study, [23], modelled the flow of aqueous humour from the anterior chamber through the trabecular meshwork and into the Schlemm canal and coupled this flow to predict changes in intraocular pressure. However, [23] only examined simple modelling cases where the trabecular meshwork and the flow speed are assumed to be undeformable and consistent. [23] also only considered the case where flow through the trabecular meshwork was determined by Darcy's law. In this current study, we extend the work of [23] in order to predict changes in intraocular pressure, by considering the permeability, k , in Darcy's law to be either constant or varying with pressure difference. The purpose of considering the permeability, k , is to take into account the physical conditions that the intercellular spaces in the trabecular meshwork become narrower when the pressure difference across it rises up and this will increase the resistance to the flow of aqueous humour [30]. We further assume that the trabecular meshwork is deformable due to the structure of the trabecular meshwork that consists of trabecular cells, elastic-like fibres and proteoglycans, and this is the main site of resistance to aqueous humour outflow [98].

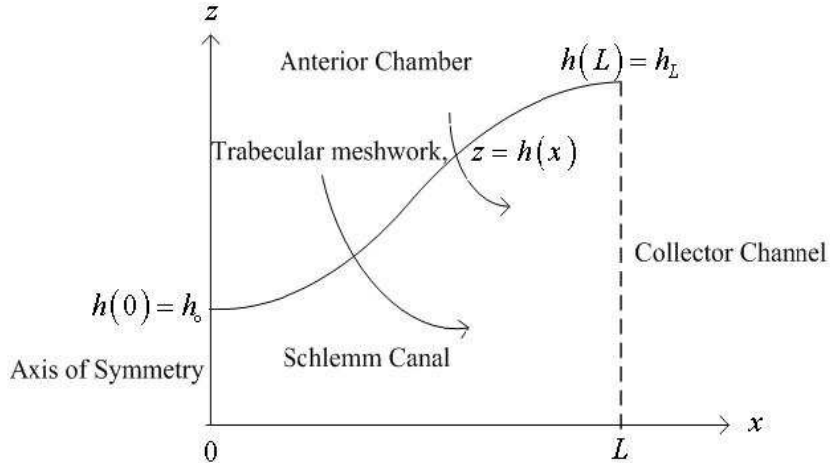


FIGURE 2.5: Schematic diagram of flow through the trabecular meshwork into the Schlemm canal.

2.4 Modelling of Aqueous Humour Flow through the Trabecular Meshwork and into the Canal of Schlemm

We shall now derive a model of aqueous humour flow through the trabecular meshwork into the Schlemm canal.

2.4.1 The Governing Equations

A two-dimensional representation of aqueous humour flow, through the trabecular meshwork into the canal of Schlemm, in order to predict changes of intraocular pressure is shown in Figure 2.5. The aqueous humour flow is assumed to be quasi-steady, Newtonian, viscous and incompressible. In this problem the parameter values are obtained from [17] and [24], such that,

$$L = 600\mu m, \quad h_o = 25\mu m, \quad \rho = 1003 kg m^{-3}, \quad \text{and} \quad \mu = 0.75 \times 10^{-3} Pas.$$

where L , h_o , ρ and μ denote a typical length, an undeformed depth, a density and a dynamic viscosity respectively. $\delta = \frac{h_o}{L}$ denotes the aspect ratio. Using these values, we obtain $\delta = 0.04$, the Reynolds number $Re \sim 4$ and the reduced Reynolds number $\delta^2 Re \sim 0.0064$. Therefore the lubrication theory limit may be used to reduce the Navier-Stokes equations for an incompressible Newtonian viscous fluid, as in [22], and thus we restate the governing equations and the boundary conditions of this problem,

such that

$$\begin{aligned} p_x &= \mu u_{zz}, \\ p_z &= 0, \\ u_x + w_z &= 0 \quad \text{for } x \in [0, L] \quad \text{and} \quad 0 \leq z \leq h(x), \end{aligned} \tag{2.1}$$

with the boundary conditions

$$\begin{aligned} u(x, 0) &= w(x, 0) = 0, \\ u(x, h(x)) &= 0, \quad w(x, h(x)) = w_h(x), \\ p_x(0, z) &= 0, \quad p(L, z) = p_{out}. \end{aligned} \tag{2.2}$$

Here L is defined to be the length between the symmetry axis and a collector channel, p is the pressure, $u(x, z)$, and $w(x, z)$ are the components of the fluid velocity, subscripts denote derivatives, w_h is the flow speed through the trabecular meshwork, and $p_{out} = 9\text{mmHg}$ ([17]) is the pressure at a collector channel. We note that [23] also developed the governing equations (2.1) and the boundary conditions (2.2) that are shown above.

2.4.2 Friedenwald's Law

To close the model, we must relate the intraocular pressure to the eye's aqueous humour production and removal. [26] states that measurements of the ocular rigidity of the sclera, choroid or retina portion of the eye have traditionally been expressed in terms of 'Friedenwald's law' rather than using a traditional linear elasticity approach involving Young's modulus and Poisson's ratio. We use Friedenwald's law to predict changes of intraocular pressure. [25] states that the volume and intraocular pressure of a human eye are related. Friedenwald's law states that p_1 and p_2 , two intraocular pressures, are related to the respective ocular volumes V_1 and V_2 via

$$K(V_1 - V_2) = \log_{10} p_1 - \log_{10} p_2.$$

Therefore,

$$p_1 = p_2 e^{(K(V_1 - V_2) \ln 10)}.$$

where K is a constant equal to $2.5 \times 10^7 \text{m}^{-3}$ [24]. We denote normal conditions using a subscript n and altered conditions using a subscript i . We therefore find that,

$$p_i = p_n e^{\tilde{K}(V_i - V_n)}$$

where $\tilde{K} = K \ln 10 \text{m}^{-3}$. If we differentiate the equation above with respect to time we get,

$$\begin{aligned} \frac{dp_i}{dt} &= \tilde{K} p_n e^{\tilde{K}(V_i - V_n)} (\dot{V}_i - \dot{V}_n), \\ \frac{dp_i}{dt} &= \tilde{K} p_i (\dot{V}_{in} - \dot{V}_{out}) \end{aligned} \tag{2.3}$$

where $\dot{V}_i = \dot{V}_{in}$ ($0.33 \times 10^{-10} m^3 s^{-1}$) [38] and $\dot{V}_n = \dot{V}_{out}$ ($m^3 s^{-1}$) denote the respective total amounts of fluid flowing in and out of the eye. Note that a linearization of Friedenwald's law has been done in Appendix A using a linear elastic theory. The purpose of doing this is to examine whether Friedenwald's law or the theory of linear elasticity is the best theory to apply in order to convert the volume changes to intraocular pressure changes. From the results, see Appendix A, we conclude that both theories can calculate the corresponding volume changes versus intraocular pressure but we derive different models. Although linear elasticity is in some agreement with Friedenwald's law, there are some differences. We also get the same results from the theory of Friedenwald's law and theory of linear elasticity if we use different values for the constants, see Appendix A. Because of this, we now use the theory of Friedenwald's law in order to predict changes in intraocular pressure.

2.4.3 Solution Procedures

The governing equations may now be solved by integrating equation (2.1) and using the boundary conditions given in equation (2.2) in order to derive the fluid velocity, u . We find that,

$$u = \frac{p_x}{2\mu} (z^2 - hz). \quad (2.4)$$

From equations (2.4), (2.1) and the boundary conditions we can determine the fluid velocity w as

$$w = \frac{p_{xx}}{2\mu} \left(\frac{hz^2}{2} - \frac{z^3}{3} \right) + \frac{1}{4\mu} p_x h_x z^2. \quad (2.5)$$

From equation (2.5) we find that the pressure, $p(x)$, satisfies

$$w_h(x) = \left[\frac{p_x h^3}{12\mu} \right]_x \quad (p(L) = p_{out}, p_x(0) = 0) \quad (2.6)$$

where $w_h(x)$ and $h(x)$ are unknown function of x to be determined. The volumetric flow rate, \dot{V}_C , in this problem for a single collector channel, is given by

$$\dot{V}_C = \int_0^{h(L)} B u|_{x=L} dz, \quad (2.7)$$

where B is undeformed breadth and is equal to $300\mu m$, [17]. Substituting equation (2.4) into equation (2.7), we find that

$$\dot{V}_C = - \frac{B p_x h^3}{12\mu} \Big|_{x=L}. \quad (2.8)$$

Generally, the total number of collector channels, N is about 30, [27], so that the total amount of fluid flowing out of the eye is $\dot{V}_{out} = N\dot{V}_C$. Therefore, the intraocular pressure $p_i(t)$ may now be determined by equation (2.3) with $p_i(0) = p_{io}$. Note that

Parameter Name	Symbol	Value
Typical length	L	$600\mu m$
Undeformed depth	h_0	$25\mu m$
Density	ρ	$1003 kg m^{-3}$
Dynamic viscosity	μ	$0.75 \times 10^{-3} Pa s$
Constant	K	2.5×10^7
Total amounts of fluid flowing in	\dot{V}_{in}	$0.33 \times 10^{-10} m^3 s^{-1}$
Undeformed breadth	B	$300\mu m$
Number of collector channel	N	30
Pressure at a coleector channel	P_{out}	9mmHg or 1200Pa
Normal pressure	P_{io}	14mmHg or 1867Pa
Trabecular meshwork resistance	R_T	1.96×10^{13}

TABLE 2.1: Standard data used for calculations.

the modelling so far is identical to that contained in [23].

2.5 Mathematical Analysis of the Results and Discussion

Several different effects have been examined in the model relating aqueous humour flow to changes in intraocular pressure for various submodels. These are: (i) the permeability, k in Darcy's law may be either constant or varying with pressure difference (not constant); (ii) the trabecular meshwork may be deformable due to the trabecular meshwork that acts as a porous filter and likes an elastic fibres, so that the general theory of a beam bending under axial loads is applicable. We consider the permeability, k is varying with pressure difference because the pores in the trabecular meshwork close when the pressure difference across it increases. Both effects that have been considered in this study are not included in the work of [23]. In this section, we present a number of different cases and a discussion of each case in terms of the aqueous humour flow behaviour and the deformation of the trabecular meshwork. Each of the cases studied have been solved analytically, but for higher order equations MAPLE [8] was used.

2.5.1 Aqueous Humour Flow through the Trabecular Meshwork determined by Darcy's Law

Darcy's law was formulated in 1856, based on research regarding the flow of water through beds of sand [148]. The law states the relationship between the flow rate through a porous medium where gravity is ignored, the viscosity of the fluid and the

pressure difference over a given distance [22], in the form

$$\bar{q} \propto \nabla p.$$

We now consider flow through the trabecular meshwork determined by Darcy's law, and assume,

$$w_h(x) = -\frac{k}{d\mu}(p_i - p) \quad (2.9)$$

where d is the width of the trabecular meshwork and the permeability k is (for the present) constant. The negative sign shows that the fluid flows from high pressure to low pressure. The permeability k has been measured from the trabecular meshwork resistance, $R_T = \frac{\mu d}{kBL}$. The value of $R_T \sim 1.96 \times 10^{13}$ derived in [23] is in very close agreement with measured values in [17, 27]. Here we extend the work of [23] which examines the simple modelling cases where $h(x) \equiv h_o$ and $w_h(x) \equiv \alpha < 0$ are both constant. [23] also examines the case of flow through the trabecular meshwork that is determined by Darcy's law and we discuss the case again in detail here. We now examine a number of different cases relating aqueous humour flow through the trabecular meshwork determined by Darcy's law by considering $h(x) \equiv h_o$, where h_o is a constant and the permeability, k , is either constant or not constant.

Case (1): The permeability, k in Darcy's law is constant

In this, the simplest case, we consider the flow through the trabecular meshwork determined by Darcy's law, equation ((2.9)) and assume that $h(x) \equiv h_o$ is constant. We now equate equation (2.9) with equation (2.6), yielding

$$\left[\frac{p_x h_o^3}{12\mu} \right]_x = -\frac{k}{d\mu}(p_i - p), \quad (2.10)$$

$$p_{xx} = \frac{-12k}{dh_o^3}(p_i - p),$$

$$p_{xx} - \beta p + \beta p_i = 0, \quad \text{where} \quad \beta = \frac{12k}{dh_o^3}. \quad (2.11)$$

The parameter β represents the relative importance of the permeability of the trabecular meshwork and the flow in Schlemm's canal. We now solve equation (2.11) by using the boundary conditions given in equation (2.6). We find that

$$p = \left(\frac{p_{out} - p_i}{e^{\sqrt{\beta}L} + e^{-\sqrt{\beta}L}} \right) \left(e^{\sqrt{\beta}x} + e^{-\sqrt{\beta}x} \right) + p_i. \quad (2.12)$$

By differentiating equation (2.12) with respect to x and substituting into equation (2.8), we find that

$$\dot{V}_c = - \left(\frac{\sqrt{\beta}Bh_o^3}{12\mu} \right) \left(\frac{e^{\sqrt{\beta}L} - e^{-\sqrt{\beta}L}}{e^{\sqrt{\beta}L} + e^{-\sqrt{\beta}L}} \right) (p_{out} - p_i)$$

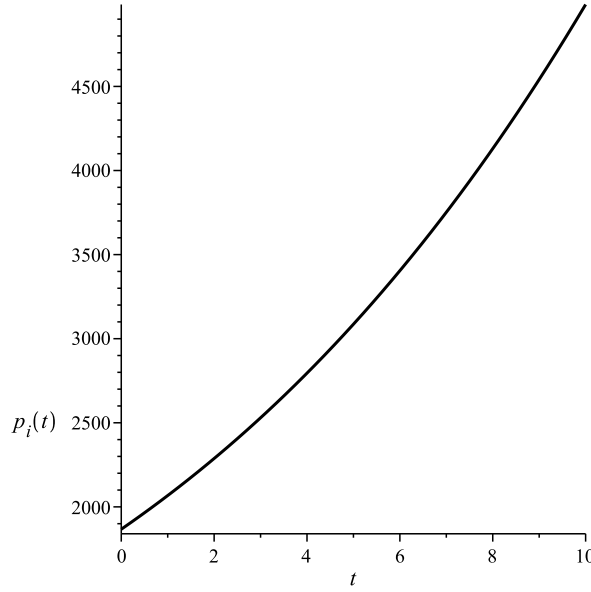


FIGURE 2.6: The changes in intraocular pressure, $p_i(t)$ in ten seconds given in equation (2.16), when the permeability, k in Darcy's law is constant. The standard parameter values, Table 2.1, have been imposed to calculate and plot this figure. The changes in intraocular pressure start from normal intraocular pressure which is equal to 14mmHg ($\cong 1867\text{Pa}$).

which can be written as

$$\dot{V}_c = \left(\frac{\sqrt{\beta} B h_o^3}{12\mu} \right) \tanh(\sqrt{\beta} L) (p_i - p_{out}).$$

Thus the total amount of fluid flowing out of the eye is

$$\dot{V}_{out} = \frac{NB\sqrt{\beta}h_o^3}{12\mu} (p_i - p_{out}) \tanh(\sqrt{\beta}L). \quad (2.13)$$

We now substitute equation (2.13) into equation (2.3) to give the total change in intraocular pressure;

$$\frac{dp_i}{dt} = p_i \left[\tilde{K} \left(\dot{V}_{in} - \frac{NB\sqrt{\beta}h_o^3}{12\mu} (p_i - p_{out}) \tanh(\sqrt{\beta}L) \right) \right]. \quad (2.14)$$

Equation (2.14) can be simplified by substituting $\frac{1}{R_T L} = \frac{k_B}{\mu d}$. Thus we obtain that

$$\frac{dp_i}{dt} = p_i \left[\tilde{K} \left(\dot{V}_{in} + \frac{N \tanh(\sqrt{\beta}L) p_{out}}{\sqrt{\beta} L R_T} \right) - \frac{\tilde{K} \tanh(\sqrt{\beta}L) p_i}{\sqrt{\beta} L R_T} \right] \quad \text{where } p_i(0) = p_{io}. \quad (2.15)$$

Equation (2.15) is a separable differential equation and therefore be solved to give the exact solution

$$p_i(t) = \frac{\alpha p_{io}}{(\alpha + \gamma p_{io}) e^{-\alpha t} - \gamma p_{io}} \quad (2.16)$$

where

$$\alpha = \tilde{K} \left(\dot{V}_{in} + \frac{N \tanh(\sqrt{\beta}L) p_{out}}{\sqrt{\beta} L R_T} \right) \quad \text{and} \quad \gamma = -\frac{\tilde{K} \tanh(\sqrt{\beta}L)}{\sqrt{\beta} L R_T}.$$

The solution of equation (2.16) is plotted in Figure 2.6. Figure 2.6 presents the intraocular pressure changes when the permeability, k in Darcy's law is assumed to be constant. From Figure 2.6 we can see the intraocular pressure increases rapidly to the high intraocular pressure, 30mmHg ($\cong 4000$ Pa) in less than eight seconds. The high intraocular pressure shows that the amount of aqueous humour inside the eye rises due to either the collector channel becoming blocked or a resistance of the trabecular meshwork increasing. This rapid increases of intraocular pressure may cause blindness. Noted that equation (2.14) has a steady state at p_i equal to $-\frac{\alpha}{\gamma}$ (constant). This value of p_i makes the right hand side of equation (2.14) equal to zero. The intraocular pressure remains normal with p_i equal to $p_{io} = 14$ mmHg ($\tilde{1867}$ Pa). Therefore

$$p_{io} = -\frac{\alpha}{\gamma} = p_{out} + \frac{\dot{V}_{in} R_T \sqrt{\beta} L}{N} \coth(\sqrt{\beta} L).$$

Case (2): The permeability, k in Darcy's law is $k \sim (p_i - p)$

In Case (2), the permeability, k , is no longer constant. We now assume that the permeability, k is proportional to the pressure difference, $k = \tilde{A}(p_i - p)$ where \tilde{A} is constant. This means that when the pressure difference across the trabecular meshwork decreases, the intercellular spaces in the trabecular meshwork becomes narrow and vice versa. Substituting the value of k into equation (2.10), gives

$$\left[\frac{p_x h_o^3}{12\mu} \right]_x = -\frac{\tilde{A}}{d\mu} (p_i - p)^2. \quad (2.17)$$

We now simplify equation (2.17), to give

$$p_{xx} + \vartheta p^2 - (2\vartheta p_i) p + \vartheta p_i^2 = 0 \quad \text{where} \quad \vartheta = \frac{12\tilde{A}}{dh_o^3}. \quad (2.18)$$

The non dimensional ϑ again expresses the relative importance of flow through the trabecular meshwork and viscous drag in Schlemm's canal. In the normal scenario, when the intercellular spaces of the trabecular meshwork become narrower, the flow of aqueous humour through the trabecular meshwork into the Schlemm canal is reduced and thus rise up the intraocular pressure. To examine this scenario, we look at the size of the parameter, ϑ . We introduce the asymptotic expansion,

$$p = p_0 + \vartheta p_1 + \vartheta^2 p_2 + \dots O(\vartheta^3). \quad (2.19)$$

By substituting equation (2.19) into equation (2.18) and applying the boundary condi-

tions (2.6), we obtain

$$\begin{aligned} & (p_0 + \vartheta p_1 + \vartheta^2 p_2 + \dots)_{xx} + \vartheta(p_0 + \vartheta p_1 + \vartheta^2 p_2 + \dots)^2 \\ & - 2\vartheta p_i(p_0 + \vartheta p_1 + \vartheta^2 p_2 + \dots)^2 + \vartheta(p_i)^2 = 0, \end{aligned} \quad (2.20)$$

with

$$\begin{aligned} p_{0x} + \vartheta p_{1x} + \vartheta^2 p_{2x} + \dots &= 0 \quad \text{at } x = 0, \\ p_0 + \vartheta p_1 + \vartheta^2 p_2 + \dots &= p_{out} \quad \text{at } x = 1. \end{aligned} \quad (2.21)$$

From equations (2.20) and (2.21), we deduce that to leading order $\vartheta^{(0)}$,

$$p_{0xx} = 0, \quad (2.22)$$

$$p_{0x}(0) = 0 \quad \text{and} \quad p_0(1) = p_{out}. \quad (2.23)$$

To first order, $\vartheta^{(1)}$,

$$p_{1xx} + p_0^2 - 2p_ip_0 + p_i^2 = 0, \quad (2.24)$$

$$p_{1x}(0) = 0 \quad \text{and} \quad p_1(1) = 0, \quad (2.25)$$

and to second order $\vartheta^{(2)}$,

$$p_{2xx} + 2p_0p_1 - 2p_ip_1 = 0, \quad (2.26)$$

with

$$p_{2x}(0) = 0 \quad \text{and} \quad p_2(1) = 0. \quad (2.27)$$

We can now solve for $\vartheta^{(0)}$, $\vartheta^{(1)}$ and $\vartheta^{(2)}$ with the relevant boundary conditions to give at leading order, $\vartheta^{(0)}$,

$$p_0(x) = p_{out}, \quad (2.28)$$

at first order, $\vartheta^{(1)}$,

$$p_1(x) = -(p_i^2 - 2p_ip_{out} + p_{out}^2)x^2 + p_i^2 - 2p_ip_{out} + p_{out}^2, \quad (2.29)$$

and at second order, $\vartheta^{(2)}$,

$$p_2(x) = (p_{out} - p_i)(p_i^2 - 2p_ip_{out} + p_{out}^2) \left[-\frac{x^4}{6} + x^2 - \frac{5}{6} \right]. \quad (2.30)$$

We now substitute equations (2.28), (2.29) and (2.30) into equation (2.19), to give the equation for the pressure as

$$\begin{aligned} p &= p_{out} + \vartheta \left[-(p_i^2 - 2p_ip_{out} + p_{out}^2)x^2 + p_i^2 - 2p_ip_{out} + p_{out}^2 \right] \\ &+ \vartheta^2 (p_{out} - p_i)(p_i^2 - 2p_ip_{out} + p_{out}^2) \left[-\frac{x^4}{6} + x^2 - \frac{5}{6} \right] + O(\vartheta^3). \end{aligned} \quad (2.31)$$

We now differentiate equation (2.31) with respect to x and substitute into equation (2.8) to find the volumetric flow rate,

$$\begin{aligned}\dot{V}_c = & \left[\frac{2\vartheta B h_o^3}{12\mu} (p_i^2 - 2p_i p_{out} + p_{out}^2) L - \frac{\vartheta^2 B h_o^3}{12\mu} (p_{out} - p_i) \right. \\ & \cdot (p_i^2 - 2p_i p_{out} + p_{out}^2) \left(-\frac{2L^3}{3} + 2L \right) \left. \right].\end{aligned}$$

Thus the total amount of fluid flowing out of the eye is

$$\begin{aligned}\dot{V}_{out} = & \left(\frac{2\vartheta N B h_o^3}{12\mu} \right) (p_i^2 - 2p_i p_{out} + p_{out}^2) L \\ & - \left(\frac{\vartheta^2 N B h_o^3}{12\mu} \right) (p_{out} - p_i) (p_i^2 - 2p_i p_{out} + p_{out}^2) \left(-\frac{2L^3}{3} + 2L \right).\end{aligned}\quad (2.32)$$

We now substitute equation (2.32) into equation (2.3) to find that the total change in intraocular pressure is given by

$$\begin{aligned}\frac{dp_i}{dt} = & p_i \left[\tilde{K} \left(\dot{V}_{in} - \left(\frac{2\vartheta N B h_o^3}{12\mu} \right) (p_i^2 - 2p_i p_{out} + p_{out}^2) L \right. \right. \\ & \left. \left. - \left(\frac{\vartheta^2 N B h_o^3}{12\mu} \right) (p_{out} - p_i) (p_i^2 - 2p_i p_{out} + p_{out}^2) \left(-\frac{2L^3}{3} + 2L \right) \right) \right]\end{aligned}\quad (2.33)$$

where $p_i(0) = p_{io}$. Thus we now attempt to solve and analyse the change of intraocular pressure, $p_i(t)$ (equation (2.33) subject to the boundary condition, $p_i(0) = p_{io}$) when ϑ is small and large. Figure 2.7 shows the change of intraocular pressure when ϑ is small. It shows that when the value of ϑ decreases (so that the permeability, k is also reducing), the intraocular pressure decreases. Then we analyse the change of intraocular pressure when ϑ is large (the graph for this case has not been shown here). We find that the permeability, k is increasing, and the intraocular pressure increases. These results show that the intercellular space of the trabecular meshwork becomes narrow and there is a resistant of flow of aqueous humour flowing out through the collector channel. However in this case the intraocular pressure does not increase to a high intraocular pressure even when the collector channel becomes blocked. The Case (2) where the permeability, k is proportional to the pressure difference, $k = \tilde{A}(p_i - p)$, seldom happens to patients with POAG. The results of Case (2) agree with those of other researchers who found that some patients with POAG have normal intraocular pressure and some patients with higher intraocular pressure do not have glaucoma.

Case (3): The permeability, k in Darcy's law is $k \sim (1/(p_i - p))$

We now consider the flow through the trabecular meshwork determined by a nonlinear Darcy's law. We consider this case due to the scenario when the pores in the trabecular meshwork close, as the pressure difference across it increase. If the pressure rises to a

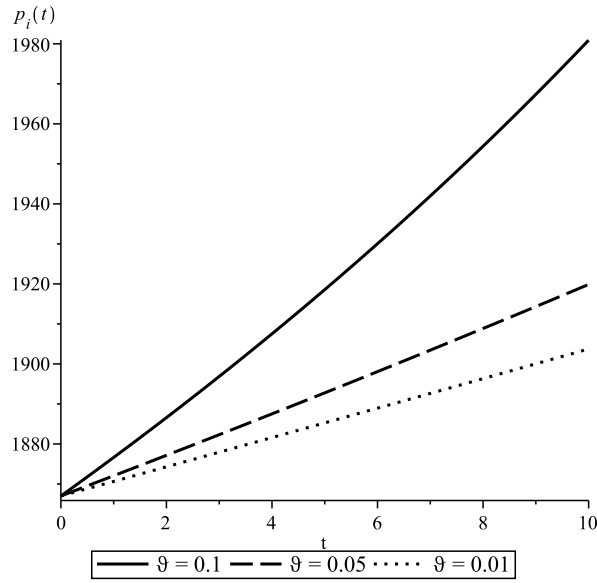


FIGURE 2.7: The changes in intraocular pressure, $p_i(t)$ in ten seconds by solving equation (2.33) numerically and using the typical parameter values such as listed in Table 2.1. In this case, the permeability, k in Darcy's law is assumed to be proportional to the pressure difference through the trabecular meshwork for different values of ϑ .

level that may damage the optic nerve, then this may result in vision loss. Assuming that the permeability, k is inversely proportional to the pressure difference through the trabecular meshwork

$$k = \frac{\tilde{B}}{(p_i - p)} \quad \text{where } \tilde{B} \text{ is constant.}$$

Substituting the value of k into equation (2.10) yields

$$p_{xx}(x) = -\zeta \quad \text{where } \zeta = \frac{12\tilde{B}}{dh_o^3}. \quad (2.34)$$

Integrating equation (2.34) twice with respect to x , we find that

$$p(x) = -\zeta \frac{x^2}{2} + C_1x + C_2. \quad (2.35)$$

We substitute the boundary conditions given in equation (2.2) into the above equation and obtain

$$p(x) = \frac{\zeta}{2} [p_{\text{out}} + (1 - x^2)] \quad (2.36)$$

By differentiating equation (2.36) with respect to x , we deduce that

$$p_x(x) = -2\zeta x.$$

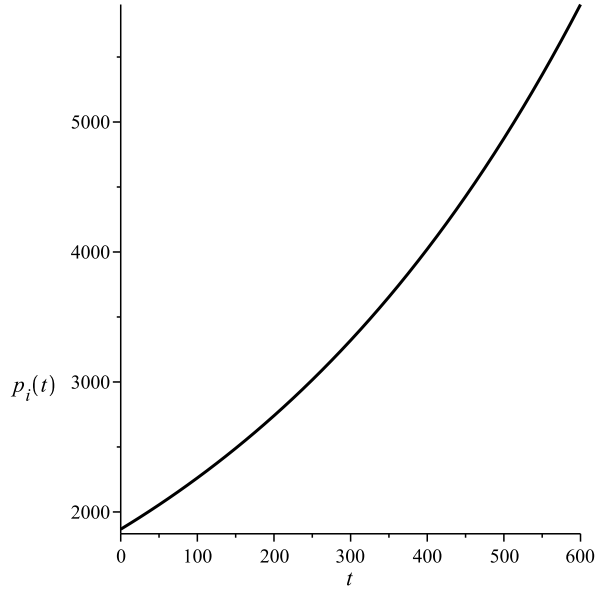


FIGURE 2.8: The changes in intraocular pressure, $p_i(t)$ given in equation (2.38), when the permeability, k in Darcy's law is inversely related to the pressure difference through the trabecular meshwork, $\frac{1}{p_i - p}$. The standard parameter values given in Table 2.1 have been employed in this calculation, whereas the total amount of fluid flowing out of the eye, \dot{V}_{out} is assumed to be zero.

The volumetric flow rate at $x = L$, \dot{V}_C , defined in equation (2.8) can be given by

$$\dot{V}_C = \frac{B\zeta L h_o^3}{6\mu}.$$

Thus the total amount of fluid flowing out of the eye is

$$\dot{V}_{out} = \frac{NB\zeta L h_o^3}{6\mu},$$

and the total intraocular pressure change is

$$\frac{dp_i}{dt} = \tilde{K} p_i \left(\dot{V}_{in} - \frac{NB\zeta h_o^3 L}{6\mu} \right). \quad (2.37)$$

We now determine the intraocular pressure, $p_i(t)$ by integrating equation (2.37) with respect to t and substituting the boundary condition ($p_i(0) = p_{io}$) and the value of ζ . Thus

$$p_i(t) = p_{io} e^{\left(\tilde{K} \left(\dot{V}_{in} - \frac{NB\zeta h_o^3 L}{6\mu} \right) t \right)}. \quad (2.38)$$

In this case, the intraocular pressure increases or decreases exponentially depending on whether the quantity $\frac{1}{d\mu}$ is less than or greater than $\frac{\dot{V}_{in}}{2NB\tilde{K}L}$. Figure 2.8 shows that if \dot{V}_{out} suddenly becomes zero (this is the total trabecular meshwork blockage) the intraocular pressure rises exponentially on a timescale of $\frac{1}{(\tilde{K}\dot{V}_{in})} \sim 521s$. Starting from a normal intraocular pressure of 14mmHg, the intraocular pressure increases to a

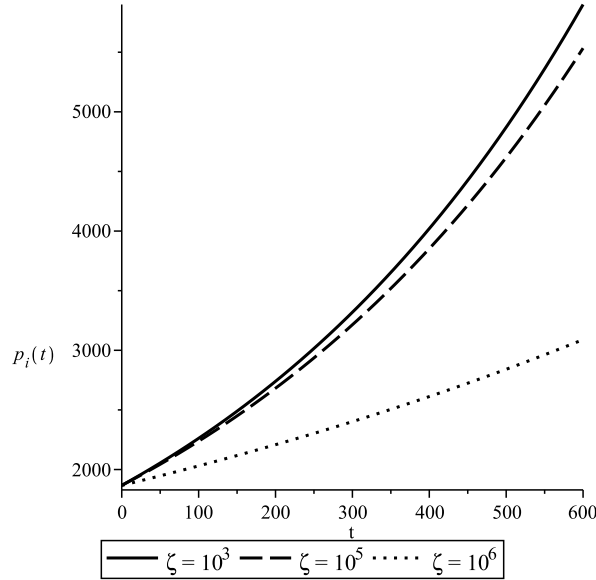


FIGURE 2.9: The changes in intraocular pressure, $p_i(t)$ given in equation (2.38), when the permeability, k in Darcy's law is inversely proportional to the pressure difference through the trabecular meshwork, $\frac{1}{p_i - p}$ for different values of ζ . The straight, the dotted and the dashed lines represent the values of ζ corresponding to $\zeta = 10^3$, $\zeta = 10^5$ and $\zeta = 10^6$. The parameter values inherent to these calculations are given in Table 2.1.

dangerous value of 30mmHg in just under seven minutes; blindness is inevitable. This case is similar to the case discussed in [23] that considered $h(x)$ and $w_h(x)$ to be both constant. Although these are the same cases, the reasoning is different. The speed turns out to be constant because of the assumption that we use in this case for the permeability, k in Darcy's law is inversely proportional to the pressure difference.

We now examine and plot equation (2.38) for three different values of ζ , Figure 2.9. When the value of ζ is increased from 10^3 to 10^6 , the changes of intraocular pressure are decreases. The solid and the dashed black lines denote the value of $\zeta = 10^3$ and $\zeta = 10^5$, both show the curves increase exponentially in ten minutes to a dangerous value of intraocular pressure, 45mmHg. However when $\zeta = 10^6$, the curve increases gradually to 23mmHg in ten minutes where the value still under the normal range of intraocular pressure. From Figure 2.9 it shows that the total amount of fluid flowing out indirectly increases when the value of ζ increases.

Case (4): The permeability, k in Darcy's law is $k \sim (1/(p_i - p)^{1/2})$

In case (4) we assume that the permeability k is inversely proportional to the square root of the pressure difference through the trabecular meshwork, $k = \frac{\tilde{C}}{\sqrt{(p_i - p)}}$ where \tilde{C} is constant. We consider this case in order to examine when the intercellular spaces of the trabecular meshwork becomes more wider compared to Case (3) as the pressure

difference across it decreases. We now substitute k into equation (2.10); thus we get that

$$p_{xx} = -\kappa\sqrt{p_i - p} \quad \text{with} \quad \kappa = \frac{12\tilde{C}}{dh_o^3} \quad (2.39)$$

We examine this case by assuming as κ may be either small or large, and this is because when the intercellular spaces of the trabecular meshwork become wider, the flow of aqueous humour through the trabecular meshwork into the Schlemm canal is increased and vice versa. We now assume the series solution for this case is

$$p(x) = p_0(x) + \kappa p_1(x) + \dots O(\kappa^2) \quad (2.40)$$

We substitute the series solution into equation (2.39) and obtain

$$(p_0 + \kappa p_1 + \dots)_{xx} = -\kappa\sqrt{p_i - (p_0 + \kappa p_1 + \dots)} \quad (2.41)$$

The boundary conditions are the same as given in equation (2.21). From equations (2.41) and (2.21), we deduce the equations and the boundary conditions for $\kappa^{(0)}$ and $\kappa^{(1)}$ such that at leading order, $\kappa^{(0)}$,

$$p_{0xx} = 0, \quad (2.42)$$

$$p_{0x}(0) = 0 \quad \text{and} \quad p_0(1) = p_{out}, \quad (2.43)$$

where $p_{out} = 9\text{mmHg}$ ([17]) is the intraocular pressure at a collector channel and at first order, $\kappa^{(1)}$,

$$p_{1xx} = -\sqrt{p_i - p_0} \quad (2.44)$$

with

$$p_{1x}(0) = 0 \quad \text{and} \quad p_1(1) = 0 \quad (2.45)$$

We now solve equation (2.42) subject to the boundary conditions in equation (2.43) and equation (2.44) subject to the boundary conditions in equation (2.45). Therefore we derive the equations for $p_0(x)$ and $p_1(x)$

$$\begin{aligned} p_0(x) &= p_{out}, \\ p_1(x) &= \frac{1}{2}\sqrt{p_i - p_{out}}(L^2 - x^2). \end{aligned} \quad (2.46)$$

We now substitute equations (2.46) into equation (2.41), yielding

$$p(x) = p_{out} + \frac{\kappa}{2}\sqrt{p_i - p_{out}}(L^2 - x^2) + O(\kappa^2). \quad (2.47)$$

Then we differentiate equation (2.47) with respect to x and substitute into equation (2.8). This gives the volumetric flow rate to be

$$\dot{V}_c = \left(\frac{Bh_o^3}{12\mu} \right) (\kappa L \sqrt{p_i - p_{out}}).$$

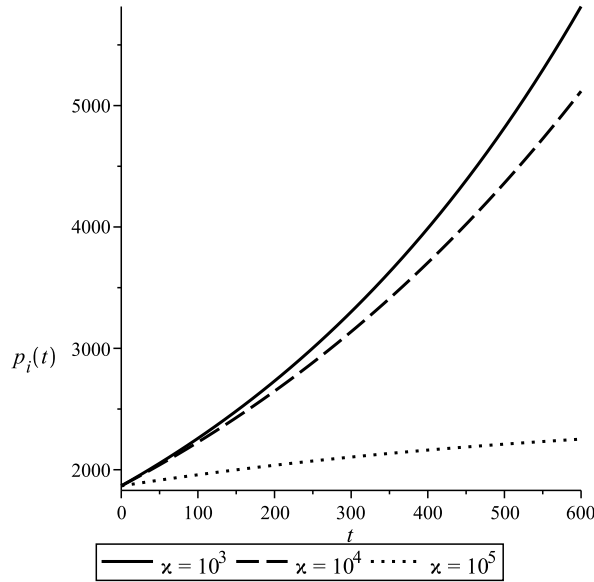


FIGURE 2.10: By solving equation (2.48) and using the parameter values given in Table 2.1, then the changes in intraocular pressure, $p_i(t)$ are plotted. The permeability, k in Darcy's law is inversely related to the square root of pressure difference through the trabecular meshwork, $(1/(p_i - p)^{1/2})$ for different values of ν . The straight, the dotted and the dashed lines show the values of ν corresponding to 10^3 , 10^4 , and 10^5 .

We can then substitute the above equation into $\dot{V}_{out} = N\dot{V}_c$ and the total amount of fluid flowing out of the eye, \dot{V}_{out} into equation (2.3), to obtain that

$$\frac{dp_i}{dt} = p_i \left[\tilde{K} \left(\dot{V}_{in} - \left(\frac{NBh_o^3 \nu L}{12\mu} \right) \sqrt{p_i - p_{out}} \right) \right] \quad (2.48)$$

where $p_i(0) = p_{io}$. Equation (2.48) may now be solved numerically and plotted for different values of ν , Figure 2.10. Figure 2.10 presents the intraocular pressure changes when ν increases (from 10^3 , 10^4 , and 10^5), then the changes of intraocular changes are decreases. The solid black line represents the intraocular changes when ν is equal to 10^3 , whereas the dashed and the dotted black lines denote the corresponding intraocular changes for ν equal to 10^4 , and 10^5 . Figure 2.10 shows that when ν is equal to 10^3 and 10^4 , the intercellular spaces of the trabecular meshwork becomes more wider, the flow of aqueous humour through the trabecular meshwork into the Schlemm canal increases, thus the intraocular changes increase exponentially to a dangerous value and when ν is equal to 10^5 the intraocular changes increase gradually in the normal range. As the values of ν decreases, the results (which we do not show here) show that the intraocular pressure rises exponentially to a dangerous value in just under several minutes. From the results it shown that there is almost no fluid flowing out of the eye, \dot{V}_{out} when ν is small, thus the intraocular pressure rises rapidly to a dangerous level.

Case (5): The permeability, k in Darcy's law is $k \sim (1/(p_i - p)^2)$

We now consider the permeability k is inversely proportional to the pressure difference squared through the trabecular meshwork, $k = \frac{\tilde{D}}{(p_i - p)^2}$ where \tilde{D} is a constant. This means that when the pores in the trabecular meshwork becomes narrow, as the pressure difference across it raised to the power two. Substituting the value of k into equation (2.10) gives,

$$p_{xx} = -\frac{\varsigma}{(p_i - p)} \quad \text{where} \quad \varsigma = \frac{12\tilde{D}}{dh_o^3}. \quad (2.49)$$

In this case, we examine the size of ς may be either large or small. We examine either ς is large or small due to the scenario that sometimes when the intercellular spaces of the trabecular meshwork become narrower and the permeability, k of the trabecular meshwork decreases, the change of intraocular pressure may be increased more than usual. We now solve using the previous series solution given in equation (2.40), such as in Case (4). By substituting equation (2.40) into equation (2.49), we find that

$$(p_0 + \varsigma p_1 + \dots)_{xx} = -\frac{\varsigma}{p_i - (p_0 + \varsigma p_1 + \dots)}. \quad (2.50)$$

The boundary conditions we use are the same as the boundary conditions in Case (2) and Case (4). Equations (2.50) and (2.21), and the boundary conditions for $\varsigma^{(0)}$ and $\varsigma^{(1)}$ are given at leading order, $\varsigma^{(0)}$, by

$$p_{0xx} = 0, \quad (2.51)$$

$$p_{0x}(0) = 0 \quad \text{and} \quad p_0(1) = p_{out}. \quad (2.52)$$

At first order, $\varsigma^{(1)}$, we have

$$p_{1xx} = -\frac{1}{(p_i - p_0)}, \quad (2.53)$$

$$p_{1x}(0) = 0 \quad \text{and} \quad p_1(1) = 0. \quad (2.54)$$

We now solve this system with the boundary conditions above in order to find $p_0(x)$ and $p_1(x)$. The solution is

$$\begin{aligned} p_0(x) &= p_{out}, \\ p_1(x) &= \frac{1}{2(p_i - p_{out})} (L^2 - x^2). \end{aligned} \quad (2.55)$$

Substituting equations (2.55) into equation (2.40), we get that

$$p(x) = p_{out} + \frac{\varsigma}{2(p_i - p_{out})} (L^2 - x^2) + O(\varsigma^2). \quad (2.56)$$

Then we differentiate equation (2.56) with respect to x , and substitute into equation (2.8) to obtain the volumetric flow rate, \dot{V}_c ,

$$\dot{V}_c = \frac{Bh_o^3}{12\mu} \left(\frac{\varsigma L}{p_i - p_{out}} \right).$$

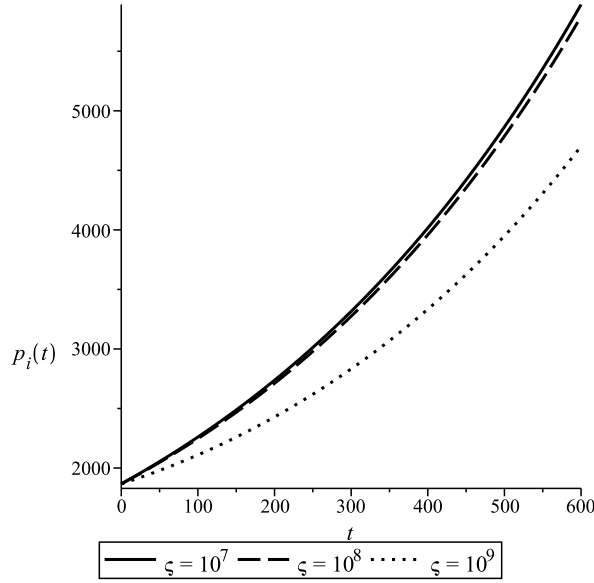


FIGURE 2.11: The change in intraocular pressure, $p_i(t)$ when the permeability, k in Darcy's law is inversely proportional to the pressure difference squared through the trabecular meshwork, $(1/(p_i - p)^2)$ for different values of ς . The straight, the dotted and the dashed lines represent the values of ς corresponding to 10^3 , 10^4 , and 10^5 .

Thus the total amount of fluid flowing out of the eye, \dot{V}_{out} is

$$\dot{V}_{out} = \frac{NB\varsigma Lh_o^3}{12\mu} \left(\frac{1}{p_i - p_{out}} \right). \quad (2.57)$$

The IOP, $p_i(t)$ may now be determined by substituting equation (2.57) into equation (2.3). Therefore the total change in IOP is

$$\frac{dp_i}{dt} = p_i \left[\tilde{K} \left(\dot{V}_{in} - \frac{NB\varsigma Lh_o^3}{12\mu} \left(\frac{1}{p_i - p_{out}} \right) \right) \right] ; \quad p_i(0) = p_{io}. \quad (2.58)$$

Equation (2.58) may now be solved and examined numerically for different values of ς in order to derive the change of intraocular pressure, $p_i(t)$. Figure 2.11 shows the change of intraocular pressure for ς is large. It shows that when the values of ς increase from 10^7 , 10^8 , and 10^9 , the intraocular pressure decreases. However when the value of ς bigger than 10^9 , the solution becomes infinite. The solid, dashed and dotted black lines represent the change of intraocular pressure associated with ς equal to 10^7 , 10^8 , and 10^9 . From Figure 2.11 we see that when ς are equal to 10^7 , 10^8 , and 10^9 , the pores of the trabecular meshwork open wider and the aqueous humour flows through the trabecular meshwork into the Schlemm canal is rises, then the changes of intraocular pressure for each corresponding values of ς is increases exponentially to a dangerous value of intraocular pressure. In this case, when we examined equation (2.58) which the size of ς is considered small, we found that the pressure in the human eye increases exponentially to the dangerous value of intraocular pressure and it seems that the total

fluid flowing out is almost zero and the trabecular meshwork is totally blockage. This high increases of intraocular pressure may cause blindness.

All these different five cases that have been examined above show the importance of using Darcy's law in order to model the flow through the trabecular meshwork into the drainage angle. Physically the trabecular meshwork acts as a porous filter and due to this circumstance, the permeability, k in Darcy's law is assumed to be either constant or not constant (the pores in the trabecular meshwork close when the pressure difference across it increase). From these five different cases that have been examined we found that we can calculate the changes in intraocular pressure that would occur if the resistance to aqueous humour drainage that are caused by an increase or decrease in the resistance to aqueous humour drainage via the trabecular meshwork (conventional or trabecular pathway). We now examine this further by assuming the trabecular meshwork to be deformable.

2.5.2 Model of the Trabecular Meshwork by Applying the Beam Bending Theory

By assuming the trabecular meshwork to be deformable we can model the trabecular meshwork using a simple model of beam bending, namely Bernoulli-Euler theory. This theory is applicable in this problem because the bending of the beam is small enough so that the elastic reaction force opposing the bending force is proportional to the deflection [28]. We assume that the beam is of length L and is located between the symmetry axis and the collector channel, as shown in Figure 2.5. The equilibrium position of the beam is described by the function $h(x)$ and is determined by the balance between the elastic forces in the beam and the loads acting on it, *i.e.* the intraocular pressure in the anterior chamber and the flow pressure. We can now formulate an equation that links the displacement $h(x)$ directly to the distributed load, which is the difference in pressure between the anterior chamber and the canal of Schlemm, thereby obtaining

$$EI \frac{d^4 h}{dx^4} = p - p_i \quad (2.59)$$

where E is the modulus of elasticity and I is the area moment of inertia. Equation (2.59) is a fourth order linear differential equation. In order to find the solution, we must have appropriate boundary conditions that describe the constraints imposed by the geometry. In this problem, we assume that the beam has a clamped end due to the structure of the trabecular meshwork which is the corneoscleral meshwork (the inner part of the trabecular meshwork) is fixed to the connective tissue in front of the ciliary muscle and to the iris root up to the cornea. Therefore the boundary conditions are

$$h_x(0) = 0, \quad h_{xxx}(0) = 0, \quad h(L) = h_L, \quad h_x(L) = 0. \quad (2.60)$$

h_L denotes respectively the undeformed depth at the length, L . The parameters can be nondimensionalised using the scaling,

$$x = Lx^*, \quad p = p_i + (p_{out} - p_i)p^*, \quad h = h_L h^*, \quad k = L^2 k^*. \quad (2.61)$$

We now non-dimensionalise equations (2.59) and (2.60) using the non-dimensional parameters in equation (2.61), to give

$$\frac{d^4 h^*}{dx^{*4}} = -\lambda p^* \quad \text{and} \quad \lambda = \frac{L^4 (p_i - p_{out})}{EIh_L} \quad (2.62)$$

with boundary conditions

$$(h^*)_{x^*}(0) = 0, \quad (h^*)_{x^*x^*x^*x^*}(0) = 0, \quad h^*(1) = 1, \quad (h^*)_{x^*}(1) = 0. \quad (2.63)$$

λ is defined in terms of the pressure difference at a collector channel and the length L between the symmetry axis and a collector channel, and is inversely proportional to the undeformed depth at length L , the modulus of elasticity and the moment of inertia of the trabecular meshwork. λ thus expresses the relative importance of the effects of the pressure difference and the elastic stiffness of the trabecular meshwork. We now non-dimensionalise equation (2.10) and get

$$\left[\frac{dp^*}{dx^*} (h^*)^3 \right]_{x^*} = \theta p^* \quad \text{and} \quad \theta = \frac{12kL^2}{dh_L^3}. \quad (2.64)$$

Here $\theta = \frac{12kL^2}{dh_L^3}$ is defined in terms of the permeability, k in Darcy's law where d , L and h_L denote respectively the width of the trabecular meshwork, a typical length and an undeformed depth at $x = L$. Thus θ again measures the relative importance of porosity and viscous drag effects. We now rearrange equation (2.62) and find

$$p^* = -\frac{1}{\lambda} \frac{d^4 h^*}{dx^{*4}}. \quad (2.65)$$

Differentiating equation (2.65) with respect to x , gives

$$\frac{dp^*}{dx^*} = -\frac{1}{\lambda} \frac{d^5 h^*}{dx^{*5}}. \quad (2.66)$$

We now substitute equations (2.65) and (2.66) into equation (2.64) and therefore obtain the governing equation for this case, which is

$$\left[(h^*)^3 (h^*)_{x^*x^*x^*x^*x^*} \right]_{x^*} = \theta (h^*)_{x^*x^*x^*x^*x^*} \quad \text{where} \quad \theta = \frac{12kL^2}{dh_L^3}. \quad (2.67)$$

Equation (2.67) is a nonlinear 6th order differential equation and in order to solve it, we need six boundary conditions. Equation (2.63) shows that we already have four boundary conditions, so we need two more. Thus we rearrange and non-dimensionalise

the boundary conditions in (2.6), to give

$$(h^*)_{x^*x^*x^*x^*} (1) = -\lambda \quad , \quad (h^*)_{x^*x^*x^*x^*x^*} (0) = 0.$$

We now rewrite the governing equation and the boundary conditions for this case and drop the stars from here onwards. Hence the system is governed by

$$[h^3 h_{xxxx}]_x = \theta h_{xxxx} \quad \text{with} \quad \theta = \frac{12kL^2}{dh_L^3} \quad (2.68)$$

with boundary conditions,

$$\begin{aligned} h_x(0) &= 0, & h_{xxx}(0) &= 0, & h_{xxxx}(0) &= 0, \\ h(1) &= 1, & h_x(1) &= 0, & h_{xxxx}(1) &= -\lambda \\ \text{where } \lambda &= \frac{L^4(p_{out} - p_i)}{EIh_L}. \end{aligned} \quad (2.69)$$

In the following Case (A), Case (B) and Case (C) that we will further examine, $h(x)$ is no longer constant since the trabecular meshwork is deformable and satisfies the beam equation, equation (2.59), and the boundary conditions in equation (2.60). The difference between these three cases is as follows: in Case (A), we will consider the permeability, k is constant such as Case (1); in Case (B), we will assume the permeability, k is inversely proportional to the pressure difference as we had discussed in Case (3); and in Case (C), we will consider the permeability, k is inversely proportional to the square of the pressure difference, (Case (5)). Since we will include the different permeability, k either it constant or not constant, and the trabecular meshwork is assumed to be deformable in each case, it important to examine the size of the parameters θ and λ in order to examine the deformation of the trabecular meshwork. Note that the parameter θ is different in Case (A), Case (B) and Case (C) due to the different permeabilities, k in Darcy's law that we will consider.

Case (A): The trabecular meshwork is deformable and k is constant

In this case, we further examine Case (1) by assuming that the trabecular meshwork as deformable. As in Case (1), we assume that the flow through trabecular meshwork is determined by Darcy's law where the permeability, k is constant. Since we assume k is constant, we now proceed to examine equation (2.68) subject to the boundary conditions (2.69) by examining a number of different subcases where either θ or λ , may be either large or small. Physically we examine these different number of subcases ($\theta \ll 1$, $\theta \gg 1$ $\theta \ll 1$, $\lambda \gg 1$) due to see the effect of increase or decrease intraocular pressure when the intercellular space in the trabecular meshwork becomes narrow or wide, and to analyse the deformation of the trabecular meshwork by changing the value of λ that corresponds to the modulus of elasticity of the trabecular meshwork. We start the examination with the subcase $\theta \ll 1$, followed by the subcase $\lambda \ll 1$, then the subcase

$\theta \gg 1$ and finally the subcase $\lambda \gg 1$.

The Case $\theta \ll 1$ where $\lambda = O(1)$

We now examine Case (A) by assuming that θ is small, λ is equal to order one and the permeability, k is constant. When the small value of θ will be considered, it means physically to have less porosity and permeability of the trabecular meshwork. If this case occurs, then how does it effects the deformation of the trabecular meshwork. The governing equation, (2.68) can now be solved by using a regular perturbation method where we assume that

$$h(x) = h_0(x) + \theta h_1(x) + \dots \quad (2.70)$$

We now substitute equation (2.70) into equation (2.68) and apply the boundary conditions (2.69) to deduce that

$$\left[(h_0(x) + \theta h_1(x) + \dots)^3 (h_0(x) + \theta h_1(x) + \dots)_{xxxxx} \right]_x = \theta (h_0(x) + \theta h_1(x) + \dots)_{xxxxx} \quad (2.71)$$

with boundary conditions

$$\begin{aligned} (h_0)_x(0) + \theta (h_1)_x(0) + \dots &= 0, \\ (h_0)_{xxx}(0) + \theta (h_1)_{xxx}(0) + \dots &= 0, \\ (h_0)_{xxxxx}(0) + \theta (h_1)_{xxxxx}(0) + \dots &= 0, \\ (h_0)(1) + \theta (h_1)(1) + \dots &= 1, \\ (h_0)_x(1) + \theta (h_1)_x(1) + \dots &= 0, \\ (h_0)_{xxxxx}(1) + \theta (h_1)_{xxxxx}(1) + \dots &= \lambda. \end{aligned}$$

From equation (2.71) and the boundary conditions given in equation (2.72), we examine the governing equation at leading order,

$$\left[(h_0(x))^3 (h_0(x))_{xxxxx} \right]_x = 0.$$

We now find that either,

$$(h_0(x))^3 = 0 \Rightarrow h_0(x) = 0$$

which can be neglected because it does not satisfy the boundary conditions given in equation (2.72) or

$$(h_0(x))_{xxxxx} = 0.$$

If we integrate the above equation five times with respect to x , we obtain

$$h_0(x) = \frac{1}{24}C_1x^4 + \frac{1}{6}C_2x^3 + \frac{1}{2}C_3x^2 + C_4x + C_5. \quad (2.72)$$

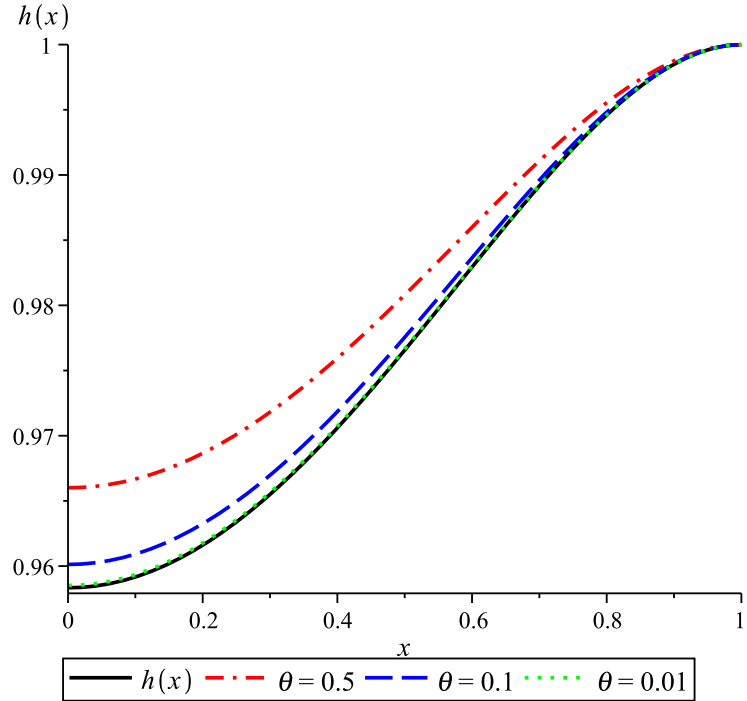


FIGURE 2.12: The deformation of the trabecular meshwork when θ is less than one and λ is assumed to be equal to order one. The solid black line represents the exact solution of the deformation of the trabecular meshwork given in equation (2.74), whereas the dashed-dotted red, the dashed blue and the dotted green lines denote the numerical solutions of the trabecular meshwork by solving equation (2.68) subject to the boundary conditions given in equation (2.69) for $\theta = 0.5$, $\theta = 0.1$ and $\theta = 0.01$.

Thus we substitute the boundary conditions in equation (2.72) at $x = 0$ and $x = 1$ into equation (2.72) to derive

$$h_{\circ}(x) = -\frac{\lambda}{24}x^4 + \frac{\lambda}{12}x^2 - \frac{\lambda}{24} + 1. \quad (2.73)$$

We now substitute equation (2.73) into equation (2.70) and obtain

$$h(x) = -\frac{\lambda}{24}x^4 + \frac{\lambda}{12}x^2 - \frac{\lambda}{24} + 1 + O(\theta). \quad (2.74)$$

Equation (2.74) may now be plotted in order to examine the deformation of the trabecular meshwork when θ is less than one, see the solid red line in Figure 2.12. Figure 2.12 shows the deformation of the trabecular meshwork when θ is small. Three different curves are shown in Figure 2.12, the dashed-dotted red, the dashed blue and the dotted green lines have been calculated numerically for different value of θ . As we can see from the Figure 2.12, the numerical calculation gives a good approximation to the analytical calculation. Furthermore, it shows that when the value of θ decreases, $h(x)$ becomes much more deformed. We find the volumetric flow rate, \dot{V}_c is equal to zero at leading order, by substituting the equations (2.66) and (2.74) into equation (2.8). This

is because when we differentiate equation (2.74) five times with respect to x , we find that

$$h''''(x) = 0 \quad \text{which implies} \quad p'(x) = 0 + O(\theta).$$

Therefore the total amount of fluid flowing out of the eye, \dot{V}_{out} , equals

$$\dot{V}_{out} = N(0 + O(\theta)) \quad (2.75)$$

and is very small. This means that the amount of aqueous humour flowing across the trabecular meshwork is also negligible. Thus the intraocular pressure, $p_i(t)$ may now be determined by substituting equation (2.75) into equation (2.3). Therefore the total change in intraocular pressure is

$$\frac{dp_i}{dt} = \tilde{K}p_i\dot{V}_{in} + O(\theta) \quad \text{where} \quad p_i(0) = p_{io},$$

which can be solved to give

$$p_i(t) = p_{io}e^{(\tilde{K})\dot{V}_{in}t}. \quad (2.76)$$

Hence the intraocular pressure (2.76) rises continually at leading order and there is nothing to stop it. Note that, though we could find $h_1(x)$ in this problem there is no need to do so because when θ is small, we can see by just considering the leading order terms, the intraocular pressure rises dramatically and blindness will be an inevitable result [29].

The Case $\lambda \ll 1$ where $\theta = O(1)$

Here we examine Case (A) by letting λ be small and assuming θ is order one. We assume λ is small because λ corresponds to the modulus of elasticity of the trabecular meshwork. If λ is taken to be small, then the value of the elasticity of the trabecular meshwork is assumed to be large. We now introduce the series solution,

$$h(x) = h_o(x) + \lambda h_1(x) + \dots . \quad (2.77)$$

We substitute equation (2.77) into equation (2.68) and boundary conditions (2.69), to give

$$\left[(h_o(x) + \lambda h_1(x) + \dots)^3 (h_o(x) + \lambda h_1(x) + \dots)^{''''} \right]' = \theta (h_o(x) + \lambda h_1(x) + \dots)^{''''} \quad (2.78)$$

with boundary conditions

$$\begin{aligned}
 (h_o)'(0) + \lambda(h_1)'(0) + \dots &= 0, \\
 (h_o)'''(0) + \lambda(h_1)'''(0) + \dots &= 0, \\
 (h_o)''''(0) + \lambda(h_1)''''(0) + \dots &= 0, \\
 (h_o)(1) + \lambda(h_1)(1) + \dots &= 1, \\
 (h_o)'(1) + \lambda(h_1)'(1) + \dots &= 0, \\
 (h_o)'''(1) + \lambda(h_1)'''(1) + \dots &= -\lambda.
 \end{aligned} \tag{2.79}$$

From equation (2.78) and the boundary conditions (2.79), we find the equations and the boundary conditions at leading order, $\lambda^{(0)}$, are given by

$$[h_0^3(h_0)_{xxxxx}]_x = \theta(h_0)_{xxxx}. \tag{2.80}$$

$$\begin{aligned}
 h_{0x}(0) &= 0, & h_{0xxx}(0) &= 0, \\
 h_{0xxxxx}(0) &= 0, & h_0(1) &= 1, \\
 h_{0x}(1) &= 0, & h_{0xxx}(1) &= 0.
 \end{aligned} \tag{2.81}$$

At first order, $\lambda^{(1)}$ is given by

$$[h_0^3(h_1)_{xxxxx} + 3h_0^2h_1(h_0)_{xxxxx}]_x = \theta(h_1)_{xxxx}, \tag{2.82}$$

$$\begin{aligned}
 (h_1)_x(0) &= 0, & (h_1)_{xxx}(0) &= 0, \\
 (h_1)_{xxxxx}(0) &= 0, & h_1(1) &= 0, \\
 (h_1)_x(1) &= 0, & (h_1)_{xxx}(1) &= -1.
 \end{aligned} \tag{2.83}$$

We now solve equation (2.80) subject to the boundary conditions in equation (2.81). We obtain that at leading order,

$$h_o(x) = 1. \tag{2.84}$$

We then substitute equation (2.84) into equation (2.82) and simplify, finding that

$$(h_1)_{xxxxxx} = \theta(h_1)_{xxxx}.$$

We now integrate the above equation six times with respect to x , and impose the boundary conditions given in equation (2.83), to give

$$h_1(x) = \frac{1}{\theta^2} \frac{1}{(\cosh \sqrt{\theta})^2} - \frac{1}{2\theta^{\frac{3}{2}}} \tanh \sqrt{\theta} + \left(\frac{1}{2\theta^{\frac{3}{2}}} \tanh \sqrt{\theta} \right) x^2 - \frac{1}{\theta^2} \frac{1}{(\cosh \sqrt{\theta})} \cosh \sqrt{\theta} x. \tag{2.85}$$

Then we substitute equations (2.84) and (2.85) into equation (2.77), thus we obtain

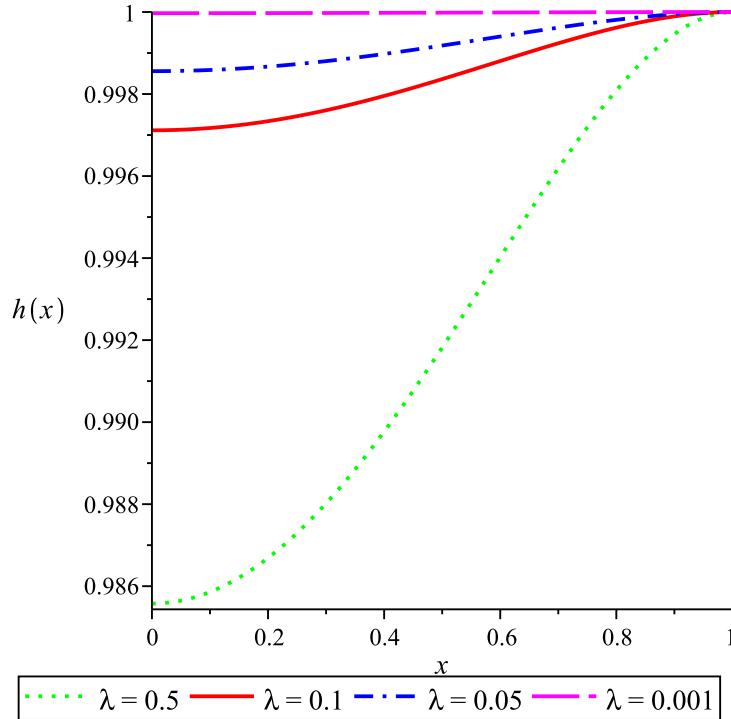


FIGURE 2.13: The deformation of the trabecular meshwork for different values of λ by solving numerically equation (2.68) subject to the boundary conditions given in equation (2.69). In this case, we assume that $\theta = O(1)$. Each graph corresponds to a different value of λ . The dotted green line represents the trabecular meshwork associated with λ equal to 0.5, whereas the solid red, the dashed-dotted blue and the long dashed magenta denote the corresponding trabecular meshwork for 0.1, 0.05 and 0.001 respectively.

$$h(x) = 1 + \lambda \left(\frac{1}{\theta^2} \frac{1}{(\cosh \sqrt{\theta})^2} + \frac{1}{2\theta^2} (x^2 - 1) \tanh \sqrt{\theta} - \frac{1}{\theta^2} \frac{1}{(\cosh \sqrt{\theta})} \cosh \sqrt{\theta} x \right) + O(\lambda^2) \quad (2.86)$$

We now examine the deformation of the trabecular meshwork given in equation (2.86) when λ is small. From equation (2.86), it shows that the trabecular meshwork, $h(x)$ tends to one if we take the value of λ to be small. This represents good agreement with the numerical calculation given in Figure 2.13. Figure 2.13 shows that when the value of λ decreases, we find that $h(x)$ hardly deforms. We differentiate equation (2.86) with respect to x five times and substitute into equation (2.66), giving

$$p_x(x) = \frac{\sqrt{\theta}}{(\cosh \sqrt{\theta})} \sinh \sqrt{\theta} x + O(\lambda^2). \quad (2.87)$$

Now we re-dimensionalize equation (2.87) by substituting $p^* = \frac{L}{p_{out} - p_i} p$ and $x^* = \frac{x}{L}$. We obtain

$$p_x\left(\frac{x}{L}\right) = \frac{\sqrt{\theta}}{L (\cosh \sqrt{\theta})} (p_{out} - p_i) \sinh \frac{\sqrt{\theta} x}{L} + O(\lambda^2). \quad (2.88)$$

We now substitute equation (2.87) and (2.86) into equation (2.8) and find that

$$\begin{aligned} \dot{V}_c = & \left[-\frac{B}{12\mu} \left(\frac{\sqrt{\theta}}{L(\cosh \sqrt{\theta})} (p_{out} - p_i) \sinh \frac{\sqrt{\theta}x}{L} + O(\lambda) \right) \cdot \left(1 + \lambda \left(\frac{1}{\theta^2} \frac{1}{(\cosh \sqrt{\theta})^2} \right)^3 \right. \right. \\ & \left. \left. + \frac{1}{2\theta^{\frac{3}{2}}} \tanh \sqrt{\theta} (x^2 - 1) - \frac{1}{\theta^2} \frac{1}{(\cosh \sqrt{\theta})} \cosh \sqrt{\theta}x \right) + O(\lambda^2) \right]_{x=L}. \end{aligned}$$

For small values of λ , the above equation can be reduced to

$$\begin{aligned} \dot{V}_c &= -\frac{B\sqrt{\theta}}{12\mu L} \tanh \sqrt{\theta} (p_{out} - p_i) + O(\lambda), \\ \dot{V}_{out} = N\dot{V}_c &= -\frac{NB\sqrt{\theta}}{12\mu L} \tanh \sqrt{\theta} (p_{out} - p_i) + O(\lambda). \end{aligned} \quad (2.89)$$

Therefore, the intraocular pressure, $p_i(t)$ may now be determined by substituting equation (2.89) into equation (2.3) with $p_i(0) = p_{io}$. Hence

$$\frac{dp_i}{dt} = p_i \left[\tilde{K} \left(\dot{V}_{in} - \frac{NB\sqrt{\theta}}{12\mu L} \tanh \sqrt{\theta} (p_i - p_{out}) + O(\lambda) \right) \right] \quad (2.90)$$

We may rewrite equation (2.90) in the following form:

$$\frac{1}{p_i(\alpha + \gamma p_i)} dp_i = dt \quad \text{with} \quad p_i(0) = p_{io} \quad (2.91)$$

where $\alpha = \tilde{K} \left(\dot{V}_{in} + \frac{NB\sqrt{\theta}}{12\mu L} \tanh \sqrt{\theta} p_{out} \right)$ and $\gamma = -\tilde{K} \left(\frac{NB\sqrt{\theta}}{12\mu L} \tanh \sqrt{\theta} \right)$. We now solve equation (2.91) to get that the exact solution of the IOP, $p_i(t)$

$$p_i(t) = \frac{\alpha p_{io}}{(\alpha + \gamma p_{io}) e^{-\alpha t} - \gamma p_{io}} + O(\lambda). \quad (2.92)$$

The changes of intraocular pressure at leading order given in equation (2.92) may now be calculated and examined by using the standard parameter values such as listed in Table 2.1. The value of θ inherent to these calculations is assumed to be equal to one. In these calculations, we find that when t tends to ∞ the exponential term in equation (2.92) will vanish and equation (2.92) will reduce to the leading term which is equal to the constant pressure at a collector channel, p_{out} . It shows that at the leading order there is almost no resistance to flow. Thus when λ is small, changes in intraocular pressure are also small, and intraocular pressure is maintained at a nearly constant level.

The Case $\theta \gg 1$ where $\lambda = O(1)$

In this Case (A), we consider θ large and λ is equal to order one. Physically, if θ is large the porosity and permeability of the trabecular meshwork is larger. By considering θ

is large, the governing equation, (2.68) subject to the boundary conditions given in equation (2.69) can now be solved by using a singular perturbation method where we let $\varepsilon^2 = \frac{1}{\theta}$. Then equation (2.68) becomes

$$\varepsilon^2 [h^3(h)_{xxxxx}]_x = (h)_{xxxx}. \quad (2.93)$$

Equation (2.93) is a boundary value problem containing a small parameter, ε^2 that cannot be approximated by letting the parameter value ε^2 equal to zero. If we equate ε^2 to zero, the order of the boundary value problem given in equation (2.68) reduces from six to four, so we cannot impose all the boundary conditions (2.69) on the solution. In general there will be a small neighbourhood close to one of the boundaries, where the solution changes rapidly to take on the boundary value. This neighbourhood is called boundary layer. We proceed to solve this boundary value problem in four steps. First we begin with the outer expansion. Next, we consider the inner expansion. Then, we continue with matching and composite expansion. Before we begin, we examine the exact solution of this problem given in equation (2.68) subject to the boundary conditions (2.69). We found that an analytical solution to this problem is not available. Because of the form of the outer solution however, h^3 terms in equation (2.68) can be ignored. Thus equation (2.68) becomes

$$\varepsilon^2 (h)_{xxxxx} = (h)_{xxxx} \quad (2.94)$$

We now solve equation (2.94) with the boundary conditions given in equation (2.69) and derive the equation of the trabecular meshwork, $h(x)$

$$h(x) = \lambda \varepsilon^4 \left(\frac{e^{\frac{x}{\varepsilon}} + e^{-\frac{x}{\varepsilon}}}{e^{\frac{1}{\varepsilon}} + e^{-\frac{1}{\varepsilon}}} \right) - \frac{x^2}{2} \left(\lambda \varepsilon^3 \left(\frac{e^{\frac{1}{\varepsilon}} - e^{-\frac{1}{\varepsilon}}}{e^{\frac{1}{\varepsilon}} + e^{-\frac{1}{\varepsilon}}} \right) \right) + 1 - \lambda \varepsilon^4 + \frac{\lambda \varepsilon^3}{2} \left(\frac{e^{\frac{1}{\varepsilon}} - e^{-\frac{1}{\varepsilon}}}{e^{\frac{1}{\varepsilon}} + e^{-\frac{1}{\varepsilon}}} \right). \quad (2.95)$$

Simplifying equation (2.95), we get that

$$h(x) = \lambda \varepsilon^4 \left(\frac{\cosh(\frac{x}{\varepsilon})}{\cosh(\frac{1}{\varepsilon})} - 1 \right) + \frac{\lambda \varepsilon^3}{2} (1 - x^2) + 1 \quad (2.96)$$

Away from $x = 1$, equation (2.96) becomes

$$h(x) \sim 1 + O(\varepsilon^3) + O(\varepsilon^4). \quad (2.97)$$

Equation (2.97) is the exact solution of the equation (2.94). This exact solution will guide and lead us to solve the boundary value problem given in equation (2.93) subject to the boundary conditions (2.69).

Outer Region:

First, we examine the outer solution. We seek a perturbation expansion of the outer

solution of the form

$$h_{out}(x) \sim \sum_{n=0}^{\infty} \varepsilon^n h_n(x) \quad \text{for } \varepsilon \rightarrow 0^+$$

$$h_{out}(x) = h_0 + \varepsilon h_1 + \dots \quad (2.98)$$

Substituting equation (2.98) into equation (2.93), we find that

$$\varepsilon^2 \left[(h_0 + \varepsilon h_1 + \dots)^3 (h_0 + \varepsilon h_1 + \dots)_{xxxxx} \right]_x = (h_0 + \varepsilon h_1 + \dots)_{xxxx} \quad (2.99)$$

From equation (2.99) we consider the leading order equation,

$$(h_0)_{xxxx}(x) = 0. \quad (2.100)$$

We now restate the boundary conditions from equation (2.69) $(h)_x(0) = 0$, and $(h)_{xxx}(0) = 0$ as

$$(h)_{0x}(0) = 0 \quad \text{and} \quad (h)_{0xxx}(0) = 0.$$

The leading order equation can now be solved subject to the boundary conditions in equation (2.100), here we get that

$$h_{out}(x) = \frac{1}{2} A_2 x^2 + A_4 + O(\varepsilon). \quad (2.101)$$

Inner Region:

From the exact solution given in equation (2.97), we expect that a boundary layer of thickness ε will develop at $x = 1$, as $\varepsilon \rightarrow 0^+$. Therefore in terms of the inner variable, $1 - x = \varepsilon X$, and we write equation (2.97) such that

$$h_{inn}(X) = 1 + \varepsilon^4 H(X) + O(\varepsilon^5). \quad (2.102)$$

We now substitute equation (2.102) into equation (2.93) and simplify the equation, to obtain,

$$\varepsilon^2 \left[(1 + \varepsilon^4 H)^3 (H)_{xxxxx} \right]_x = (H)_{xxxx}. \quad (2.103)$$

From equation (2.103) we consider the leading order equation

$$(H)_{xxxxxx} = (H)_{xxxx}. \quad (2.104)$$

Then we restate the boundary conditions $h(1) = 1$, $(h)_x(1) = 0$ and $(h)_{xxx}(1) = -\lambda$ thus we get that

$$H(1) = 1, \quad (H)_x(1) = 0, \quad (H)_{xxx}(1) = -\lambda. \quad (2.105)$$

We now solve equation (2.104) subject to the boundary conditions in equation (2.105)

and find that

$$H(X) = B_1 e^X + (\lambda - B_1) e^{-X} + \frac{B_3 X^3}{6} + \frac{B_4 X^2}{2} + X(\lambda - 2B_1) - \lambda. \quad (2.106)$$

Thus we substitute equation (2.106) into equation (2.102), to give

$$h_{inn}(X) = 1 + \varepsilon^4 \left(B_1 e^X + (\lambda - B_1) e^{-X} + \frac{B_3 X^3}{6} + \frac{B_4 X^2}{2} + X(\lambda - 2B_1) - \lambda \right) + O(\varepsilon^5). \quad (2.107)$$

Matching:

Here we have three unknowns B_1 , B_3 and B_4 in the expansion of $h_{inn}(X)$ to order ε^5 and we also have two unknowns ε^5 and A_4 in the expansion of $h_{out}(x)$ to order ε^1 . Thus we can find the constants by using the Van Dyke's matching principle [9]. We expand equation (2.101) in powers of ε :

$$\begin{aligned} h_{out}(1 - \varepsilon X) &= \frac{1}{2} A_2 (1 - \varepsilon X)^2 + A_4 + \varepsilon h_1(1 - \varepsilon X), \\ h_{out}(x) &= A_2 x + A_4 - \frac{A_2}{2} + \varepsilon h_1(x), \end{aligned} \quad (2.108)$$

and equation (2.107) also in powers of ε :

$$\begin{aligned} h_{inn}\left(X = \frac{1-x}{\varepsilon}\right) &= 1 + \varepsilon^4 \left(B_1 e^{(\frac{1-x}{\varepsilon})} + (\lambda - B_1) e^{-(\frac{1-x}{\varepsilon})} + \frac{B_3}{6} \left(\frac{1-x}{\varepsilon}\right)^3 \right. \\ &\quad \left. + \frac{B_4}{2} \left(\frac{1-x}{\varepsilon}\right)^2 + (\lambda - 2B_1) \left(\frac{1-x}{\varepsilon}\right) - \lambda \right). \end{aligned}$$

When $x \rightarrow 0$ we can reduce the above equation, yielding

$$h_{inn}\left(X = \frac{1-x}{\varepsilon}\right) = 1 + \varepsilon^4 (B_1 - \lambda) \quad \text{where } B_3 = 0 \text{ and } B_4 = 0. \quad (2.109)$$

We now match the outer expansion given in equation (2.108) and the inner expansion, equation (2.109), obtaining that

$$A_2 = 0, \quad A_4 = 1, \quad B_1 = \lambda.$$

Hence we may rewrite the full outer and inner expansions as

$$h_{out}(x) = 1 + \varepsilon h_1(x) \quad (2.110)$$

and

$$h_{inn}(X) = 1 + \varepsilon^4 (\lambda e^X - \lambda X - \lambda). \quad (2.111)$$

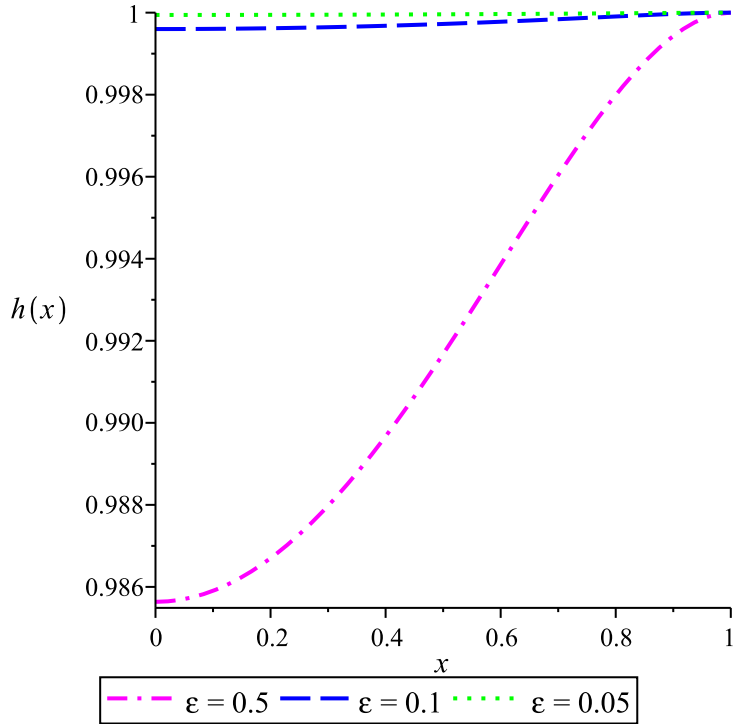


FIGURE 2.14: The deformation of the trabecular meshwork, $h(x)$ when θ is large by solving equation (2.93) with the boundary conditions given in equation (2.69). In this case, λ is assumed to be equal to one and θ is equal to $\frac{1}{\varepsilon^2}$. Each curve corresponds to a different value of ε . The dashed-dotted magenta line represents the trabecular meshwork associated with $\varepsilon = 0.5$, whereas the dashed blue and the dotted green lines denote the corresponding trabecular meshwork for $\varepsilon = 0.1$ and $\varepsilon = 0.05$.

Composite Expansion:

We now write the uniformly valid composite expansion, as,

$$h(x) = h_{out}(x) + [h_{inn}(X) - h_{out}(1 - \varepsilon X)].$$

Thus we substitute equations (2.110) and (2.111) and $X = \frac{1-x}{\varepsilon}$ into the above equation, yielding

$$h(x) = 1 + \varepsilon^4 \left(\lambda e^{\frac{1-x}{\varepsilon}} - \lambda \left(\frac{1-x}{\varepsilon} + 1 \right) \right) + O(\varepsilon^5) \quad (2.112)$$

Equation (2.112) is the uniformly valid composite expansion for this case. It tends to one, $h(x) \sim 1$, if we take the value of ε to be small. This shows good agreement with the exact solution, equation (2.97)). We now analyse equation (2.93) subject to the boundary conditions given in equation (2.69) in order to examine the deformation of the trabecular meshwork when θ is large, ($\theta \gg 1$). Figure 2.14 shows the deformation of the trabecular meshwork for different values of ε . It shows that when the value of ε decreases, $h(x)$ is hardly deformed. We now differentiate equation (2.112) with respect to x , five times and substitute into equation (2.66), to find that

$$p'(x) = -\frac{e^{\left(\frac{1-x}{\varepsilon}\right)}}{\varepsilon}. \quad (2.113)$$

If we now re-dimensionalise equation (2.113), we obtain

$$p'(x) = -\frac{1}{\varepsilon L} (p_{out} - p_i) e^{\left(\frac{1}{\varepsilon} - \frac{x}{\varepsilon L}\right)}.$$

We substitute the above equation and (2.112) into equation (2.8), to give

$$\dot{V}_c = \frac{B}{12\mu} \left(\frac{1}{\varepsilon L} (p_{out} - p_i) \right) \left[1 + \varepsilon^4 \left(\lambda e^{\frac{1-x}{\varepsilon}} - \lambda \left(\frac{1-x}{\varepsilon} + 1 \right) \right) + O(\varepsilon^5) \right]_{x=L}.$$

By using a Taylor series expansion, we find that

$$\dot{V}_c \cong \frac{B}{12\mu\varepsilon L} (p_{out} - p_i).$$

Thus the total outflow is

$$\dot{V}_{out} = \frac{NB}{12\mu\varepsilon L} (p_{out} - p_i) \quad (2.114)$$

We now substitute equation (2.114) into equation (2.3) and therefore the total change in intraocular pressure is

$$\frac{dp_i}{dt} = p_i \left[\tilde{K} \left(\dot{V}_{in} - \frac{NB}{12\mu\varepsilon L} (p_{out} - p_i) \right) \right] \quad (2.115)$$

where $p_i(0) = p_{io}$. We rewrite equation (2.115) in the following form;

$$\frac{1}{p_i(\alpha + \gamma p_i)} dp_i = dt$$

where

$$\alpha = \tilde{K} \left(\dot{V}_{in} - \frac{NBp_{out}}{12\mu\varepsilon L} \right) \quad \text{and} \quad \gamma = -\tilde{K} \frac{NB}{12\mu\varepsilon L}.$$

We now solve the above equation subject to the boundary conditions $p_i(0) = p_{io}$ and we get that the exact solution for the intraocular pressure, $p_i(t)$, is

$$p_i(t) = \frac{\alpha p_{io}}{(\alpha + \gamma p_{io}) e^{-\alpha t} - \gamma p_{io}}. \quad (2.116)$$

Equation (2.116) may now be calculated and examined using the typical parameter values given in Table 2.1. Here we find that when θ is large there is no problem because there is almost no resistance to flow. We found that in the steady state the intraocular pressure is quite low. Physically the porosity and permeability of the trabecular mesh-work increase, so the process of aqueous humour outflow via the trabecular pathway is flow constantly to maintain a constant intraocular pressure level. Therefore when θ is large the intraocular pressure cannot increase and remains normal.

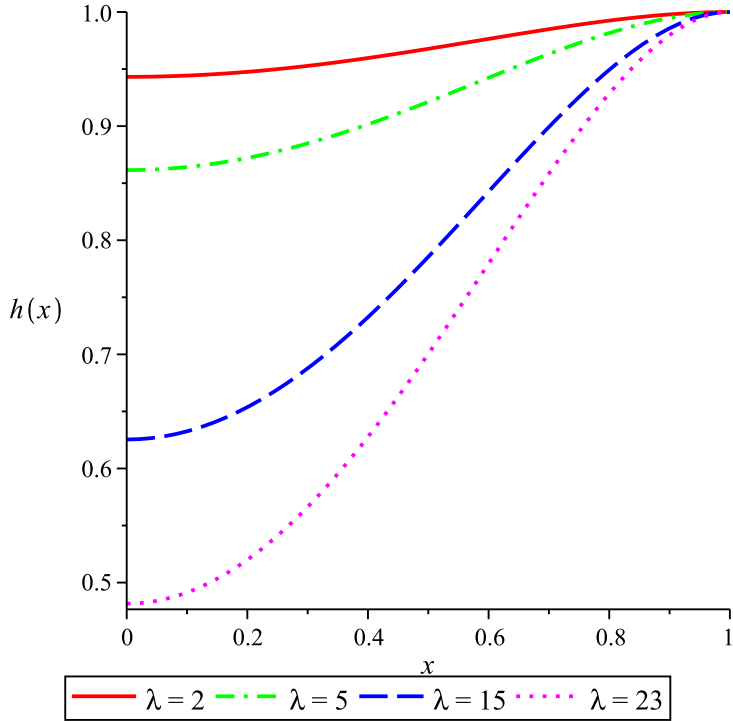


FIGURE 2.15: The deformation of the trabecular meshwork for different values of λ by solving numerically equation (2.117) subject to the boundary conditions given in equation (2.118). The value of θ inherent to these calculations is taken to be equal to one. The solid red line represents the trabecular meshwork when λ is equal to 2, whereas the dashed-dotted green, the dashed blue and the dotted magenta lines denote the corresponding trabecular meshwork for $\lambda = 5$, $\lambda = 15$ and $\lambda = 23$ respectively.

The Case $\lambda \gg 1$ where $\theta = O(1)$

We now examine Case (A) by assuming λ is large θ is equal to order one. We assume λ is large due to examine the deformation of the trabecular meshwork when the amount of the modulus of elasticity of the trabecular meshwork is considered to be small. We now restate the governing equation and the boundary conditions of this subcase, previously given in equations (2.68) and (2.69)

$$[h^3(h)_{xxxxx}]_x = \theta(h)_{xxxx} \quad \text{where} \quad \theta = \frac{12kL^2}{dh_L^3}. \quad (2.117)$$

with boundary conditions,

$$\begin{aligned} h_x(0) &= 0, & h_{xxx}(0) &= 0, \\ h_{xxxxx}(0) &= 0, & h(1) &= 1, \\ h_x(1) &= 0, & h_{xxxx}(1) &= -\lambda. \end{aligned} \quad (2.118)$$

We now numerically analyse equation (2.117) subject to the boundary conditions in equation (2.118). Figure 2.15 presents the deformation of the trabecular meshwork

when λ is large. The result shows that when the value of λ increases, we find that the trabecular meshwork, h_x is easily deforms. Physically, if λ is large which corresponds to the less amount of the modulus of elasticity of the trabecular meshwork, then the trabecular meshwork is so “floppy” that it touches the canal of Schlemm. In this circumstance, the aqueous humour cannot exit quickly into a collector channel because the trabecular meshwork is partially blocked. Therefore, the intraocular pressure increases rapidly and vision may be lost forever.

Case (B): The trabecular meshwork is deformable and $k \sim (1/(p_i - p))$

In Case (B), we further examine the deformation of the trabecular meshwork by considering the trabecular meshwork is deformable and the permeability, k is inversely proportional to the pressure difference as we had discusses in Case (3). We now assume $k = \frac{\tilde{B}}{(p_i - p)}$. Since k is not constant, we have to derive the governing equation for Case (B). We begin with non-dimensionalising k using the scalings in (2.61), to give

$$k^* = \frac{\tilde{B}}{L^2 (p_i - p_{out}) p^*} \quad (2.119)$$

Then we substitute equation (2.119) into equation (2.64), to find that

$$\left[\frac{dp^*}{dx^*} (h^*)^3 \right]_{x^*} = \frac{12L^2 \tilde{B}}{dh_L^3 (p_i - p_{out})}. \quad (2.120)$$

We now substitute equation (2.66) into equation (2.120) and therefore write the governing equation for Case (B) as

$$\left[(h^*)^3 (h^*)_{xxxxx} \right]_x = -\omega \quad \text{where } \omega = \frac{12L^6 \tilde{B}}{dEIh_L^4}. \quad (2.121)$$

Here ω is defined in terms of the constant \tilde{B} , the length between the symmetry axis and a collector channel over the undeformed depth at length L , the width, the modulus of elasticity and the moment of inertia of the trabecular meshwork. ω therefore compares the relative importance of the effects of porosity and the elastic stiffness. In order to avoid cumbersome notation we immediately drop the stars, so that equation (2.121) becomes

$$[h^3 h_{xxxxx}]_x = -\omega \quad (2.122)$$

with boundary conditions,

$$\begin{aligned} h_x(0) &= 0, & h_{xxx}(0) &= 0, \\ h_{xxxxx}(0) &= 0, & h(1) &= 1, \\ h_x(1) &= 0, & h_{xxx}(1) &= -\lambda \end{aligned} \quad (2.123)$$

which is similar to the boundary conditions in equation (2.69). Physically, we examine

these different subcases ($\omega \ll 1$, $\lambda \ll 1$, $\omega \gg 1$ and $\lambda \gg 1$) in order to see the effect of the deformation of the trabecular meshwork when we change the relative sizes of the parameters ω and λ . This corresponds to changes in the constant of the permeability, k the pressure difference proportionality and the modulus of elasticity of the trabecular meshwork.

The Case $\omega \ll 1$ where $\lambda = O(1)$

We now examine Case (B) by assuming ω is small and λ is equal to order one. We assume the small value of ω in this case means that we considered the small value of constant, \tilde{B} which indirectly we refer to less pressure difference across the trabecular meshwork. We start to solve this subcase by substituting the series solution equation (2.70) into the governing equation (2.122), and thus we obtain

$$\left[(h_o(x) + \omega h_1(x) + \dots)^3 (h_o(x) + \omega h_1(x) + \dots)_{xxxxx} \right]_x = -\omega.$$

At leading order, the governing equation is

$$\left[(h_o(x))^3 (h_o(x))_{xxxxx} \right]_x = 0. \quad (2.124)$$

We now solve the equation (2.124) using the boundary conditions in equation (2.72), to give

$$h_o(x) = -\frac{\lambda}{24}x^4 + \frac{\lambda}{12}x^2 - \frac{\lambda}{24} + 1. \quad (2.125)$$

Then we substitute equation (2.125) into equation (2.70), yielding

$$h(x) = -\frac{\lambda}{24}x^4 + \frac{\lambda}{12}x^2 - \frac{\lambda}{24} + 1 + O(\omega). \quad (2.126)$$

From this solution (2.126) we obtain that the volumetric flow rate, \dot{V}_C and the total amount of fluid flowing out of the eye, \dot{V}_{out} are equal to zero at leading order. This shows that the total change in intraocular pressure when ω is very small (which is physically represents the less amount of pressure difference across the trabecular meshwork), thus the result shows that the trabecular meshwork, $h(x)$ becomes much more deformed when the value of ω decreases and the intraocular pressure increases continually at the leading order. The result shows in this subcase is similar to the subcase in Case (A) where θ is small, see equations (2.74) and (2.76).

The Case $\lambda \ll 1$ where $\omega = O(1)$

Here we examine Case (B) where in this case we assume the trabecular meshwork is deformable and the permeability, k is inversely proportional to the pressure difference, by considering λ is small and ω is equal to order one. As in Case (A), we consider the small value of λ due to examine the deformation of the trabecular meshwork when the large

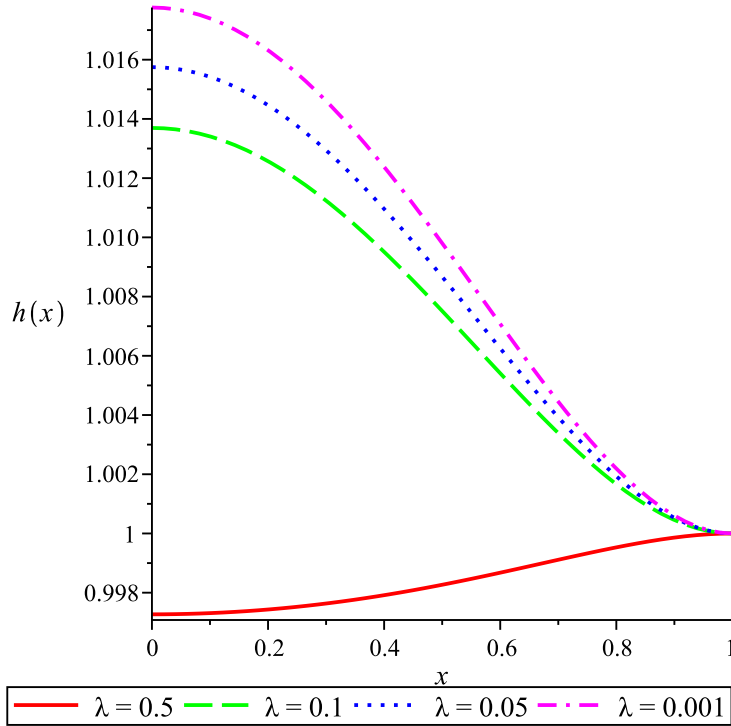


FIGURE 2.16: The deformation of the trabecular meshwork when λ is small by solving numerically equation (2.122) subject to the boundary conditions given in equation (2.123). Here ω is assumed to be equal to order one. Each graph corresponds to a different value of λ . The solid red, the dashed green, the dotted blue and the dashed-dotted magenta lines represent the corresponding trabecular meshwork for λ equal to 0.5, 0.1, 0.05 and 0.001 respectively.

amount of modulus of elasticity is taken into account. We now numerically solve equation (2.122) subject to the boundary conditions in equation (2.123) by using MAPLE [8]. Four different curves are shown in Figure 2.16, the solid red, the dashed green, the dotted blue and the dashed-dotted magenta lines have been calculated numerically for different values of λ . It shows that when λ is small the trabecular meshwork becomes much more deformed. The result shows that the trabecular meshwork starts bending up even though the trabecular meshwork is hardly to deform because its amount of modulus of elasticity is large. Physically from this result, it seems that intraocular pressure rises because either the collector channel has been blocked or the trabecular meshwork is not functioning properly, so aqueous humour drainage is decreased.

The Case $\omega \gg 1$ where $\lambda = O(1)$

In this Case (B), we consider ω is large where λ is equal to order one. We assume the large value of ω due to the fact that, physically, ω corresponds to more pressure difference across the trabecular meshwork. We now examine equation (2.122) subject to the boundary conditions (2.123) when ω is large by using the regular perturbation

method. If we let $\omega = \frac{1}{\varepsilon}$ then equation (2.122) becomes

$$\varepsilon [h^3 h_{xxxxx}]_x = -1. \quad (2.127)$$

If we assume that

$$h = \frac{H}{\varepsilon^{\frac{1}{4}}} \quad (2.128)$$

and substitute into equation (2.127) and impose the boundary conditions in equation (2.69), we get

$$[H^3 H_{xxxxx}]_x = -1 \quad (2.129)$$

and the boundary conditions,

$$\begin{aligned} H_x(0) &= 0, & H_{xxx}(0) &= 0, \\ H_{xxxxx}(0) &= 0, & H(1) &= \varepsilon^{\frac{1}{4}}, \\ H_x(1) &= 0, & H_{xxxx}(1) &= -\lambda \varepsilon^{\frac{1}{4}}. \end{aligned} \quad (2.130)$$

We now introduce the series solution,

$$H = H_0 + \varepsilon^{\frac{1}{4}} H_1 + \dots \quad (2.131)$$

We substitute the series solution into equations (2.130) and (2.131) to obtain

$$\left[\left(H_0 + \varepsilon^{\frac{1}{4}} H_1 + \dots \right)^3 \left(H_0 + \varepsilon^{\frac{1}{4}} H_1 + \dots \right)_{xxxxx} \right]_x = -1 \quad (2.132)$$

with the boundary conditions,

$$\begin{aligned} \left(H_0 + \varepsilon^{\frac{1}{4}} H_1 + \dots \right)_x(0) &= 0, & \left(H_0 + \varepsilon^{\frac{1}{4}} H_1 + \dots \right)_{xxx}(0) &= 0, \\ \left(H_0 + \varepsilon^{\frac{1}{4}} H_1 + \dots \right)_{xxxxx}(0) &= 0, & \left(H_0 + \varepsilon^{\frac{1}{4}} H_1 + \dots \right)(1) &= \varepsilon^{\frac{1}{4}}, \\ \left(H_0 + \varepsilon^{\frac{1}{4}} H_1 + \dots \right)_x(1) &= 0, & \left(H_0 + \varepsilon^{\frac{1}{4}} H_1 + \dots \right)_{xxxx}(1) &= -\lambda \varepsilon^{\frac{1}{4}}. \end{aligned} \quad (2.133)$$

From equations (2.132) and (2.133), we solve at leading order

$$[H_0^3 H_{0xxxxx}]_x = -1 \quad (2.134)$$

with boundary conditions

$$\begin{aligned} H_{0x}(0) &= 0, & H_{0xxx}(0) &= 0, \\ H_{0xxxxx}(0) &= 0, & H_0(1) &= 0, \\ H_{0x}(1) &= 0, & H_{0xxxx}(1) &= 0. \end{aligned} \quad (2.135)$$

From equation (2.134), we get

$$H_0^3 H_{0xxxxx} = -x + C.$$

When $x = 0$, we obtain

$$H_{0xxxxx} = 0.$$

If $C = 0$ then we find

$$H_0^3 H_{0xxxxx} = -x. \quad (2.136)$$

We now assume a solution of the form $H_0(x) = A + Bx^n$ when x is near zero and we substitute into equation (2.136), to yield

$$(A + Bx^n)^3 Bn(n-1)(n-2)(n-3)(n-4)x^{n-5} = -x.$$

From the equation above, we get that $n = 6$. Thus

$$H_0(x) = A + Bx^6 ; \quad (x \sim 0). \quad (2.137)$$

We substitute equation (2.137) into equation (2.136), to give

$$(A + Bx^6)^3 (A + Bx^6)_{xxxxx} = -x.$$

When x is near zero, we obtain that

$$720BA^3 = -1.$$

We now let $H_\circ(x) = D(1-x)^n$ when x is near one, and substitute into equation (2.136). We find that

$$-D^3(1-x)^{3n}Dn(n-1)(n-2)(n-3)(n-4) = -1.$$

From the equation above we get that $n = 0$ which this is not allowed because it does not satisfy the boundary conditions below,

$$H_0(1) = 0, \quad H_{0x}(1) = 0, \quad H_{0xxxx}(1) = 0.$$

Therefore we can see that asymptotic solution is valid when x is near zero but not when x is near one. This does not mean that there is no solution however, rather that the solution is not valid for $h(x) < 0$ because there is a solid boundary.

The Case $\lambda \gg 1$ where $\omega = O(1)$

We now examine Case (B) by assuming λ is large and ω is order one. We consider the large value of λ due to examine the deformation of the trabecular meshwork when the

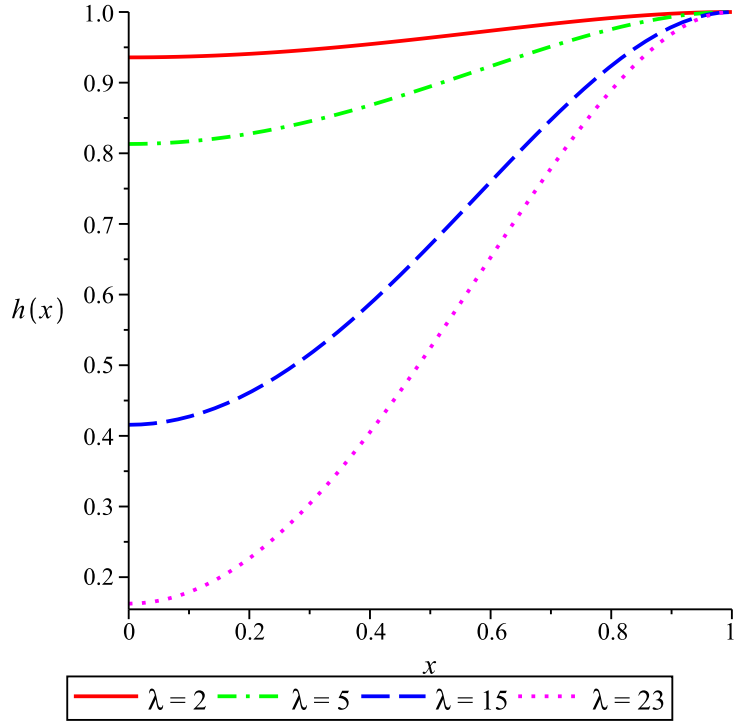


FIGURE 2.17: The deformation of the trabecular meshwork for different values of λ by solving numerically equation (2.122) subject to the boundary conditions given in equation (2.123). In this case, the permeability, k in Darcy's law is inversely related to the pressure difference through the trabecular meshwork, $\frac{1}{(p_i-p)}$. The solid red line denotes the trabecular meshwork associated with $\lambda = 2$, whereas the dashed-dotted green, the dashed blue and the dotted magenta lines represent the corresponding trabecular meshwork for λ equal to 5, 15 and 23 respectively.

amount of modulus of elasticity of the trabecular meshwork is assumed to be large. The governing equation (2.122) and the boundary conditions given in equation (2.123) can now be solved and numerically. Figure 2.17 shows the deformation of the trabecular meshwork when λ is large. The result suggests that when λ is large (which corresponds to a smaller modulus of elasticity of the trabecular meshwork), the trabecular meshwork starts bending down to close to the Schlemm canal. If we compare the result when λ is 23, see Figure 2.17 for comparison, it shows that the trabecular meshwork in this case much more "floppy". This is because the permeability, k in Darcy law is no longer constant but it depends on the pressure difference. In this case, the intraocular pressure increases rapidly and blindness will be inevitable.

Case (C): The trabecular meshwork is deformable and $k \sim \frac{1}{(p_i-p)^2}$

In Case (C), we further examine Case (5) by considering the trabecular meshwork is deformable. As in Case (5), we consider the permeability, k is inversely proportional to the pressure difference raised to the power two, $k \sim \frac{1}{(p_i-p)^2}$. Since we consider

$k = \frac{\tilde{D}}{(p_i - p)^2}$, we have to derive the governing equations for this case. We start with non-dimensional k using the non-dimensional parameters in equation (2.61). We find that

$$k^* = \frac{\tilde{D}}{L^2(p_i - p_{out})^2(p^*)^2}.$$

Repeating the same process as in Case (A) and Case (B), we derive that

$$[h^3 h_{xxxxx}]_x = \frac{\psi}{h_{xxxx}} \quad \text{where} \quad \psi = \frac{12L^{10}\tilde{D}}{d(EI)^2 h_L^5}. \quad (2.138)$$

Here ψ is defined in terms of the constant \tilde{D} of the permeability k that is inversely proportional to the square of the pressure difference, where d , E , I and h_L denote respectively to the width of the trabecular meshwork, the modulus of elasticity and the moment of inertia of the trabecular meshwork and an undeformed depth at $x = L$. ψ therefore again compares the relative effects of porosity and the elastic stiffness. The boundary conditions given below are the same as the boundary conditions for Case (A) and Case (B) which are given in equation (2.69).

$$\begin{aligned} h_x(0) &= 0, & h_{xxx}(0) &= 0, \\ h_{xxxxx}(0) &= 0, & h(1) &= 1, \\ h_x(1) &= 0, & h_{xxxx}(1) &= -\lambda. \end{aligned} \quad (2.139)$$

We now proceed to examine the governing equation (2.138) subject to the boundary conditions (2.139) by examining a number of different subcases where either ψ or λ , may be either small or large. We examine these different cases ($\psi \ll 1$, $\psi \gg 1$ and $\lambda \gg 1$) because we want to examine the scenario when the intercellular spaces in the trabecular meshwork becomes either narrow or wide, as the pressure difference raised to the power two across it increases or decreases and we also want to examine the effect of the trabecular meshwork that is considered to be deformable. We begin with the subcase where $\psi \ll 1$, followed by the subcase $\psi \gg 1$ and finally the subcase $\lambda \gg 1$.

The Case $\psi \ll 1$ where $\lambda = O(1)$

We now examine Case (C) by considering ψ is small where λ is equal to order one. We assume the small value ψ in this case means that we consider very small amount of pressure difference across the trabecular meshwork. The governing equation (2.138) can now be solved by using the series solution that we introduced in Case (A), see equation (2.70). We substitute the series solution in equation (2.70) into equation (2.138), yielding

$$\left[(h_\circ(x) + \psi h_1(x) + \dots)^3 (h_\circ(x) + \psi h_1(x) + \dots)_{xxxxx} \right]_x = \frac{\psi}{(h_\circ(x) + \psi h_1(x) + \dots)_{xxxx}}. \quad (2.140)$$

We now examine the governing equation at leading order, to give

$$\left[(h_\circ(x))^3 (h_\circ(x))_{xxxxx} \right]_x = 0.$$

The boundary conditions for this subcase at leading order are the same as the boundary conditions in Case (A) and Case (B) when $\psi \ll 1$. As we can see in these three subcases, Case (A), Case (B) and Case (C), we are solving the same governing equation and the boundary conditions at leading order. Thus the solution for $h(x)$ is,

$$h(x) = 1 + \lambda \left(-\frac{x^4}{24} + \frac{x^2}{12} - \frac{1}{24} \right) + O(\psi) \quad (2.141)$$

and $h_{xxxxx}(x)$ is equal to zero at leading order. Therefore, \dot{V}_{out} is very small and the total change in intraocular pressure is

$$\frac{dp_i}{dt} = \tilde{K} p_i \dot{V}_{in} \quad \text{where } p_i(0) = p_{io}. \quad (2.142)$$

This case is similar to the subcases $\theta \ll 1$ in Case (A) and $\omega \ll 1$ in Case (B) which the intraocular pressure increases gradually and there is nothing to stop it. Thus, when ψ is very small, blindness is inevitable.

The Case $\psi \gg 1$ where $\lambda = O(1)$

In this Case (C), we consider ψ is large where λ is equal to order one. We assume the large value of ψ due to physically ψ corresponds to large pressure difference across the trabecular meshwork. We now examine equation (2.138) and the boundary conditions given in equation (2.139) may now be solved using regular perturbation methods, the same approach as in Case (B) when $\psi \gg 1$. For Case (C) when ψ is large, we found that $h(x)$ only satisfies the boundary conditions when x is near zero, but does not satisfy the boundary conditions when x is near one. Thus, we conclude that there are no solutions for these both cases, Case (B) and Case (C), because each case only holds when $h(x) > 0$ otherwise $h(x) = 0$. The solution is not allowed for $h(x) < 0$ because there is a solid boundary.

The Case $\lambda \gg 1$ where $\psi = O(1)$

Here we examine Case (C) by assuming λ is large and ψ is order one. We assume the large value of λ means that we take into account the large modulus of elasticity of the trabecular meshwork. We now examine equation (2.138) subject to the boundary conditions in equation (2.139) when λ is large. We numerically solve this boundary value problem in equation with same as we solved Case (A) and Case (B). Figure 2.18 shows the deformation of the trabecular meshwork for $\lambda \gg 1$. The results show that when λ is large, the deformation of the trabecular meshwork rapidly becomes large,

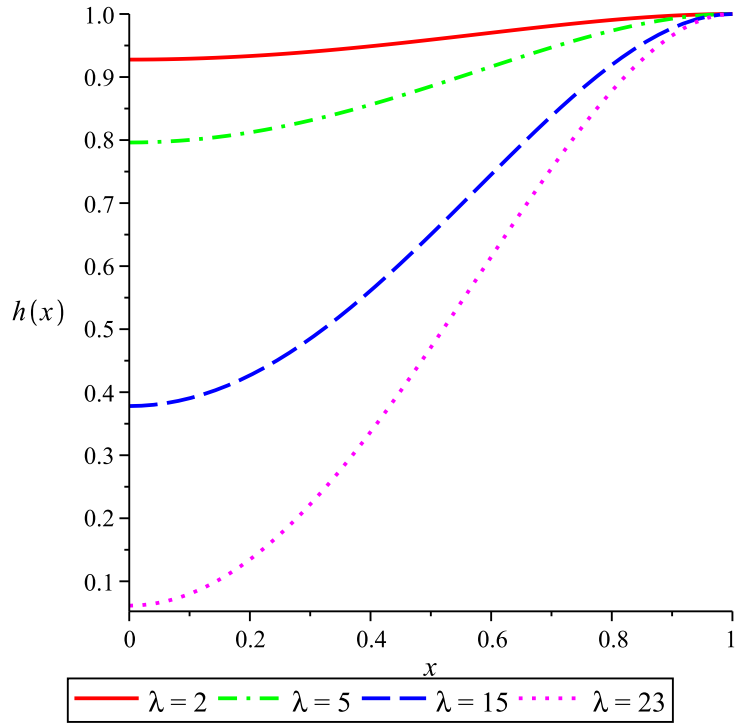


FIGURE 2.18: The deformation of the trabecular meshwork when λ is large by solving numerically equation (2.138) subject to the boundary conditions given in equation (2.139). In this case, the permeability, k in Darcy's law is inversely related to the square of pressure difference, $\frac{1}{(p_i-p)^2}$ and the value of ψ inherent to these calculations is equal to order one. Each graph corresponds to a different value of λ . The solid red, the dashed-dotted green, the dashed blue and the dotted magenta lines associated with $\lambda = 2$, $\lambda = 5$, $\lambda = 15$ and $\lambda = 23$ respectively.

bending towards the Schlemm canal, compared to Case (A) and Case (B), see Figure 2.15, Figure 2.17 and Figure 2.18 for comparison. Hence the intraocular pressure rises dramatically and vision may be lost forever.

2.6 Conclusions

In this study, we have discussed a model of aqueous humour flow through the trabecular meshwork and into the Schlemm canal in order to predict changes in intraocular pressure. We categorized this problem into different cases including simple cases, where important functions were assumed to be constant, and more complex cases.

Firstly, we examined the consequence of using Darcy's law in modelling the flow through the trabecular meshwork by considering the permeability, k to be either constant or varying with a pressure different and assuming the trabecular meshwork, $h(x)$ is still given as a constant. From the cases that have been examined we found that the

changes of intraocular pressure increases exponentially to the dangerous value of intraocular pressure in just under several minutes when the permeability, k is assumed to be inversely proportional to varying with the pressure different through the trabecular meshwork. Meanwhile when k is constant, the intraocular pressure rapidly increases to the high intraocular pressure in just under couple of seconds.

The results also show that the high intraocular pressure due to the amount of aqueous humour flowing out through the collector channels becomes zero. The aqueous humour insides the eye then rises and indirectly increases the level of intraocular pressure that may damage the optic nerve which may result in loss of vision. These cases have proved that the Darcy's law is important to take into account in order to predict the intraocular pressure because physically the trabecular meshwork is acts as a porous medium.

Secondly, we considered the flow through the trabecular meshwork is determined by Darcy's law and the trabecular meshwork is deformable. Case (A), Case (B) and Case (C) have been investigated through the sizes of four dimensionless parameters, θ , ω , ψ and λ , in order to examine the deformation of the trabecular meshwork. Several subcases where either θ , ω , ψ or λ may be either large or small. The results have shown that for subcases θ , ω and ψ were small for each Case (A), Case (B) and Case (C), the trabecular meshwork becomes much less deformed because the amount of aqueous humour through the trabecular meshwork is very small. Thus the intraocular pressure rises rapidly to the dangerous value of intraocular pressure. This rapid increases of intraocular pressure may cause blindness.

The results also shown that when λ was large in Case (A), Case (B) and Case (C), the deformation of the trabecular meshwork rapidly becomes large and "floppy". The aqueous humour then could not leave through the canal of Schlemm and exit at collector channels, thereby the intraocular pressure within the eye builds up dramatically and that may damage the optic nerve which may result in vision loss. When θ and λ were large in Case (A), we found that there is no problems because the trabecular meshwork was function properly, and no resistant to the aqueous humour outflow through the Schlemm canal and exit at collector channels. Thus for these both subcases, $\theta \gg 1$ and $\lambda \ll 1$, the intraocular pressure could not rises up and remains normal.

This study extended the study of [23] by considering the permeability, k in Darcy's law to be either constant or varying with pressure different and assuming the trabecular meshwork are elastic and deformable, thereby the general theory of a beam under axial load has been applied. The results in this work relating aqueous humour outflow to changes in intraocular pressure for various cases have shown that we now can calculate and examine the intraocular pressure increase when the pores in the trabecular meshwork close and the trabecular meshwork is deformable.

Note that we have examined cases where the permeability both increases and decreases with pressure difference. It is not clear which of these two phenomena actually happens.

To determine this would require the solution of a complicated compressible porous medium problem. It is clear that much more information is required about the response of the trabecular meshwork to an imposed pressure difference.

This model ignored the effects of uveoscleral outflow because the aqueous humour drainage mechanism is much weaker compared to the effects of the trabecular pathway. The simplified model studied here could further be extended to a three dimensional model, but this would lead to geometric complications and it is not clear what the benefits would be. Therefore this simplified model undertaken in this study may be regarded as finished.

Finally, it seems unlikely that the increases in intraocular pressure that lead to POAG come from some instability. It appears more likely that POAG is the result of a slow process where the trabecular meshwork progressively becomes less porous and insufficient aqueous humour drainage takes place.

Chapter 3

The Flow of Liquefied Vitreous Humour and Its Contribution to RRD

3.1 Introduction

Retinal Detachment is a disorder of the eye in which the retina peels away or tears from its underlying layer of support tissue. When retinal detachment occurs as a result of tears or breaks in the retina, it is known as rhegmatogenous retinal detachment (RRD). Either posterior vitreous detachment or injury to the head or eye may cause a small tear in the retina. When this happens liquefied vitreous humour may flow through the tear and push the retina away. If it remains detached, the retina will lose the ability to function and the patient will become permanently blind in the affected eye.

Paradigm mathematical models of fluid flow through the detached retina have been developed: the first approach to the problem considers a two-dimensional case which considers the fluid flow driven by a pressure difference (this pressure difference is caused by a small tear inside the wall of retina); the second approach concerns the nature of flow driven by saccadic eye motion in order to find the fluid flow and the deformation of the detached retina. The detached retina is assumed to be elastic and deformable; allowing the general theory of beam bending to be applied.

This chapter contains a literature review of the study; Anatomy and physiology of the retina, RRD in human eyes, treatment of RRD and saccadic motions of the eye. Then several models are presented in terms of the governing equations, the solution procedures, the mathematical analysis and discussion. We also summarise the problem and suggest further work.

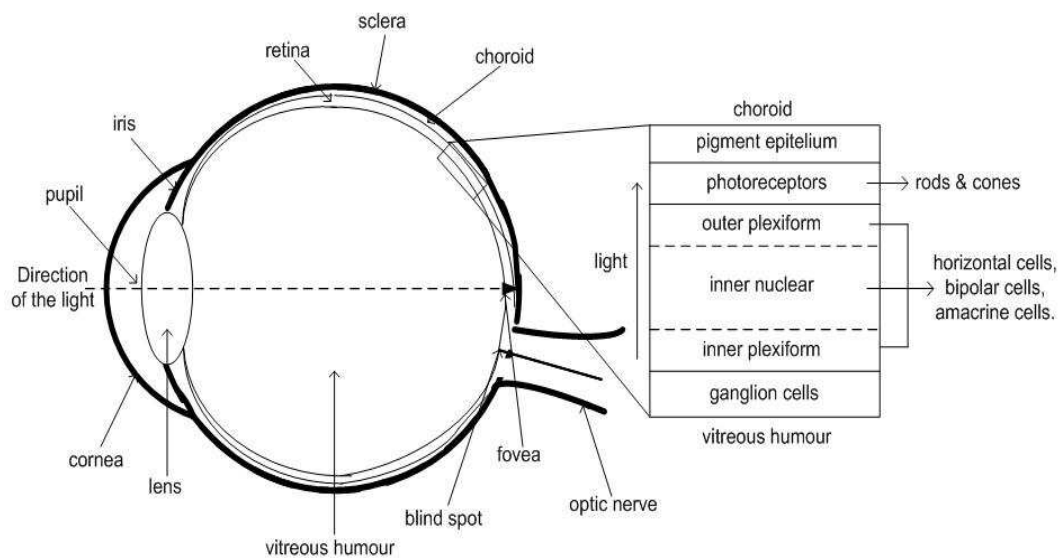


FIGURE 3.1: Diagram of a human eye and a structure of the retina.

3.2 The Retina

The retina is the innermost of the three layers of the human eye. The outermost layer of the human eye is the sclera and the layer between the retina and the sclera is the choroid. The retina is the most important part of the eye and may be considered to be part of the brain. Figure 3.1 shows a diagram of the human eye and the structure of the retina. The retina is made up of a number of layers namely three layers of nerve cells consisting of photoreceptors, inner nuclear and ganglion cells, and two layers of synaptic connections. It contains different types of cell and cells in the retina lie in discrete layers. The photoreceptors consist of the sensitive layer of rods and cones that lie in the outermost layer in the retina against the pigment epithelium and the choroid. The inner nuclear layer consists of one to four types of horizontal cells, 11 types of bipolar cells and 22 to 30 types of amacrine cells. The amacrine cells lie close to the ganglion cells and 20 types of the ganglion cells lie to the innermost layer in the retina, [41, 42, 99]. [41] explained that the outerplexiform layer contains the photoreceptors with the bipolar and the horizontal cells, and the inner plexiform layer consists of the bipolar and the amacrine cells connect to the ganglion cells.

The retina is a complex nervous structure that is responsible for the visual process. Note that the centre of the retina known as the fovea is the greatest importance region for vision due to the highest visual acuity. Light passes through the cornea and the pupil to the lens, and is projected onto the retina. The light then must travel through the thickness of the retina to reach the photoreceptors. The photoreceptors of the human eye respond to the action of light and transduce the light energy into electrical signals.

The electrical signals then transmit back to the amacrine and the ganglion cells. The axons of these ganglion cells will propagate signals to the optic nerve. The optic nerve takes the ganglion cell axons to the brain for further visual processing [41, 42, 99].

3.2.1 RRD in the Human Eye

A retinal detachment happens when the retina is pulled away from the choroid, which supplies most of the retinal nutrients. A detached retina is a serious problem which can cause significant vision loss unless it is treated. Retinal detachments can be classified into rhegmatogenous, tractional and exudative conditions depending on the mechanism of subretinal fluid accumulation [153]. [153] pointed out that a rhegmatogenous retinal detachment (RRD) may form due to a tear or break in the retina which allows liquefied vitreous humour to flow through the space between the retina and the retinal pigment epithelium (RPE) and this is the most common type of retinal detachment.

A number of researchers have discussed the clinical problem of retinal detachment (see, for example [43], [44] and [45]). [43] identified complex cellular responses that may affect reattachment of retinal detachment by using animal models. They used these models in order to find ways to control and prevent complications after reattachment surgery. [44] investigated the cause of the gray appearance of a detached retina and the result shows that the cause is from light scattering and it might cause visual loss in retinal detachment. Meanwhile, [45] examined the consequences of hyperoxia on retinal oxygenation and oxygen consumption in the detached feline retina. Many other researchers (which we do not review here) studied the problem of retinal detachment clinically, but only a few studies were of a mathematical nature.

The first model attempting to study mathematically how retinal detachment occurs was developed in [2]. [2] modelled the detached retina by assuming it to be a free surface on which pressure is exerted by surface tension effects (from the resulting force exerted by subretinal fluid) between the fluid and the detached retina without considering the shear stress. The results obtained in [2] assume that the surface tension and a constant pulling force exerted by the vitreous humour over the retina affect the progress of retinal detachment. However, this model did not include the elastic properties of the retina and did not consider the strength of adherence between the vitreous humour and the detached retina. In this current study, we develop paradigm mathematical models of fluid flow through the detached retina by considering the fluid flow induced by a pressure difference and flow in a channel; i) flow between rigid walls, ii) flow through one stationary and one moving wall in order to find the fluid flow behaviour.

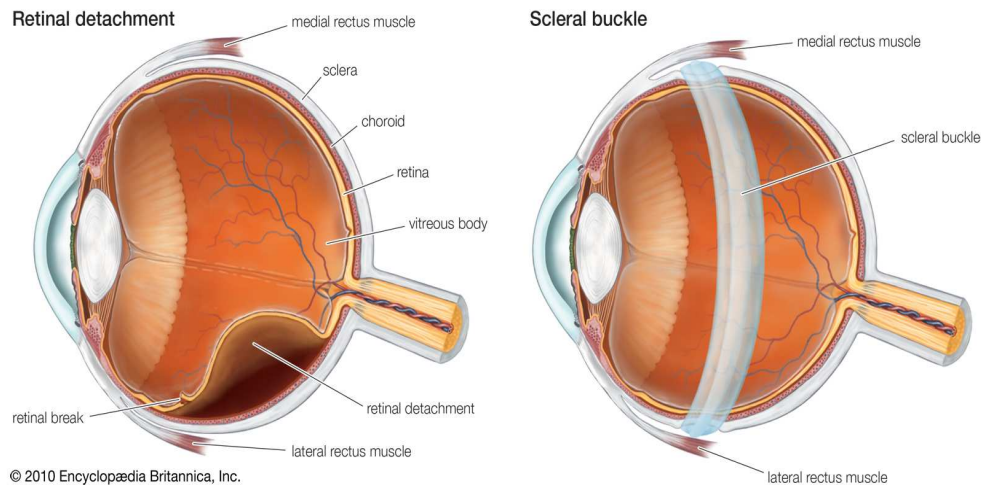


FIGURE 3.2: The retinal detachment and the scleral buckle. This figure was taken from [154].

3.2.2 Scleral Buckling in the Treatment of RRD

There are several approaches to treating a retinal detachment. One is the most commonly used in treating most eyes with rhegmatogenous retinal detachment (RRD) when there is no complicating factor is scleral buckling surgery, [41]. The purposes of the scleral buckling surgery are to close the retinal detachment and to reduce vitreous humour traction.

In the scleral buckling surgical procedure, the ophthalmologist first severs one of the rectus muscles of the eye to gain access to the sclera and then cuts open the small part of the sclera. Secondly, the ophthalmologist treats the detached retina by securing the detached retina back onto the choroid of the eye using either laser photocoagulation or a freeze treatment known as cryopexy and drains the vitreous humour that interferes with the retinal reattachment. After a detached retina has been secured, a silicone band or buckle is placed around the eyeball which is beneath the rectus muscle to gently push the eyeball against the detached retina until scarring seals the tear, Figure 3.2. This is called encircling scleral buckling surgery. If no buckle is placed, it is known as segmental scleral buckling surgery, [54]. The buckle also prevents fluid leakage which could cause further retinal detachment. Finally the severed muscle is repaired. For less severe detachment, the ophthalmologist may choose a temporary buckle, which could be removed later. However, the buckle usually stays beneath the rectus muscle permanently.

Laser photocoagulation is normally used when the retinal detachment is small. For larger detachments and case where the location of the detachment that cannot be reached with a laser, cryopexy is more suitable to use than laser photocoagulation. [41] stated that cryopexy is easy to apply and frequently used in the past, however it could

compromise the blood ocular barrier and cause proliferative vitreoretinopathy (which is simply scar tissue formation within the eye). If this occurs additional treatment including vitrectomy is required. To avoid this happening, the author of [41] suggests to use laser photocoagulation as an alternative method.

Risks can never be completely removed, but complications are rare. In some instances, scleral buckling surgery can involve the following, infection, pain, buckle extrusion and reduced vision which are the small possible risks, [41]. The high risk is cataract formation and this is due to using a gas bubble in the surgery. In this study, [55] recommended primary vitrectomy as the better method of choice for treating RRD with the grade C_1 proliferative vitreoretinopathy and the multiple detachments of the retina.

Since the scleral buckling surgery is one of the most common surgery to treating a retinal detachment, we hope to investigate scleral buckling more in Chapter 5.

3.3 Liquefied Vitreous Humour Flow driven by Saccadic Eye Motion

A number of studies have concerned the possible flow that might take place after vitrectomy surgery and have considered how the flow might cause “post reattachment” retinal detachment. Some have considered whether flows may be driven by buoyancy forces that arise from the different temperature of parts of the eye (see, for example [56]). [56] investigated the wall shear stress that was generated by buoyancy-driven flow in the limit of very small temperature differences and by saccadic motion-driven flow. In the latter driven flow case, two special limits have been considered; the limit of small amplitudes and the limit of high frequency oscillations of the eyeball. From the results [56], we learn that fluid flow driven by saccadic motions of the eye induces much more wall shear stress compared to buoyancy driven motion. This study also emphasized that saccadic motions of the eye are the more important factor in retinal detachment.

A saccade is a fast eye-head movement that rapidly redirects the eyes from one point to another [68]. Some examples of saccadic movement occur when reading (people move their eyes from left to right, see [57] and [58]), visual search [57], slow eye movement (SEM) during the onset of human sleep [59], when people blink [60] and rapid eye movement whilst sleeping [59]. A number of researchers have developed simple models of saccadic motion. [61] modelled the time-dependent shear stress force that occurs in the thin eye wall shell (whose material properties are isotropic and can be modelled by thin shell theory) supporting the vitreous humour inside the eyeball during the acceleration and deceleration of saccadic eye motion.

As a further study to [61], [62] developed an appropriate mathematical model which included much more information regarding the natural movement of the eye - saccadic motion. [62] presented both analytical and numerical solutions for the motion of the vitreous humour owing to eyeball rotations. From the results, [62] found that the shearing force exerted on the vitreo-retinal interface was due to the vitreous motion. However [61] showed that the muscle force and the viscous force exerted on the retina during saccadic motion could enhance the possibility of retinal tearing and detachment.

[63] presented an experimental study of vitreous motion driven by saccadic eye movements. [63] aimed to verify the results of [62] for purely viscous fluid; with saccadic motion described in terms of a simple sine function. [63] found good agreement with results shown by [62]: for larger values of the Womersley number, the non-zero velocities formed an oscillating boundary layer near the wall which drives steady streaming in the interior of the sphere.

Many previous studies (see [64, 65, 66, 67, 69]) have examined steady streaming flows. [64] considered the flow induced by a sphere oscillating with velocities in a viscous fluid where the amplitude, ε of the oscillation is small compared with the radius of the sphere ($\varepsilon \ll 1$). They also consider an axisymmetric flow with velocities, $U_\infty \cos(\omega t)$ and use spherical polar coordinates. [65] concerned the flow driven by a body oscillating in an unbounded viscous fluid. [65], used the technique of matched asymptotic expansions. Its main aim is to find the structure of the steady streaming. The flow induced by small amplitude torsional harmonic oscillations of a sphere in a viscous fluid has been studied by [67] with special attention on the second-order streaming motion. A review of the work done on normal steady streaming flow has been considered in a homogeneous fluid. However [66] stated that the study might be markedly different for free-surface flows. [66] also presented important areas of application in steady streaming such as fluid dynamical problems of the inner ear, the growth of protein crystals, the growth rate of bubbles in a sound field and others. The most recent work on steady streaming was carried out in [69]. In [69], they considered flow in a hollow sphere undergoing torsional oscillation. The flow is governed by two dimensionless parameters, the amplitude, ε and Womersley number, α . They calculate and analyse the flow behaviour both theoretically (which is in terms of vector spherical harmonics) and experimentally under consideration of small-amplitude oscillations.

[68] formulated the problem regarding liquefied vitreous humour driven by saccadic eye movement by modelling the real shape of the vitreous chamber as a weakly deformed sphere. [68] assumed the liquefied vitreous to be a low viscosity Newtonian incompressible fluid. It is important to note that after vitrectomy surgery, the viscous humour is often replaced by other liquids such as silicone oil - known as liquefied vitreous humour. [70] extended the work of [68] by examining theoretically the effect of the posterior chamber geometry upon the flow field during saccades of the eye. [70] assumed the deformed sphere had the shape of a spherical cap and [70] presented good

qualitative agreement with the experimental results of [71]. In this current study, we develop a mathematical model of liquefied vitreous humour driven by saccadic motions of the eye and assess its role as a cause of RRD. We consider the flow induced by a hollow sphere oscillating in a viscous fluid (which is in the limit of small amplitude, $\varepsilon \ll 1$) and we also assume the detached retina to be elastic and deformable so that the general theory of beam bending can be applied. In particular, asymptotic analysis will be used in order to find and analyse the flow behaviour and the deformation of the detached retina.

3.4 Motivation for the Mathematical Model

Several mathematical models will be developed in order to approach a more realistic perspective of the problem. The paradigm mathematical models will be set up to study the fluid flow through the detached retina. The detached retina is assumed to be a thin flap which is attached to a plane wall (the choroid) and it is also assumed to be elastic and deformable. Thus the general theory of beam bending will be applied. In the first paradigm mathematical model, we will present the flow of liquefied vitreous humour between rigid walls where the fluid is driven by a pressure gradient (that caused by the retina tears from its underlying layer of support tissue). In the second paradigm mathematical model, we will examined liquefied vitreous humour flow in a channel with one moving wall and one stationary wall. In particular, these models will be studied using the lubrication theory limit of the Navier-Stokes equations. Using asymptotic analysis the flow behaviour and the deformation of the detached retina will be analysed. To pose a more realistic problem, we will present a more complicated mathematical model of retinal detachment. Specifically the liquefied vitreous humour flows during the nature of the flow induced by the saccadic rotations of the eyeball and assess its role in RRD. The governing equations will be developed using the full Navier-Stokes equations for the fluid flow in the sphere. We will then solve the equations explicitly to determine and examine the fluid flow in certain parameter regimes.

In both the paradigm problems that we are going to consider, our aims will be the same: we wish to examine whether, in a simple thin layer channel flow where an idealised “detachment” is present, flow driven by either a pressure gradient or a moving upper wall can lead to fluid mechanical effects that tend to make the detachment more extreme.

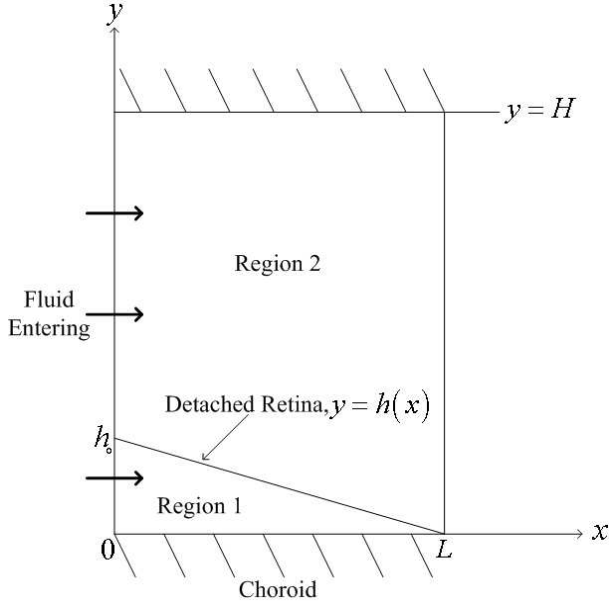


FIGURE 3.3: Schematic diagram of liquefied vitreous humour flow through the detached retina.

3.5 Modelling of Paradigm Problem: Flow in a Channel with Rigid Walls

A steady two-dimensional flow of an incompressible Newtonian fluid with constant viscosity, μ and density, ρ is shown in Figure (3.3). We introduce a Cartesian coordinate system (x, y) with the wall, $y = 0$ and $y = H$ as fixed walls. The detached retina occupies $0 \leq x \leq L$ and is given by $y = h(x)$. Denote the velocities in the x and y directions, pressures and volume fluxes in the x direction (per unit width) by u_k , v_k , p_k and Q_k where $k = 1$ denotes values in $0 \leq x \leq L, 0 \leq y \leq h(x)$ (that is the region ‘below’ the detached retina, termed ‘Region 1’), $k = 2$ denotes values in $0 \leq x \leq L, h(x) \leq y \leq H$ (that is the region ‘above’ the detached retina, termed ‘Region 2’), see [46] for further details.

3.5.1 Mathematical Model

[2] noted that it is possible to assume that the choroid is a plane wall to which the retina is attached since the curvature of the eye is not perceptible from the detached retina. In Figure (3.3), the choroid is represented by the x -axis ($y = 0$) and the detached retina (which is a thin flap) determined by the unknown function, $y = h(x)$. We now assume that the initial height of the detached retina, is $h_0 = 0.1\text{mm}$, the length of the detached retina, is $L = 1.0\text{mm}$ and the kinematic viscosity of the aqueous humour, is $\nu = \frac{\mu}{\rho} \sim 0.9 \times 10^{-6}\text{m}^2\text{s}^{-1}$ (all the parameter values are obtained from [2] and [47]). Using the values from [47], a typical diameter of a human eye is $H = 25\text{mm}$ and a

typical velocity, $U \sim 2.1 \times 10^{-5} \text{ ms}^{-1}$, we now find that the aspect ratio of detached retina, $\delta = \frac{h_0}{L}$ is about 0.1 and thus we obtain the Reynolds number $\text{Re} = \frac{LU}{\nu} \sim 0.025$ and the reduced Reynolds number, $\delta^2 \text{Re} \sim 2.5 \times 10^{-4}$. Therefore, the lubrication theory approximation of the Navier-Stokes equations can be applied, thereby

$$\begin{aligned} p_{kx} &= \mu u_{kyy}, \\ p_{ky} &= 0, \\ u_{kx} + v_{ky} &= 0, \end{aligned} \tag{3.1}$$

so the pressure in each region is independent of y and $k = 1, 2$ (the two regions) and subscripts denote derivatives, to be solved subject to the no slip conditions on $y = 0$, $y = h(x)$ and $y = H$. The boundary conditions are:

at $k = 1$ ($0 \leq x \leq L$, $0 \leq y \leq h(x)$),

$$\begin{aligned} u_1(x, 0) &= v_1(x, 0) = 0, \\ u_1(x, h(x)) &= v_1(x, h(x)) = 0, \end{aligned} \tag{3.2}$$

and at $k = 2$ ($0 \leq x \leq L$, $h(x) \leq y \leq H$),

$$\begin{aligned} u_2(x, h(x)) &= v_2(x, h(x)) = 0, \\ u_2(x, H) &= v_2(x, H) = 0. \end{aligned} \tag{3.3}$$

We now let

$$p_1(0) = p_2(0) = p_o \quad \text{and} \quad p_2(L) = p_L. \tag{3.4}$$

3.5.2 Solution Procedures

The governing equations (3.1) may now be solved to get,

$$u_k = \frac{1}{\mu} \left[p_{kx} \frac{y^2}{2} + C_1 y + C_2 \right] \tag{3.5}$$

where C_1 and C_2 are arbitrary constants, that are different in each region.

Region (1)

We now substitute the boundary conditions (3.2) into equation (3.5), to find that in Region (1)

$$C_1 = -\frac{p_{1x}h}{2} \quad \text{and} \quad C_2 = 0.$$

We rewrite equation (3.5) by substituting the values above, yielding

$$u_1 = \frac{1}{\mu} \left[p_{1x} \frac{y^2}{2} - p_{1x} \frac{hy}{2} \right]. \tag{3.6}$$

Then we differentiate equation (3.6) with respect to x , to get that

$$u_{1x} = \frac{1}{\mu} \left[p_{1xx} \frac{y^2}{2} - p_{1xx} \frac{hy}{2} - p_{1x} \frac{h_xy}{2} \right].$$

We may now substitute the equation above into equation (3.1), integrate it with respect to y , and we then substitute the boundary condition given in equation (3.2). Therefore

$$v_1 = -\frac{1}{\mu} \left[p_{1xx} \frac{y^3}{6} - p_{1xx} \frac{hy^2}{4} - p_{1x} \frac{h_xy^2}{4} \right],$$

and also

$$\left[-\frac{p_{1x}h^3}{12} \right]_x = 0. \quad (3.7)$$

If we integrate equation (3.7) and substitute the boundary condition (3.4), we obtain

$$p_1(x) = p_o. \quad (3.8)$$

Therefore the pressure in Region (1) is constant.

Region (2)

We now repeat the same steps as in Region (1) by solving equation (3.1) with the boundary conditions given in equation (3.3). We obtain the velocities in this region as

$$u_2 = \frac{1}{\mu} \left[p_{2x} \frac{y^2}{2} - p_{2x} \frac{y}{2} (H + h) + p_{2x} \frac{hH}{2} \right], \quad (3.9)$$

and

$$v_2 = -\frac{1}{2\mu} \left[p_{2xx} \frac{y^3}{3} - p_{2xx} \frac{y^2}{2} (H + h) - p_{2x} \frac{h_xy^2}{2} + (p_{2xx}hH + p_{2x}h_xH)y \right] + \frac{1}{2\mu} \left[-p_{2xx} \frac{h^3}{6} + p_{2xx} \frac{h^2H}{2} - p_{2x} \frac{h_xh^2}{2} + p_{2x}h_xhH \right], \quad (3.10)$$

and also the equation for pressure,

$$-\left[p_{2xx} \frac{H^3}{3} - p_{2xx} \frac{H^2}{2} (H + h) - p_{2x} \frac{h_xH^2}{2} + (p_{2xx}hH + p_{2x}h_xH)H \right] - p_{2xx} \frac{h^3}{6} + p_{2xx} \frac{h^2H}{2} - p_{2x} \frac{h_xh^2}{2} + p_{2x}h_xhH = 0. \quad (3.11)$$

By simplifying equation (3.11), we deduce that

$$p_{2xx} \left[\left(\frac{h^3 - H^3}{3} \right) + Hh(H - h) \right] + p_{2x} [H^2h_x + h_xh^2 - 2hh_xH] = 0,$$

which may be written as

$$\left[p_{2x} \left(\left(\frac{h^3 - H^3}{3} \right) + Hh(H-h) \right) \right]_x = 0. \quad (3.12)$$

We now formulate an equation that links the displacement directly to the distributed load which arises from the different pressures in the Region (2) and Region (1), thereby obtaining

$$EI \frac{d^4 h}{dx^4} = p_1(x) - p_2(x)$$

where E and I are the modulus of elasticity and the moment of inertia of retina. The equation above represents the beam equation (see [49, 50] for further details). By substituting (3.8) into the equation above, we may get that

$$EI \frac{d^4 h}{dx^4} = p_o - p_2(x) \quad (3.13)$$

In this problem, we assume that one end of the detached retina is free to move and the other end of the detached retina is still attached to the choroid thus we assume that the beam has a clamped end. Therefore the boundary conditions are

$$\begin{aligned} h_{xx}(0) &= 0, & h_{xxx}(0) &= 0, \\ h(L) &= 0, & h_x(L) &= 0. \end{aligned} \quad (3.14)$$

3.5.3 Analytical Results

Let us now introduce the non-dimensional parameters,

$$x = L\bar{x}, \quad p_2 = p_o + (p_L - p_o)\bar{p}_2 \quad \text{and} \quad h = H\bar{h}. \quad (3.15)$$

Note that bars denote non-dimensional variables. We non-dimensionalise equations (3.12), (3.13) and the boundary conditions given in equations (3.4), (3.14) by substituting the non-dimensional parameters in (3.15), to find that

$$\left[\bar{p}_{2\bar{x}} \left(\left(\frac{\bar{h}^3 - 1}{3} \right) + \bar{h}(1 - \bar{h}) \right) \right]_{\bar{x}} = 0, \quad (3.16)$$

and

$$\frac{d^4 \bar{h}}{d\bar{x}^4} = \alpha \bar{p}_2(\bar{x}) \quad \text{where} \quad \alpha = \frac{L^4(p_o - p_L)}{HEI}, \quad (3.17)$$

with the boundary conditions,

$$\begin{aligned} \bar{p}_2(0) &= 0, & \bar{h}_{xx}(0) &= 0, \\ \bar{h}_{xxx}(0) &= 0, & \bar{p}_2(1) &= 1, \\ \bar{h}(1) &= 0, & \bar{h}_x(1) &= 0. \end{aligned} \quad (3.18)$$

Since this is a paradigm problem, it is rather hard to give an unambiguous value for α (which represents the relative importance of the effects of pressure difference and elastic stiffness). Suppose however that we use the plausible values $L \sim 10^{-3}\text{m}$, $H \sim 10^{-2}\text{m}$, $\Delta p \sim 10^2\text{Pa}$, and assume that the “detachment” is a rectangular plate so that $EI = 12Et^3/(1 - \nu^2)$, with plate thickness $t \sim 10^{-4}\text{m}$ and $E \sim 10^8\text{Pa}$, we immediately find that $\alpha \ll 1$.

We may now solve the equations (3.16) and (3.17) subject to the boundary conditions (3.18) in order to find $p = p_2(x)$ and $h = h(x)$. Note that from here onward we omit the bars for simplicity. We now analyze the problem by assuming that $\alpha \ll 1$ and introducing the asymptotic expansions,

$$\begin{aligned} h &= h_0 + \alpha h_1 + \alpha^2 h_2 + \dots, \\ p &= p_0 + \alpha p_1 + \alpha^2 p_2 + \dots \end{aligned} \quad (3.19)$$

By substituting (3.19) into the equations (3.16), (3.17) and the boundary conditions (3.18), we may get that

$$\left[(p_0 + \alpha p_1 + \alpha^2 p_2 + \dots)_x \left(\frac{(h_0 + \alpha h_1 + \alpha^2 h_2 + \dots)^3}{3} \right. \right. \\ \left. \left. - \frac{1}{3} + (h_0 + \alpha h_1 + \alpha^2 h_2 + \dots)(1 - h_0 - \alpha h_1 - \alpha^2 h_2 - \dots) \right) \right]_x = 0, \quad (3.20)$$

and

$$(h_0 + \alpha h_1 + \alpha^2 h_2 + \dots)_{xxxx} = \alpha (p_0 + \alpha p_1 + \alpha^2 p_2 + \dots), \quad (3.21)$$

with

$$\begin{aligned} h_{xx}(0) &= h_{0xx}(0) + \alpha h_{1xx}(0) + \alpha^2 h_{2xx}(0) + \dots = 0 \\ h_{xxx}(0) &= h_{0xxx}(0) + \alpha h_{1xxx}(0) + \alpha^2 h_{2xxx}(0) + \dots = 0 \\ h(1) &= h_0(1) + \alpha h_1(1) + \alpha^2 h_2(1) + \dots = 0 \\ h_x(1) &= h_{0x}(1) + \alpha h_{1x}(1) + \alpha^2 h_{2x}(1) + \dots = 0 \\ p(0) &= p_0(0) + \alpha p_1(0) + \alpha^2 p_2(0) + \dots = 0 \\ p(1) &= p_0(1) + \alpha p_1(1) + \alpha^2 p_2(1) + \dots = 1. \end{aligned} \quad (3.22)$$

From equations (3.20) and (3.21), and the boundary conditions (3.22), we may now extract the equations and the boundary conditions that we are going to solve to leading order, $\alpha^{(0)}$,

$$\left[p_{0x} \left(\left(\frac{h_0^3 - 1}{3} \right) + h_0(1 - h_0) \right) \right]_x = 0, \quad (3.23)$$

and

$$h_{0xxxx} = 0, \quad (3.24)$$

with

$$\begin{aligned} p_0(0) &= 0, \quad h_{0xx}(0) = 0, \\ h_{0xxx}(0) &= 0, \quad p_0(1) = 1, \\ h_0(1) &= 0, \quad h_{0x}(1) = 0. \end{aligned} \tag{3.25}$$

To first order, $\alpha^{(1)}$,

$$\left[p'_0 (h_0^2 h_1 + h_1 - 2h_0 h_1) + p'_1 \left(\frac{h_0^3 - 1}{3} + h_0 (1 - h_0) \right) \right]_x = 0, \tag{3.26}$$

and

$$h_{1xxxx} = p_0, \tag{3.27}$$

with

$$\begin{aligned} p_1(0) &= 0, \quad h_{1xx}(0) = 0, \\ h_{1xxx}(0) &= 0, \quad p_1(1) = 0, \\ h_1(1) &= 0, \quad h_{1x}(1) = 0. \end{aligned} \tag{3.28}$$

We now solve the problems above.

$\alpha^{(0)}$: Integrating equation (3.24) four times with respect to x and substituting the boundary conditions in equation (3.25), we may find that the equation at leading order is

$$h_0(x) = 0. \tag{3.29}$$

We now substitute equation (3.29) into equation (3.23), thus we obtain

$$\left[p_{0x} \left(-\frac{1}{3} \right) \right]_x = 0. \tag{3.30}$$

By solving equation (3.30) and substituting the boundary conditions (3.25), we may get the equation of $p(x)$ at leading order:

$$p_0(x) = x. \tag{3.31}$$

$\alpha^{(1)}$: We now substitute equation (3.31) into equation (3.27) and we then integrate the equation four times with respect to x substitute the boundary conditions given in equation (3.28), to obtain that

$$h_1 = \frac{x^5}{120} - \frac{x}{24} + \frac{1}{30}. \tag{3.32}$$

We now substitute equations (3.29) and (3.32) into equation (3.26), to find that

$$\left[h_1 - \frac{p_{1x}}{3} \right]_x = 0. \tag{3.33}$$

We now solve equation (3.33) subject to the boundary conditions (3.28), therefore we

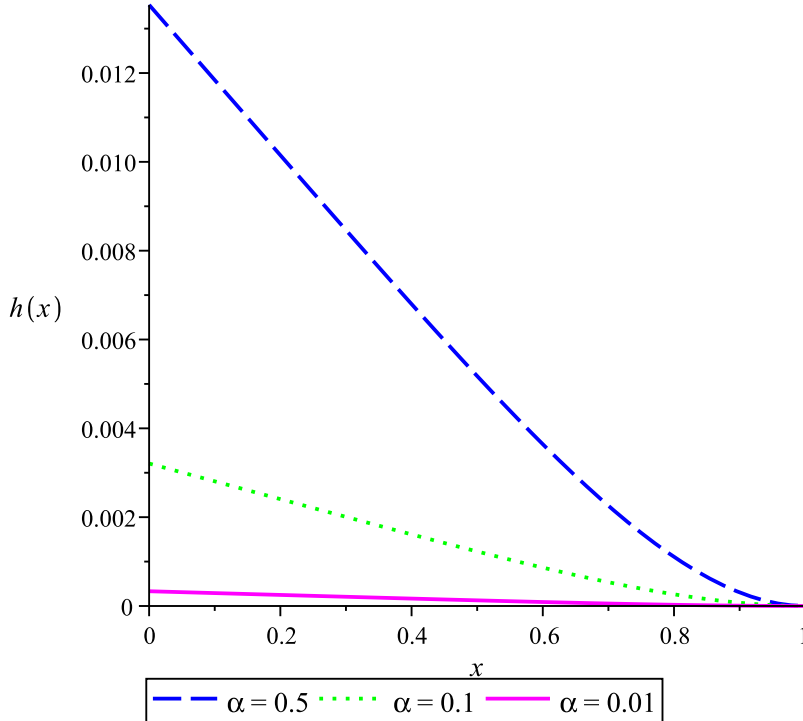


FIGURE 3.4: The deformation of detached retina, $h(x)$ given in equation (3.36) for different values of α . The solid magenta line represents the detached retina associated with an α equal to 0.01, whereas the dotted-dashed green line and the dashed blue line denote the corresponding detached retina for α equal to 0.1 and 0.5.

get the equation of pressure as

$$p_1(x) = \frac{x^6}{240} - \frac{x^2}{16} + \frac{7x}{20}. \quad (3.34)$$

Then we substitute equations (3.31) and (3.34) into equation (3.19), to get the equation of $p(x)$ in Region (2).

$$p = p_2(x) = x + \frac{x^6}{240} - \frac{x^2}{16} + \frac{7x}{20} + O(\alpha^2). \quad (3.35)$$

We now substitute equations (3.29) and (3.32) into equation (3.19), to find that $h(x)$ is given by

$$h(x) = \alpha \left(\frac{x^5}{120} - \frac{x}{24} + \frac{1}{30} \right) + O(\alpha^2). \quad (3.36)$$

Equation (3.36) may now be plotted (see Figure (3.4)) in order to examine the deformation of the detached retina when α is small. Figure (3.4) shows the deformation of the detached retina for different values of α . It shows that when the value α of decreases, then $h(x)$ becomes much less deformed. The volume fluxes (per unit length in the axial direction) in the two regions are given by

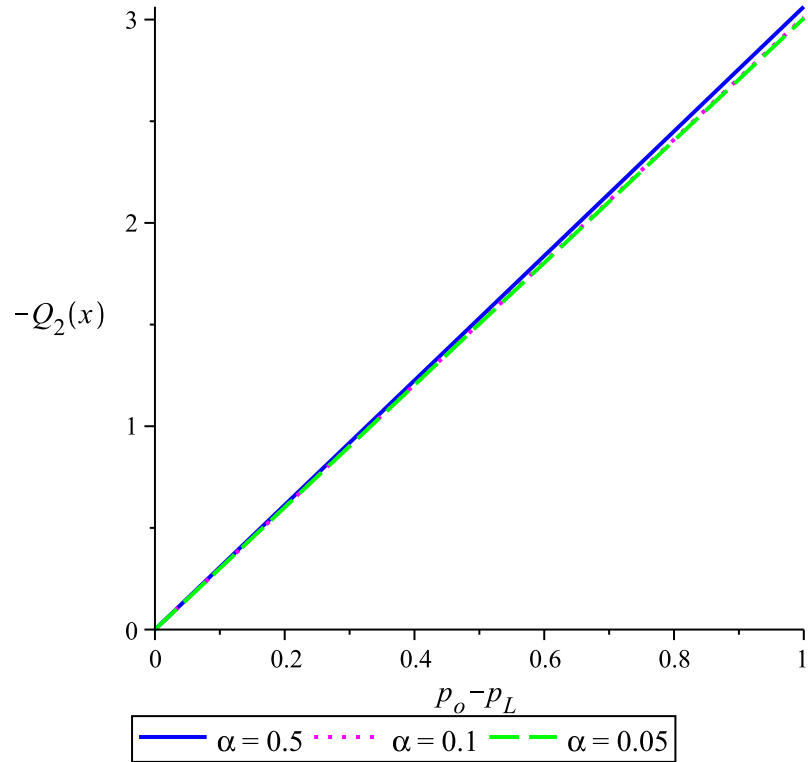


FIGURE 3.5: The volume flux in Region (2), $Q_2(x)$ given in equation (3.38) versus the pressure different, $p_o - p_L$. Each graph corresponds to a different value of α . The solid blue line, the dotted magenta line and the dashed green line represent the corresponding detached retina for α equal to 0.5, 0.1, and 0.05.

$$Q_1 = 0. \quad (3.37)$$

Equation (3.37) shows that there is no flux in Region (1) due to the fact that the velocity in this region is equal to zero.

$$Q_2 = \frac{p_o - p_L}{\int_0^1 \left(\left(\frac{h^3 - 1}{3} \right) + h(1-h) \right) dx}$$

Then we substitute equation (3.36) into the equation above, we may get that

$$Q_2(x) = \frac{p_o - p_L}{\frac{1231}{483840000}\alpha^3 - \frac{47}{151200}\alpha^2 + \frac{7}{480}\alpha - \frac{1}{3}}. \quad (3.38)$$

We now plot equation (3.38) showing the volume flux in Region (2), $Q_2(x)$ versus the pressure difference (see Figure (3.5)). Figure (3.5) presents four different curves for different values of α . It presents that when the value of pressure difference increases, then the value of volume flux, $Q_2(x)$ also increases. It also shows that the volume flux is nearly the same in all different cases of α . This means that the volume flux in Region

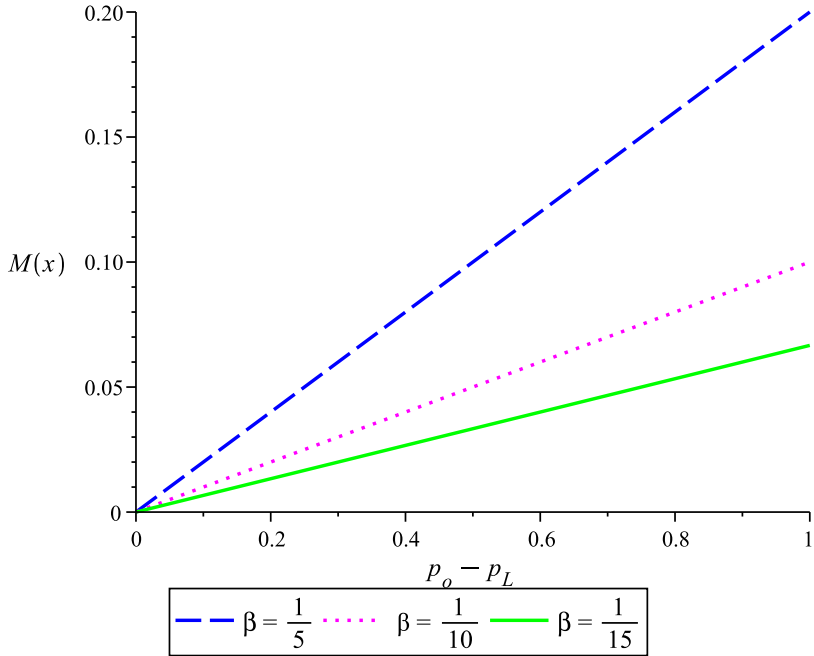


FIGURE 3.6: Bending moment, $M(x)$ at the end of the detached retina, $x = L$ given in equation (3.40) versus pressure different, $p_o - p_L$ for different values of $\beta = \frac{L^7}{6H}$ where $\varepsilon = \frac{1}{\beta}$. The dashed blue line represents the bending moment associated with β equal to $\frac{1}{5}$, whereas the dotted magenta line and the solid green line denote the corresponding bending moment for β equal to $\frac{1}{10}$ and $\frac{1}{15}$.

(2) is weak and it does not really depend on α . We now examine the bending moment, M at the end of the detached retina ($x = L$) in term of pressure different and length. We know that $M = EI h_{xx}(x)|_{x=L}$, thus we may find that

$$M = EI \left[\frac{\alpha x^3}{6} \right]_{x=L} ; \quad \alpha = \frac{L^4 (p_o - p_L)}{EI H}. \quad (3.39)$$

We simplify equation (3.39), yielding

$$M = (p_o - p_L) \frac{L^7}{6H}. \quad (3.40)$$

Equation (3.40) may now be plotted in terms of the bending moment versus the pressure difference by assuming that $\beta = \frac{L^7}{6H} \Rightarrow \varepsilon = \frac{1}{\beta}$ (see Figure (3.6)). Figure (3.6) shows four different linear curves at different value of ε . It shows that when the value of ε is large (L^7 is very small) then the beam becomes much less deflected. Physically it is because the length of the detached retina is very tiny thus the bending moment decreases. We now plot the graph of bending moment versus length (see Figure (3.7)) when the value of ε decreases. It presents that when the value of ε is small ($p_o - p_L$ is large), then the beam becomes much more deflected. We considered the length of the detached retina, $L = 10mm$ which is a very big flap. If $p_o - p_L$ is increases then it shows the bending

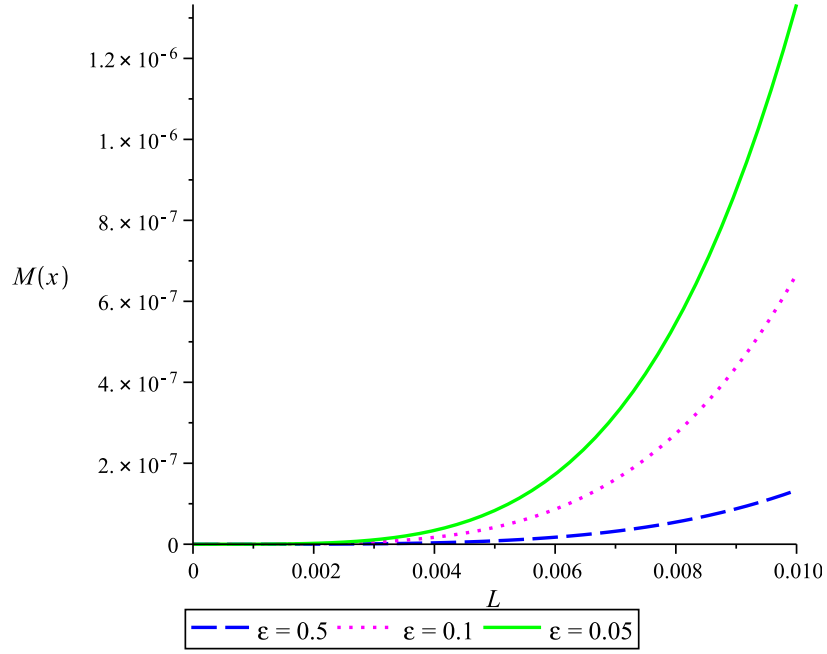


FIGURE 3.7: Bending moment, $M(x)$ versus length of the detached retina, L given in equation (3.40). The value chosen for the L is 10mm. Each graph corresponds to a different value of ε . The dashed blue line, the dotted magenta line and the solid green line denote the corresponding bending moment for ε equal to 0.5, 0.1 and 0.05.

moment also increases.

3.6 Modelling of Paradigm Problem: Flow in a Channel with One Stationary and One Moving Wall

The model examined in the previous section may be thought of as a paradigm problem for the flow of liquefied vitreous humour in the presence of a detachment. We also want to investigate how the motion of a detachment might be influenced by saccadic eye motions. We therefore now consider flow over a detachment where the driving force is provided by an oscillating upper wall, as might be the case when saccadic eye motion takes place.

Therefore consider the steady 2D flow of a Newtonian fluid with constant viscosity, μ and density, ρ . Introduce a Cartesian coordinate system (x, y) with the plates, $y = 0$ as fixed plate and $y = H$ is a moving plate. We now improve our first model by assuming that the top plate is moving with speed, $u = U_\infty \sin(\omega t)$. The detached retina occupies $0 \leq x \leq L$ and is given by $y = h(x)$. It has a very small angle that denotes as α . Denote the velocities and pressures by $u_k \vec{i} + v_k \vec{j}$ and p_k where $k = 1$ denotes values in $0 \leq x \leq L, 0 \leq y \leq h(x)$ (that is the region ‘below’ the detached retina, termed ‘R1 = Region 1’), $k = 2$ denotes values in $0 \leq x \leq L, h(x) \leq y \leq H$

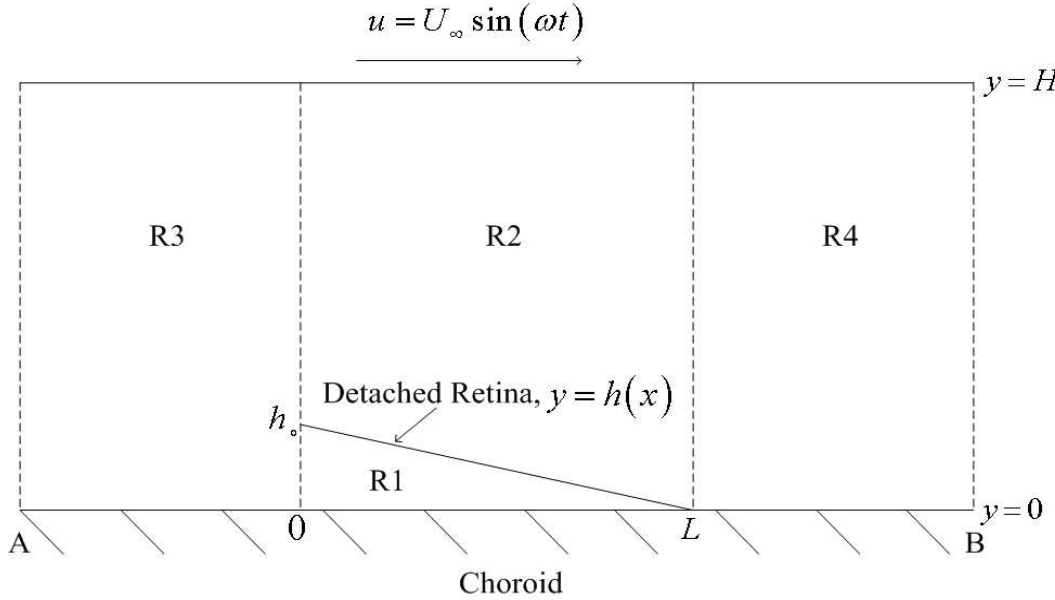


FIGURE 3.8: Schematic diagram of flow with One Moving and One Stationary Plate.

(that is the region ‘above’ the detached retina, termed ‘R2 = Region 2’), $k = 3$ denotes values in $A \leq x \leq 0, 0 \leq y \leq H$ (this is ‘R3 = Region 3’) and $k = 4$ denotes values in $L \leq x \leq B, 0 \leq y \leq H$ (this is ‘R4 = Region 4’).

3.6.1 Mathematical Model

By using the lubrication theory limit of the Navier-Stokes equations, we develop the governing equations for this problem, see Figure 3.8 for nomenclature. These are:

$$\begin{aligned} p_{kx} &= \mu u_{kyy}, \\ p_{ky} &= 0, \\ u_{kx} + v_{ky} &= 0, \end{aligned} \tag{3.41}$$

where $k = 1, 2, 3, 4$ (region) and subscripts denote derivatives, to be solved subject to the no slip conditions on $y = 0$, $y = h(x)$ and $y = H$. The boundary conditions:

at $k = 1$ ($0 \leq x \leq L, 0 \leq y \leq h(x)$),

$$\begin{aligned} u_1(x, 0) &= v_1(x, 0) = 0, \\ u_1(x, h(x)) &= v_1(x, h(x)) = 0, \\ p_1(0) &= p_o, \quad p_1(L) = p_o, \end{aligned} \tag{3.42}$$

at $k = 2 \quad (0 \leq x \leq L, h(x) \leq y \leq H)$,

$$\begin{aligned} u_2(x, h(x)) &= v_2(x, h(x)) = 0, \\ u_2(x, H) &= U_\infty \sin(\omega t), \quad v_2(x, H) = 0, \\ p_2(0) &= p_o, \quad p_2(L) = p_o. \end{aligned} \tag{3.43}$$

at $k = 3 \quad (A \leq x \leq 0, 0 \leq y \leq H)$,

$$\begin{aligned} u_3(x, 0) &= v_3(x, 0) = 0, \\ u_3(x, H) &= U_\infty \sin(\omega t), \quad v_3(x, H) = 0, \\ p_3(A) &= p_o, \quad p_3(0) = p_o, \end{aligned} \tag{3.44}$$

and at $k = 4 \quad (B \leq x \leq L, 0 \leq y \leq H)$,

$$\begin{aligned} u_4(x, 0) &= v_4(x, 0) = 0, \\ u_4(x, H) &= U_\infty \sin(\omega t), \quad v_4(x, H) = 0, \\ p_4(L) &= p_o, \quad p_4(B) = p_o. \end{aligned} \tag{3.45}$$

The pressure in each region is independent of y .

3.6.2 Solution Procedures

The governing equations (3.41) may now be solved to get,

$$u_k = \frac{1}{\mu} \left[p_{kx} \frac{y^2}{2} + C_1 y + C_2 \right] \tag{3.46}$$

where C_1 and C_2 are arbitrary constants.

Region (1)

We now substitute the boundary conditions given in equation (3.42) into equation (3.46), to obtain

$$u_1 = \frac{1}{\mu} \left[p_{1x} \frac{y^2}{2} - p_{1x} \frac{hy}{2} \right]. \tag{3.47}$$

We differentiate equation (3.47) with respect to x and substitute into equation (3.41), yielding

$$v_{1y} = -\frac{1}{2\mu} [p_{1xx}y(y-h) - p_{1x}h_xy].$$

We may now integrate the equation above with respect to y and substitute the boundary condition in equation (3.42), thus we get that

$$v_1 = -\frac{1}{2\mu} \left[p_{1xx} \frac{y^3}{3} - p_{1xx} \frac{hy^2}{2} - p_{1x} \frac{h_xy^2}{2} \right].$$

At $y = h(x)$ and $v_1 = 0$, we may find that

$$\left[\frac{p_{1x}h^3}{12} \right]_x = 0.$$

If we integrate the above equation and substitute the boundary condition (3.42), we find that

$$p_1(x) = p_o. \quad (3.48)$$

Region (2)

We now substitute the boundary conditions given in equation (3.43), to obtain that

$$u_2 = \frac{1}{\mu} \left[p_{2x} \frac{y^2}{2} + \frac{\mu U_\infty \sin(\omega t)}{(H-h)} (y-h) - \frac{p_{2x}}{2} y (H+h) + \frac{p_{2x}}{2} h H \right]. \quad (3.49)$$

Then we differentiate equation (3.49) with respect to x , to find that

$$u_{2x} = \frac{1}{\mu} \left[p_{2xx} \frac{y^2}{2} + \mu U_\infty \sin(\omega t) \left(-\frac{h_x}{(H-h)} + \frac{h_x(y-h)}{(H-h)^2} \right) - p_{2xx} \frac{y}{2} (H+h) - p_{2x} \frac{h_x y}{2} + p_{2xx} \frac{h H}{2} + p_{2x} \frac{h_x H}{2} \right]. \quad (3.50)$$

We now substitute equation (3.50) into equation (3.41), then integrate the equation with respect to y and substitute the boundary condition given in equation (3.43). Therefore we obtain

$$v_2 = -\frac{1}{\mu} \left[p_{2xx} \frac{y^3}{6} + \mu U_\infty \sin(\omega t) \left[\frac{h_x}{(H-h)^2} \left(\frac{y^2}{2} - yh \right) - \frac{yh_x}{(H-h)} \right] - p_{2xx} \frac{y^2}{4} (H+h) - p_{2x} \frac{h_x y^2}{4} + \left(p_{2xx} \frac{h H}{2} + p_{2x} \frac{h_x H}{2} \right) y \right] + \frac{1}{\mu} \left[p_{2xx} \left(-\frac{h^3}{12} + \frac{h^2 H}{4} \right) + p_{2x} \left(-\frac{h_x h^2}{4} + \frac{h h_x H}{2} \right) + \frac{\mu U_\infty \sin(\omega t) h h_x}{(H-h)} \left[\frac{h}{2(H-h)} - 1 \right] \right]. \quad (3.51)$$

We now substitute $y = H$ and $v_2 = 0$ into equation (3.51) and simplify to get

$$\left[p_{2x} \left(\frac{h^3 - H^3}{3} + Hh(H-h) \right) \right]_x + 4\mu U_\infty \sin(\omega t) \left[\frac{h_x}{2(H-h)^2} (H^2 + h^2 - 2hH) - h_x \right] = 0. \quad (3.52)$$

Noted that $h = h(x)$ is an unknown function of x which we should be determined. We now formulate an equation that links the displacement $h(x)$ directly to the distributed load which is the different pressure between Region (1) and Region (2), thereby obtaining

$$EI \frac{d^4 h}{dx^4} = p_1(x) - p_2(x).$$

where E is the modulus of elasticity and I is the moment of inertia. We now substitute

(3.48) into the equation above, to get that

$$EI \frac{d^4 h}{dx^4} = p_o - p_2(x) \quad (3.53)$$

In this problem, we consider that one end of the retina detach is free to move and we assume that the other end of the retina detach is clamped end with a constant angle of inclination, ψ . We assume the other of the detached retina is clamped end due to the physical condition that the other end is still attached to the choroid. Therefore the boundary conditions are

$$\begin{aligned} h_{xx}(0) &= 0, & h_{xxx}(0) &= 0, \\ h(L) &= 0, & h_x(L) &= -\psi. \end{aligned} \quad (3.54)$$

Region (3)

We now substitute the boundary conditions given in equation (3.44) into equation (3.46) to get

$$u_3 = \frac{1}{\mu} \left[p_{3x} \frac{y}{2} (y - H) + \frac{\mu y U_\infty \sin(\omega t)}{H} \right]. \quad (3.55)$$

We differentiate equation (3.55) with respect to x and we then substitute into equation (3.41) and integrate the equation with respect to y to obtain that

$$v_3 = -\frac{1}{2\mu} \left[p_{3xx} \frac{y^3}{3} - p_{3xx} \frac{Hy^2}{2} \right] + C_3.$$

If we now substitute the boundary condition given in equation (3.44) into equation above, we get that

$$v_3 = -\frac{1}{2\mu} \left[p_{3xx} \frac{y^3}{3} - p_{3xx} \frac{Hy^2}{2} \right].$$

At $y = H$ and $v_3 = 0$, we have

$$\frac{p_{3xx} H^3}{12\mu} = 0.$$

If we integrate the above equation and substitute the boundary condition (3.44), we find that

$$p_3(x) = p_o. \quad (3.56)$$

Region (4)

We now repeat the same steps as in Region (1), (2), and (3) to find that the arbitrary constants, the velocities in x and y directions in this Region (4) are similar to those in Region (3). We obtain

$$u_4 = \frac{1}{\mu} \left[p_{4x} \frac{y}{2} (y - H) + \frac{\mu y U_\infty \sin(\omega t)}{H} \right], \quad (3.57)$$

$$v_4 = -\frac{1}{2\mu} \left[p_{4xx} \frac{y^3}{3} - p_{4xx} \frac{Hy^2}{2} \right], \quad (3.58)$$

$$p_4(x) = p_o. \quad (3.59)$$

3.6.3 Analytical Results

Let us introduce the non-dimensional parameters

$$\begin{aligned} x &= Lx^*, \quad p_1 = p_o p_1^*, \\ p_2 &= p_o p_2^*, \quad h = Hh^* \quad \text{and} \quad t = \frac{t^*}{\omega}. \end{aligned} \quad (3.60)$$

We may now non-dimensional equations (3.52), (3.53) and the boundary conditions given in equations (3.43) and (3.54) using the following non-dimensional parameters given in equation (3.60) in order to find $p = p_2(x)$ and $h = h(x)$ in the Region (2). Here we obtain that

$$\left[p_{x^*}^* \left(\frac{h^{*3} - 1}{3} + h^* (1 - \bar{h}) \right) \right]_{x^*} - \frac{2\mu LU_\infty}{p_o H^2} h_x^* \sin(t^*) = 0, \quad (3.61)$$

and

$$\frac{d^4 h^*}{dx^{*4}} = \theta (1 - p^*) \quad ; \quad \theta = \frac{p_o L^4}{HEI}, \quad (3.62)$$

with

$$\begin{aligned} p^*(0) &= 1, \quad h_{xx}^*(0) = 0, \\ h_{xxx}^*(0) &= 0, \quad p^*(1) = 1, \\ h^*(1) &= 0, \quad h_x^*(1) = -\varepsilon \quad \text{where} \quad \varepsilon = \frac{L\psi}{H}. \end{aligned} \quad (3.63)$$

Note that from here onward we discard the bars and solve the non-dimensional problem. If ψ is order one and the detachment length L , is much smaller than the channel height H , or if $L \sim H$ and $\psi \ll 1$ then $\varepsilon \ll 1$ and we can analyse the problem in the limit $\varepsilon \rightarrow 0$ and $\theta \leq O(1)$. We therefore introduce the asymptotic expansions

$$\begin{aligned} h &= h_0 + \varepsilon h_1 + \dots, \\ p &= p_0 + \varepsilon p_1 + \dots. \end{aligned} \quad (3.64)$$

We now substitute the asymptotic expansion above (3.64) into equations (3.61), (3.62) and the boundary conditions given in equation (3.63) and extract the equations and the boundary conditions that we are going to solve for $\varepsilon^{(0)}$ and $\varepsilon^{(1)}$.

$\varepsilon^{(0)}$:

$$\left[p_{0x} \left(\frac{h_0^3 - 1}{3} + h_0 (1 - h_0) \right) \right]_x = \frac{2\mu LU_\infty}{p_o H^2} \sin(t) h_{0x}, \quad (3.65)$$

and

$$h_{0xxxx} = \theta (1 - p_0), \quad (3.66)$$

with

$$\begin{aligned} p_0(0) &= 1, \quad h_{0xx}(0) = 0, \\ h_{0xxx}(0) &= 0, \quad p_0(1) = 1, \\ h_0(1) &= 0, \quad h_{0x}(1) = 0. \end{aligned} \quad (3.67)$$

$\varepsilon^{(1)}$:

$$\left[p_{1x} \left(\frac{h_0^3 - 1}{3} + h_0(1 - h_0) \right) + p_{0x} (h_0^2 h_1 + h_1 - 2h_0 h_1) \right]_x = \frac{2\mu L U_\infty}{p_o H^2} \sin(t) h_{1x}, \quad (3.68)$$

and

$$h_{1xxxx} = -\theta p_1, \quad (3.69)$$

with

$$\begin{aligned} p_1(0) &= 0, \quad h_{1xx}(0) = 0, \\ h_{1xxx}(0) &= 0, \quad p_1(1) = 0, \\ h_1(1) &= 0, \quad h_{1x}(1) = -1. \end{aligned} \quad (3.70)$$

We may now solve the problem at leading order (equations (3.65) and (3.66) with the boundary conditions (3.67)), to get

$$h_0(x) = 0 \quad \text{and} \quad p_0(x) = 1. \quad (3.71)$$

We now solve the problem at the next order, by substituting equation (3.71) into equation (3.68), so that equation (3.68) becomes

$$\left[-\frac{p_{1x}}{3} \right]_x = \frac{2\mu L U_\infty}{p_o H^2} \sin(t) h_{1x}. \quad (3.72)$$

If we now differentiate equation (3.69) twice with respect to x , we obtain that

$$h_{1xxxxx} = -\theta p_{1xx}. \quad (3.73)$$

We now substitute equation (3.73) into equation (3.72), yielding

$$h_{1xxxxx} = \beta h_{1xx} \quad \text{where} \quad \beta = \frac{6\mu U_\infty L^5}{EIH^3} \sin(t) \quad (3.74)$$

and we may write the boundary conditions for this equation (3.74) as

$$\begin{aligned} h_{1xxxx}(0) &= 0, \quad h_{1xx}(0) = 0, \\ h_{1xxx}(0) &= 0, \quad h_{1xxx}(1) = 0, \\ h_1(1) &= 0, \quad h_{1x}(1) = -1. \end{aligned} \quad (3.75)$$

Thus we solve equation (3.74) subject to the boundary conditions given in equation (3.75) (by using MAPLE [8]), and we may now plot the solution in order to analyse

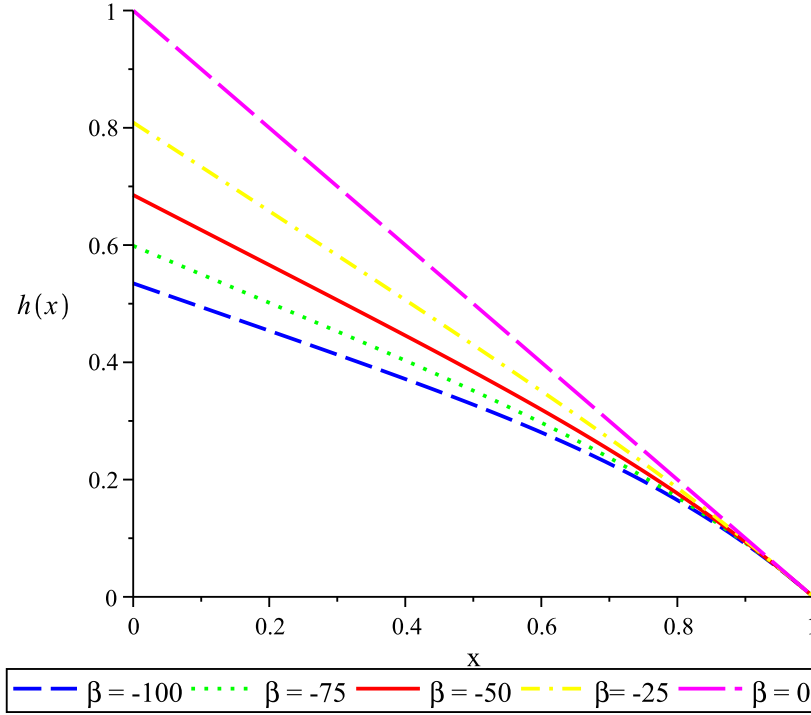


FIGURE 3.9: The deformation of the detached retina, $h(x)$ for different value of small β . The dashed blue line represents the detached retina associated with β equal to -100 whereas the dotted green line, the solid red line, the dashed dotted yellow line and the long dashed magenta line denote the corresponding detached retina for β equal to -75, -50, -25 and 0.

the deformation of the detached retina, see Figure (3.9) and Figure (3.10). Figure (3.9) shows the deformation of the detached retina for different value of β from -100 to 0. It shows that when the value of β decreases (from 0 to -100), then $h(x)$ starts bending down. From the result we found that the flow becomes less strong and hence exerts a smaller force on the detached retina, and so its angle of deflection alls decreases. Figure (3.10) presents the deformation of the detached retina for different value of large β . It implies that when the value of β increases (from 0 to 100), then $h(x)$ becomes much more deflected. However when the value of β is bigger than 91 ($\beta > 91$), the solution becomes infinite which is the beam is rapidly bending down. It is shown that this case is valid for $\beta \leq 91$.

3.7 Conclusion for Retinal Detachment

When flow is driven past a detachment by a pressure gradient the flap deforms much as might be expected. The amount of deformation is largely determined by the quantity $\alpha = L^4(p_o - p_L)/H(EI)$. Though α has only a small influence on the volume flux, larger values of α lead to larger detachment deflections, which are likely to increase the

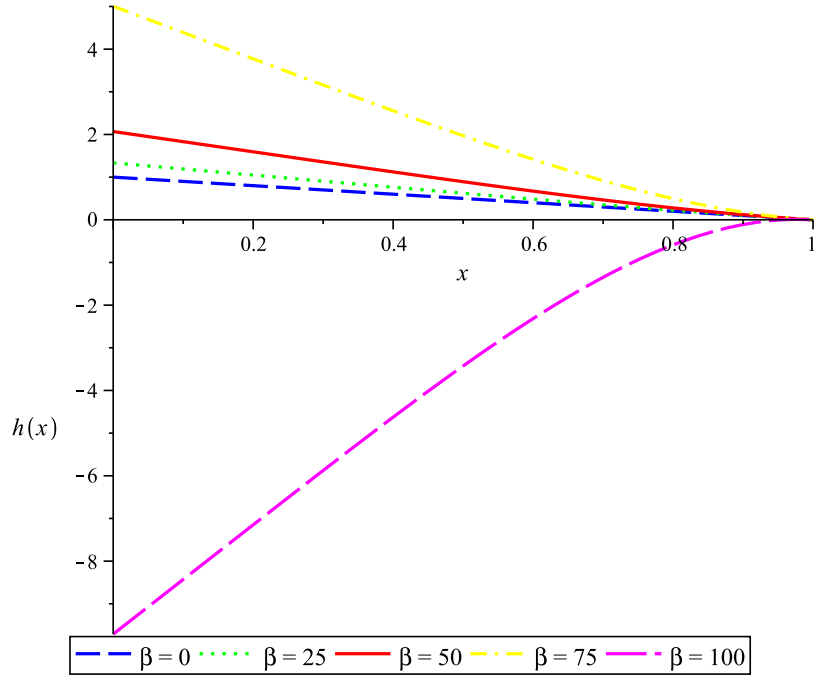


FIGURE 3.10: The deformation of the detached retina $h(x)$. Each graph corresponds to different value of β from 0 to 100. The dashed blue line, the dotted green line, the solid red line, the dashed dotted yellow line and the long dashed magenta line represent the corresponding detached retina for β equal to 0, 25, 50, 75 and 100.

severity of a retinal detachment.

In contrast, when saccadic eye motions take place, there are always times in the flow when the retina attempts to reattach to the choroid, and this is likely to make the detachment much less serious. It should be borne in mind, however, that the paradigm models are simple ones and may not give an accurate picture of reality.

3.8 Modelling of the Liquefied Vitreous Humour Flow during Retinal Detachment

A paradigm problem of retinal detachment has been developed by considering the nature of the flow driven by the saccadic motion of the eye in order to find the fluid flow and to examine the deformation of the detached retina. In this study, we model the posterior chamber of the human eye as a hollow sphere with radius, a . The liquefied vitreous humour is assumed to be an incompressible Newtonian fluid with constant viscosity, ν and density, ρ . The flow in the posterior chamber is induced by saccadic motions of the eyeball as it performs periodic torsional oscillations about a vertical axis of amplitude, ε and frequency, ω (radians per second). Note that appendix C presents a summary of the work that have been done, including the method of solving and the

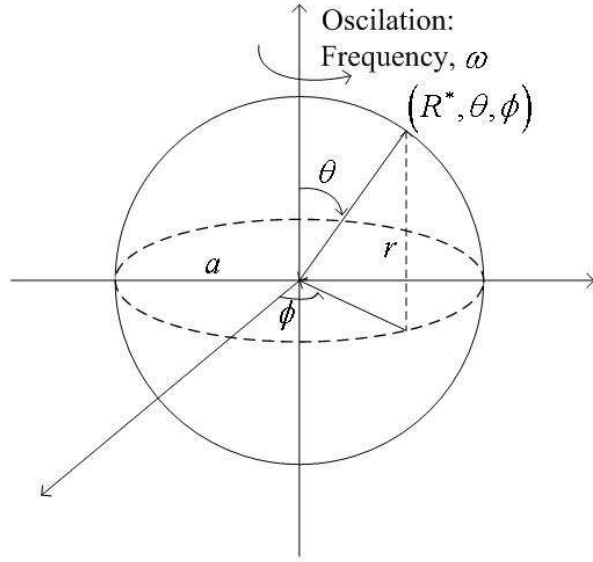


FIGURE 3.11: Spherical coordinate system which illustrates the model of saccadic eye motion.

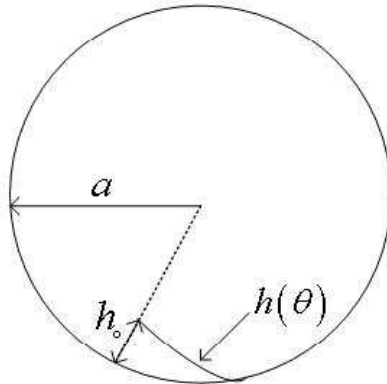


FIGURE 3.12: Schematic diagram of the human eye presenting a two dimensional cross section of retinal detachment for illustrating the detached retina, $h(\theta)$.

solution, by Fitt'04, [56], Repetto'08, [69] and Repetto'09, [70] and also the work that has been extended and done by us is noted as ALiC'09.

3.8.1 The Governing Equations

In this section, we assume that the governing equations of motion are the Navier-Stokes equations for an incompressible viscous flow [56]:

$$\bar{u}_t^* + \bar{u}^* \cdot \nabla \bar{u}^* = -\frac{\nabla p}{\rho} + \nu \nabla^2 \bar{u}^*, \quad (3.76)$$

$$\nabla \cdot \bar{u}^* = 0. \quad (3.77)$$

Here $\bar{u}^* = (u^*, v^*, w^*)$ denotes the velocity components in the directions of the respective coordinates (R^*, θ, ϕ) (where R^* denotes the radial coordinate, θ denotes the zenithal coordinate and ϕ denotes the azimuthal coordinate, see Figure (3.11)), superscript stars denote dimensional variables, t^* is time, p^* denotes the pressure and $v = \frac{\mu}{\rho}$ represents the kinematic viscosity of water at $40^\circ C$, i.e. $6.8 \times 10^{-7} m^2 s^{-1}$ [56]. The no slip boundary conditions at the wall (see [56], [61] and [70]) are

$$u^* = v^* = 0, \quad w^* = \frac{R^* U_\infty}{a} \sin(\theta) \sin(\omega t^*) \quad \text{on} \quad R^* = a + h^*(\theta), \quad (3.78)$$

where a is the radius of a sphere ($a = 0.011m$ [61]), U_∞ is the maximum circumferential velocity, $h^*(\theta)$ denotes position of the detached retina, h_o is the initial height of the detached retina [2] and ω represents the angular frequency of the saccadic motion (see Figure (3.12) for nomenclature). The following dimensionless variables have been used (see [56], [61] and [70]):

$$\begin{aligned} R^* &= aR, \quad \bar{u}^* = a\omega \bar{u} \quad \text{where} \quad \bar{u} = (u, v, w), \\ p^* &= \rho a^2 \omega^2 p, \quad t^* = \frac{t}{\omega}, \quad \text{and} \quad h^*(\theta) = h_o h(\theta). \end{aligned} \quad (3.79)$$

We now non-dimensionalise equations (3.76), (3.77) and (3.78) by substituting the dimensionless parameters (3.79): Equation (3.76) becomes

R component:

$$\begin{aligned} \frac{\partial u}{\partial t} + u \frac{\partial u}{\partial R} + \frac{v}{R} \frac{\partial u}{\partial \theta} + \frac{w}{R \sin(\theta)} \frac{\partial u}{\partial \phi} - \left(\frac{v^2 + w^2}{R^2} \right) \\ = -\frac{\partial p}{\partial R} + \frac{1}{\alpha^2} \left[\nabla^2 u - 2 \left(\frac{u + \frac{\partial v}{\partial \theta} + v \cot(\theta)}{R^2} \right) + \frac{2}{R^2 \sin(\theta)} \frac{\partial w}{\partial \phi} \right], \end{aligned} \quad (3.80)$$

θ component:

$$\begin{aligned} \frac{\partial v}{\partial t} + u \frac{\partial v}{\partial R} + \frac{v}{R} \frac{\partial v}{\partial \theta} + \frac{w}{R \sin(\theta)} \frac{\partial v}{\partial \phi} + \frac{uv}{R} - \frac{w^2 \cot(\theta)}{R} \\ = -\frac{1}{R} \frac{\partial p}{\partial \theta} + \frac{1}{\alpha^2} \left[\nabla^2 v + \frac{2}{R^2} \frac{\partial u}{\partial \theta} - \frac{v + 2 \cos(\theta) \frac{\partial w}{\partial \phi}}{R^2 \sin^2(\theta)} \right], \end{aligned} \quad (3.81)$$

ϕ component:

$$\begin{aligned} \frac{\partial w}{\partial t} + u \frac{\partial w}{\partial R} + \frac{v}{R} \frac{\partial w}{\partial \theta} + \frac{w}{R \sin(\theta)} \frac{\partial w}{\partial \phi} + \frac{uw}{R} + \frac{vw \cot(\theta)}{R} \\ = -\frac{1}{R \sin(\theta)} \frac{\partial p}{\partial \phi} + \frac{1}{\alpha^2} \left[\nabla^2 w + \frac{2 \frac{\partial u}{\partial \phi} + 2 \cos(\theta) \frac{\partial v}{\partial \phi} - w}{R^2 \sin^2(\theta)} \right]. \end{aligned} \quad (3.82)$$

Equation (3.77) becomes

$$\frac{1}{R^2} \frac{\partial}{\partial R} (R^2 u) + \frac{1}{R \sin(\theta)} \frac{\partial}{\partial \theta} (v \sin(\theta)) + \frac{1}{R \sin(\theta)} \frac{\partial w}{\partial \phi} = 0. \quad (3.83)$$

The boundary conditions become,

$$u = v = 0, \quad w = \varepsilon R \sin(\theta) \sin(t) \quad \text{on} \quad R = 1 + \delta h(\theta). \quad (3.84)$$

In the above equations, (3.80) - (3.84), there are three dimensionless parameters, which are the amplitude, $\varepsilon = \frac{U_\infty}{a\omega}$, the Womersley number, $\alpha = \sqrt{\frac{a^2\omega}{v}}$ (this α represents the balance between viscosity and angular rotation, and note that this α is different with α given in Section 3.5) and the aspect ratio, $\delta = \frac{h_\infty}{a}$. Assuming the solution as axisymmetric (rotational symmetric), where $\frac{\partial}{\partial \phi} = 0$ and subscripts denote derivatives, the above equations reduce to:

$$u_t + uu_R + \frac{vu_\theta}{R} - \frac{v^2}{R} - \frac{w^2}{R} = -p_R + \frac{1}{\alpha^2} \left[\nabla^2 u - \frac{2u}{R^2} - \frac{2}{R^2 \sin(\theta)} (v \sin(\theta))_\theta \right], \quad (3.85)$$

$$v_t + uv_R + \frac{vv_\theta}{R} + \frac{uv}{R} - \frac{w^2 \cot(\theta)}{R} = -\frac{p_\theta}{R} + \frac{1}{\alpha^2} \left[\nabla^2 v + \frac{2u_\theta}{R^2} - \frac{v}{R^2 \sin^2(\theta)} \right], \quad (3.86)$$

$$w_t + uw_R + \frac{vw_\theta}{R} + \frac{uw}{R} - \frac{vw \cot(\theta)}{R} = \frac{1}{\alpha^2} \left[\nabla^2 w - \frac{w}{R^2 \sin^2(\theta)} \right], \quad (3.87)$$

$$\frac{1}{R^2} (R^2 u)_R + \frac{1}{R \sin(\theta)} (v \sin(\theta))_\theta = 0, \quad (3.88)$$

with no slip boundary conditions at the wall, $R = 1 + \delta h(\theta)$,

$$u = v = 0 \quad \text{and} \quad w = \varepsilon R \sin(\theta) \sin(t). \quad (3.89)$$

3.8.2 Solution Procedures

In this section, we solve the Navier-Stokes equations explicitly in order to find the fluid flow in the sphere in various limits of three dimensionless parameters. We now estimate the sizes of these three dimensionless parameters. First, we assume that $\alpha = O(1)$ (so that there are no boundary layers) and $\varepsilon \ll 1$ (which is in the limit of small amplitude oscillations). In particular, we consider the case where $\delta \sim \varepsilon$. We seek a series solution by expanding in powers of the small parameters, ε

$$\begin{aligned} u &= \varepsilon^2 \bar{u} + \quad \text{where} \quad \bar{u} = u_1 + \varepsilon u_2 + \dots, \\ v &= \varepsilon^2 \bar{v} + \quad \text{where} \quad \bar{v} = v_1 + \varepsilon v_2 + \dots, \\ w &= \varepsilon \bar{w} + \quad \text{where} \quad \bar{w} = w_1 + \varepsilon w_2 + \dots, \\ p &= \varepsilon^2 \bar{p} + \quad \text{where} \quad \bar{p} = p_1 + \varepsilon p_2 + \dots \end{aligned} \quad (3.90)$$

We now substitute the series solution above (3.90) into equations (3.85), (3.86), (3.87), (3.88) and the boundary conditions given in equation (3.89), and simplify to get that

R component:

$$\bar{u}_t + \varepsilon^2 \bar{u} \bar{u}_R + \varepsilon^2 \frac{\bar{v} \bar{u}_\theta}{R} - \varepsilon^2 \frac{\bar{v}^2}{R} - \frac{\bar{w}^2}{R} = -\bar{p}_R + \frac{1}{\alpha^2} \left[\nabla^2 \bar{u} - \frac{2\bar{u}}{R^2} - \frac{2}{R^2 \sin(\theta)} (\bar{v} \sin(\theta))_\theta \right]. \quad (3.91)$$

θ component:

$$\bar{v}_t + \varepsilon^2 \bar{u} \bar{v}_R + \frac{\varepsilon^2 \bar{v} \bar{v}_\theta}{R} + \frac{\varepsilon^2 \bar{u} \bar{v}}{R} - \frac{\bar{w}^2 \cot(\theta)}{R} = -\frac{\bar{p}_\theta}{R} + \frac{1}{\alpha^2} \left[\nabla^2 \bar{v} + \frac{2\bar{u}_\theta}{R^2} - \frac{\bar{v}}{R^2 \sin^2(\theta)} \right]. \quad (3.92)$$

ϕ component:

$$\bar{w}_t + \varepsilon^2 \bar{u} \bar{w}_R + \frac{\varepsilon^2 \bar{v} \bar{w}_\theta}{R} + \frac{\varepsilon^2 \bar{u} \bar{w}}{R} - \frac{\varepsilon^2 \bar{v} \bar{w} \cot(\theta)}{R} = \frac{1}{\alpha^2} \left[\nabla^2 \bar{w} - \frac{\bar{w}}{R^2 \sin^2(\theta)} \right]. \quad (3.93)$$

Continuity Equation:

$$\frac{1}{R^2} (R^2 \bar{u})_R + \frac{1}{R \sin(\theta)} (\bar{v} \sin(\theta))_\theta = 0. \quad (3.94)$$

Boundary conditions:

$$\bar{u} = \bar{v} = 0, \quad \bar{w} = R \sin(\theta) \sin(t) \quad \text{on} \quad R = 1 + \varepsilon h(\theta). \quad (3.95)$$

By using a Taylor series expansion, we now apply the perturbation on $R = 1 + \varepsilon h(\theta)$ for the boundary conditions, (3.95):

$$u_1(1, \theta, t) + \varepsilon h(\theta) \frac{\partial u_1}{\partial R}(1, \theta, t) + \frac{\varepsilon^2 h^2(\theta)}{2!}(\theta) \frac{\partial^2 u_1}{\partial R^2}(1, \theta, t) + \dots \\ + \varepsilon \left(u_2(1, \theta, t) + \varepsilon h(\theta) \frac{\partial u_2}{\partial R}(1, \theta, t) + \dots \right) + \dots = 0, \quad (3.96)$$

$$v_1(1, \theta, t) + \varepsilon h(\theta) \frac{\partial v_1}{\partial R}(1, \theta, t) + \frac{\varepsilon^2 h^2(\theta)}{2!}(\theta) \frac{\partial^2 v_1}{\partial R^2}(1, \theta, t) + \dots \\ + \varepsilon \left(v_2(1, \theta, t) + \varepsilon h(\theta) \frac{\partial v_2}{\partial R}(1, \theta, t) + \dots \right) + \dots = 0, \quad (3.97)$$

$$w_1(1, \theta, t) + \varepsilon h(\theta) \frac{\partial w_1}{\partial R}(1, \theta, t) + \frac{\varepsilon^2 h^2(\theta)}{2!}(\theta) \frac{\partial^2 w_1}{\partial R^2}(1, \theta, t) + \dots \\ + \varepsilon \left(w_2(1, \theta, t) + \varepsilon h(\theta) \frac{\partial w_2}{\partial R}(1, \theta, t) + \dots \right) + \dots = (1 + \varepsilon h(\theta)) \sin(\theta) \sin(t) \quad (3.98)$$

From equations (3.91)-(3.94) and the boundary conditions (3.96)-(3.98), we may now extract the governing equations and the boundary conditions at leading order and the correction.

$O(\varepsilon^0)$:

The governing equations,

$$u_{1t} - \frac{w_1^2}{R} = -p_{1R} + \frac{1}{\alpha^2} \left[\nabla^2 u_1 - \frac{2u_1}{R^2} - \frac{2}{R^2 \sin(\theta)} (v_1 \sin(\theta))_\theta \right], \quad (3.99)$$

$$v_{1t} - \frac{w_1^2 \cot(\theta)}{R} = -\frac{p_{1\theta}}{R} + \frac{1}{\alpha^2} \left[\nabla^2 v_1 + \frac{2u_{1\theta}}{R^2} - \frac{v_1}{R^2 \sin^2(\theta)} \right], \quad (3.100)$$

$$w_{1t} = \frac{1}{\alpha^2} \left[\nabla^2 w_1 - \frac{w_1}{R^2 \sin^2(\theta)} \right], \quad (3.101)$$

$$\frac{1}{R^2} (R^2 u_1)_R + \frac{1}{R \sin(\theta)} (v_1 \sin(\theta))_\theta = 0. \quad (3.102)$$

The boundary conditions,

$$u_1 = v_1 = 0, \quad w_1 = \sin(\theta) \sin(t) \quad \text{on} \quad R = 1. \quad (3.103)$$

The solution of the governing equations (3.99)-(3.102) subject to the boundary conditions (3.103) at the leading order was considered in [56]. They solved only equation (3.101) with the boundary conditions (3.103) in order to find the azimuthal fluid velocity, w_1 :

$$w_1 = \text{Im} \left(\frac{1}{R^2} \phi(R) e^{it} \right) \sin(\theta) \\ \text{where } \phi(R) = \frac{e^{\sqrt{i}\alpha R} (1 - \sqrt{i}\alpha R) - e^{-\sqrt{i}\alpha R} (1 + \sqrt{i}\alpha R)}{e^{\sqrt{i}\alpha} (1 - \sqrt{i}\alpha) - e^{-\sqrt{i}\alpha} (1 + \sqrt{i}\alpha)}. \quad (3.104)$$

$O(\varepsilon^1)$:

The governing equations,

$$u_{2t} - \frac{w_2^2}{R} = -p_{2R} + \frac{1}{\alpha^2} \left[\nabla^2 u_2 - \frac{2u_2}{R^2} - \frac{2}{R^2 \sin(\theta)} (v_2 \sin(\theta))_\theta \right], \quad (3.105)$$

$$v_{2t} - \frac{w_2^2 \cot(\theta)}{R} = -\frac{p_{2\theta}}{R} + \frac{1}{\alpha^2} \left[\nabla^2 v_2 + \frac{2u_{2\theta}}{R^2} - \frac{v_2}{R^2 \sin^2(\theta)} \right], \quad (3.106)$$

$$w_{2t} = \frac{1}{\alpha^2} \left[\nabla^2 w_2 - \frac{w_2}{R^2 \sin^2(\theta)} \right], \quad (3.107)$$

$$\frac{1}{R^2} (R^2 u_2)_R + \frac{1}{R \sin(\theta)} (v_2 \sin(\theta))_\theta = 0. \quad (3.108)$$

The boundary conditions on $R = 1$

$$u_2(1, \theta, t) = -h(\theta) \frac{\partial u_1(1, \theta, t)}{\partial R}, \\ v_2(1, \theta, t) = -h(\theta) \frac{\partial v_1(1, \theta, t)}{\partial R}, \\ w_2(1, \theta, t) = h(\theta) \sin(\theta) \sin(t) \left[3 + \text{Im} \left(\frac{i\alpha^2 (e^{-\sqrt{i}\alpha} - e^{\sqrt{i}\alpha})}{e^{\sqrt{i}\alpha} (1 - \sqrt{i}\alpha) - e^{-\sqrt{i}\alpha} (1 + \sqrt{i}\alpha)} \right) \right]. \quad (3.109)$$

Note that the retinal detachment $h(\theta)$ does not enter the problem until $O(\varepsilon)$. We therefore need to solve the $O(\varepsilon)$ problem. We can make progress by determining the solution of the azimuthal fluid velocity, w_2 at the correction order. To do this, we now rewrite equation (3.107) and we find that

$$R^2\alpha^2 \frac{\partial w_2}{\partial t} = 2R \frac{\partial w_2}{\partial R} + R^2 \frac{\partial^2 w_2}{\partial R^2} + \frac{1}{\sin(\theta)} \left[\cos(\theta) \frac{\partial w_2}{\partial \theta} + \sin(\theta) \frac{\partial^2 w_2}{\partial \theta^2} \right] - \frac{w_2}{\sin^2(\theta)}. \quad (3.110)$$

We now seek a separable solution for w_2 in the form

$$w_2 = \text{Im} \left(\frac{1}{R^2} \phi(R) e^{it} \right) F(\theta). \quad (3.111)$$

Thus we substitute equation (3.111) into equation (3.110), to obtain that

$$\begin{aligned} R^2\alpha^2 \left(\frac{1}{R^2} \phi(R) i e^{it} F(\theta) \right) - 2R \left(-\frac{2\phi(R)}{R^2} + \frac{\phi'(R)}{R^2} \right) e^{it} F(\theta) - R^2 \left(\frac{\phi''(R)}{R^2} \right. \\ \left. - \frac{4\phi'(R)}{R^3} + \frac{6\phi(R)}{R^4} \right) e^{it} F(\theta) = \frac{1}{R^2} \phi(R) e^{it} \left[F''(\theta) + \frac{\cos(\theta)}{\sin(\theta)} F'(\theta) - \frac{F(\theta)}{\sin^2(\theta)} \right] \end{aligned} \quad (3.112)$$

If we simplify the equation above, here we get that

$$R^2 \frac{\phi''(R)}{\phi(R)} - 2R \frac{\phi'(R)}{\phi(R)} - i\alpha^2 R^2 + 2 = -\frac{F''(\theta)}{F(\theta)} - \frac{\cos(\theta)}{\sin(\theta)} \frac{F'(\theta)}{F(\theta)} + \frac{1}{\sin^2(\theta)}. \quad (3.113)$$

Since the left hand side of equation (3.113) only depends on one variable R and the right hand side of equation (3.113) only depends on θ , therefore we may equate equation (3.111) to an arbitrary constant, C yielding

$$\phi''(R) - \frac{2}{R} \phi'(R) + \frac{1}{R^2} (2 - i\alpha^2 R^2 - C) \phi(R) = 0 \quad (3.114)$$

and

$$-F''(\theta) - \frac{\cos(\theta)}{\sin(\theta)} F'(\theta) + \left(\frac{1}{\sin^2(\theta)} - C \right) F(\theta) = 0. \quad (3.115)$$

The solutions to (3.114) and (3.115) are

$$\phi(R, C) = D_1 R^{\frac{3}{2}} I_{\frac{1}{2}\sqrt{1+4C}}(-\sqrt{i}\alpha R) + D_2 R^{\frac{3}{2}} K_{\frac{1}{2}\sqrt{1+4C}}(-\sqrt{i}\alpha R) \quad (3.116)$$

and

$$\begin{aligned} F(\theta, C) = D_3 \sin(2\theta) {}_2F_1 \left(\left[\frac{5}{4} + \frac{1}{4}\sqrt{1+4C}, \frac{5}{4} - \frac{1}{4}\sqrt{1+4C} \right], \left[\frac{3}{2} \right], \frac{1}{2} + \frac{1}{2} \cos(\theta) \right) \\ + D_4 \sin(\theta) {}_2F_1 \left(\left[\frac{3}{4} + \frac{1}{4}\sqrt{1+4C}, \frac{3}{4} - \frac{1}{4}\sqrt{1+4C} \right], \left[\frac{1}{2} \right], \frac{1}{2} + \frac{1}{2} \cos(\theta) \right). \end{aligned} \quad (3.117)$$

The series solutions which are equations (3.116) and (3.117) are found in terms of modified spherical Bessel function and hypergeometric function that depend on value of C . Note that D_i where $i = 1, 2, 3, 4$ are arbitrary constants.

3.8.3 Mathematical Analysis and Discussion

We now analyse equations (3.116) and (3.117) in order to get the complete solution for w_2 . Here we restate the solution of w_2 (see equation (3.111)), as

$$w_2(R, \theta, t) = \text{Im} \left(\frac{1}{R^2} \phi(R, C) e^{it} \right) F(\theta, C) A(C). \quad (3.118)$$

In this problem we found that the values of C are the positive values and very special. The values of C are equal only to 2, 6, 12, 20, 30, 42, 56, 72, 90, Thus we may write the formula of C , as

$$C = m(m+1) \quad \text{where } m = 1, 2, 3, \dots \quad (3.119)$$

We now examine equation (3.116) which the solution is composed of Bessel functions (see [52]). We expect that one of the terms in this equation will become unbounded depending on the values of C . If we substitute the values of C given in equation (3.119) into equation (3.116), we can see that the Bessel K terms can be neglected from this equation, so that we obtain

$$\phi(R, C) = D_1 R^{\frac{3}{2}} I_{\frac{1}{2}\sqrt{1+4C}}(-\sqrt{i}\alpha R). \quad (3.120)$$

We now examine the series solutions of the hypergeometric function (3.117) in terms of special values of C . These series solutions must be periodic and bounded (there exists a number of $C > 0$ such that $F(\theta) \leq C$ for all $\theta \in [0, \pi]$) [53], thus we may obtain that $(F_m(\theta, C) = (\text{periodic and bounded})$ where C is defined in equation (3.119)),

$$F_1(\theta, 2) = D_4 \sqrt{2} \sin(\theta), \quad (3.121)$$

$$F_2(\theta, 6) = D_3 \sin(2\theta), \quad (3.122)$$

$$F_3(\theta, 12) = D_4 \sqrt{2} \sin(\theta) (-1 + 5\cos^2(\theta)), \quad (3.123)$$

$$F_4(\theta, 20) = -\frac{2}{3} D_3 \sin(\theta) \cos(\theta) (-3 + 7\cos^2(\theta)), \quad (3.124)$$

$$F_5(\theta, 30) = D_4 \sqrt{2} \sin(\theta) (1 - 14\cos^2(\theta) + 21\cos^4(\theta)), \quad (3.125)$$

$$F_6(\theta, 42) = \frac{2}{5} D_3 \sin(\theta) \cos(\theta) (5 - 30\cos^2(\theta) + 33\cos^4(\theta)), \quad (3.126)$$

$$F_7(\theta, 56) = -\frac{\sqrt{2}}{5} D_4 \sin(\theta) (-5 + 135\cos^2(\theta) - 495\cos^4(\theta) + 429\cos^6(\theta)), \quad (3.127)$$

$$F_8(\theta, 72) = -\frac{2}{35} D_3 \sin(\theta) \cos(\theta) (-35 + 385\cos^2(\theta) - 1001\cos^4(\theta) + 715\cos^6(\theta)). \quad (3.128)$$

$$F_9(\theta, 90) = -\frac{\sqrt{2}}{5} D_4 \sin(\theta) (7 - 308\cos^2(\theta) + 2002\cos^4(\theta) - 4004\cos^6(\theta) + 2431\cos^8(\theta)) \quad (3.129)$$

⋮

Before we can proceed, we have to prove that the functions above (3.121)-(3.129) are mutually orthogonal with respect to the weighting function, $\varpi(\theta)$ over the interval $0 \leq \theta \leq \pi$. Mathematically, we can write that

$$\langle F_i(\theta) | F_j(\theta) \rangle \equiv \int_0^\pi F_i(\theta) \cdot F_j(\theta) \cdot \varpi(\theta) d\theta = 0.$$

The most important advantage of orthogonality is that the functions (3.121)-(3.129) can be used as a basic function space. It means that we can use these functions, in the same way as we use trigonometric functions, to make good approximations to any functions of interest (see [51] for further details). In this study, we present two ways to prove the functions are orthogonal to each other; the first is a Sturm-Liouville analysis which we will discuss it here and secondly we prove completeness, see Appendix B. We may now rewrite equation (3.115) in the general form of the homogeneous linear Sturm-Liouville problem [51], to get

$$-(\sin(\theta)) F''(\theta) - (\cos(\theta)) F'(\theta) + \left(\frac{1}{\sin(\theta)} - C \sin(\theta) \right) F(\theta) = 0. \quad (3.130)$$

Then we transform the ODE (3.130) into the standard “symmetric” self adjoint form:

$$\frac{d}{d\theta} [-\sin(\theta) F'(\theta)] + \left(\frac{1}{\sin(\theta)} - C \sin(\theta) \right) F(\theta) = 0$$

or

$$[\sin(\theta) F'(\theta)]' + \left(-\frac{1}{\sin(\theta)} + C \sin(\theta) \right) F(\theta) = 0, \quad (3.131)$$

where C is the eigenvalue and $0 \leq \theta \leq \pi$. From equation (3.131), we have been able to find the eigenvalues, C_i and the eigenfunctions, $F_i(\theta)$.

$$F_i : (\sin(\theta) F'_i)' + \left(-\frac{1}{\sin(\theta)} + C_i \sin(\theta) \right) F_i = 0. \quad (3.132)$$

$$F_j : (\sin(\theta) F'_j)' + \left(-\frac{1}{\sin(\theta)} + C_j \sin(\theta) \right) F_j = 0. \quad (3.133)$$

Note that each of the eigenvectors satisfies the ODE (3.130). We may now multiply equation (3.132) by F_j and multiply equation (3.133) by F_i , to obtain

$$F_j (\sin(\theta) F'_i)' + \left(-\frac{1}{\sin(\theta)} + C_i \sin(\theta) \right) F_i F_j = 0, \quad (3.134)$$

$$F_i (\sin(\theta) F'_j)' + \left(-\frac{1}{\sin(\theta)} + C_j \sin(\theta) \right) F_i F_j = 0. \quad (3.135)$$

Then we subtract equation (3.134) and equation (3.135), to find that

$$[\sin(\theta)(F_j F'_i - F_i F'_j)]' + (C_i - C_j) \sin(\theta) F_i F_j = 0. \quad (3.136)$$

We may now integrate equation (3.136) with respect to θ over the domain $[0, \pi]$ leading to

$$[\sin(\theta)(F_j F'_i - F_i F'_j)]_0^\pi + (C_i - C_j) \int_0^\pi \sin(\theta) F_i F_j d\theta = 0. \quad (3.137)$$

The first term will vanish identically because the eigenfunctions satisfy the same boundary conditions since they are both solutions of the original Sturm-Liouville problem. Equation (3.137) now becomes

$$(C_i - C_j) \int_0^\pi \sin(\theta) F_i F_j d\theta = 0 \Rightarrow \int_0^\pi \sin(\theta) F_i F_j d\theta = 0. \quad (3.138)$$

From equation (3.138), we can conclude that the eigenfunctions $\{F_i(\theta)\}$ are orthogonal with respect to the weighting function, $\varpi(\theta)$ over the domain $[0, \pi]$. We may now continue solving the hypergeometric series problem in order to get the good approximations to any functions of interest. For simplicity, we now let $\sin \theta = z$ and $\cos \theta = \sqrt{1 - z^2}$ and then we rewrite the series $F_m(\theta, C)$ in terms of z ($m = 1, 2, 3, \dots$), so that we obtain

$$\begin{aligned} F_1(z, 2) &= \sqrt{2} D_4 z, \\ F_2(z, 6) &= 2 D_3 z \sqrt{1 - z^2}, \\ F_3(z, 12) &= \sqrt{2} D_4 z (-4 + 5z^2), \\ F_4(z, 20) &= \frac{2}{3} D_3 z \sqrt{1 - z^2} (-4 + 7z^2), \\ F_5(z, 30) &= \sqrt{2} D_4 z (8 - 28z^2 + 21z^4), \\ F_6(z, 42) &= \frac{2}{5} D_3 z \sqrt{1 - z^2} (8 - 36z^2 + 33z^4), \\ F_7(z, 56) &= \frac{\sqrt{2}}{5} D_4 z (-64 + 432z^2 - 792z^4 + 429z^6), \\ F_8(z, 72) &= \frac{2}{35} D_3 z \sqrt{1 - z^2} (-64 + 528z^2 - 1144z^4 + 715z^6), \\ F_9(z, 90) &= \frac{\sqrt{2}}{7} D_4 z (128 - 1408z^2 + 4576z^4 - 5720z^6 + 2431z^8), \\ &\vdots \end{aligned} \quad (3.139)$$

We may now classify the series above into odd and even series, yielding $F_m(z, C)$ where m odd :

$$F_1(z, 2) = \sqrt{2} D_4 z,$$

$$\begin{aligned}
 F_3(z, 12) &= \sqrt{2}D_4z(-4 + 5z^2), \\
 F_5(z, 30) &= \sqrt{2}D_4z(8 - 28z^2 + 21z^4), \\
 F_7(z, 56) &= \frac{\sqrt{2}}{5}D_4z(-64 + 432z^2 - 792z^4 + 429z^6), \\
 F_9(z, 90) &= \frac{\sqrt{2}}{7}D_4z(128 - 1408z^2 + 4576z^4 - 5720z^6 + 2431z^8), \\
 &\vdots
 \end{aligned}$$

$F_m(z, C)$ where m is even:

$$\begin{aligned}
 F_2(z, 6) &= 2D_3z\sqrt{1-z^2}, \\
 F_4(z, 20) &= \frac{2}{3}D_3z\sqrt{1-z^2}(-4 + 7z^2), \\
 F_6(z, 42) &= \frac{2}{5}D_3z\sqrt{1-z^2}(8 - 36z^2 + 33z^4), \\
 F_8(z, 72) &= \frac{2}{35}D_3z\sqrt{1-z^2}(-64 + 528z^2 - 1144z^4 + 715z^6), \\
 &\vdots
 \end{aligned}$$

Both infinite series (m odd and m even) resemble power series in z (see, for further details [48]), so that we may rewrite the above series into the following form:

$$F_m(z, C) = \begin{cases} \sum_{n=0}^{\infty} a_n z^n &; \quad m \text{ odd} \\ \sqrt{1-z^2} \sum_{n=0}^{\infty} b_n z^n &; \quad m \text{ even} \end{cases} \quad (3.140)$$

We now find the values of the coefficients, a_n and b_n by using the Frobenius method ([48]) and we may now demonstrate how the Frobenius method works in this problem, see equation (3.114). Substituting the following equations,

$$\begin{aligned}
 \sin \theta &= z, \quad \cos \theta = \sqrt{1-z^2}, \\
 F(\theta, C) &= F(z, C), \quad F'(\theta, C) = \sqrt{1-z^2}F'(z, C), \\
 F''(\theta, C) &= (1-z^2)F''(z, C) - zF'(z, C),
 \end{aligned}$$

into equation (3.114)), we restate equation (3.115)), to get that

$$(z^4 - z^2)F''(z, C) + (2z^3 - z)F'(z, C) + (1 - Cz^2)F(z, C) = 0. \quad (3.141)$$

A trial solution is given by

$$F(z, C) = \sum_{n=0}^{\infty} a_n z^n,$$

so differentiating this gives

$$F'(z, C) = \sum_{n=0}^{\infty} n a_n z^{n-1},$$

and differentiating again:

$$F''(z, C) = \sum_{n=0}^{\infty} n(n-1) a_n z^{n-2}.$$

We substitute these expressions into the differential equation (3.141):

$$(z^4 - z^2) \sum_{n=0}^{\infty} n(n-1) a_n z^{n-2} + (2z^3 - z) \sum_{n=0}^{\infty} n a_n z^{n-1} + (1 - Cz^2) \sum_{n=0}^{\infty} a_n z^n = 0.$$

Next we alter the summation indices to identify a highest power of z for all three terms. The differential equation then becomes

$$\sum_{n=0}^{\infty} [n(n-1)a_n - (n+1)(n+2)a_{n+2} + 2na_n - (n+2)a_{n+2} + a_{n+2} - Ca_n] z^{n+2} = 0.$$

For the expression to be zero, each power of z must identically vanish, so that

$$a_{n+2} [-(n+1)(n+2) - (n+2) + 1] + a_n [n(n-1) + 2n - C] = 0.$$

This equation gives a recurrence relation for the coefficients, a_n , yielding

$$a_{n+2} = \frac{a_n (n^2 + n - C)}{(n+2)^2 - 1} ; \quad n = 0, 1, 2, 3, \dots \quad (3.142)$$

We now repeating the previous step in order to find a recurrence relation for the coefficients, b_n . The trial solution is given by

$$F(z, C) = \sqrt{1-z^2} \sum_{n=0}^{\infty} b_n z^n.$$

We have

$$F'(z, C) = \sqrt{1-z^2} \sum_{n=0}^{\infty} n b_n z^{n-1} - \frac{z}{\sqrt{1-z^2}} \sum_{n=0}^{\infty} b_n z^n$$

and

$$\begin{aligned} F''(z, C) &= \sqrt{1-z^2} \sum_{n=0}^{\infty} n(n-1) b_n z^{n-2} - \frac{2z}{\sqrt{1-z^2}} \sum_{n=0}^{\infty} n b_n z^{n-1} \\ &\quad + \left(-\frac{z^2}{(1-z^2)^{\frac{3}{2}}} - \frac{1}{\sqrt{1-z^2}} \right) \sum_{n=0}^{\infty} b_n z^n. \end{aligned} \quad (3.143)$$

As before, we may find that

$$(z^4 - z^2) \left[\sqrt{1-z^2} \sum_{n=0}^{\infty} n(n-1)b_n z^{n-2} - \frac{2z}{\sqrt{1-z^2}} \sum_{n=0}^{\infty} nb_n z^{n-1} \right. \\ + \left(-\frac{z^2}{(1-z^2)^{\frac{3}{2}}} - \frac{1}{\sqrt{1-z^2}} \right) \sum_{n=0}^{\infty} b_n z^n \left. \right] + (2z^3 - z) \left[\sqrt{1-z^2} \sum_{n=0}^{\infty} nb_n z^{n-1} \right. \\ \left. - \frac{z}{\sqrt{1-z^2}} \sum_{n=0}^{\infty} b_n z^n \right] + (1-Cz^2) \sqrt{1-z^2} \sum_{n=0}^{\infty} b_n z^n = 0. \quad (3.144)$$

We may now rewrite the equation in terms of the highest power of z , to obtain that

$$\sum_{n=0}^{\infty} \left[b_{n+2} [-(n+2)^2 + 1] + b_n [n^2 + 3n + 2 - C] \right] z^{n+2} = 0, \\ b_{n+2} [-(n+2)^2 + 1] + b_n [n^2 + 3n + 2 - C] = 0.$$

Therefore a recurrence relation for the coefficients, b_n is given by

$$b_{n+2} = \frac{b_n (n^2 + 3n + 2 - C)}{(n+2)^2 - 1} ; \quad n = 0, 1, 2, 3, \dots \quad (3.145)$$

Equation (3.142) and equation (3.145) could be solved in order to find the general form of the coefficients, a_n and b_n . By using the command “rsolve” in MAPLE [8], here we obtain that

$$a_n = \begin{cases} \frac{\pi a_0 \Gamma(\frac{n}{2} + \frac{1}{4}(1 - \sqrt{1+4C})) \Gamma(\frac{n}{2} + \frac{1}{4}(1 + \sqrt{1+4C}))}{\Gamma(\frac{1}{4}(1 - \sqrt{1+4C})) \Gamma(\frac{1}{4}(1 + \sqrt{1+4C})) \Gamma(\frac{n}{2} + \frac{1}{2})^2 (n+1)} & ; \quad n \text{ even} \\ \frac{\Gamma(\frac{n}{2} + \frac{1}{4}(1 - \sqrt{1+4C})) \Gamma(\frac{n}{2} + \frac{1}{4}(1 + \sqrt{1+4C})) (\frac{n}{2} + \frac{1}{2}) a_1}{\Gamma(\frac{3}{4} - \frac{1}{4}\sqrt{1+4C}) \Gamma(\frac{3}{4} + \frac{1}{4}\sqrt{1+4C}) \Gamma(\frac{n}{2} + \frac{3}{2})^2} & ; \quad n \text{ odd} \end{cases} \quad (3.146)$$

$$b_n = \begin{cases} \frac{\pi b_0 \Gamma(\frac{n}{2} + \frac{3}{4} + \frac{1}{4}\sqrt{1+4C}) \Gamma(\frac{n}{2} + \frac{3}{4} - \frac{1}{4}\sqrt{1+4C})}{\Gamma(\frac{3}{4} + \frac{1}{4}\sqrt{1+4C}) \Gamma(\frac{3}{4} - \frac{1}{4}\sqrt{1+4C}) \Gamma(\frac{n}{2} + \frac{1}{2})^2 (n+1)} & ; \quad n \text{ even} \\ \frac{\Gamma(\frac{n}{2} + \frac{3}{4} + \frac{1}{4}\sqrt{1+4C}) \Gamma(\frac{n}{2} + \frac{3}{4} - \frac{1}{4}\sqrt{1+4C}) (\frac{n}{2} + \frac{1}{2}) b_1}{\Gamma(\frac{5}{4} - \frac{1}{4}\sqrt{1+4C}) \Gamma(\frac{5}{4} + \frac{1}{4}\sqrt{1+4C}) \Gamma(\frac{n}{2} + \frac{3}{2})^2} & ; \quad n \text{ odd} \end{cases} \quad (3.147)$$

For both infinite series, $F_m(z, C)$ (m odd and m even), we can see that the power series in z depends only on odd sequences and the coefficients at $n = 0$, a_0 and b_0 are equal to zero, thus we may rewrite the above series into the following form:

$$F_m(z, C) =$$

$$\left\{ \begin{array}{l} \sum_{n=1,3,\dots}^{\infty} \left[\frac{\Gamma(\frac{n}{2} + \frac{1}{4}(1 - \sqrt{1+4C})) \Gamma(\frac{n}{2} + \frac{1}{4}(1 + \sqrt{1+4C})) (\frac{n}{2} + \frac{1}{2}) a_1}{\Gamma(\frac{3}{4} - \frac{1}{4}\sqrt{1+4C}) \Gamma(\frac{3}{4} + \frac{1}{4}\sqrt{1+4C}) \Gamma(\frac{n}{2} + \frac{3}{2})^2} \right] z^n \\ ; \quad m \text{ odd}, \\ \sqrt{1-z^2} \sum_{n=1,3,\dots}^{\infty} \left[\frac{\Gamma(\frac{n}{2} + \frac{3}{4} + \frac{1}{4}\sqrt{1+4C}) \Gamma(\frac{n}{2} + \frac{3}{4} - \frac{1}{4}\sqrt{1+4C}) (\frac{n}{2} + \frac{1}{2}) b_1}{\Gamma(\frac{5}{4} - \frac{1}{4}\sqrt{1+4C}) \Gamma(\frac{5}{4} + \frac{1}{4}\sqrt{1+4C}) \Gamma(\frac{n}{2} + \frac{3}{2})^2} \right] z^n \\ ; \quad m \text{ even}. \end{array} \right.$$

From the series solutions (3.139), we might guess the values of a_1 and b_1 by looking at the first coefficient of the series solutions. So that we assume $a_1 = \sqrt{2}$ and $b_1 = 2$. We can check whether the values are right or wrong by substituting the values of a_1 and b_1 into equation (3.142) and equation (3.145), and then we compare with the second coefficient in the series solutions (3.139). We may now substitute back the values of $z = \sin \theta$ and $\sqrt{1-z^2} = \cos \theta$, and restate the equation above, yielding

$$\left\{ \begin{array}{l} F_m(\theta, C) = \\ \sum_{n=1,3,\dots}^{\infty} \left[\frac{\Gamma(\frac{n}{2} + \frac{1}{4}(1 - \sqrt{1+4C})) \Gamma(\frac{n}{2} + \frac{1}{4}(1 + \sqrt{1+4C})) (\frac{n}{2} + \frac{1}{2}) \sqrt{2}}{\Gamma(\frac{3}{4} - \frac{1}{4}\sqrt{1+4C}) \Gamma(\frac{3}{4} + \frac{1}{4}\sqrt{1+4C}) \Gamma(\frac{n}{2} + \frac{3}{2})^2} \right] \sin^n \theta \\ ; \quad m \text{ odd}, \\ \cos \theta \sum_{n=1,3,\dots}^{\infty} \left[\frac{\Gamma(\frac{n}{2} + \frac{3}{4} + \frac{1}{4}\sqrt{1+4C}) \Gamma(\frac{n}{2} + \frac{3}{4} - \frac{1}{4}\sqrt{1+4C}) (\frac{n}{2} + \frac{1}{2}) 2}{\Gamma(\frac{5}{4} - \frac{1}{4}\sqrt{1+4C}) \Gamma(\frac{5}{4} + \frac{1}{4}\sqrt{1+4C}) \Gamma(\frac{n}{2} + \frac{3}{2})^2} \right] \sin^n \theta \\ ; \quad m \text{ even}. \end{array} \right. \quad (3.148)$$

We now substitute equations (3.120) and (3.148) into equation (3.118), to obtain that

$$\left\{ \begin{array}{l} w_2(R, \theta, t) = \operatorname{Im} \left(\frac{1}{\sqrt{R}} D_1 I_{\frac{1}{2}\sqrt{1+4C}}(-\sqrt{i}\alpha R) \right) \sin(t) A(C) \cdot \\ \sum_{n=1,3,\dots}^{\infty} \left[\frac{\Gamma(\frac{n}{2} + \frac{1}{4}(1 - \sqrt{1+4C})) \Gamma(\frac{n}{2} + \frac{1}{4}(1 + \sqrt{1+4C})) (\frac{n}{2} + \frac{1}{2}) \sqrt{2}}{\Gamma(\frac{3}{4} - \frac{1}{4}\sqrt{1+4C}) \Gamma(\frac{3}{4} + \frac{1}{4}\sqrt{1+4C}) \Gamma(\frac{n}{2} + \frac{3}{2})^2} \right] \sin^n \theta \\ ; \quad m \text{ odd}, \\ \cos \theta \sum_{n=1,3,\dots}^{\infty} \left[\frac{\Gamma(\frac{n}{2} + \frac{3}{4} + \frac{1}{4}\sqrt{1+4C}) \Gamma(\frac{n}{2} + \frac{3}{4} - \frac{1}{4}\sqrt{1+4C}) (\frac{n}{2} + \frac{1}{2}) 2}{\Gamma(\frac{5}{4} - \frac{1}{4}\sqrt{1+4C}) \Gamma(\frac{5}{4} + \frac{1}{4}\sqrt{1+4C}) \Gamma(\frac{n}{2} + \frac{3}{2})^2} \right] \sin^n \theta \\ ; \quad m \text{ even}. \end{array} \right. \quad (3.149)$$

When $R = 1$, equation (3.149) becomes

$$w_2(1, \theta, t) = \operatorname{Im} \left(D_1 I_{\frac{1}{2}\sqrt{1+4C}}(-\sqrt{i}\alpha) \right) \sin(t) A(C) \cdot \\ \begin{cases} \sum_{n=1,3,\dots}^{\infty} \left[\frac{\Gamma(\frac{n}{2} + \frac{1}{4}(1 - \sqrt{1+4C})) \Gamma(\frac{n}{2} + \frac{1}{4}(1 + \sqrt{1+4C})) (\frac{n}{2} + \frac{1}{2}) \sqrt{2}}{\Gamma(\frac{3}{4} - \frac{1}{4}\sqrt{1+4C}) \Gamma(\frac{3}{4} + \frac{1}{4}\sqrt{1+4C}) \Gamma(\frac{n}{2} + \frac{3}{2})^2} \right] \sin^n \theta \\ ; \quad m \text{ odd}, \\ \cos \theta \sum_{n=1,3,\dots}^{\infty} \left[\frac{\Gamma(\frac{n}{2} + \frac{3}{4} + \frac{1}{4}\sqrt{1+4C}) \Gamma(\frac{n}{2} + \frac{3}{4} - \frac{1}{4}\sqrt{1+4C}) (\frac{n}{2} + \frac{1}{2}) 2}{\Gamma(\frac{5}{4} - \frac{1}{4}\sqrt{1+4C}) \Gamma(\frac{5}{4} + \frac{1}{4}\sqrt{1+4C}) \Gamma(\frac{n}{2} + \frac{3}{2})^2} \right] \sin^n \theta \\ ; \quad m \text{ even}. \end{cases}$$

Then we compare the equation above with the boundary condition (3.109), to get that

$$f(\theta) = \sum_{n=1,3,\dots}^{\infty} A(C) ALiC_i(\theta, C) \quad (3.150)$$

where

$$f(\theta) = h(\theta) \sin \theta$$

and we define

$$ALiC_i(\theta) = \frac{D_1}{1 + \operatorname{Im} \left(\frac{i\alpha^2(e^{-\sqrt{i}\alpha} - e^{\sqrt{i}\alpha})}{e^{\sqrt{i}\alpha}(1 - \sqrt{i}\alpha) - e^{-\sqrt{i}\alpha}(1 + \sqrt{i}\alpha)} - 2 \right)} \operatorname{Im} \left(I_{\frac{1}{2}\sqrt{1+4C}}(-\sqrt{i}\alpha) \right) \cdot \\ \begin{cases} \sum_{n=1,3,\dots}^{\infty} \left[\frac{\Gamma(\frac{n}{2} + \frac{1}{4}(1 - \sqrt{1+4C})) \Gamma(\frac{n}{2} + \frac{1}{4}(1 + \sqrt{1+4C})) (\frac{n}{2} + \frac{1}{2}) \sqrt{2}}{\Gamma(\frac{3}{4} - \frac{1}{4}\sqrt{1+4C}) \Gamma(\frac{3}{4} + \frac{1}{4}\sqrt{1+4C}) \Gamma(\frac{n}{2} + \frac{3}{2})^2} \right] \sin^n \theta \\ ; \quad m \text{ odd}, \\ \cos \theta \sum_{n=1,3,\dots}^{\infty} \left[\frac{\Gamma(\frac{n}{2} + \frac{3}{4} + \frac{1}{4}\sqrt{1+4C}) \Gamma(\frac{n}{2} + \frac{3}{4} - \frac{1}{4}\sqrt{1+4C}) (\frac{n}{2} + \frac{1}{2}) 2}{\Gamma(\frac{5}{4} - \frac{1}{4}\sqrt{1+4C}) \Gamma(\frac{5}{4} + \frac{1}{4}\sqrt{1+4C}) \Gamma(\frac{n}{2} + \frac{3}{2})^2} \right] \sin^n \theta \\ ; \quad m \text{ even}. \end{cases}$$

We may now find the value of the coefficient $A(C)$ by multiplying both sides of the equation (3.150) by $ALiC_j(\theta, C)$ and the weight function, $\varpi(\theta) = \sin \theta$, then integrating the equation with respect to θ over the domain $[0, \pi]$ (we will assume that we can interchange the order in which we can integrate and sum). Thus

$$\int_0^\pi f(\theta) \sin \theta ALiC_j(\theta, C) d\theta = \sum_{n=1,3,\dots}^{\infty} A(C) \int_0^\pi \sin \theta ALiC_i(\theta, C) ALiC_j(\theta, C) d\theta. \quad (3.151)$$

Note that since all the terms in the sum are zero except for $i = j$, the equation above becomes

$$A(C) = \frac{1}{\gamma} \int_0^\pi f(\theta) \sin \theta ALiC_i(\theta, C) d\theta \quad (3.152)$$

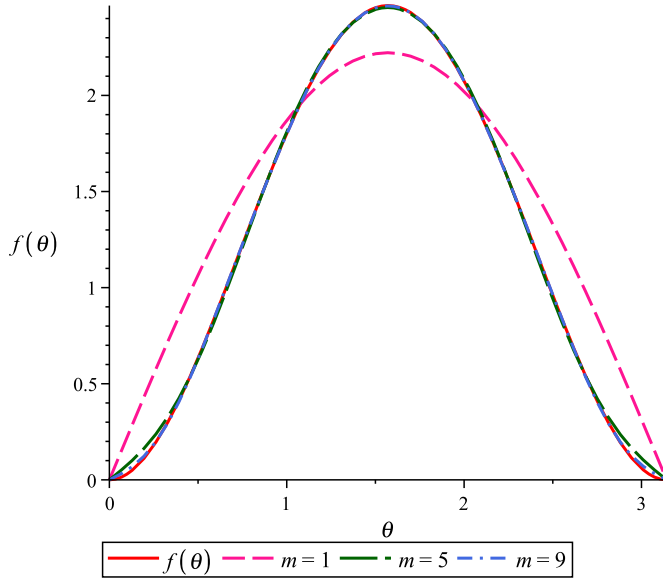


FIGURE 3.13: The $ALiC$ series approximation for the function, $f(\theta) = \theta(\pi - \theta)\sin(\theta)$ that satisfies the odd part of the hypergeometric function over the interval $[0, \pi]$ and its given by the solid red line. The dashed magenta line represents the $ALiC$ series approximation of degree 1 ($m = 1$) whereas the long dashed green line and the dashed-dotted blue line denote the $ALiC$ series approximation for m equal to 5 and 9. In this case when $m = 9$, the $ALiC$ series approximation is equivalent to the original function.

where

$$\gamma = \int_0^\pi \sin \theta (ALiC_i(\theta, C))^2 d\theta.$$

Using MAPLE [8], we solved the problem and we also plotted the $ALiC$ series for various functions, $f(\theta)$ (for functions symmetric at $\theta = \frac{\pi}{2}$), and then analysed how well the series approximate the function. Figures 3.13 - 3.24 show the approximation for different functions of $f(\theta)$. It is seen that the $ALiC$ series give a good approximation to functions that are symmetric at $\theta = \frac{\pi}{2}$. Figures 3.13 - 3.17 and, Figures 3.19, 3.21 and 3.24 present the $ALiC$ series that satisfies the odd part of the hypergeometric functions meanwhile Figures 3.18, 3.20, 3.22 and 3.23 present the $ALiC$ series that satisfies the even part of the hypergeometric functions. Thus, these show that the hypergeometric functions are orthogonal to each other. This means that w_2 in the $O(\varepsilon)$ problem may be determined in closed form.

For further analysis, we are interested to find the pressure difference in order to examine the deformation of the detached retina in this problem. Here we consider the leading order problem (see equations (3.99)-(3.102)) and we introduce the Stokes stream functions, ψ_1 , via

$$u_1 = \frac{\psi_{1\theta}}{R^2 \sin \theta} , \quad v_1 = -\frac{\psi_{1R}}{R \sin \theta}.$$

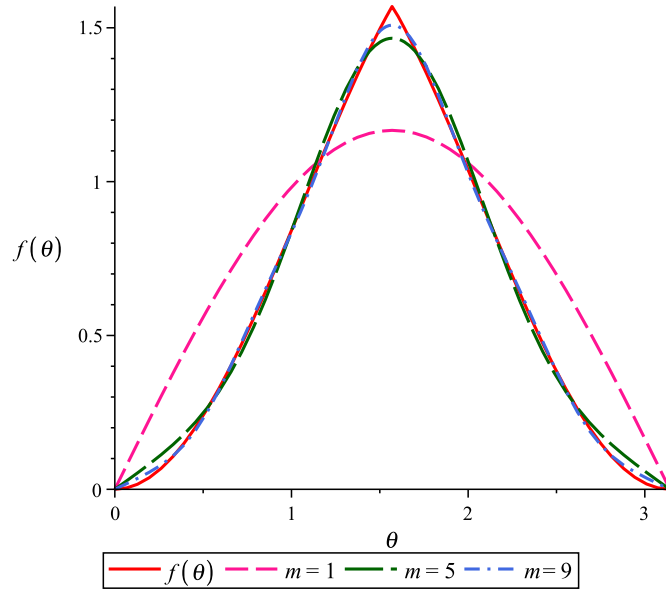


FIGURE 3.14: The *ALiC* series approximation for the piecewise function, $f(\theta) = \theta \cdot \sin(\theta)$ over the interval $[0, \frac{\pi}{2}]$ and $f(\theta) = (\pi - \theta) \sin(\theta)$ in between $\frac{\pi}{2}$ and π . The solid red line denotes the piecewise function. Each graph corresponds to a different degree of approximation. The dashed magenta line, the long dashed green line and the dashed-dotted blue line represent the corresponding *ALiC* series approximation for m equal to 1, 5 and 9. As the degree of *ALiC* series approximation rises to 9, it approaches a close approximation to $f(\theta)$.

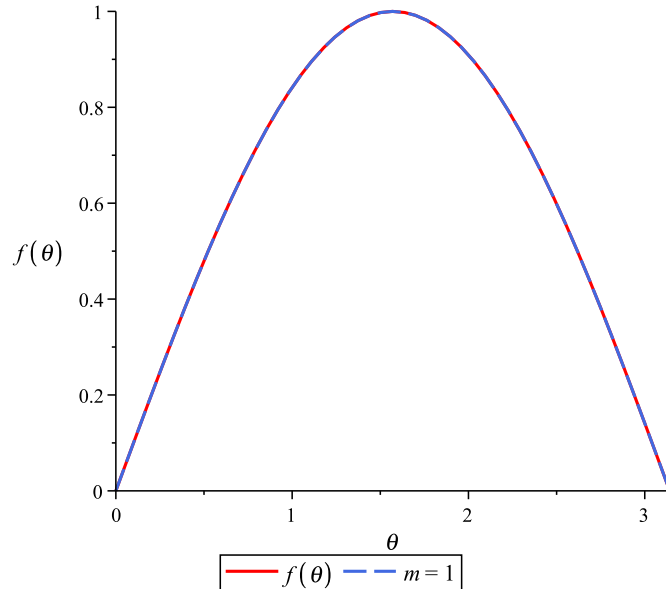


FIGURE 3.15: Approximation to the function, $f(\theta) = \sin(\theta)$ over the interval $[0, \pi]$ by *ALiC* series. The solid red line represents the function $f(\theta) = \sin(\theta)$ and the dashed blue line shows the *ALiC* series approximation of degree 1. The *ALiC* series obtained when $m = 1$ is algebraically equivalent to the original function.

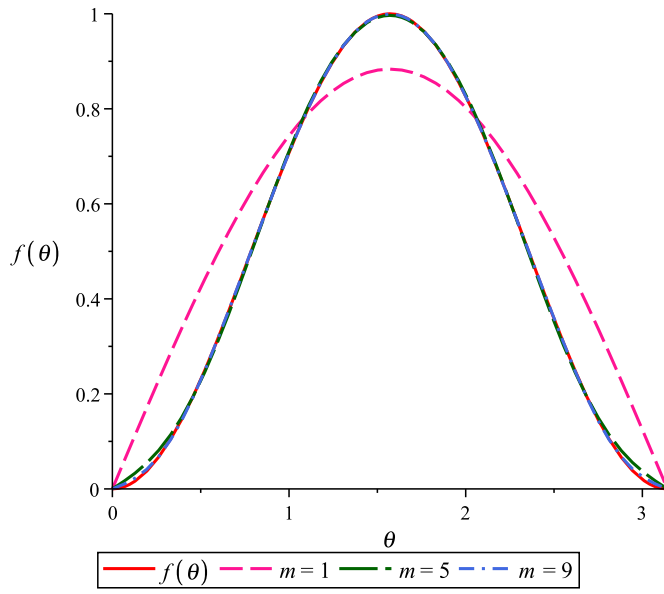


FIGURE 3.16: The *ALiC* series approximation for the function, $f(\theta) = \sin^2(\theta)$ over the interval $[0, \pi]$ represented by the solid red line. The dashed magenta line denotes the *ALiC* series approximation of degree 1 ($m = 1$) whereas the long dashed green line and the dashed-dotted blue line represent the *ALiC* series approximation of degree 5 and 9. As the degree of *ALiC* series approximation equal to 9, it approaches the correct function.

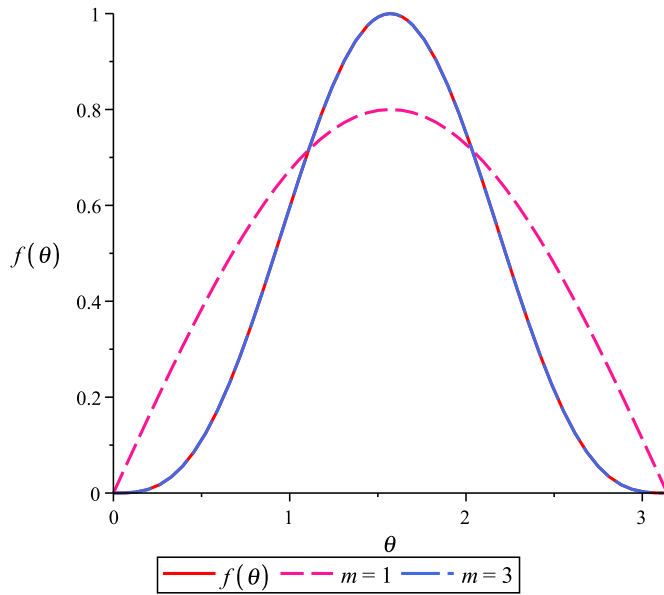


FIGURE 3.17: Approximation to the function, $f(\theta) = \sin^3(\theta)$ over the interval $[0, \pi]$ by *ALiC* series. The solid red line denotes $f(\theta)$ and, the dashed magenta line and the long dashed blue line represent the *ALiC* series approximation of degree 1 and 3. The *ALiC* series obtained when $m = 3$ is algebraically equivalent to the function,

$$f(\theta) = \sin^3(\theta).$$

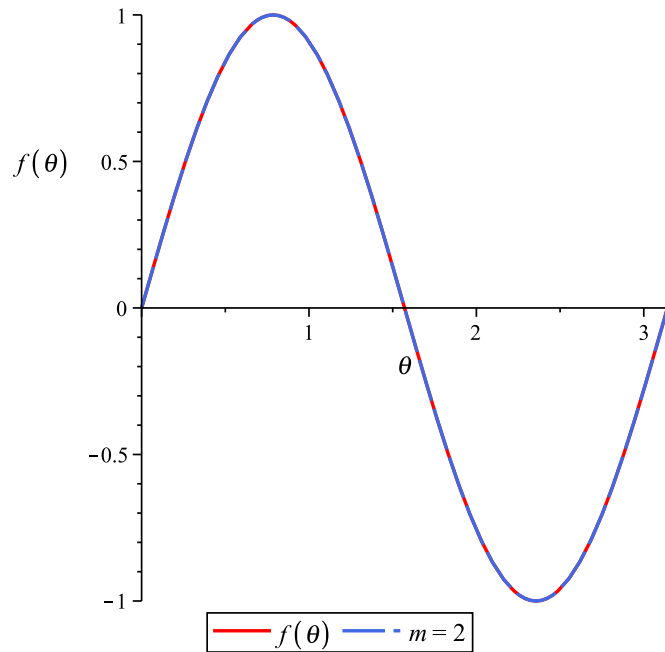


FIGURE 3.18: The *ALiC* series approximation for the function, $f(\theta) = \sin(2\theta)$ that satisfies the even part of the hypergeometric function over the interval $[0, \pi]$ and its given by the solid red line. The long dashed blue line represents the *ALiC* series approximation of degree 2. When $m = 2$ the *ALiC* series approximation look a good representation of $f(\theta)$.

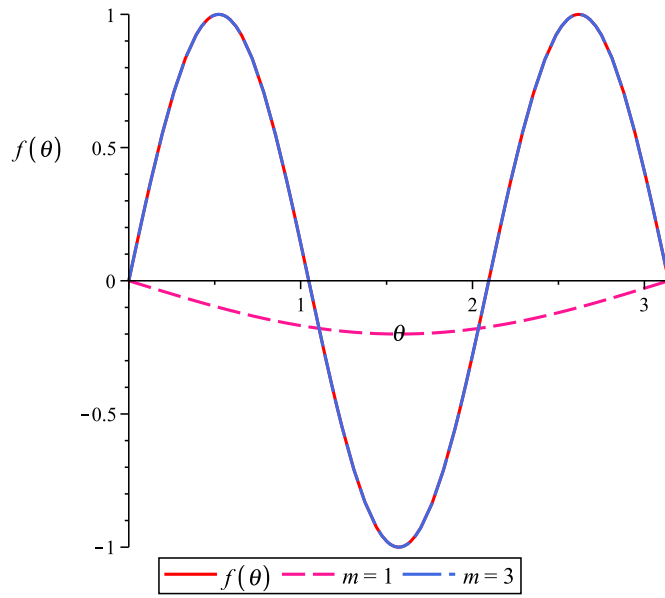


FIGURE 3.19: Approximation to the function, $f(\theta) = \sin(3\theta)$ that satisfies the odd part of the hypergeometric function over the interval $[0, \pi]$ by *ALiC* series. The function $f(\theta) = \sin(3\theta)$ is shown in solid red line. The dashed magenta line and the long dashed blue line denote the *ALiC* series approximation of degree 1 and 3. As the degree of *ALiC* series approximation equal to 3, it approaches the correct function.

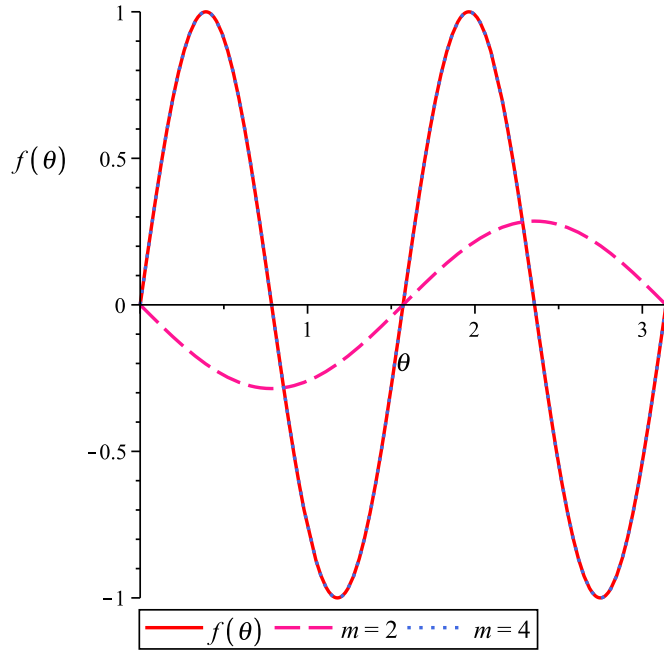


FIGURE 3.20: Approximation to the function, $f(\theta) = \sin(4\theta)$ that satisfies the even part of the hypergeometric function over the interval $[0, \pi]$ by $ALiC$ series. The original function is given by solid red line. The dashed magenta line and the dotted blue line represent the $ALiC$ series approximation of degree 2 and 4. The $ALiC$ series obtained when $m = 4$ is algebraically equivalent to the original function.

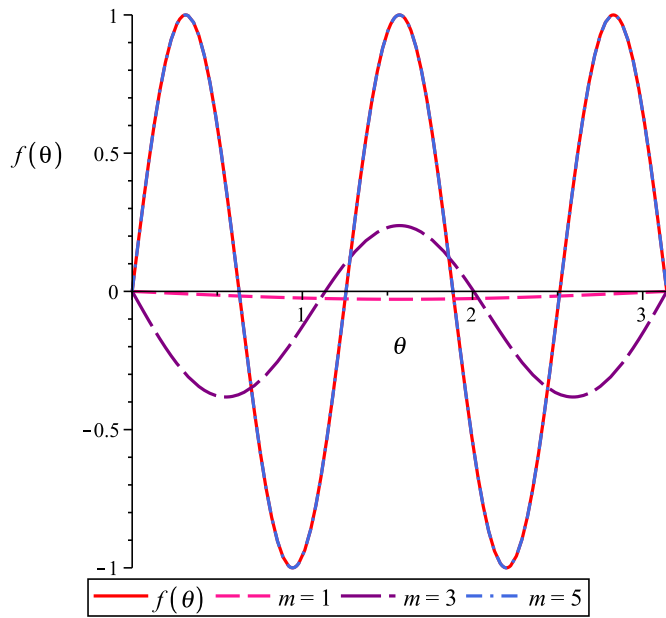


FIGURE 3.21: The $ALiC$ series approximation for the function, $f(\theta) = \sin(5\theta)$. The solid red line denotes the original function. Each graph corresponds to a different degree of approximation. The dashed magenta line, the long dashed purple line and the dashed-dotted blue line represent the corresponding $ALiC$ series approximation for m equal to 1, 3 and 5. As the degree of $ALiC$ series approximation rises to 5, it approaches a close approximation to $f(\theta)$.

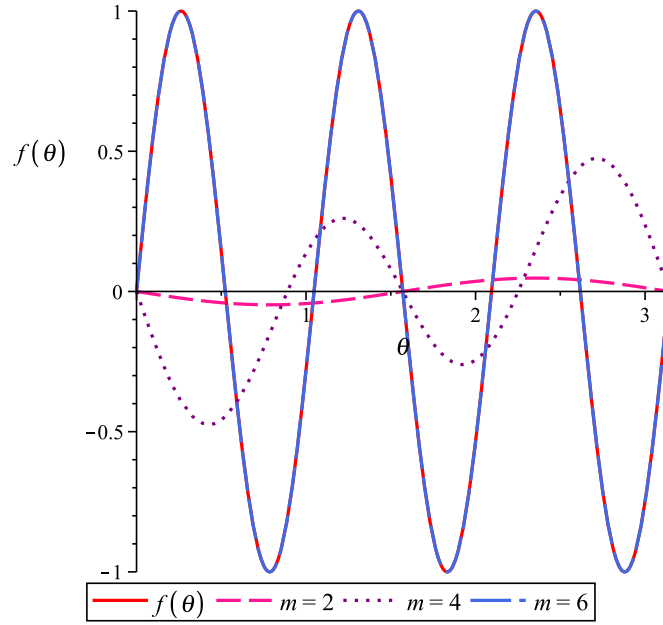


FIGURE 3.22: Approximation to the function, $f(\theta) = \sin(6\theta)$ that satisfies the even part of the hypergeometric function in between $[0, \pi]$ by $ALiC$ series. The original function, $f(\theta) = \sin(6\theta)$ is shown in solid red line. The dashed magenta line, the dotted purple line and the long dashed blue line represent the $ALiC$ series approximation of degree 2, 4 and 6. The $ALiC$ series obtained when $m = 6$ is equivalent to the original function.

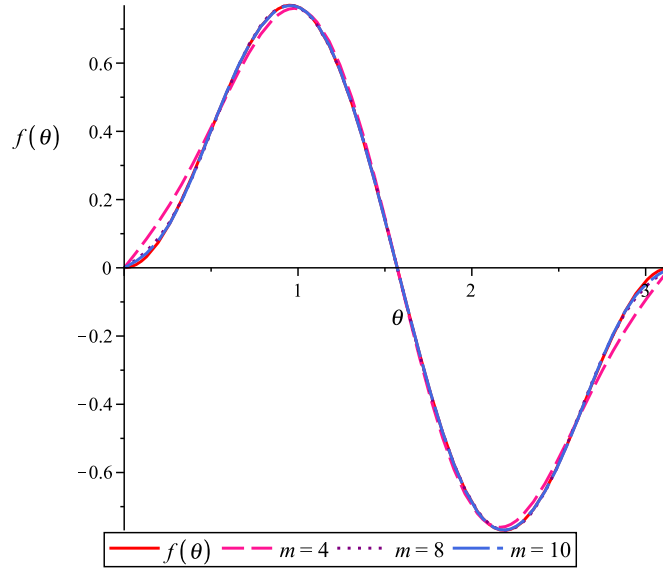


FIGURE 3.23: The $ALiC$ series approximation for the function, $f(\theta) = \sin(2\theta)\sin(\theta)$ over the interval $[0, \pi]$ that represented by the solid red line. The dashed magenta line denotes the $ALiC$ series approximation of degree 4 ($m = 4$) whereas the dotted purple line and the long dashed blue line represent the $ALiC$ series approximation of degree 8 and 10. As the degree of $ALiC$ series approximation approximation rises to 10, it approaches the correct function.

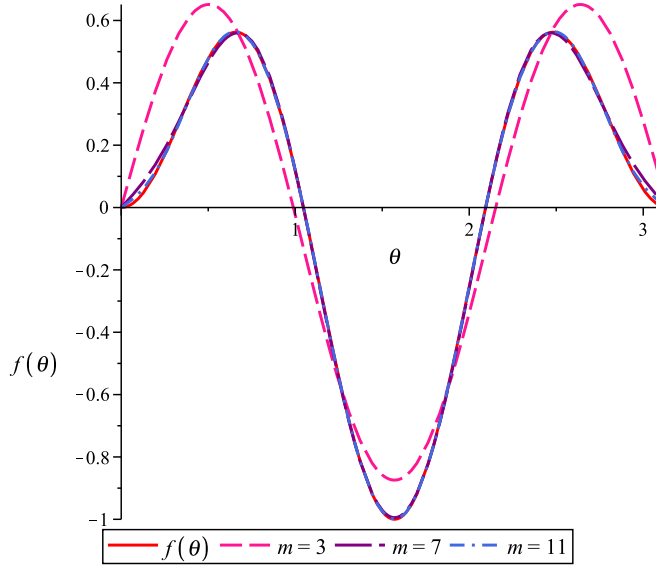


FIGURE 3.24: Approximation to the function, $f(\theta) = \sin(3\theta)\sin(\theta)$ that satisfies the odd part of the hypergeometric function over the interval $[0, \pi]$ by $ALiC$ series. The solid red line denotes the function, $f(\theta) = \sin(3\theta)\sin(\theta)$. Each graph corresponds to a different degree of approximation. The dashed magenta line, the long dashed purple line and the dashed-dotted blue line denote the $ALiC$ series approximation of degree 3, 7 and 11. The $ALiC$ series obtained when $m = 11$ is algebraically equivalent to the function, $f(\theta)$.

Though u_1 and v_1 do not enter into the equations (3.105) - (3.108), they enter the boundary conditions given in equation (3.109). So both u_1 and v_1 must be determined to solve the $O(\varepsilon)$ problem. By using the Stokes stream functions, we may now reduce equation (3.99) and equation (3.100) in terms of variables p_1 , w_1 and ψ_1 , yielding

$$-\frac{w_1^2}{R} = -p_{1R} + \frac{1}{\alpha^2} \left[\frac{\psi_{1\theta RR}}{R^2 \sin \theta} + \frac{\psi_{1\theta} \cos^2 \theta}{R^4 \sin^3 \theta} - \frac{\psi_{1\theta\theta} \cos \theta}{R^4 \sin^2 \theta} + \frac{\psi_{1\theta}}{R^4 \sin \theta} + \frac{\psi_{1\theta\theta\theta}}{R^2} \right], \quad (3.153)$$

and

$$\begin{aligned} -w_1^2 \cot \theta &= -p_{1\theta} + \frac{1}{\alpha^2} \left[-\frac{\psi_{1RRR}}{R \sin \theta} - \frac{\psi_{1R} \cos^2 \theta}{R^2 \sin^3 \theta} + \frac{\psi_{1R\theta} \cos \theta}{R^2 \sin^2 \theta} - \frac{\psi_{1R}}{R^2 \sin \theta} \right. \\ &\quad \left. - \frac{\psi_{1R\theta\theta}}{R^2 \sin \theta} - \frac{\psi_{1\theta} \cos \theta}{R^3 \sin^2 \theta} + \frac{2\psi_{1\theta\theta}}{R^3 \sin \theta} + \frac{\psi_{1R}}{R^2 \sin^3 \theta} \right]. \end{aligned} \quad (3.154)$$

Then we differentiate equation (3.153) with respect to and also differentiate equation (3.154) with respect to R , thus get rid the variable p_1 (which is $p_{1R\theta} = p_{1\theta R}$) by subtracting those equations, here we may get that

$$\begin{aligned} -\frac{(w_1^2)_\theta}{R} + (w_1^2)_R \cot \theta &= \frac{1}{\alpha^2} \left[\left[\frac{\psi_{1\theta RR}}{R^2 \sin \theta} + \frac{\psi_{1\theta} \cos^2 \theta}{R^4 \sin^3 \theta} - \frac{\psi_{1\theta\theta} \cos \theta}{R^4 \sin^2 \theta} + \right. \right. \\ &\quad \left. \left. \frac{\psi_{1\theta}}{R^4 \sin \theta} + \frac{\psi_{1\theta\theta\theta}}{R^2} \right]_\theta + \left[-\frac{\psi_{1RRR}}{R \sin \theta} - \frac{\psi_{1R} \cos^2 \theta}{R^2 \sin^3 \theta} + \frac{\psi_{1R\theta} \cos \theta}{R^2 \sin^2 \theta} - \right. \right. \\ &\quad \left. \left. \frac{\psi_{1R\theta\theta}}{R^2 \sin \theta} - \frac{\psi_{1\theta} \cos \theta}{R^3 \sin^2 \theta} + \frac{2\psi_{1\theta\theta}}{R^3 \sin \theta} + \frac{\psi_{1R}}{R^2 \sin^3 \theta} \right] \right]. \end{aligned}$$

$$\left. \frac{\psi_{1R}}{R^2 \sin \theta} - \frac{\psi_{1R\theta\theta}}{R^2 \sin \theta} - \frac{\psi_{1\theta} \cos \theta}{R^3 \sin^2 \theta} + \frac{2\psi_{1\theta\theta}}{R^3 \sin \theta} + \frac{\psi_{1R}}{R^2 \sin^3 \theta} \right]_R.$$

By substituting equation (3.104) into the equation above, we may obtain

$$\begin{aligned} & -\frac{1}{R} \left[\left(\text{Im} \left(\frac{1}{R^2} \frac{e^{\sqrt{i}\alpha R} (1 - \sqrt{i}\alpha R) - e^{-\sqrt{i}\alpha R} (1 + \sqrt{i}\alpha R)}{e^{\sqrt{i}\alpha} (1 - \sqrt{i}\alpha) - e^{-\sqrt{i}\alpha} (1 + \sqrt{i}\alpha)} \right) \sin(\theta) \right) \right]_\theta + \\ & \left[\left(\text{Im} \left(\frac{1}{R^2} \frac{e^{\sqrt{i}\alpha R} (1 - \sqrt{i}\alpha R) - e^{-\sqrt{i}\alpha R} (1 + \sqrt{i}\alpha R)}{e^{\sqrt{i}\alpha} (1 - \sqrt{i}\alpha) - e^{-\sqrt{i}\alpha} (1 + \sqrt{i}\alpha)} \right) \sin(\theta) \right) \right]_R \cot \theta \\ & = \frac{1}{\alpha^2} \left[\left[\frac{\psi_{1\theta RR}}{R^2 \sin \theta} + \frac{\psi_{1\theta} \cos^2 \theta}{R^4 \sin^3 \theta} - \frac{\psi_{1\theta\theta} \cos \theta}{R^4 \sin^2 \theta} + \frac{\psi_{1\theta}}{R^4 \sin \theta} + \frac{\psi_{1\theta\theta\theta}}{R^2} \right]_\theta + \left[-\frac{\psi_{1RRR}}{R \sin \theta} \right. \right. \\ & \left. \left. - \frac{\psi_{1R} \cos^2 \theta}{R^2 \sin^3 \theta} + \frac{\psi_{1R\theta} \cos \theta}{R^2 \sin^2 \theta} - \frac{\psi_{1R}}{R^2 \sin \theta} - \frac{\psi_{1R\theta\theta}}{R^2 \sin \theta} - \frac{\psi_{1\theta} \cos \theta}{R^3 \sin^2 \theta} + \frac{2\psi_{1\theta\theta}}{R^3 \sin \theta} + \frac{\psi_{1R}}{R^2 \sin^3 \theta} \right]_R \right] \end{aligned} \quad (3.155)$$

Equation (3.155) is a 4th order PDE which we cannot solve analytically. By using MAPLE [8] we tested the ‘separability’ which is checking either there is a complete solution of the PDE through separation of variables or not. It shown that either ‘separability’ by sum or ‘separability’ by product is not the complete solution of this equation (3.155). We can find ψ_1 by solving equation (3.155) numerically. However it is not too easy as we can see and the problem becomes much more complicated once we are in the stage to find u_1 , v_1 and p_1 . Thus we left this part for further work. Though we can find w_2 and hence determine some information about the retinal detachment, the difficulty of finding ψ_1 means that determining the pressure is a formidable problem.

3.9 Conclusions and Further Work

The modelling of paradigm problems of retinal detachment were presented. In the first and second paradigm mathematical models, the lubrication theory limit of the Navier-Stokes equations and the general theory of beam bending have been applied. Both models have been set up into different regions in order to examine the behaviour of aqueous humour flow through a detached retina and the deformation of the retinal detachment.

Firstly, we modelled the fluid flow between fixed walls which concerned the aqueous humour flow driven by pressure gradient through the detached retina. We then calculated and examined the deformation of the detached retina, the volume fluxes and the bending moments. From the results we found that there is almost no aqueous humour flow under the small retinal detachment and the deflection of the detached retina depends on several physical factor such as the length of the retinal detachment, the pressure difference and also the modulus of elasticity of the retina.

Secondly, we considered the aqueous humour flow in a channel with one moving and

one rigid wall. In this study the pressure is not constant everywhere and the flow of aqueous humour driven by moving the top plate with a typical speed. The results were examined numerically and it was shown that no flow of aqueous humour takes place under the detached retina, and the deformation of the detached retina has been examined through the size of one dimensionless parameter β . The results also showed that when β is small the detached retina becomes much less deformed. Physically when β is small, the potential of the detached retina to reattach back to the choroid is greater. However when β is large we found that the detached retina becomes much more deformed. Because β takes both negative and positive values during saccadic motion it seems that at some point in the saccadic cycle the retina will lie flat against the choroid. This seems to suggest the saccadic motion is unlikely to make a typical retinal detachment worse.

Thirdly, we have discussed a model of aqueous humour flow driven by saccadic eye motion by considering the Navier-Stokes equations in a spherical coordinate system in order to find the fluid flow in the eyeball and to examine the deformation of a detached retina. We considered non-dimensional flow governed by three dimensionless parameters which are ε , the amplitude oscillations, α (known as the Wormesley number) equal to the square root of the frequency multiplied by the viscosity of the fluid, and δ , the ratio of initial height of the detached retina over the radius of the eyeball. The sizes of these three dimensionless parameters have been classified and examined into several cases.

Fitt'04, [56] considered two different cases which are Case (1): $\alpha = O(1)$, thus there is no boundary layer and $\varepsilon \ll 1$ which is in the limit of small amplitude oscillations; Case (2): the values of ε is assumed quite small and α tends to be large. In Case (3), Repetto'08, [69] has been studied the case where ε is in the limit of small amplitude oscillations whilst α tends to be less or equal to one. All these three cases, Case (1), Cases (2) and Case(3), no retinal detachment which is no flap has been involved, therefore δ is assumed equal to zero. Appendix C shows that Repetto'09, [70] (Case(4)) had extended the work in Case (3) and had considered the large flap of retinal detachment, is given as $\delta \gg \varepsilon$. In this model, we extended Case (1) into three different cases which are Case (5), Case (6) and Case (7). Though this model looks similar to the model in Case(4), however this model is the first study to look at the retinal detachment. We think that the cases that have been considered in this model are more realistic compared to Case (4).

All the three cases, Case (5), Case (6) and Case (7) have been examined in this study. For these three cases we concluded that we could find the azimuthal fluid velocity at leading and correction order. We determined *ALiC* series solutions of the azimuthal fluid velocity at the correction order in terms of modified spherical Bessel function and hypergeometric function that depend on the special value of C . We proved the series solutions of the hypergeometric function are mutually orthogonal with respect to the weighting function over the interval $[0, \pi]$ by using the Sturm-Liouville theory. From

the results represented in Figures 3.13 - 3.24, it was shown that the *ALiC* series could be considered as a good approximation to any function, $f(\theta)$ that is symmetric at $\theta = \pi/2$ for various values of m . However we always get a leading order problem that cannot be solved analytically.

Then we extended Case (2) into three others different cases which are Case (8), Case (9) and Case (10). For Case (8) and Case (9) we expected that there would be no exact solution because the flap has the same width with the boundary layer and the other reason is the flap width is greater than the boundary layer. In Case (10) we found that this was a realistic case of retinal detachment to solve. We assumed that there are a small flap in the boundary layer thickness and the limit of amplitude oscillations is considered small, which can be written as $\alpha^{-1} \ll \varepsilon \ll 1$ where $\delta \ll \varepsilon$. For Case (10) we summarized that we could determine the solutions of fluid flow at leading order that exactly the same as given in Case (2), [56]. However this case becomes much more complicated and there are analytical difficulties in solving the correction order and examining the deformation of the detached retina.

Several cases studied here which are Case (5), Case (6), Case (7) and Case (10) could further be extended and solved numerically by using any numerical methods in order to find the solutions for flow velocities and pressure in terms of leading and next order of the problem. The third model could be improved consists of three-dimensional retinal detachment shapes. The other option could be carried out for further work by solving the models using numerical simulation such as COMSOL Multiphysic and many others.

The overall conclusion from this study is that though some closed-form progress can be made in examining the detachment of a retina by saccadic forces, a large numerical study may be required in general.

Chapter 4

Flow in the Anterior Chamber during DMD

4.1 Introduction

Descemet membrane detachment (DMD) is a rare but potentially serious complication which can arise during cataract surgery. It can develop in the human eye if there is a descemet membrane break or tear. This allows the aqueous humour to enter the descemet membrane space through the break and causes the membrane to separate from the stroma; the main layer of cornea which makes up ninety percent of the corneal thickness. A mathematical model of aqueous humour flow in the anterior chamber around a DMD has been developed. This model is based on the lubrication theory limit of the Navier-Stokes equations. Specifically, aqueous humour flow in the anterior chamber is described as flow driven by buoyancy effects due to the existing temperature difference between the anterior surface of the cornea and the pupil. The DMD which is kept in contact with the stroma is assumed to be elastic and deformable, so that the general theory of beams under axial loading can be applied. Using this fluid mechanical model the flow of aqueous humour behaviour and the deformation of the DMD have been analysed analytically and numerically using COMSOL Multiphysics [72].

This chapter includes a brief introduction to the anatomy and physiology of the cornea, DMD, the possible causes of DMD and the management, and mechanisms that drive flow in the anterior chamber. The modelling of aqueous humour flow in the anterior chamber during DMD is considered in two different shaped regions. First, we develop the paradigm problem by assuming the anterior chamber resembles a rectangular shaped region. We then generalise by considering the anterior chamber as a dome shaped region. In both models, we will present the governing equations, the boundary conditions, the solution procedures and also the analytical and numerical results and their discussion.

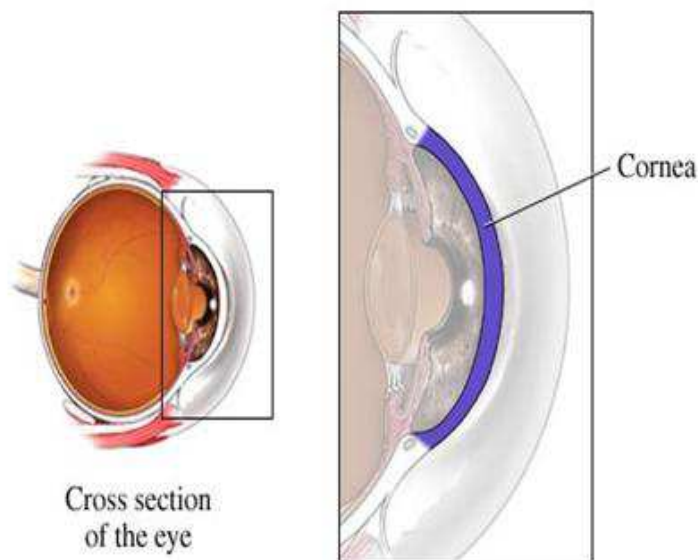


FIGURE 4.1: The Cornea. This figure was extracted from [155].

4.2 Corneal Structure

The cornea, shown in Figure 4.1, is a clear dome-shaped surface that covers the iris and the pupil in the human eye. Contaminants such as dust and the use of contact lenses can cause irritation of the cornea. The region that is bounded by the cornea, the iris and the pupil is the anterior chamber. It is filled with aqueous humour. The cornea is the most important optical lens of the eye [85]. Together with the crystalline lens it focuses light onto the retina where it can be absorbed and detected.

The cornea consists of three main layers, (as shown in Figure 4.2) the epithelium, the stroma and the endothelium, and two auxiliary layers; the bowman layer and the Descemet membrane. The epithelium contains five layers of cells and the total thickness is approximately fifty microns. It can regenerate itself and it has free nerve endings which feel irritation caused by the contaminants on the eye. The stroma is the thickest part of the layer, making up ninety percent of the corneal thickness. Its main function is to give the cornea its strength and shape. The stroma consists of stroma cells that are known as keratocytes which produce transparent collagen fibers. The inner most layer of the cornea is the endothelium. Its structure resembles a transparent ‘honeycomb’ and its primary task is to pump excess water out of the stroma. The bowman layer lies between the epithelium and the stroma. The Descemet membrane lies between the stroma and the endothelium and it provides a lining for the cornea. Small changes in the structure of the cornea can make a big difference to the focusing function, see [24] and [1] for further details.

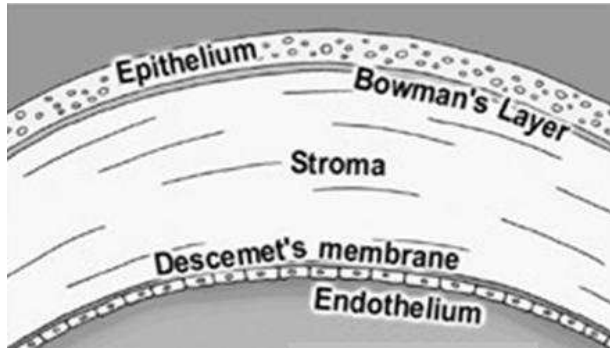


FIGURE 4.2: The structure of the Cornea. This figure was extracted from [156].

4.3 Descemet Membrane Detachment (DMD) in Human Eyes

Descemet membrane detachment (DMD) is an uncommon but serious complication of intraocular surgery, most commonly occurring during cataract extraction [87]. It is unknown what causes the Descemet membrane to separate from the stroma. One popular idea is that it is caused by the mechanical force applied to the cornea during surgery [86]. DMD occurs when aqueous humour enters a Descemet membrane tear or break, and causes the membrane to separate from the stroma, as shown in Figure 4.3. When the separation is greater the detachment could progress towards the centre of the cornea. If this occurs it may lead to a lack of focused light on the retina and severe visual loss.

DMDs can be classified as planar or non-planar [84] and [83], scrolled or non-scrolled and peripheral or peripheral with central cornea involvement, for details see [87]. [84] and [83] have stated that in planar DMD the separation distance between the stroma and the Descemet membrane is less than one millimetre while the distance in non-planar DMD is greater than one millimetre. It is important to classify the type or severity of detachment because it can influence treatment, either non-surgical or surgical.

The possible causes of DMD and the management and outcome of patients after cataract surgery have been studied in [82], [73], [90] and [86]. [82] stated that planar detachments had the best medical prognosis for spontaneous reattachment, while non-planar detachments were difficult to reattach spontaneously. In contrast, [73] concluded that for non-scrolled detachments with a length of one millimetre, or greater, separation from the stroma might be able to reattach spontaneously. According to [90], the non planar and non scrolled DMD will often spontaneously reattach if given enough time. [90] believed that DMD did not require urgent treatment and that waiting a few months for DMD to spontaneously reattach is acceptable before doing surgical repairs. In [86] it was noted that small DMD is rarely problematic, and repair may not be required because it may be repaired itself. However more extensive detachment can affect the

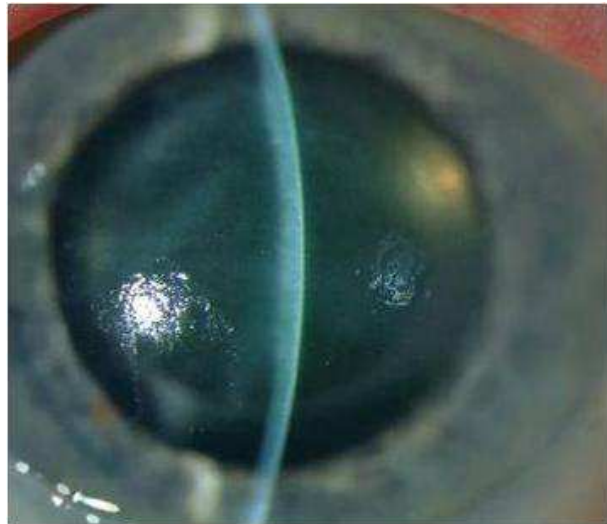


FIGURE 4.3: DMD. This figure was taken from [76] with permission.

acuteness or clearness of vision. Despite reports of spontaneous reattachment, many previous studies have established early repair techniques of DMD, [86], [87], [80], [88] and [76].

4.3.1 Causes and Management of DMD

Large number of cases of DMD have been reported, due to cataract surgery, iridectomy, trabeculectomy, corneal transplantation, deep lamellar keratoplasty, holmium laser sclerostomy, alkali burn and viscocanalostomy, for examples see [87], [79], [89] and [84]. DMD is a well-recognised complication of cataract extraction and it was first described by Weve in 1927 and formally reported by Samuels in 1928, [86]. Since then, it has been reported most often due to cataract surgery [86], [87], [80], [88] and [76]. [86] discussed a persistent case of Descemet membrane tear and the progress after surgical treatment via suture and injection of air. [87] shows the successful repair of a scrolled DMD by injecting fourteen percent of intracameral perfluoropropane (C_3F_8) into the anterior chamber after unsuccessful treatment with topical hyperosmotics and steroids. According to [80], three cases of DMD after uncomplicated cataract surgery have been reported. In the first case it was managed without surgical treatment because the type of the DMD was planar and peripheral. In the second case, the patient was treated using an intracameral injection and the last case a treatment involved the injecting of C_3F_8 . [88] presents a case of DMD after cataract surgery which was successfully treated with twenty percent sulphur hexafluoride injection. The recent paper, [76] has reported two cases of delayed bilateral Descemet membrane which in one eye it was fixed surgically and the other eye improved spontaneously.

Studies in [82], [73], [90], [86] and [76] have reported that spontaneous reattachment of

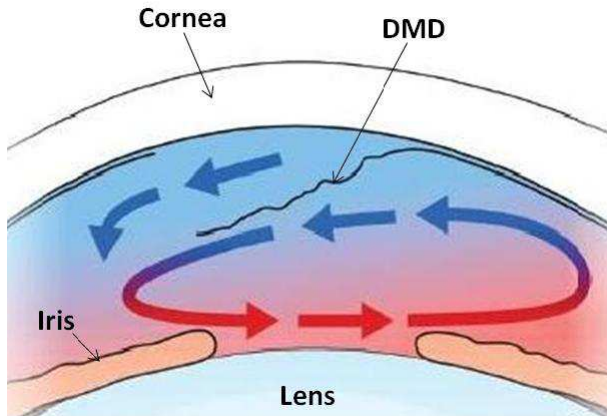


FIGURE 4.4: Mechanism of spontaneous Descemet membrane reattachment. This figure was reproduced from [76] with permission.

the detached part of the descemet membrane can occur. However, it is unknown what factors influence the spontaneous reattachment and how it occurs. Following the work in [75], [76] notes that buoyancy effects may be the cause of the aqueous humour flow in the anterior chamber and hence, this may cause the spontaneous reattachment. In [76] no fluid mechanical explanation is given for this phenomenon. There are various mechanisms that drive the flow of aqueous humour in the anterior chamber; buoyancy effects, flow from the ciliary body through the pupil aperture, gravity, flow generated by phakodenesis, and Rapid Eye Movement (REM) during sleep, [78]. Many previous researchers have studied the buoyancy-driven flow in the anterior chamber, [81], [75], [77], [74] and [78]. It has long been agreed that under normal conditions the flow of aqueous humour driven by buoyancy effects is present because of the temperature difference between the front and the back of the anterior chamber, [78]. In this study we use a fluid mechanical model of flow in anterior chamber, developed in [75], to include the presence of a detached Descemet membrane in the flow. This simplified model is able to explain how and why either spontaneous re-attachment or worsening of the tear occurs as noted in [76] and how the process can be controlled.

4.4 Motivation for the Mathematical Model

A mathematical model of buoyancy-driven flow in the anterior chamber of the human eye has been developed in [75]. The buoyancy effect is driven by the temperature gradient between the anterior surface of the cornea and the plane formed by the pupil aperture and the iris. This mechanism may cause the motion of aqueous humour in the anterior chamber and may become even more important when Descemet membrane detachment is present. In this chapter, we present the equations that govern the flow in the anterior chamber, for which [75] has shown that the lubrication theory limit of the Navier-Stokes equations is an appropriate model. We also build on the work

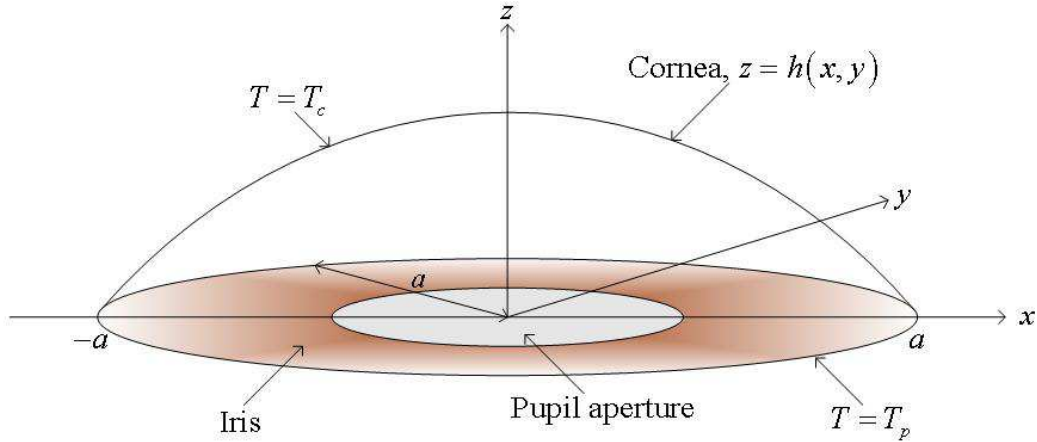


FIGURE 4.5: Schematic diagram of a three-dimensional of the anterior chamber. The function selected for $h_o \left(1 - \frac{x^2}{a^2} - \frac{y^2}{a^2}\right)^{\frac{1}{2}}$, whereas the temperature difference between the cornea, T_c and the circular plane formed by the pupil aperture and the iris, T_p with the radius, $r = a$, is given by $T = T_p - T_c$.

presented in [75] to develop a new mathematical model of the aqueous humour flow in the anterior chamber during DMD. We start by looking at a simple model, considering the fluid to be driven by buoyancy effects in a rectangular-shaped region. We assume there to be a thin, small flap, which is elastic and deformable, and is kept in contact with the bottom plate. Thus we shall apply the general theory of beam bending under axial load. In this study, we use an asymptotic analysis to analyse the flow behaviour and the deformation of the flap. We then apply the same methods to examine a more realistic-shaped region of the anterior chamber, *i.e.* the dome shape. For comparison, both simplified models were solved numerically using COMSOL Multiphysics [72].

4.5 Aqueous Humour Flow in the Anterior Chamber

We consider flow driven by buoyancy effects in the anterior chamber between the anterior surface of the cornea and the plane formed by pupil aperture and the iris. In this section, we will derive the equations that govern the fluid motion in the anterior chamber and determine the streamlines for buoyancy-driven flow in the anterior chamber. Figure 4.5 presents a schematic diagram of a three-dimensional of the anterior chamber. The aqueous humour is assumed to be an incompressible Newtonian fluid with constant viscosity, ν and we assume the temperature of the aqueous humour contained in the cornea is held fixed at $T = T_c$ while at $z = 0$ the temperature is held fixed, $T = T_p$; this will be given by the temperature of blood, $37^\circ C$ [91]. Gravity is assumed to be acting parallel to the x -axis, a is the radius of the pupil aperture and h_o is a typical depth

of the anterior chamber under normal conditions. Considering the classical Boussinesq model for buoyancy driven convective flow, (see [75] and [2]), we assume that the fluid density, ρ varies slightly with temperature, giving

$$\rho = \rho_\circ (1 - \alpha (T - T_c)).$$

Here T denotes temperature, ρ_\circ is the fluid density at a temperature T_c and α is the coefficient of linear thermal expansion of the fluid. The fluid density, ρ may be replaced by ρ_\circ in every term in the Navier-Stokes equation for an incompressible Newtonian viscous fluid [22], except in the gravity term. The governing equations of motion become

$$\rho_\circ \bar{q}_t + \rho_\circ (\bar{q} \cdot \nabla) \bar{q} = -\nabla p + \rho_\circ v \nabla^2 \bar{q} + \rho_\circ (1 - \alpha (T - T_c)) \bar{g}, \quad (4.1)$$

$$\nabla \cdot \bar{q} = 0, \quad (4.2)$$

$$T_t + (\bar{q} \cdot \nabla) T = \frac{k}{\rho_\circ c_p} \nabla^2 T + \frac{\bar{\phi}}{\rho_\circ c_p}. \quad (4.3)$$

The quantities $u(x, y, z), v(x, y, z)$ and $w(x, y, z)$ are the components of the fluid velocity, \bar{q} and the quantities p_x, p_y and p_z are the components of a vector, ∇p where p denotes pressure. Here subscripts denote derivatives, t is time, v is the kinematic viscosity, ϕ is the viscous dissipation, k and c_p are thermal conductivity and the specific heat at a constant pressure. We non-dimensionalise equations (4.1) - (4.3), using the dimensionless variable given in [75] and [2]; these are,

$$x = Lx^*, \quad y = Ly^*, \quad z = L\delta z^*, \quad u = Uu^*, \quad v = Uv^*, \quad w = U\delta w^*,$$

$$t = \frac{L}{U} t^*, \quad p = \left(\frac{\mu UL}{h_\circ^2} \right) p^*, \quad T = T_c + (T_p - T_c) \bar{T},$$

where $L = 2a$, U and h_\circ denote a typical length, a typical flow velocity and an undeformed depth respectively. $\delta = \frac{h_\circ}{L}$ denotes the aspect ratio. Now we define the Reynolds, Prandtl, Froude and Brinkmann numbers respectively as,

$$\text{Re} = \frac{UL}{v}, \quad \text{Pr} = \frac{\rho_\circ v c_p}{k}, \quad \text{Fr} = \frac{U^2}{gL}, \quad \text{Br} = \frac{\rho_\circ v U^2}{k(T_p - T_c)}.$$

Then in non-dimensional form we drop the stars for convenience and equations (4.1) - (4.3) can be written in component form as,

$$\begin{aligned} & \delta^2 \text{Re} (u_t + uu_x + vu_y + wu_z) \\ &= -p_x + \delta^2 (u_{xx} + u_{yy}) + u_{zz} + \frac{\delta^2 \text{Re}}{\text{Fr}} (1 - \alpha (T_p - T_c) T), \end{aligned} \quad (4.4)$$

$$\delta^2 \text{Re} (v_t + uv_x + vv_y + wv_z) = -p_y + \delta^2 (v_{xx} + v_{yy}) + v_{zz}, \quad (4.5)$$

$$\delta^2 \text{Re} (w_t + uw_x + vw_y + ww_z) = -\frac{p_z}{\delta^2} + \delta^2 (w_{xx} + w_{yy}) + w_{zz}, \quad (4.6)$$

$$u_x + v_y + w_z = 0, \quad (4.7)$$

$$T_t + uT_x + vT_y + wT_z = \frac{1}{\text{Re Pr}} \left(T_{xx} + T_{yy} + \frac{1}{\delta^2} T_{zz} \right) + \frac{\text{Br}}{\delta^2 \text{Re Pr}} (u_z^2 + v_z^2). \quad (4.8)$$

A three-dimensional model of aqueous humour flow in the anterior chamber is shown in Figure 4.5. We note that a three-dimensional extension of the two-dimensional system studied here is straight forward. However, for ease of visualising results we restrict our interest to two dimensions. In this model, the typical values for a human eye are obtained from [75], giving;

$$\begin{aligned} h_0 &= 0.00275m, & L &= 0.011m, & U &= 10^{-4}ms^{-1}, & v &= 0.9 \times 10^{-6}m^2s^{-1}, \\ g &= 9.8ms^2, & \alpha &= 3 \times 10^{-4}K^{-1}, & T_p &= 371.2K, & T_c &= 371.1K, \\ \rho_0 &= 10^3kgm^{-3}, & c_p &= 4.2 \times 10^3 J kg^{-1} K^{-1}, & k &= 0.57 W m^{-1} K^{-1}. \end{aligned} \quad (4.9)$$

Using the values above, we obtain that

$$\begin{aligned} \delta &\sim 0.25, & \text{Re} &\sim 1.22, & \delta^2 \text{Re} &\sim 0.076, \\ \frac{1}{\text{Re Pr}} &\sim 0.12, & \frac{1}{\delta^2 \text{Re Pr}} &\sim 2, & \frac{\text{Br}}{\delta^2 \text{Re Pr}} &\sim \frac{3 \times 10^{-11}}{T_p - T_c}, \\ \frac{\delta^2 \text{Re} \alpha}{\text{Fr}} (T_p - T_c) &\sim 250 (T_p - T_c). \end{aligned}$$

Since the reduced Reynolds number $\delta^2 \text{Re}$ is much smaller than one therefore the lubrication theory limit may be used to reduce equations equations (4.4) - (4.6). We also note that the value of the temperature gradients required to derive a non trivial flow are very small. By these assumption and neglecting the viscous dissipation term, equations (4.4) - (4.8) can be simplified significantly. Thus, the dimensional governing equations that are to be solved are,

$$-\frac{p_x}{\rho_0} + vu_{zz} + g(1 - \alpha(T - T_c)) = 0, \quad (4.10)$$

$$p_z = 0, \quad (4.11)$$

$$T_{zz} = 0, \quad (4.12)$$

$$u_x + w_z = 0. \quad (4.13)$$

The boundary conditions are no slip, $u = w = 0$, on $z = h(x)$, $T = T_p$ on $z = 0$, $T = T_c$ on $z = h(x)$ and $p = p_a$ at $x = -a$. A mathematical model of buoyancy-driven flow in the anterior chamber of the human eye has been developed by [75] (see Figure 4.6(a)). This mechanism may cause the motion of aqueous humour in the anterior chamber and may become even more important when Descemet membrane detachment is present. A numerical simulation using COMSOL [72] has been carried out as a comparison for this simplified model [75]. Figure 4.6 shows the numerical result, Figure 4.6(b) agreed

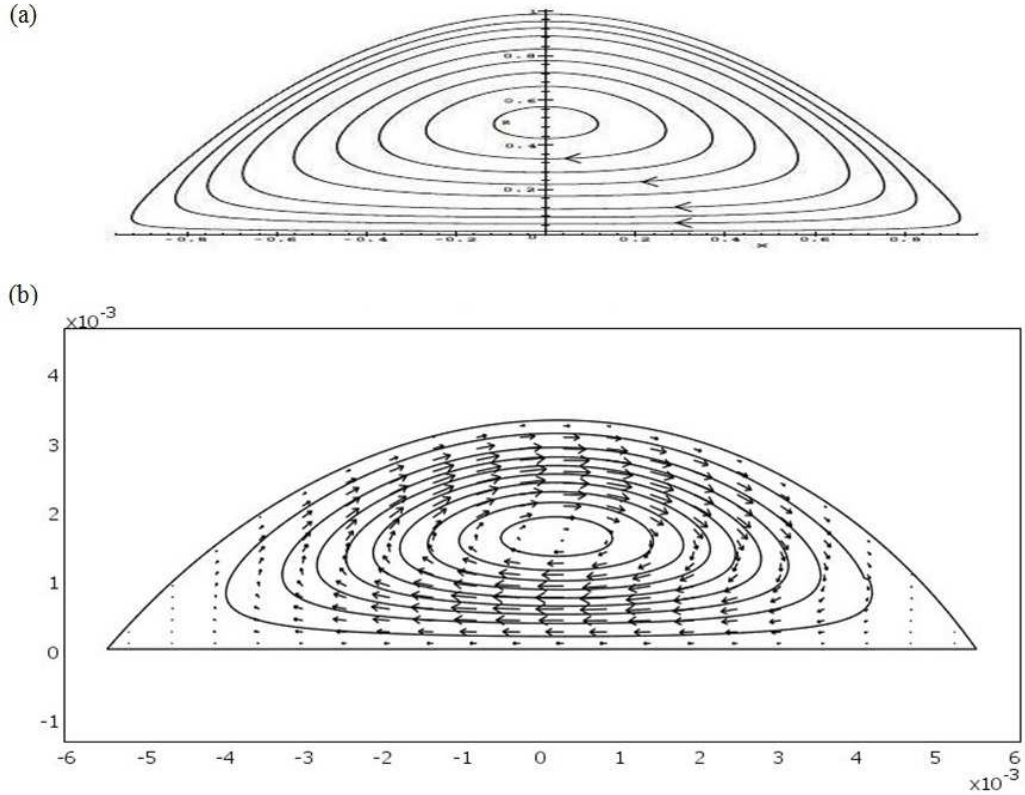


FIGURE 4.6: Streamlines for buoyancy-driven flow in the plane $y = 0$. Gravity, g is assumed to be acting horizontally to the right and the function, $h(x) = h_0 \left(1 - \frac{x^2}{a^2}\right)$ represents the cornea. The typical values of a human eye given in equation (4.9) are employed in this numerical simulation using COMSOL [72], Figure 4.6(b), in order to compare with the result that produced by [75], Figure 4.6(a). This figure was taken from [75] with permission.

qualitatively with the analytical result, Figure 4.6(a). These results show that buoyancy effects may be responsible for driving the flow in the anterior chamber during DMD, as stated in [76]. We now investigate this further.

4.6 Modelling of Paradigm Problem: Flow in the Rectangular-shaped region

We start by applying the analogy of buoyancy effects to a paradigm problem of flow through a flap in the simple-shaped region. We are doing this problem first in order to examine the fluid flow behaviour and to determine the pressure difference across the flap. If we can analyse this simple problem, we then proceed with the full problem. Let us now derive a model of flow through the flap in the rectangular-shaped region.

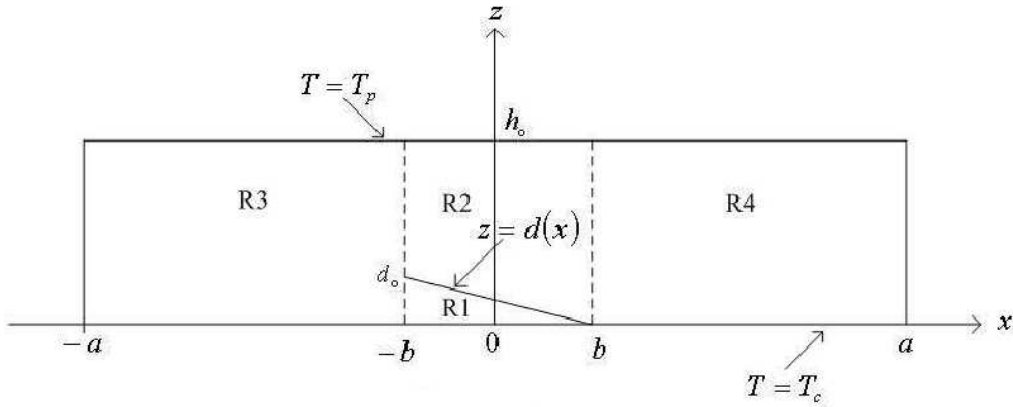


FIGURE 4.7: Schematic diagram of fluid flow through a small flap in a rectangular shaped region.

4.6.1 Mathematical Model

A two-dimensional flow driven by buoyancy effects in the rectangular shaped region through a thin and small flap has been considered, as shown in Figure 4.7. We introduce a Cartesian coordinate system (x, z) with fixed plates in the planes $z = 0$, $z = h_o$, $x = -a$ and $x = a$. There are no fluxes through these plates. A thin and small flap occupies $-b \leq x \leq b$ and is given by $z = d(x)$. We denote the velocities, pressures and streamlines by $u_k \bar{i} + w_k \bar{k}$, p_k and ψ_k where $k = 1, 2, 3, 4$ denote values in Region 1 (R1), Region 2 (R2), Region 3 (R3) and Region 4 (R4). We now consider the governing equations of motion as shown in Chapter 4.5. These are:

$$-\frac{p_{kx}}{\rho_o} + vu_{kzz} + g(1 - \alpha(T - T_c)) = 0, \quad (4.14)$$

$$p_{kz} = 0, \quad (4.15)$$

$$T_{zz} = 0, \quad (4.16)$$

$$u_{kx} + w_{kz} = 0, \quad (4.17)$$

where the equations above are subject to the no slip condition on $z = 0$, $z = d(x)$ and $z = h_o$. The no slip boundary conditions for the velocity in each region are:

When $k = 1$, $(-b \leq x \leq b, 0 \leq z \leq d(x))$,

$$u_1(x, 0) = w_1(x, 0) = u_1(x, d(x)) = w_1(x, d(x)) = 0, \quad (4.18)$$

$$k = 2, \quad (-b \leq x \leq b, d(x) \leq z \leq h_o),$$

$$u_2(x, d(x)) = w_2(x, d(x)) = u_2(x, h_o) = w_2(x, h_o) = 0, \quad (4.19)$$

$$k = 3, \quad (-a \leq x \leq -b, 0 \leq z \leq h_o),$$

$$u_3(x, 0) = w_3(x, 0) = u_3(x, h_o) = w_3(x, h_o) = 0, \quad (4.20)$$

$$k = 4, \quad (b \leq x \leq a, 0 \leq z \leq h_o),$$

$$u_4(x, 0) = w_4(x, 0) = u_4(x, h_o) = w_4(x, h_o) = 0. \quad (4.21)$$

The boundary condition for the temperature at $z = 0$ is assumed to be a constant and the temperature condition at $z = h_o$ is taken to be a constant flux. Thus:

$$T = T_p \quad \text{on} \quad z = 0 \quad \text{and} \quad T_z = \frac{T_c - T_p}{h_o} \quad \text{on} \quad z = h_o \quad (4.22)$$

Finally, boundary conditions are required in order to determine the pressure in each region. Here we assume that the fluxes at each point x are continuous. We also assume that the pressure is known and equal to the constant [75] pressure $p = p_a$ at $x = a$. Here the boundary conditions for the pressure are given by

$$\int_0^{d(x)} u_1 dz = 0, \quad \int_{d(x)}^{h_o} u_2 dz = 0, \quad \int_0^{h_o} u_3 dz = 0, \quad \int_0^{h_o} u_4 dz = 0, \quad (4.23)$$

and

$$p_3(-b) = p_1(-b), \quad p_3(-b) = p_2(-b), \quad p_4(b) = p_2(b), \quad p_4(a) = p_a. \quad (4.24)$$

Now, we may proceed to determine the solutions for velocities, pressures and streamlines for the system of equations (4.14) - (4.17) subject to the boundary conditions given in equations (4.18) - (4.24).

4.6.2 Solution Procedures

Equation (4.15) shows that p only depends on x . The equation for temperature, (4.16), may now be solved by using the boundary condition (in equation 4.22) to give,

$$T(z) = T_p - \eta z, \quad (4.25)$$

where $\eta = \frac{T_p - T_c}{h_o}$. We shall now consider each region individually.

Region (1)

We substitute equation (4.25) into equation (4.14) and find that,

$$u_{1zz} = \frac{p_{1x}}{\rho_o v} - \frac{g}{v} (1 - \alpha(T_p - T_c) + \alpha\eta z).$$

If we integrate the above equation and substitute the boundary condition given in equation (4.18) we obtain that

$$u_1 = z(z-d) \left[\frac{p_{1x}}{2\rho_o v} - \frac{g}{2v} \left(1 - \alpha(T_p - T_c) + \frac{\alpha\eta}{3}(z+d) \right) \right]. \quad (4.26)$$

We differentiate equation (4.26) with respect to x , give such that

$$u_{1x} = \frac{1}{2\rho_o v} [p_{1x}z(z-d)]_x + \frac{g}{2v} \left(zd_x (1 - \alpha(T_p - T_c)) + \frac{\alpha\eta}{3} (2zdd_x) \right). \quad (4.27)$$

Then we substitute equation (4.27) into equation (4.17) yielding,

$$w_{1z} = -\frac{1}{2\rho_o v} [p_{1x}z(z-d)]_x - \frac{g}{2v} \left(zd_x (1 - \alpha(T_p - T_c)) + \frac{\alpha\eta}{3} (2zdd_x) \right).$$

We may now solve the above equation subject to the boundary condition given in equation (4.18), to obtain

$$w_1 = -\frac{1}{2\rho_o v} \left[p_{1x} \left(\frac{z^3}{3} - \frac{z^2d}{2} \right) \right]_x - \frac{g}{4v} z^2 d_x \left(1 - \alpha(T_p - T_c) - \frac{2\alpha\eta d}{3} \right). \quad (4.28)$$

By substituting $z = d(x)$ and $w_1 = 0$, we find that,

$$p_{1x} = g\rho_o \left[1 - \alpha(T_p - T_c) + \frac{\alpha\eta d}{2} \right] + \frac{A_1}{d^3},$$

where A_1 is the arbitrary constant. If we substitute the above equation into the boundary condition given in equation (4.23), we find that $A_1 = 0$. Therefore,

$$p_{1x} = g\rho_o \left[1 - \alpha(T_p - T_c) + \frac{\alpha\eta d}{2} \right]. \quad (4.29)$$

We shall now determine the streamline in this region, given that $u_1 = \psi_{1z}$ and $w_1 = -\psi_{1x}$. If we integrate $u_1 = \psi_{1z}$ with respect to z , we find,

$$\psi_1 = \left(\frac{z^3}{3} - \frac{dz^2}{2} \right) \left[\frac{p_{1x}}{2\rho_o v} - \frac{g}{2v} \left(1 - \alpha(T_p - T_c) + \frac{\alpha\eta}{2} \left(\frac{z^2 - 2d^2}{2z - 3d} \right) \right) \right] + f_1(x) \quad (4.30)$$

where $f_1(x)$ is the arbitrary function. Differentiating equation (4.30) with respect to x , gives

$$\psi_{1x} = \frac{1}{2\rho_o v} \left[p_{1x} \left(\frac{z^3}{3} - \frac{z^2d}{2} \right) \right]_x + \frac{g}{2v} \left((1 - \alpha(T_p - T_c)) \frac{d_x z^2}{2} + \frac{\alpha\eta}{3} (z^2 dd_x) \right) [f_1(x)]_x.$$

We now compare with this equation (4.28) and find that $f_1(x) = C_1$ where C_1 is an arbitrary constant. Thus, the equation for streamlines in Region (1) is,

$$\psi_1 = \left(\frac{z^3}{3} - \frac{dz^2}{2} \right) \left[\frac{p_{1x}}{2\rho_o v} - \frac{g}{2v} \left(1 - \alpha(T_p - T_c) + \frac{\alpha\eta}{2} \left(\frac{z^2 - 2d^2}{2z - 3d} \right) \right) \right] + C_1.$$

From the no slip conditions we know that $\psi_1 = 0$ on $z = 0$ and $z = d(x)$, here we get that $C_1 = 0$. Therefore, we obtain,

$$\psi_1 = \left(\frac{z^3}{3} - \frac{dz^2}{2} \right) \left[\frac{p_{1x}}{2\rho_o v} - \frac{g}{2v} \left(1 - \alpha(T_p - T_c) + \frac{\alpha\eta}{2} \left(\frac{z^2 - 2d^2}{2z - 3d} \right) \right) \right]. \quad (4.31)$$

Region (2)

We now substitute equation (4.25) into equation (4.14) to obtain,

$$u_{2zz} = \frac{p_{2x}}{\rho_o v} - \frac{g}{v} (1 - \alpha(T_p - T_c) + \alpha\eta z).$$

Then we integrate the above equation with respect to z , such that,

$$u_2 = \frac{p_{2x}}{2\rho_o v} z^2 - \frac{g}{2v} \left((1 - \alpha(T_p - T_c)) z^2 - \frac{\alpha\eta}{3} z^3 \right) + B_1 z + B_2.$$

By substituting the boundary conditions given in equation (4.19), we get

$$B_1 = -\frac{p_{2x}}{2\rho_o v} (d + h_o) + \frac{g}{2v} \left((1 - \alpha(T_p - T_c)) (d + h_o) + \frac{\alpha\eta}{3} (d^2 + dh_o + h_o^2) \right)$$

and

$$B_2 = \frac{p_{2x}}{2\rho_o v} (dh_o) - \frac{g}{2v} \left((1 - \alpha(T_p - T_c)) dh_o + \frac{\alpha\eta}{3} (d^2 h_o + dh_o^2) \right).$$

Therefore we obtain,

$$u_2 = (z - d)(z - h_o) \left[\frac{p_{2x}}{2\rho_o v} - \frac{g}{2v} \left(1 - \alpha(T_p - T_c) + \frac{\alpha\eta}{3} (z + d + h_o) \right) \right]. \quad (4.32)$$

We now differentiate equation (4.31) with respect to x , to find that,

$$\begin{aligned} u_{2x} &= \frac{1}{2\rho_o v} [p_{2x}(z - d)(z - h_o)]_x - \frac{g}{2v} (1 - \alpha(T_p - T_c)) (-zd_x + h_o d_x) \\ &\quad - \frac{g\alpha}{6vh_o} (-z(d_x h_o + 2dd_x) + d_x h_o (2d + h_o)). \end{aligned}$$

Then we substitute the above equation into equation (4.17), integrate the equation with respect to z and substitute the boundary condition (4.19) to give,

$$\begin{aligned} w_2 &= -\frac{1}{12\rho_o v} \left[p_{2x}(z - d)^2 (2z + d - 3h_o) \right]_x + \frac{g}{2v} \left[(1 - \alpha(T_p - T_c)) \frac{d_x}{2} (d^2 - z^2) \right. \\ &\quad \left. + 2h_o(z - d) \right] + \frac{\alpha\eta}{3} d_x \left\{ (h_o^2 + 2dh_o)(z - d) - (2d + h_o) \left(\frac{z^2}{2} - \frac{d^2}{2} \right) \right\}. \end{aligned} \quad (4.33)$$

By considering the leading order problem at $z = h_o$ and $w_2 = 0$, we find that,

$$p_{2x} = g\rho_o \left[1 - \alpha(T_p - T_c) + \frac{\alpha\eta}{2} (d + h_o) \right] + \frac{A_2}{(d - h_o)^3}, \quad (4.34)$$

where A_2 is an arbitrary constant. We now substitute equation (4.34) into the boundary condition for u_2 in equation (4.23) to determine that $A_2 = 0$. Therefore, we may restate equation (4.34) to give,

$$p_{2x} = g\rho_\circ \left[1 - \alpha(T_p - T_c) + \frac{\alpha\eta}{2} (d + h_\circ) \right]. \quad (4.35)$$

By using equations (4.32) and (4.33), we may now solve these equations $u_2 = \psi_{2z}$ and $w_2 = -\psi_{2x}$ in order to get the streamline in this region. Thereby obtaining,

$$\begin{aligned} \psi_2 = & \frac{p_{1x}}{12\rho_\circ v} (z - d)^2 (2z + d - 3h_\circ) - \frac{g}{12v} \left[(1 - \alpha(T_p - T_c))(z - d)^2 \cdot \right. \\ & \left. (2z + d - 3h_\circ) + \frac{\alpha\eta}{2} (z - d)^2 (d^2 - 2dh_\circ + 2dz - 2h_\circ^2 + z^2) \right]. \end{aligned} \quad (4.36)$$

Region (3)

In this region we find that,

$$u_{3zz} = \frac{p_{3x}}{\rho_\circ v} - \frac{g}{v} [1 - \alpha(T_p - T_c) + \alpha\eta z].$$

We solve the above equation subject to the boundary condition given in equation (4.20) and obtain

$$u_3 = \frac{p_{3x}}{2\rho_\circ v} z(z - h_\circ) - \frac{g}{2v} \left[(1 - \alpha(T_p - T_c)) z(z - h_\circ) + \frac{\alpha\eta}{3} z(z^2 - h_\circ^2) \right]. \quad (4.37)$$

We now differentiate equation (4.37) with respect to x , to give,

$$u_{3x} = \frac{p_{3xx}}{2\rho_\circ v} z(z - h_\circ). \quad (4.38)$$

We now substitute equation (4.38) into equation (4.17) and integrate with respect to z to obtain

$$w_3 = -\frac{p_{3xx}}{2\rho_\circ v} \left(\frac{z^3}{3} - \frac{z^2 h_\circ}{2} \right) + C,$$

where C is an arbitrary constant. If we now substitute the boundary condition given in equation (4.20) into the equation above, we find that $C = 0$. Therefore,

$$w_3 = -\frac{p_{3xx}}{2\rho_\circ v} \left(\frac{z^3}{3} - \frac{z^2 h_\circ}{2} \right). \quad (4.39)$$

At $z = h_\circ$ and $w_3 = 0$, we have,

$$\begin{aligned} p_{3xx} &= 0, \\ p_{3x} &= A_3, \end{aligned} \quad (4.40)$$

where A_3 is an arbitrary constant. By substituting equation (4.40) into the boundary

condition in equation (4.23) for u_3 we obtain

$$A_3 = g\rho_\circ \left[1 - \alpha(T_p - T_c) + \frac{\alpha\eta h_\circ}{2} \right].$$

Thus we may rewrite equation (4.38) such that,

$$p_{3x} = g\rho_\circ \left[1 - \alpha(T_p - T_c) + \frac{\alpha\eta h_\circ}{2} \right]. \quad (4.41)$$

We now determine the streamline in Region (3) by substituting equations (4.37) and (4.39) into equations $u_3 = \psi_{3z}$ and $w_3 = -\psi_{3x}$. Therefore, we obtain,

$$\psi_3 = \frac{p_{3x}}{2\rho_\circ v} \left[\frac{z^3}{3} - \frac{h_\circ z^2}{2} \right] - \frac{g}{2v} \left[(1 - \alpha(T_p - T_c)) \left(\frac{z^3}{3} - \frac{h_\circ z^2}{2} \right) + \frac{\alpha\eta}{3} \left\{ \frac{z^4}{4} - \frac{z^2 h_\circ^2}{2} \right\} \right]. \quad (4.42)$$

Region (4)

In this region, we now repeat the same steps as in Regions (1), (2) and (3) to find u_4 , w_4 , p_{4x} and ψ_4 . Here we may obtain those solutions are the same as in Region (3). These are,

$$\begin{aligned} u_4 &= \frac{p_{4x}}{2\rho_\circ v} z(z - h_\circ) - \frac{g}{2v} \left[(1 - \alpha(T_p - T_c)) z(z - h_\circ) + \frac{\alpha\eta}{3} z(z^2 - h_\circ^2) \right], \\ w_4(x, z) &= -\frac{p_{4xx}}{2\rho_\circ v} \left(\frac{z^3}{3} - \frac{z^2 h_\circ}{2} \right), \\ p_{4x} &= g\rho_\circ \left[1 - \alpha(T_p - T_c) + \frac{\alpha\eta h_\circ}{2} \right], \end{aligned} \quad (4.43)$$

$$\psi_4 = \frac{p_{4x}}{2\rho_\circ v} \left[\frac{z^3}{3} - \frac{h_\circ z^2}{2} \right] - \frac{g}{2v} \left[(1 - \alpha(T_p - T_c)) \left(\frac{z^3}{3} - \frac{h_\circ z^2}{2} \right) + \frac{\alpha\eta}{3} \left\{ \frac{z^4}{4} - \frac{z^2 h_\circ^2}{2} \right\} \right]. \quad (4.44)$$

Using equations (4.29), (4.34), (4.41) and (4.44), we now solve for the pressure gradient in each region defined as $p_1(x)$, $p_2(x)$, $p_3(x)$, and $p_4(x)$, subject to the boundary conditions given in equation (4.24). Thus we obtain,

$$p_1(x) = p_a + g\rho_\circ \left[(1 - \alpha(T_p - T_c))(x - a) + \frac{\alpha\eta}{2} \{D(x) - D(b) + h_\circ(-b - a)\} \right] \quad (4.45)$$

$$p_2(x) = p_a + g\rho_\circ \left[(1 - \alpha(T_p - T_c))(x - a) + \frac{\alpha\eta}{2} \{D(x) - D(b) + h_\circ(x - a)\} \right] \quad (4.46)$$

$$p_3(x) = p_a + g\rho_\circ \left[(1 - \alpha(T_p - T_c))(x - a) + \frac{\alpha\eta}{2} \{D(-b) - D(b) + h_\circ(x - a)\} \right]$$

$$p_4(x) = p_a + g\rho_\circ \left[1 - \alpha(T_p - T_c) + \frac{\alpha\eta h_\circ}{2} \right] (x - a),$$

where $D(x) = \int_0^{d_\circ} d dx$.

4.6.3 Analytical Results and Simulations

Specifically we assume that the temperature at the bottom plate, T_c is less than the temperature at the top plate, T_p ($T_c < T_p$). Consistent with this, we impose the temperature difference between the top and bottom plates is constant (which is equal to 2). Then by using known values for a human eye, given in equation (4.9) and assuming that the position of the flap is given by $d(x) = -0.15x + 0.00015$, where $x \in [-0.001, 0.001]$. We plot the streamlines defined in equations (4.31), (4.36), (4.42) and (4.44). The plotted streamlines given in Figure 4.8(a) do not join up perfectly. This is because these calculations are based on the lubrication theory limit of Navier-Stokes equations and it has been analysed in four different regions.

Numerical simulation of flow driven by buoyancy effects in the rectangular-shaped region through the flap attached to the bottom plane have been studied. COMSOL Multiphysics [72], is used to plot streamlines, surface and the velocities field, see Figure 4.8(b). The flow behaviour shown in Figure 4.8 is qualitatively the same as in Figure 4.6. However the presence of the flap leads to qualitative differences. Figures 4.8(a) and Figure 4.8(b) show the flow streamlines when gravity is acting horizontally to the right (positive, g). The flow direction in both results depending on which way gravity acts, so in these both figures the streamlines are close in this region. As we can see in the results, there is much less flow under the flap than the other regions and this shows that the flow is very weak. Both results are due to the assumption that the temperature at the top plane is higher than the temperature at the bottom plane. Furthermore, the quantitative agreement between analytical and COMSOL Multiphysics [72] calculations is also satisfactory. The maximum speed in the COMSOL calculation is 3.9008×10^{-4} m/s, at position $(x, z) = (0.00253, 0.00218)$. While the analytical calculation gave the speed at the same location is 3.9607×10^{-4} m/s.

We now proceed with the analysis of the deformation of the flap in the rectangular-shaped region. We assume the flap to be elastic and deformable, thereby we can apply the general theory of beam bending (cantilever beam). By considering a flap of length, $L' = 2b$ and the beam to be attached to the centre of the bottom plate. The cantilever equilibrium position of the beam is determined by the flap, $d(x)$, which describes the deflection, d of the beam at some position x , subject to the difference in pressure gradient between Region (1) and Region (2). We can now formulate an equation that describes the relationship between the beam's deflection and the applied load. This is given by,

$$EI d_{xxxx} = p_1(x) - p_2(x). \quad (4.47)$$

Note that E is the elastic modulus, I is the second moment of area (EI is a constant), $p_1 - p_2$ denotes the pressure difference across the flap and x subscript denotes derivatives. Equation (4.47) is a fourth order derivative in x , hence it requires four boundary conditions. In this study, we consider two sets of boundary conditions. The first set

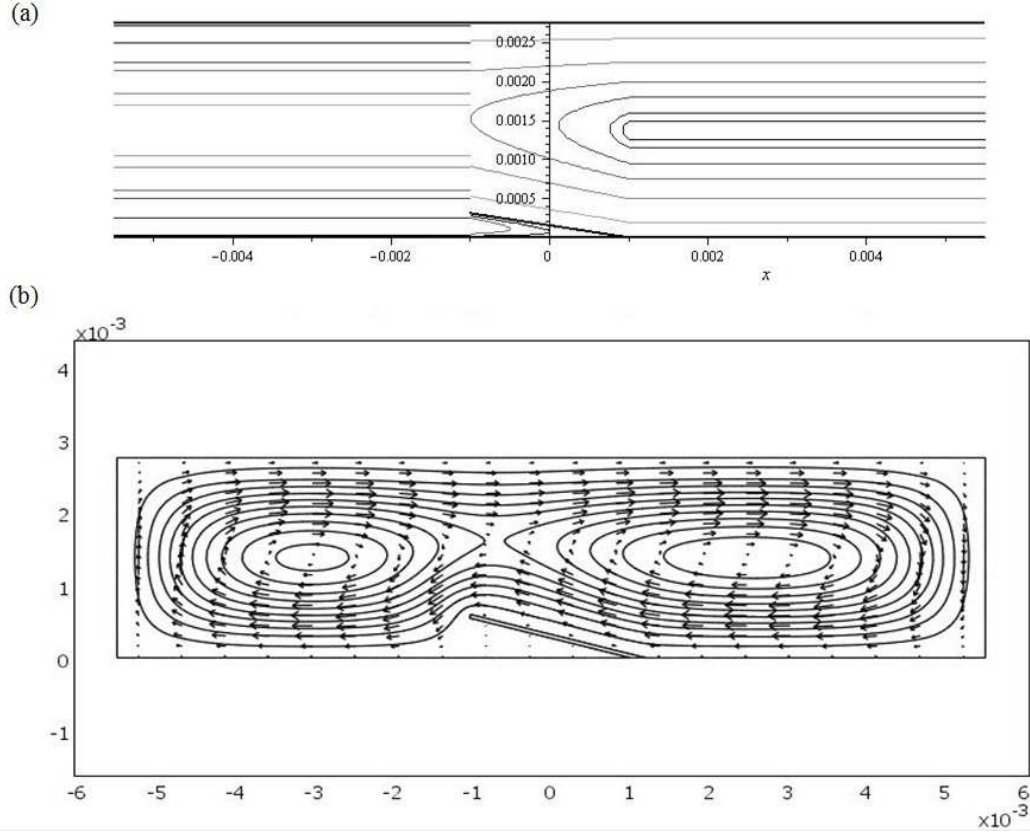


FIGURE 4.8: Streamlines for buoyancy-driven flow in the rectangular shaped region when gravity is acting horizontally to the right. The function selected for the flap, $d(x)$ is $d(x) = -0.15x + 0.00015$ over the interval $x \in [-0.001, 0.001]$ and the temperature gradient between the top and the bottom plates is equivalent to 2. (a) Streamlines in all regions given in equations (4.31), (4.36), (4.42) and (4.44) are plotted using Maple [8]. (b) Numerical simulation for streamline plots are carried out using COMSOL Multiphysics [72] in the purpose of comparison with the analytical calculation. Both figures are plotted using the standard parameter values of a human eye given in equation (4.9).

of boundary conditions assume the flap is clamped at $x = b$ with a constant angle of inclination, ϕ . The other end, $x = -b$ is free to move. The set of boundary conditions are such that,

$$d(b) = 0, \quad d_x(b) = -\phi, \quad d_{xx}(-b) = 0, \quad d_{xxx}(-b) = 0. \quad (4.48)$$

The second set of boundary conditions that we consider are such that the flap, $d(x)$ is assumed to be hinged at $x = b$ and free at $x = -b$. In this case the boundary conditions may be expressed by,

$$d(b) = 0, \quad d_{xx}(b) = 0, \quad d_{xx}(-b) = 0, \quad d_{xxx}(-b) = 0. \quad (4.49)$$

We now substitute equations (4.45) and (4.46) into equation (4.47) and obtain the

equation of the flap is,

$$EI d_{xxxx} = -\frac{g\rho_o \alpha \eta h_o}{2} (x + b). \quad (4.50)$$

For the non-dimensionalisation of equations (4.48) - (4.50), we rescale the variables by setting,

$$x = b\bar{x} \quad \text{and} \quad d = d_o \bar{d},$$

where b is the half length of the flap and d_o is the height of the flap. Thus in non-dimensional form and dropping bars for convenience, the equations (4.48) - (4.50) can be written as,

$$d_{xxxx} = -\beta (x + 1) \quad \text{where} \quad \beta = \frac{g\rho_o \alpha \eta h_o b}{2EI}, \quad (4.51)$$

subject to the boundary conditions,

$$d(1) = 0, \quad d_x(1) = -\gamma \quad \text{where} \quad \gamma = \frac{\phi b}{d_o}, \quad d_{xx}(-1) = 0, \quad d_{xxx}(-1) = 0 \quad (4.52)$$

or

$$d(1) = 0, \quad d_{xx}(1) = 0, \quad d_{xx}(-1) = 0, \quad d_{xxx}(-1) = 0. \quad (4.53)$$

Note that the parameter β estimates the relative importance of the effects of gravity, buoyancy and elastic stiffness. We now examine a case when β is small ($\beta \ll 1$) and we assume that $\gamma = O(1)$. To solve equation (4.51) we introduce an asymptotic expansion by expanded d in power of β such that,

$$d(x) = d_0(x) + \beta d_1(x) + \dots \quad (4.54)$$

We then substitute equation (4.54) into equation (4.51) and impose the boundary conditions given in equation (4.52). Thus,

$$d_{0xxxx} + \beta d_{1xxxx} + \dots = -\beta(x + 1), \quad (4.55)$$

with boundary conditions

$$\begin{aligned} d_0(1) + \beta d_1(1) + \dots &= 0, & d_{0x}(1) + \beta d_{1x}(1) + \dots &= -1, \\ d_{0xx}(-1) + \beta d_{1xx}(-1) + \dots &= 0, & d_{0xxx}(-1) + \beta d_{1xxx}(-1) + \dots &= 0. \end{aligned} \quad (4.56)$$

From equation (4.55) and the boundary conditions given in equation (4.56), we now find the equations and the boundary conditions for $\beta^{(0)}$ and $\beta^{(1)}$. These are
 $\beta^{(0)} :$

$$d_{0xxxx} = 0,$$

$$d_0(1) = 0, \quad d_{0x}(1) = -1, \quad d_{0xx}(-1) = 0, \quad d_{0xxx}(-1) = 0.$$

$\beta^{(1)} :$

$$d_{1xxxx} = -x - 1,$$

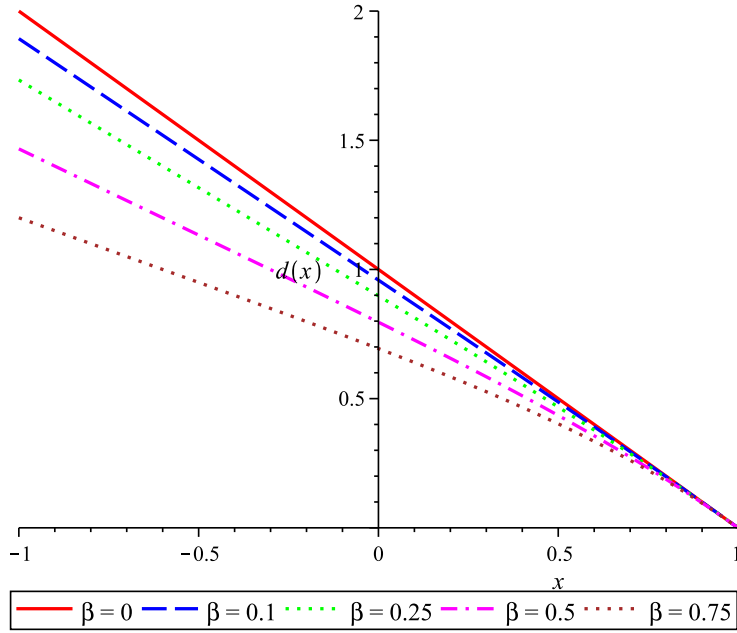


FIGURE 4.9: The deformation of the flap given in equation (4.57) for different positive values of $\beta = \frac{g\rho_0\alpha\eta h_0 b}{2EI}$. The solid red line represents the flap when β is equal to zero, whereas the dashed blue line, the dotted green line, the dashed-dotted magenta line and the dotted brown line denote the corresponding flap for β equal to 0.1, 0.25, 0.5 and 0.75.

$$d_1(1) = 0, \quad d_{1x}(1) = 0, \quad d_{1xx}(-1) = 0, \quad d_{1xxx}(-1) = 0.$$

At leading order, $\beta^{(0)}$ we obtain,

$$d_0(x) = 1 - x.$$

At the next order, $\beta^{(1)}$ we find that,

$$d_1(x) = -\frac{x^5}{120} - \frac{x^4}{24} - \frac{x^3}{12} - \frac{x^2}{12} + \frac{5x}{8} - \frac{49}{120}.$$

Thus equation (4.54) can be written as,

$$d(x) = 1 - x + \beta \left(-\frac{x^5}{120} - \frac{x^4}{24} - \frac{x^3}{12} - \frac{x^2}{12} + \frac{5x}{8} - \frac{49}{120} \right) + O(\beta^2). \quad (4.57)$$

Equation (4.57) may now be plotted, see Figures 4.9 and 4.10 in order to examine the deformation of the flap when β is small. In this case we also examine β may be either positive or negative values due to the directions of the gravity. Figure 4.9 shows the deformation of the flap, d for different positive values of β (0, 0.1, 0.25, 0.5, 0.75). These results show that when the value of β increases then the flap becomes much more deformed, *i.e.* the flap bends down more at the free end because the other end is fixed. As β increases, it is like modulus of elasticity, E decreases. So the flap becomes

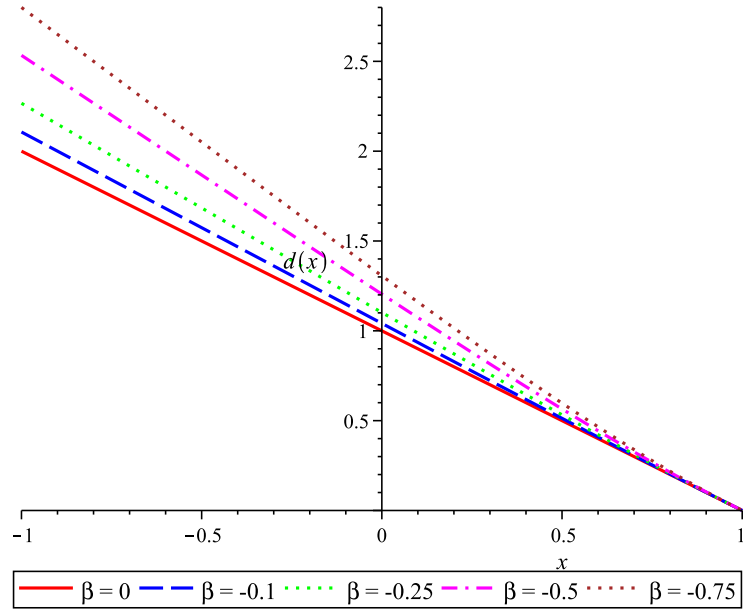


FIGURE 4.10: The deformation of the flap given in equation (4.57). Each graph corresponds to a different negative values of β . The solid red, the dashed blue, the dotted green, the dashed-dotted magenta and the dotted brown lines denote the corresponding flap for β equal to 0, -0.1, -0.25, -0.5 and -0.75.

more bendable and that is why the deformation increases. In this case the flap will re-attach onto the bottom plane back. Figure 4.10 presents the deformation of the flap for different negative values of β (0, -0.1, -0.25, -0.5, -0.75). These results show that when the value of β decrease, the flap becomes much more deformed. Physically this is because the pressure difference increases and thus causes the flap to re-detach from the bottom plane that it previously attached too. In the second case, one end of the flap is assumed to be hinged and at the other end is considered free. We now repeat the previous steps by substituting equation (4.54) into equation (4.51) and impose the boundary conditions given in equation (4.53). We solve this case and we conclude that no steady solution is found, and two possibilities may be happen either the flap is spontaneously reattach or it may be got worse. In this first model, the results show that the fluid flow behaviour and the pressure difference across the flap have been determined. Since we can examine this paradigm model, we will now proceed with the full problem, by considering a more realistic geometry shaped in order to examine the spontaneous reattachment (as stated in [76]) or redetachment of Descemet membrane.

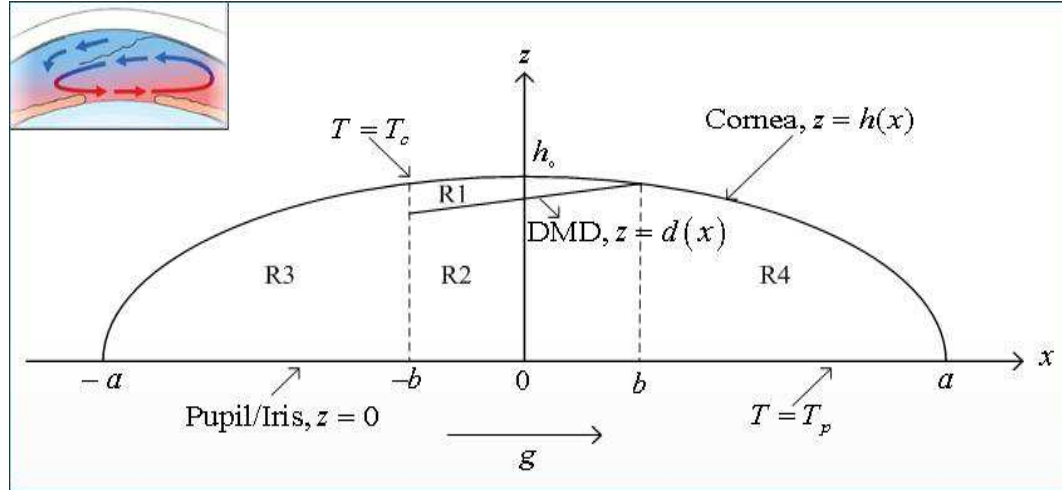


FIGURE 4.11: Schematic diagram of the detached Descemet membrane in the anterior chamber in the plane $y = 0$ when gravity is acting horizontally to the right. The function, $h(x) = h_o \left(1 - \frac{x^2}{a^2}\right)^{\frac{1}{2}}$ represents the cornea and the function selected for the DMD, $d(x)$ is given by $0.2x + 0.002455$ over the interval $[-b, b]$.

4.7 Modelling of Aqueous Humour Flow during Descemet Membrane Detachment

We shall now derive a model of aqueous humour in the anterior chamber around a detached Descemet membrane.

4.7.1 Mathematical Model

In this study, we attempt to model and analyse the mechanism of buoyancy-driven flow in the anterior chamber during Descemet membrane detachment as noted in [76], see Figure 4.4. A more sophisticated model has been developed by considering the more realistic-shaped region of the anterior chamber which is the dome shape. A two-dimensional aqueous humour flow driven by buoyancy effects in the anterior chamber during DMD in the plane $y = 0$ has been considered, as shown in Figure 4.11. We note that a three-dimensional extension of the two-dimensional system studied here is straight forward. However, for ease of visualising results we restrict our interest to two dimensions. We introduce a Cartesian coordinate system (x, z) which aqueous humour flow between the plane formed by pupil aperture and the iris, $z = 0$ and the anterior surface of the cornea, $z = h(x)$. The aqueous humour is assumed to be Newtonian, viscous and incompressible. A detached Descemet membrane is assumed to be a thin and small flap attached onto the anterior surface of the cornea. The flap occupies $-b \leq x \leq b$ and is defined by $z = d(x)$. Due to the slender geometry of the problem the lubrication theory limit of the Navier-Stokes equations are taken to govern the flow

of aqueous humour in the anterior chamber, [75]). These are,

$$-\frac{p_{kx}}{\rho_\circ} + vu_{kzz} + g(1 - \alpha(T - T_c)) = 0, \quad (4.58)$$

$$p_{kz} = 0, \quad (4.59)$$

$$u_{kx} + w_{kz} = 0, \quad (4.60)$$

$$T_{zz} = 0. \quad (4.61)$$

The region between the cornea surface and the DMD, Region (1), is given by $k = -1$ where $-b \leq x \leq b$ and $d(x) \leq z \leq h(x)$. The region between the DMD and the plane formed by the pupil and the iris, Region (2), is given by $k = 2$ where $-b \leq x \leq b$ and $0 \leq z \leq d(x)$. The regions between the cornea surface and the plane formed by the pupil and the iris, Region (3) and Region (4) are given by $a \leq x \leq -b$ and $0 \leq z \leq h(x)$ and $b \leq x \leq a$, $0 \leq z \leq h(x)$. Here subscripts denote derivatives, T_c and T_p denote the temperature at the cornea and the plane formed by the pupil and the iris, ρ_\circ is the fluid density at a temperature T_c and α is the coefficient of linear thermal expansion of the fluid. The quantities $u(x, z)$ and $w(x, z)$ are the components of the fluid velocities, v , g , a , h_\circ denote the kinematic viscosity, gravity, the radius of the anterior chamber and the typical depth of the anterior chamber respectively. Flow through the pupil aperture is not considered in this problem, thus, the no slip boundary conditions for the velocity in each region are,

$$u_1(x, d(x)) = w_1(x, d(x)) = u_1(x, h(x)) = w_1(x, h(x)) = 0, \quad (4.62)$$

$$u_2(x, 0) = w_2(x, 0) = u_2(x, d(x)) = w_2(x, d(x)) = 0, \quad (4.63)$$

$$u_3(x, 0) = w_3(x, 0) = u_3(x, h(x)) = w_3(x, h(x)) = 0, \quad (4.64)$$

$$u_4(x, 0) = w_4(x, 0) = u_4(x, h(x)) = w_4(x, h(x)) = 0. \quad (4.65)$$

The boundary conditions for temperature are as follows: At $z = 0$ the temperature is assumed to be a constant, and at $z = h(x)$ we assume a constant flux. Thus

$$T = T_p \quad \text{on} \quad z = 0 \quad \text{and} \quad T_z = -\eta \quad \text{on} \quad z = h(x). \quad (4.66)$$

Here η denotes the temperature difference between the plane formed by the pupil aperture and the iris, T_p and the cornea, T_c divided by the typical depth of the anterior chamber, $\frac{(T_p - T_c)}{h_\circ}$. This set of boundary conditions completes the problem. We now aim to determine the pressure in each region. By assuming that the fluxes and the pressures at each point x are continuous, the pressure is known and is equal to the constant pressure $p = p_a$ at $x = a$. The boundary conditions for the pressure are given

by,

$$\int_{d(x)}^{h(x)} u_1 dz = 0, \quad \int_0^{d(x)} u_2 dz = 0, \quad \int_0^{h(x)} u_3 dz = 0, \quad \int_0^{h(x)} u_4 dz = 0, \quad (4.67)$$

and

$$p_3(-b) = p_1(-b), \quad p_3(-b) = p_2(-b), \quad p_4(b) = p_2(b), \quad p_4(a) = p_a. \quad (4.68)$$

4.7.2 Solution Procedures

By solving the system of equations (4.58) - (4.60) subject to the boundary conditions given in equations (4.62) - (4.68), the exact solution in each region may be determined. The temperature given by equation (4.61), may be solved subject to the boundary condition, equation (4.66), to yield,

$$T(z) = T_p - \eta z, \quad (4.69)$$

where $\eta = \frac{(T_p - T_c)}{h_o}$. We shall now consider the individual regions.

Region (1)

Equation (4.59) shows that pressure, p_1 in Region (1), only depends on x i.e. $p_1 = p_1(x)$. By substituting equation (4.69) into equation (4.58) and we find that,

$$u_{1zz} = \frac{p_{1x}}{\rho_o v} - \frac{g}{v} [1 - \alpha (T_p - T_c - \eta z)].$$

The equation above can be integrated twice with respect to z and can be solved using the boundary condition given in equation (4.62). Hence we obtain

$$u_1 = \frac{p_{1x}}{2\rho_o v} (z - h)(z - d) - \frac{g}{2v} [(1 - \alpha (T_p - T_c))(z - h)(z - d) + \frac{\alpha\eta}{3}(z - h)(z - d)(z + d + h)]. \quad (4.70)$$

We differentiate equation (4.70) with respect to x and substitute the equation into equation (4.60), to give

$$w_{1z} = -\frac{1}{2\rho_o v} [p_{1x}(z - h)(z - d)]_x + \frac{g}{2v} [(1 - \alpha (T_p - T_c))(-h_x(z - d) - d_x(z - h)) + \frac{\alpha\eta}{3} [(dh^2 + hd^2)_x - z(h^2 + hd + d^2)_x]].$$

We then solve the above equation above subject to the boundary condition in equation

(4.62), such that

$$\begin{aligned} w_1 = & -\frac{1}{12\rho_o v} \left[p_{1x}(z-d)^2 (2z+d-3h) \right]_x \\ & + \frac{g}{4v} [(1-\alpha(T_p-T_c))(z-d) \{-h_x(z-d)-d_x(z+d-2h)\} \\ & + \frac{\alpha\eta}{3}(z-d)\{-2[dh^2+hd^2]_x(z+d)[h^2+hd+d^2]_x\}] . \end{aligned} \quad (4.71)$$

By substituting the boundary condition in equation (4.62) which is $w_1(x, z=d(x))=0$ into equation (4.71), we get

$$p_{1x} = g\rho_o \left[1 - \alpha(T_p - T_c) + \frac{\alpha\eta}{2}(h+d) \right] + \frac{A_1}{(h-d)^3}, \quad (4.72)$$

where A_1 is an arbitrary constant. If we now substitute equation (4.72) and equation (4.70) into the boundary condition in equation (4.67), for u_1 we determine that $A_1 = 0$. Equation (4.72) thus becomes

$$p_{1x} = g\rho_o \left[1 - \alpha(T_p - T_c) + \frac{\alpha\eta}{2}(h+d) \right]. \quad (4.73)$$

Defining a stream function in this region, $\psi_1(x, z)$ by $u_1 = \psi_{1z}$ and $w_1 = -\psi_{1x}$, we thereby obtain,

$$\begin{aligned} \psi_1(x, z) = & \frac{p_{1x}}{12\rho_o v} (z-d)^2 (2z+d-3h) - \frac{g}{12v} \left[(1-\alpha(T_p-T_c))(z-d)^2 \cdot \right. \\ & \left. (2z+d-3h) + \frac{\alpha\eta}{2}(z-d)^2 (d^2-2dh+2dz-2h^2+z^2) \right]. \end{aligned} \quad (4.74)$$

Region (2)

We shall now determine the velocities in the x and z directions within this region by solving equations (4.58) - (4.60) subject to the boundary conditions given in equation (4.63). These are,

$$u_2 = \frac{p_{2x}}{2\rho_o v} z(z-d) - \frac{g}{2v} \left[z(z-d)(1-\alpha(T_p-T_c)) + \frac{\alpha\eta}{3} z(z^2-d^2) \right], \quad (4.75)$$

$$w_2 = -\frac{1}{2\rho_o v} \left[p_{2x} \left(\frac{z^3}{3} - \frac{dz^2}{2} \right) \right]_x - \frac{g}{2v} \left[\frac{d_x z^2}{2} (1-\alpha(T_p-T_c)) + \frac{\alpha\eta}{3} d d_x z^2 \right]. \quad (4.76)$$

At $z = d(x)$ and $w_2 = 0$, we find that,

$$p_{2x} = g\rho_o \left[1 - \alpha(T_p - T_c) + \frac{\alpha\eta}{2}d \right] - \frac{A_2}{d^3}.$$

Here A_2 is an arbitrary constant. We can determine A_2 by substituting equation (4.75) and the equation above into the boundary condition for u_2 and hence obtain $A_2 = 0$. Therefore,

$$p_{2x} = g\rho_o \left[1 - \alpha(T_p - T_c) + \frac{\alpha\eta}{2}d \right]. \quad (4.77)$$

By substituting equations (4.75) and (4.76) into the equations $u_2 = \psi_{2z}$ and $w_2 = -\psi_{2x}$, we obtain the streamline in Region (2), where,

$$\psi_2 = \frac{p_{2x}}{2\rho_0 v} \left(\frac{z^3}{3} - \frac{dz^2}{2} \right) - \frac{g}{2v} \left[\left(\frac{z^3}{3} - \frac{dz^2}{2} \right) (1 - \alpha(T_p - T_c)) + \frac{\alpha\eta}{3} \left(\frac{z^4}{4} - \frac{d^2 z^2}{2} \right) \right]. \quad (4.78)$$

Region (3)

Following an analogous method to that used above, the exact solutions in Region (3) take the form,

$$u_3 = \frac{p_{3x}}{2\rho_0 v} z(z-h) - \frac{g}{2v} \left(z(z-h)(1 - \alpha(T_p - T_c)) + \frac{\alpha\eta}{3} z(z^2 - h^2) \right),$$

$$w_3 = -\frac{1}{2\rho_0 v} \left[p_{3x} \left(\frac{z^3}{3} - \frac{hz^2}{2} \right) \right]_x - \frac{g}{2v} \left[\frac{h_x z^2}{2} (1 - \alpha(T_p - T_c)) + \frac{\alpha\eta}{3} h h_x z^2 \right].$$

The differential equation for the pressure gradient that respect to x is:

$$p_{3x} = g\rho_0 \left[1 - \alpha(T_p - T_c) + \frac{\alpha\eta}{2} h \right]. \quad (4.79)$$

The streamline in Region (3) is,

$$\psi_3 = \frac{p_{3x}}{2\rho_0 v} \left[\frac{z^3}{3} - \frac{hz^2}{2} \right] - \frac{g}{2v} \left[\left(\frac{z^3}{3} - \frac{hz^2}{2} \right) (1 - \alpha(T_p - T_c)) + \frac{\alpha\eta}{3} \left\{ \frac{z^4}{4} - \frac{h^2 z^2}{2} \right\} \right]. \quad (4.80)$$

Region (4)

In Region (4), we obtain that the exact solutions are almost the same as in Region (3). These are,

$$u_4 = \frac{p_{4x}}{2\rho_0 v} z(z-h) - \frac{g}{2v} \left(z(z-h)(1 - \alpha(T_p - T_c)) + \frac{\alpha\eta}{3} z(z^2 - h^2) \right),$$

$$w_4 = -\frac{1}{2\rho_0 v} \left[p_{4x} \left(\frac{z^3}{3} - \frac{hz^2}{2} \right) \right]_x - \frac{g}{2v} \left[\frac{h_x z^2}{2} (1 - \alpha(T_p - T_c)) + \frac{\alpha\eta}{3} h h_x z^2 \right].$$

$$p_{4x} = g\rho_0 \left[1 - \alpha(T_p - T_c) + \frac{\alpha\eta}{2} h \right]. \quad (4.81)$$

$$\psi_4 = \frac{p_{4x}}{2\rho_0 v} \left[\frac{z^3}{3} - \frac{hz^2}{2} \right] - \frac{g}{2v} \left[\left(\frac{z^3}{3} - \frac{hz^2}{2} \right) (1 - \alpha(T_p - T_c)) + \frac{\alpha\eta}{3} \left\{ \frac{z^4}{4} - \frac{h^2 z^2}{2} \right\} \right]. \quad (4.82)$$

The pressure gradient in each region will now be determined by solving the equations (4.73), (4.77), (4.79) and (4.81) subject to the boundary conditions given in equation (4.68). We thus obtain,

$$p_1(x) = p_a + g\rho_0 \left[(1 - \alpha(T_p - T_c))(x-a) + \frac{\alpha\eta}{2} \{ H(x) + D(x) + H(b) - H(a) - H(-b) - D(b) \} \right], \quad (4.83)$$

$$\begin{aligned}
p_2(x) &= p_a + g\rho_o \left[(1 - \alpha(T_p - T_c))(x - a) + \frac{\alpha\eta}{2} \{D(x) - D(b) + H(b) - H(a)\} \right] \\
p_3(x) &= p_a + g\rho_o \left[(1 - \alpha(T_p - T_c))(x - a) + \frac{\alpha\eta}{2} \{H(x) + D(-b) - D(b) + H(b) - H(a) - H(-b)\} \right] \\
p_4(x) &= p_a + g\rho_o \left[(1 - \alpha(T_p - T_c))(x - a) + \frac{\alpha\eta}{2} \{H(x) - H(a)\} \right].
\end{aligned} \tag{4.84}$$

where,

$$D(x) = \int d(x) dx \text{ and } H(x) = \int h(x) dx.$$

Note that the pressure gradient in Region (1) and Region (2) given in equation (4.83) and equation (4.84) may be used to find the pressure difference across the DMD and hence to analyse the deformation of the DMD.

4.7.3 Analytical Results and Simulations

Using typical parameter values for the human eye given in Section 4.5 and assuming that the cornea surface is defined by $h(x) = h_o \left(1 - \frac{x^2}{a^2}\right)^{\frac{1}{2}}$, we can analyse the relevant fluid flow equations both analytically and numerically. The streamline equations (4.74), (4.78), (4.80) and (4.82) may now be plotted in Figure 4.12a and Figure 4.13a by considering different locations of the Descemet membrane tear. The black and grey contours show the streamlines associated with the flow that determined by the velocities in x and z directions in each region. As noted before, the streamlines plots that in Figure 4.12a and Figure 4.13a also do not join perfectly at region boundaries. This is because these calculations are based on the lubrication theory limit of Navier-Stokes equations and it has been examined separately in four separate regions.

Numerical simulations of flow driven by buoyancy effects in the anterior chamber, *i.e* the dome-shaped region, during DMD have been studied using COMSOL Multiphysics software, [72] (see Figure 4.12b and Figure 4.13b). Both analytical and numerical results are due to the assumptions that the buoyancy effects are present because of the temperature difference between the anterior surface of the cornea and the plane formed by the pupil aperture; the orientation of the human eye such that gravity is acting horizontally to the right and the aqueous humour flow from the pupil aperture through the anterior chamber has been neglected.

The analytical results show the flow streamlines agree both qualitatively and quantitatively with the numerical results. As we can see from Figures 4.12 and 4.13, the flow streamlines for the flow in Region (1) (which is the region between the cornea surface and the DMD) differ. Figures 4.12a and 4.13a show that flow in Region (1) are able to “turn the corner”. While Figures 4.12b and 4.13b do not present Moffatt vortices in Region (1) and this is due to the lubrication theory limit, where the fluid circulation

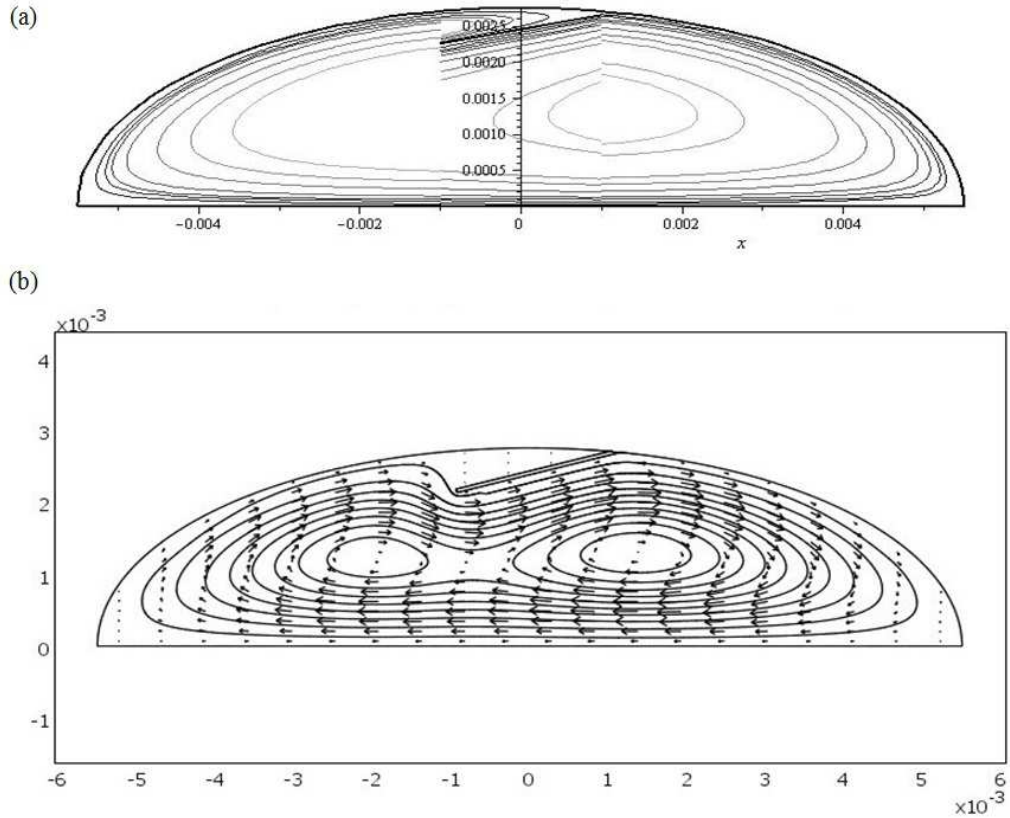


FIGURE 4.12: Streamlines for buoyancy-driven flow in the anterior chamber around a DMD in the plane $y = 0$. Gravity is assumed to be acting horizontally to the right. The function selected for the detached Descemet membrane is considered to be $d(x) = 0.2x + 0.002455$ over the interval $[-0.001, 0.001]$, whereas the function for the corneal shape is assumed to be $h(x) = h_0 \left(1 - \frac{x^2}{a^2}\right)^{\frac{1}{2}}$. The temperature gradient between the cornea, T_c and the plane formed by pupil aperture and the iris, T_p is given by $T_p - T_c = 2$. The typical values for a human eye given in equation (4.9) are employed in these graph: (a) Streamlines given in equations (4.74), (4.78), (4.80) and (4.82) are combined in one plot using Maple [8]; (b) Numerical simulation for streamlines, arrow and surface velocity field are carried out using COMSOL Multiphysics [72].

has induced movement of fluid in and out of the region between the cornea surface and the DMD. In reality, the flow between the cornea surface and the DMD is slow and we expect to observe Moffatt vortices (see [92]). Figure 4.14 shows a magnification of COMSOL streamline plots (Figure 4.12b and Figure 4.13b) for the flow in Region (1). In Figure 4.14 we can see that Moffatt vortices are clearly present and this result convince that the flow in the region between the cornea surface and the DMD are extremely weak. However both analytical and numerical results show the value of velocity field at any given point in Region (1) (for example at $(0, 0.0026)$, the velocity field given by analytical result is $1.3095 \times 10^{-7} \text{ ms}^{-1}$ and numerical result is $1.6325 \times 10^{-7} \text{ ms}^{-1}$) are very close to each other.

The aqueous humour flow circulation in the anterior chamber presented in Figure 4.13

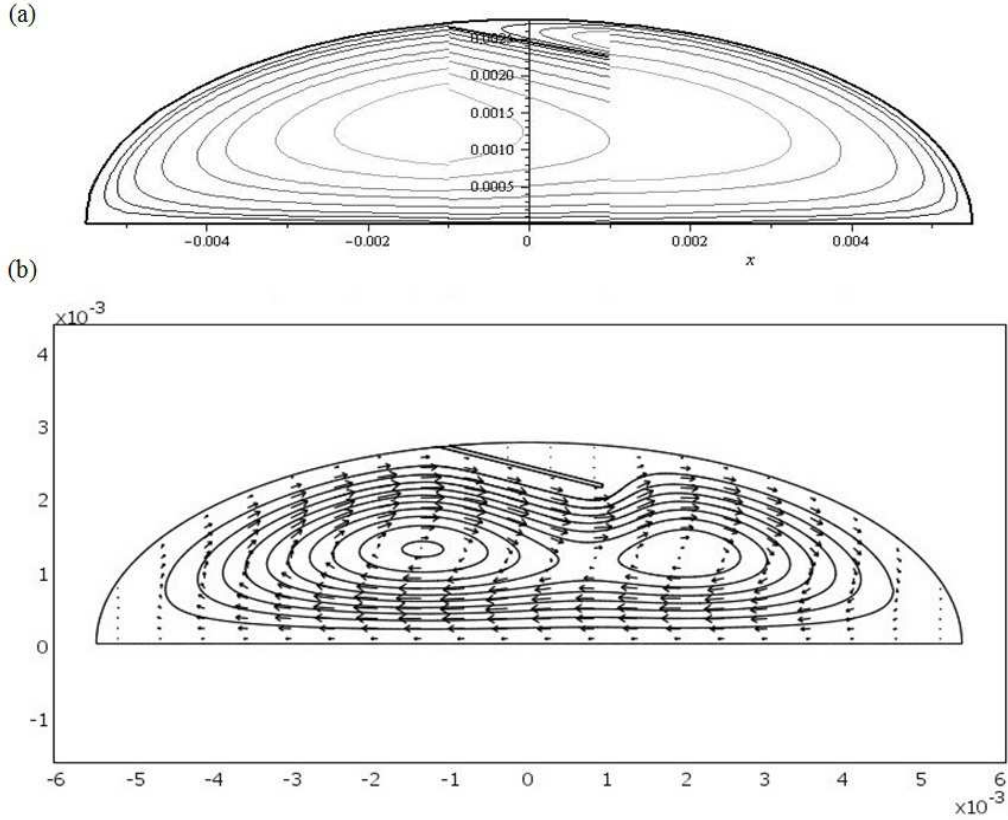


FIGURE 4.13: Streamlines for buoyancy-driven flow in the anterior chamber around a DMD in the plane $y = 0$, when gravity is pointing from left to right. The same conditions and parameter values applied in Figure 4.12 have been employed in the production of this comparison figure. The DMD equation is given by $d(x) = -0.2x + 0.002455$ over the interval $[-0.001, 0.001]$.

agrees qualitatively with the proposed mechanism for spontaneous Descemet membrane reattachment, as noted in [76]. Our results, see Figure 4.13, have shown that under the correct conditions, the location of the Descemet membrane tear and the orientation of the human eye must be carefully controlled. Thus spontaneous reattachment may indeed occur. By choosing a different location of the Descemet membrane tear, as in Figure 4.12, the flow behaviour shows the Descemet membrane may separate from the stroma and eventually worsening of the DMD may occur. For further details regarding this problem, see [93].

4.7.4 DMD Equations

To close the model, we must analyse the deformation of the DMD in the anterior chamber by considering the DMD. The DMD is assumed to be elastic and deformable so the general theory of beams under axial loading is applied. Using asymptotic analysis as shown in Section 4.6.3, the deformation of the DMD has been examined. Equations that describe the deflection of DMD at some position x , subject to the different pressure

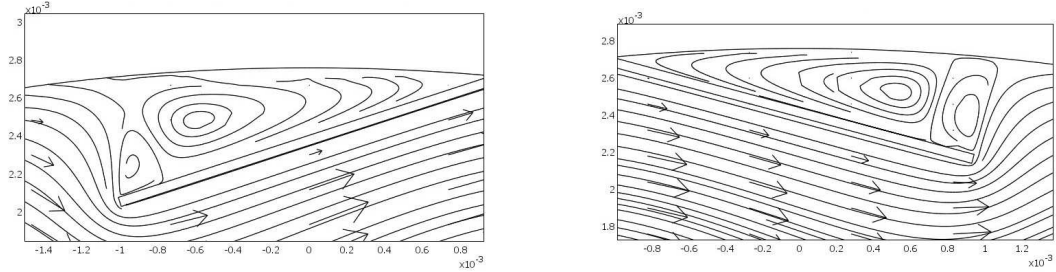


FIGURE 4.14: Magnification of numerical predictions for the flow in the region between the cornea surface and the DMD presenting Moffatt vortices.

gradient between Region (1) and Region (2) can now be formulated by substituting equations (4.83) and (4.84) into equation (4.47). The non-dimensional form of this is

$$d_{xxxx} = \beta \left(x - \frac{x^3}{3} \right) \quad \text{where} \quad \beta = \frac{g\rho_o\alpha\eta h_o b^7}{2EIa^2 d_o}, \quad (4.85)$$

subject to the boundary conditions that consider the DMD is assumed to be clamped at $x = b$ and free at $x = -b$. The boundary conditions may be expressed by,

$$d(1) = 0, \quad d_x(1) = -1, \quad d_{xx}(-1) = 0, \quad d_{xxx}(-1) = 0.$$

The DMD equation, (4.85), can be solved subject to the boundary conditions above, by using a classical fluid mechanics approach, such as in equation (4.54). We examine the clamped end case with constant angle inclination at one end and the other end is free, for further details see Section 4.6.3. Here the steady solution is

$$d(x) = 1 - x + \beta \left(-\frac{x^7}{2520} + \frac{x^5}{120} - \frac{5x^3}{72} - \frac{2x^2}{15} + \frac{157x}{360} - \frac{76}{315} \right) + O(\beta^2). \quad (4.86)$$

Equation (4.86) may now be plotted, see Figure 4.15 and Figure 4.16 in order to examine the deformation of the DMD for different values of β . Figure 4.15 shows the deformation of the DMD, $d(x)$ for different negative values of β . It shows that when the value of β increases then the deformation of d decreases. Physically this is because the pressure difference increases so it will cause the Descemet membrane to separate from the stroma and eventually the DMD may be come further detached. Figure 4.16 presents the deformation of the DMD for different positive values of β . This figure shows that when the value of β increases then d becomes much less deflected. A detached Descemet membrane, d bends down more at the free end because the other end is fixed.

4.8 Conclusions and Further Work

The modelling of buoyancy-driven flow inside the anterior chamber during DMD has been developed. The buoyancy mechanism has been chosen due to the existing tem-

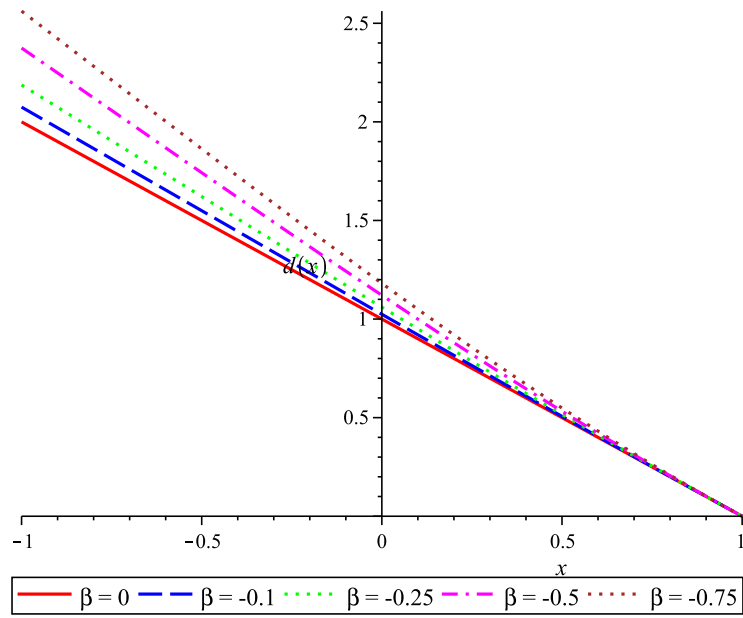


FIGURE 4.15: The deformation of the detached Descemet membrane given in equation (4.86) for different negative values of $\beta = \frac{g\rho_0\alpha\eta h_0 b^7}{2EIa^2d_0}$. The solid red line denotes the DMD when β is equal to zero, whereas the dashed blue line, the dotted green line, the dashed-dotted magenta line and the dotted brown line represent the corresponding DMD for β equal to -0.1, -0.25, -0.5 and -0.75.

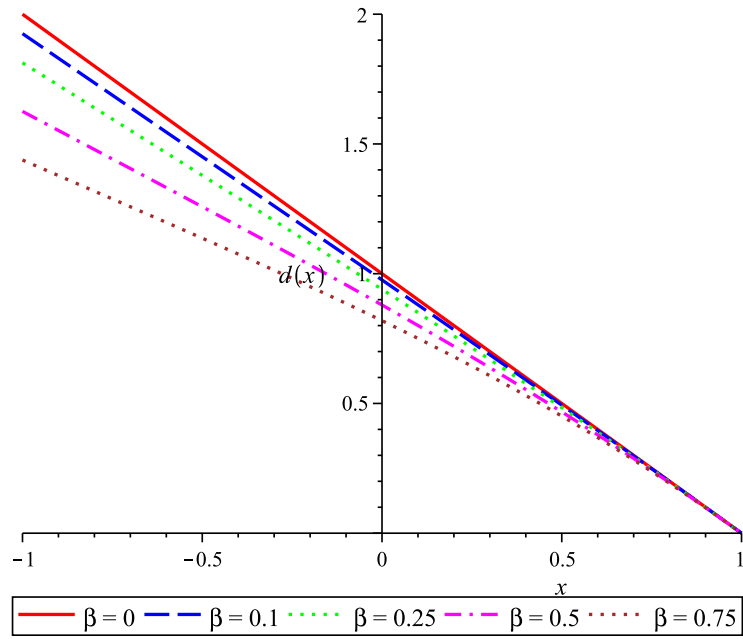


FIGURE 4.16: The deformation of the detached Descemet membrane given in equation (4.86) at different positive values of β . The solid red line represents the detached Descemet membrane at $\beta = 0$, whereas the dashed blue, the dotted green, the dashed-dotted magenta and the dotted brown lines are associated with $\beta = 0.1$, $\beta = 0.25$, $\beta = 0.5$ and $\beta = 0.75$ respectively.

perature difference between the front and the back of the anterior chamber, and this mechanism has been reported in [75] and [78] to be the dominant flow compared to the various mechanisms that drive the flow of aqueous humour in the anterior chamber. In this study, the fluid mechanical model of flow in the anterior chamber developed in [75] has been applied. By using COMSOL Multiphysics [72] we have compared and shown that our numerical simulation result was qualitatively in agreement with the analytical result from [75]. Then we modified the fluid mechanical model by changing the boundary condition for the temperature at the cornea to be a constant flux and also including the presence of a detached Descemet membrane in the flow.

The first model considered in this chapter consisted of fluid flow in the rectangular-shaped region in the presence of a thin, small flap that was kept in contact with the bottom plane. The flap was assumed to be elastic and deformable, and then we applied the general theory of beam bending. In this simple geometry, we found that there was a very small velocity under the flap. The results of the flow streamlines in this study were shown to have good agreement with the numerical results. In this study we determined the pressure difference the above and the below flap, which is important in order to analyse the deformation of the flap. The results obtained from this paradigm study show that we should proceed with a more realistic case.

The second model concerned a more realistic geometry shaped, *i.e* a dome, to improve the first model and to explain how and why either the spontaneous reattachment (as stated in [76]) or redetachment of Descemet membrane happens using fluid mechanical models of flow in the anterior chamber. Both our analytical and simulation results have shown that it is possible to predict the flow around a detached Descemet membrane in the anterior chamber of a human eye. The simulation results provided independent verification that the exact solutions that were used were accurate, and the exact solutions allowed a detailed consideration to be given of the pressures that act on different location of the detached Descemet membrane in the presence of buoyancy effects. Consequently, these results presented that there are fluid mechanical reasons that encouraging either spontaneous reattachment or worsening of the detached Descemet membrane, and clearly explained the results presented in the [76]. In this second model, the most important conclusion is that different treatment approaches should be used for the sort of DMD (*i.e* which way it goes). Under the correct conditions, such as given the location of the detachment and carefully controlled the orientation of the patient eye, thus spontaneous resolution of Descemet membrane detachment may indeed occur. The results shown in Figures 4.12 and 4.13 quantify the circumstances under which either patient positioning or the application of hot or cold eye patches (depending on the sleeping posture and the details of the detachment) may encourage a DMD to spontaneously reattach. For further explanations on influences of buoyancy-driven flow on DMD reattachment and redetachment, refer to our paper [93].

The model could be improved to take into account three-dimensional DMD shapes, but

that would make things a lot more complicated. [75] has been explained that when gravity and buoyancy are the only causal factors of flow in the anterior chamber, flow takes place in slices parallel to the direction of gravity. So the problem is essentially two dimensional. The simplified two-dimensional shape studied here was straight forward and this work ease for visualising and examining. This two-dimensional model shows that we could easily calculate the solutions analytically, and also showed good comparisons with the numerical simulation results under reasonable conditions. We could also explain the behaviour of aqueous humour flow in the anterior chamber around a detached Descemet membrane and suggest some non surgical approaches for DMD treatments. The other alternative can be carried out for further work by considering the other mechanisms that drive the aqueous humour flow in the anterior chamber such as rapid eye movement during sleep, phakodenesis and flow from the ciliary body through the pupil aperture. Besides that, it would be possible to apply the methods that have been developed to study other problem such as some treatments for eye conditions that involve internally floating drugs.

Chapter 5

Modelling of Tonometry and Scleral Buckling

5.1 Introduction

The accurate measurement of intraocular pressure is important for the treatment of patients with glaucoma. Ophthalmologists require an accurate and reliable method to measure the intraocular pressure level in order to detect glaucoma and determine the best treatment for the patient. Therefore tonometry is used to measure the intraocular pressure in the human eye. Several tonometers have been made based on the classic measurement technique of Goldmann applanation tonometry, until the recent measurement method of rebound tonometry was introduced. Neither mathematical nor engineering principles have been able to validate the accuracy of these measurements. This chapter includes a brief introduction on the anatomy and physiology of the outer layer of the eyeball, intraocular pressure and the devices for measuring intraocular pressure. The derivation of the governing equations will be given using the membrane theory of shells in spherical coordinates for a linearly elastic material. We will then develop a mathematical model of the eyeball membrane and numerically examine the shape of the eyeball membrane under various loading conditions due to the tonometer and a scleral buckle.

5.2 Anatomy and Physiology of the Eyeball

The human eye essentially consists of three layers. The outermost layer is made up of the sclera and the cornea (see Figure 5.1). The sclera maintains the eyeball's shape and protects the eye from both internal and external forces. The primary function of the cornea is to refract, transmit and focus the light onto the lens and the retina. The

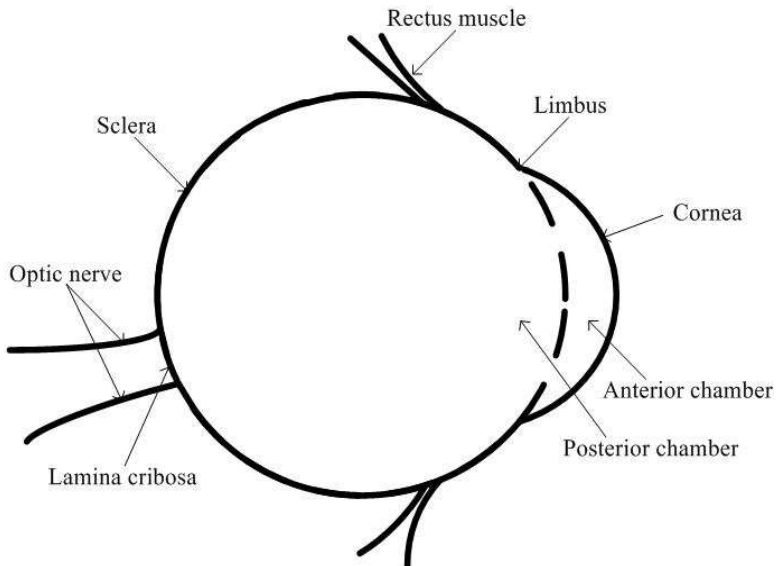


FIGURE 5.1: The diagram of the eyeball.

cornea also helps to protect the eye against infection and structural damage to the inner layers. The middle layer of the eyeball is composed of the choroid, the ciliary body and the iris. The innermost layer is the retina, a complex layered structure of neurons that is responsible for vision [99].

The human eyeball is approximately a sphere 25mm in diameter with a volume of 6.5ml. In real life, the eyeball differs slightly from a sphere. It may be conveniently thought to be composed of two spheres. The larger sphere is the sclera, which forms five-sixths of the circumference of the eyeball and has a radius of 11.5mm. The remaining one-sixth of the circumference of the eyeball is formed by the cornea. The cornea has a higher curvature than the sclera with a radius of curvature of about 7.8mm. The axial length of the eyeball varies between individuals and lies in the range 21mm to 26mm. However the average axial length is approximately 24mm. The diameter and the horizontal length of the eyeball are approximately 23mm and 23.5mm. The area that connects the edge of the cornea and the opaque sclera is known as the limbus or corneascleral junction [98], Figure 5.1.

Both the cornea and the sclera form the opaque strong fibrous outer layer of the eye, that acts as a shield to protect the ocular tissues from injury. The sclera is an important structural support for attachment of extraocular muscles, which allow the eye to move. It also protects the intraocular contents and keeps the shape of the eyeball even during contraction of the extraocular muscles and distension when the intraocular pressure increases [98, 115]. The sclera exhibits visco elastic behaviour with high tensile strength, rigid extensibility and high flexibility that provides limited movement and relatively constant conditions. Thus when the eyeball is moved the IOP does not fluctuate and

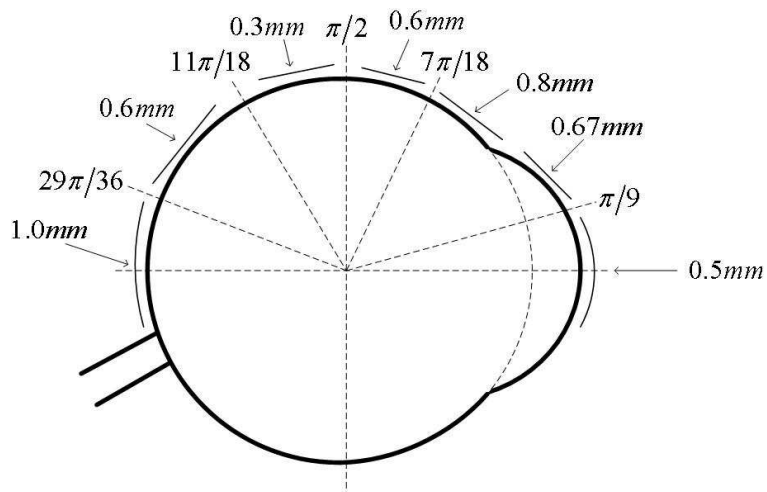


FIGURE 5.2: The eyeball thickness distribution.

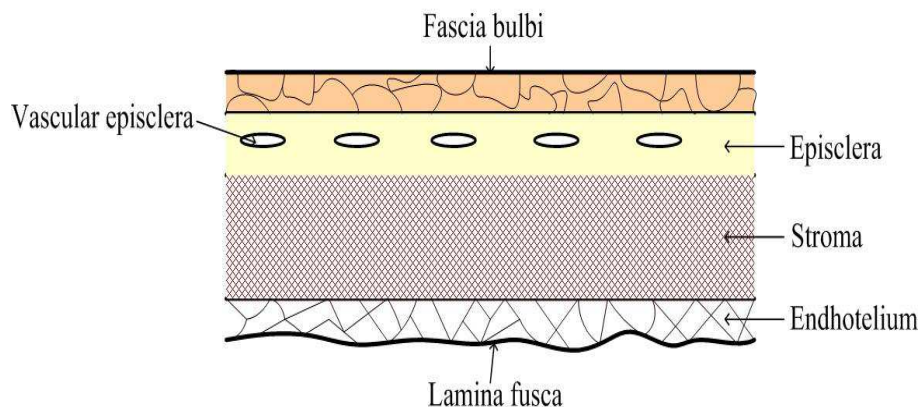


FIGURE 5.3: The structure of the sclera.

adversely affect vision [98, 115].

A typical thickness distribution of the human eyeball can be summarised as shown in Figure 5.2. The thickness of the human sclera is not uniform and it can vary from being as thick as 1.35mm at the posterior pole (near the optic nerve) to 0.4mm under the recti muscles. From the posterior pole the sclera thickness decreases gradually to between 0.4mm - 0.6mm at the equator [98, 115, 116, 117], and then after the recti muscle gradually increases in thickness up to 0.8mm near the limbus [115, 117]. From the limbus to the centre of the cornea, the thickness gradually decreases to 0.5mm [117].

The cornea is composed of five layers: the corneal epithelium, the Bowman's layer, the stroma, the Descemet's membrane and the endothelium, see Section 4.2 for further details. From the outer to the innermost, there are four layers of the sclera, these are the episclera, the stroma, the lamina fusca and the endothelium, see Figure 5.3. The stroma is a layer of collagen fibres that runs continuously through the sclera and the cornea,

keeping the eyeball bound together. The outermost layer of the sclera, the episclera, is covered by the fascia bulbi, also known as Tenon's capsule [98]. The episclera has been recognised as a distinct hypocellular layer of radially-arranged compact collagen bundles running parallel to the sclera surface and it is important in being a muscle pulley for the extraocular muscles [115]. The episclera is a thin layer of dense vascular connective tissue, near the limbus, which is under tension and progressively reduces in tissue density towards the equator. It lies between the fascia bulbi and the superficial scleral stroma. The bundles of collagen fibrils in the episclera are larger than the fascia bulbi and circumferentially arranged with tight attachments to the walls of the blood vessels. This prevents the independent movement over the sclera.

The scleral stroma is a thicker layer than the other layer of the sclera. The strength, toughness and resilience of the scleral stroma is determined by the structure and organisation of the collagen fibrils within superficial sites, grouped into dense superimposed lamellae, which comprise the eyeball. The collagen organisation provides the sclera with considerable visco-elastic properties. [115] explained that an indentation of the stroma may cause a rapid lengthening of the collagen. The visco-elastic properties of the sclera are important in protecting the eye from injury during transient elevations of IOP [115]. The endothelium is the innermost layer of the scleral structure. Like the cornea, the sclera also has an endothelium layer that rests on the lamina fusca, and contains pigment cells at a high density. The sclera meets the cornea at the limbus, and at the optic nerve at the region known as the lamina cribrosa [98]. [98] listed several functions of the limbus, these included providing nourishment to the peripheral cornea, healing the wound of the corneal and hypersensitivity responses. The limbus also contains the aqueous humour outflow pathways, which indirectly control the intraocular pressure. The lamina cribrosa forms a pressure barrier between the intraocular space and retrobulbar space.

Material properties of the cornea and the sclera are important for maintaining the shape of the eye. [118] and [119] agreed that the material and the anatomical properties (Young's modulus, Poisson's ratio, thickness and radius) of the sclera and the cornea are the main features in determining the biomechanical environment within the eye. A range of material parameter values have been reported in previous studies and are summarised in Table 5.1. We note from this table that there is by no means unanimity regarding the values reported. In fact we conclude from the table that the values for E_s and E_c vary hugely in various different previous studies. Note also that in measuring the Young's modulus Poisson's ratio an implicit assumption of linear elasticity is being made. We will see later that this is a crucial matter in the modelling of tonometry.

Parameters	Values	Ref.
a	$1.25 \times 10^{-2}m$	[98].
	$1.15 \times 10^{-2}m$	[104].
a_c	$7.8 \times 10^{-2}m$	[120], [117], [98].
a_s	$1.15 \times 10^{-2}m$	[98].
α_c in the centre	$5.2 \times 10^{-4}m$	[98].
	$5.0 \times 10^{-4}m$	[121].
α_c at the periphery	$6.7 \times 10^{-4}m$	[98].
	$7.5 \times 10^{-4}m$	[121].
α_s at the posterior pole	$1.0 \times 10^{-3}m$	[98], [117].
	$1.0 \times 10^{-3}m - 1.35 \times 10^{-3}m$	[115].
α_s under the recti muscle	$3.0 \times 10^{-4}m - 4.0 \times 10^{-4}m$	[98].
	$3.0 \times 10^{-4}m$	[115], [117].
	$4.0 \times 10^{-4}m - 8.0 \times 10^{-4}m$	[98].
α_s towards the limbus	$6.0 \times 10^{-4}m - 8.0 \times 10^{-4}m$	[115], [117].
	$(3.9 \times 10^{-4}m \pm 1.7 \times 10^{-4}m) -$	[116].
	$(5.3 \times 10^{-4}m \pm 1.4 \times 10^{-4}m)$	
α_s near the optic nerve	$9.0 \times 10^{-4}m - 1.0 \times 10^{-3}m$	[116].
ν	0.46 - 0.5	[122].
	0.47	[117].
	0.49	[123].
	0.42	[117].
E_s	4.76MPa	[122].
	5.5MPa	[123], [124].
	1.8MPa - 2.9Mpa	[125].
E_c	0.19MPa	[120].
	0.026MPa	[126].
	9.03MPa	[127].
	57MPa	[128].
	0.2MPa, 1.2Mpa, 10MPa	[129].

TABLE 5.1: Summary of material parameters values for the cornea and the sclera from the previous studies showing: radius of the human eye (a), central corneal radius of curvature (a_c), radius of curvature of the equatorial sclera (a_s), cornea thickness (α_c), scleral thickness (α_s), corneal Young's modulus (E_c), scleral Young's modulus (E_s), Poisson's ratio of the cornea (ν_c) and Poisson's ratio of the sclera (ν_s).

5.3 Measurement of the Intraocular Pressure (IOP)

Ophthalmologists define intraocular pressure to be the difference between the pressure inside a human eye and atmospheric pressure. Normal intraocular pressure in a healthy human eye lies in the range 10mmHg to 20mmHg. Intraocular pressure that is consistently above 21mmHg indicates ocular hypertension. High levels of intraocular pressure may indicate glaucoma which is a serious disease that causes damage to the optic nerve. If the level of intraocular pressure rapidly increases to 50mmHg and above, then it will rapidly lead to permanent blindness. Low intraocular pressure, less than or equal to 5mmHg, also may cause ocular hypotony. This usually occurs as a complication to an underlying ocular disorder, trauma or surgery. Low intraocular pressure usually is a sign of fluid leakage. When the intraocular pressure is too low it can cause several distortions of the retina, lens and cornea that can reduce vision.

The level of intraocular pressure may rapidly increase or decrease due to external influences such as direct pressure on the eye, *i.e.* tightly closed lids or by a finger, or a change in body position. A small variation in intraocular pressure at low pressure results from physical activity, stress, rapid fluid intake and even caffeine. High intraocular pressure can occur in the human eye due to a build up of aqueous humour. The aqueous humour is continually being produced by the ciliary body, however if the drainage system is not functioning well, the aqueous humour cannot drain out normally. In this situation, excessive aqueous humour is produced and the intraocular pressure within the eye builds up, see Chapter 2 for details.

There are three main methods for measuring the intraocular pressure, these are: palpation, manometry and tonometry. Palpation (which simply consists of a medical professional feeling a patient's eyeball) is the oldest, simplest, least expensive and least accurate method of estimating intraocular pressure. It is the only practicable technique in patients who are unwilling to undergo the other methods of intraocular pressure measurement [1, 100]. Manometry (taking a direct pressure measurement of the eye using a manometer) is not suitable for continuous noninvasive intraocular pressure measurement. [1] pointed out that using manometry would necessitate penetrating the eye with a cannula and this is impossible in practice. However manometry remains a useful instrument in measuring pressure in the laboratory [101]. Thus several types of device known as tonometers have been developed for determining an accurate measurement of the intraocular pressure with the least disturbance to the eye. Tonometers are the instruments for performing tonometry. Indentation, applanation and rebound are the main physical principles of tonometers that are applicable in clinical practise today [100].



FIGURE 5.4: The indentation (Schiotz) tonometer in 1905. This figure was extracted from [158].

5.3.1 The Indentation (Schiotz) Tonometer

Hjalmar Schiotz developed a tonometer in 1905 and demonstrated his tonometer in the Norwegian Medical Society [100]. The indentation (Schiotz) tonometer (see Figure 5.4) measures the amount of corneal indentation that occurs when a given weight is placed on the cornea. It uses a plunger to gently push the surface of the cornea [1, 100]. The plunger rides inside a metal cylinder that is attached to a footplate, curved to match the curvature of the average human cornea. The plunger indents the cornea until the ocular resistance stops it. For each 0.05mm that the plunger sinks under the level of the footplate, a pointer moves up one scale unit. The unit is then converted into mmHg using the tables of Schiotz scale reading [1]. The relationship between the corneal indentation and the intraocular pressure on the area of indentation has been given as $W = p \times A$ where W is the downward force of the plunger (gN), p is the intraocular pressure (gNcm^{-2}) and A is the cross section area of the plunger indentation (cm^2) [102].

5.3.2 The Goldmann Applanation Tonometer

In 1888, Fick invented a tonometer that maintained a fixed area of applanation. The intraocular pressure was measured by adjusting the force necessary to flatten an area of the cornea. However, significant skill was required to obtain accurate and reproducible tonometer readings until Goldmann published and developed the tonometer in 1955 [100]. In most areas of the world the Goldmann applanation tonometer (see Figure 5.5) remains the most widely used instrument to measure intraocular pressure. It is considered the current “gold standard” for intraocular pressure measurement [1, 100, 103, 104]. The Imbert-Fick law states that IOP is equal to the force, F_c per



FIGURE 5.5: The Goldmann Applanation tonometer. This figure was extracted from [157].

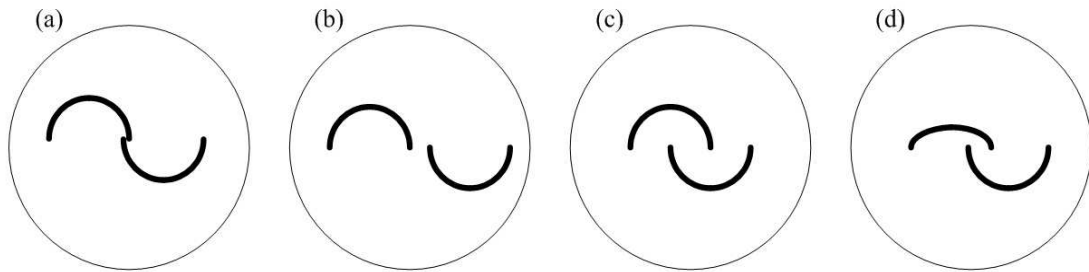


FIGURE 5.6: Schematic represent a variety of appearances of the meniscus semicircles through the Goldmann applanation prism.

unit area of applanation, A , for a spherical container which is assumed to be infinitely thin, dry and perfectly elastic [103, 104]. This law can be written as

$$IOP = \frac{F_c}{A}.$$

The Goldmann applanation tonometer probe is a plastic cylinder, 7mm in diameter, that has been attached to a spring-loaded arm. It is then pushed forward slowly until the prism rests gently on the centre of the cornea and the cornea applanates to the standard area, $7.35 \times 10^{-6} m^2$. The prism within the cylinder, viewed using a slit lamp, is seen as two semicircles, one above the other (see Figure 5.6). These semicircles form an uninterrupted letter **S** and the intraocular pressure is derived from the applied force [1]. In an ideal case the desired applanation area and the uninterrupted letter **S** will occur at the same force. However this does not always occur. Therefore the force is varied to alter the semicircles' separation until a correct endpoint is reached, where the

inner edges of the semicircles are just touching, see Figure 5.6(a). If the semicircles are separated too far, then more force is needed, Figure 5.6(b). While if the inner edge of the semicircles intersect, Figure 5.6(c), then the force needs to be reduced [1, 103]. The consequence of the force reading to be adjusted is that the intraocular pressure is underestimated or overestimated. Similarly the position of the semicircles in the prism also needs to be altered to ensure the semicircles are the same size, the ideal thickness being one tenth of the arc diameter [103]. This can also lead to an underestimated or overestimated intraocular pressure reading, see Figure 5.6(d).

The accuracy of the Goldmann applanation tonometer is well established [1, 100, 103, 104, 105]. However the performance in clinical practise is more problematic and has been called into question over recent years. This is due to the measurements being affected by a variety of factors such as the biomechanics of applanation, the accommodation and the examiner [105]. Many studies have shown that biomechanical features of the cornea such as thickness, rigidity, hydration, curvature, epithelial abnormalities and astigmatism have a significant effect on the intraocular pressure reading [100, 103, 104, 105, 106, 107]. For example the corneal thickness varies from person to person. A greater force is needed to applanate a given area when the cornea thickness is greater than the average cornea thickness, $540 \times 10^{-6} m$. However a lower force is required to applanate a thinner cornea, which may lead to the intraocular pressure being underestimated [103].

[106] investigated the effect of central corneal thickness, curvature and material properties on measuring the intraocular pressure using Goldmann applanation tonometry. [106] stated that corneal curvature has a low effect and the central corneal thickness has the largest effect on the structural resistance and will cause large discrepancies in intraocular pressure measurement. The author of [106] also reported that material properties, such as the range of variation in Young's modulus, will cause overestimation of intraocular pressure when increasing the material stiffness and vice versa. [107] and [108] investigate the effect of increased hydration on the accuracy of intraocular pressure measurement using Goldmann tonometry. [108] shows that measurements of intraocular pressure obtained by the Pascal Dynamic Contour tonometer caused a small underestimation error, while Goldmann tonometry measurements resulted in an overestimation of error. Recent studies [109, 110] stated that Goldmann applanation tonometers are not as accurate since, as the manufacturers point out, calibration errors may be important. [109] reported that Goldmann tonometers did not satisfy the manufacturer's recommended range $\pm 2.5\text{mmHg}$ in 28 percent of checked devices. According to a study in [110], there is a relationship between calibration error and clinical error in the measurement of the intraocular pressure, the error overestimates the intraocular pressure and is consistent over a clinical range of intraocular pressure.



FIGURE 5.7: The iCare rebound tonometer. This figure was extracted from [159]

5.3.3 The iCare Rebound Tonometer

The innovative iCare rebound tonometer is a relatively new device and that is different to the Goldmann applanation tonometer. It is a portable contact tonometer that uses the ‘rebound’ method and does not require an anaesthetic [103]. The iCare rebound tonometer features a small single use disposable probe [97] and has the advantages that it is convenient, small, low in cost, portable, handheld, useful for measuring intraocular pressure in children or adults, and proven to be accurate by several independent clinical studies. [111] found that the iCare rebound tonometer correlates well and provides intraocular pressure measurements that are similar to Goldmann tonometry. However intraocular pressure readings from rebound tonometers are influenced by variation of corneal properties.

[112], [113] and [114] explain how the *rebound* method has been applied and how the iCare tonometer functions. The method involves the rebound movement of a rod probe that comes into contact with the cornea of the eye. The probe consists of a magnetised steel wire shaft. The tip has a 1mm diameter plastic cover that is used to minimise corneal injury [112]. Once activated, the probe hits the cornea and bounces back. The movement is detected by a solenoid inside the iCare tonometer and the moving magnet induces a voltage in the solenoid [113]. [114] shows that the Goldmann tonometer is more accurate than the iCare rebound tonometer. On average the iCare overestimates the intraocular pressure value by 1.34mmHg. However, [114] stated that the iCare tonometer may be more useful as a screening tool because it is able to estimate intraocular pressure within a range of $\pm 3.0\text{mmHg}$ in more than 80 percent of the population.

5.4 Motivation for Mathematical Modelling

We will develop a mathematical model of the eyeball membrane which will be used to analyse the effects of the tonometer and to establish the validity of the Imbert-Fick principle which describes the functioning of a Goldmann applanation tonometer. We shall then develop the eyeball model to model scleral buckling in order to examine the shape of the eyeball when a scleral buckle has been placed either around or near the equator of the eye. In addition this model helps to analyse the focal length of the eyeball under the action of an external force. Scleral buckling is a surgical technique to treat rhegmatogenous retinal detachment (RRD). A scleral buckle is a silicone or nylon band which is placed around the eyeball permanently. In some instances, vision may be affected by a scleral buckle. Since the band is pushed into the sclera towards the detached retina, it may change the shape and the focal length of the eyeball. In particular, these models will be studied using the membrane equations of equilibrium for axisymmetric spherical shells. Using numerical analysis the resulting stresses and displacements of the eyeball will be determined and examined.

5.5 The Membrane Theory of Shells

[94] defined the difference between plates and shells, where plates are plane walls and shells are all curved surfaces. [130] pointed out that a flat plate is a special case of a shell having no curvature and defined a curved plate to be a shell that has a small curvature. Studies of shells, [94, 95, 96, 130] have described that a shell is different from a plate because the shell can be curved and carry membrane and bending forces. Usually in studies of shell theory, the thickness of the shell is considered small in comparison with the other dimensions, such as the radius of the curvature. However [94] explains that the thickness is not required to be extremely small and the material of the shell does not necessarily need to be either elastic or made of a solid material; it could be the surface of a liquid, for example a soap bubble. A liquid bubble can be considered by shell theory because of the surface tension acting on it and the properties of the shell. [94] noted that the thickness of the shells could be either uniform or vary from point to point. The geometry of a shell is fully described if we know the thickness at every single point and the shape of the middle surface [94]. Membrane theory is a simplified version of shell theory and is based on neglecting bending and twisting moments in the stress analysis. Essentially, when applying the membrane theory of shells, only the normal and shearing forces, (which we denote here by N_θ , N_ϕ , $N_{\theta\phi}$ and $N_{\phi\theta}$) and the loads (denoted by P_ϕ , P_θ and P_R), proportional to the area of the elements are considered. [95] stated that the main problem in this theory is therefore to determine the resultant forces for a given shape of shell, in terms of either the loads or the displacements applied to the edges and surface of the shell.

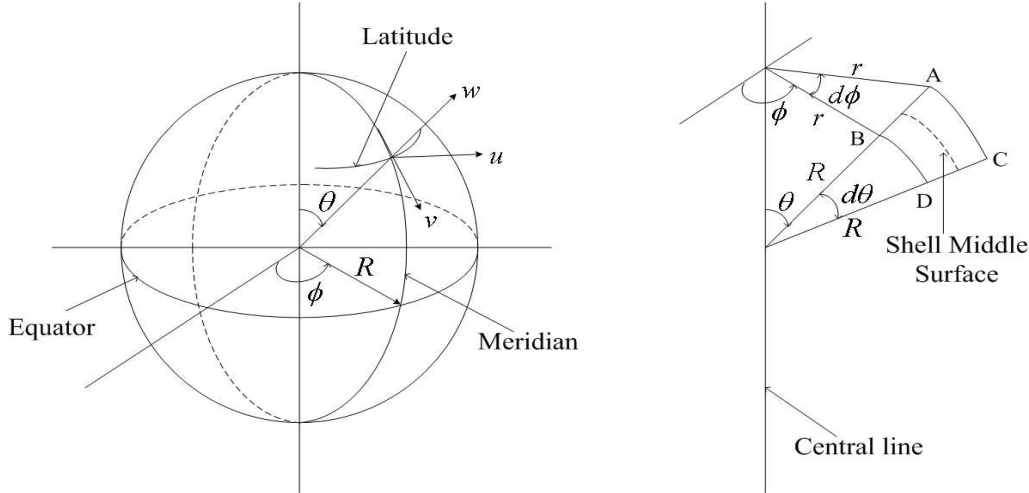


FIGURE 5.8: Geometry of Spherical Shell.

The stroma of the sclera is continuous with the stroma of the cornea and plays an important role in the biomechanics of the eyeball. Due to the structure of the collagen fibrils that make up the stroma, we can model the human eyeball as a spherical shell with symmetry at the central axis and isotropic elasticity in the middle of the shell surface (*i.e.* the Young's modulus is the same in all directions tangent to the middle shell surface). Using the membrane theory of shells we attempt to develop a model of the eyeball with application to tonometry and scleral buckling in order to examine changes in the shape of the eyeball. Next, we present the derivation of the governing equations of membrane shells in spherical coordinates under equilibrium and axisymmetric conditions.

5.5.1 Derivation of the Membrane equations of Equilibrium for Axisymmetric Spherical Shells

Let us consider a spherical shell of radius R where the angle parallel to the equator is defined as ϕ and the angle down from the north pole, perpendicular to the equator, is defined as θ , as shown in 5.8. By considering a point on the shell, then the displacement field is defined in terms of u , v and w , see Figure 5.8. If we now consider a section of the shell, with vertices ABCD, bounded by two meridian lines, AC, and BD, and two parallel circles, AB, and CD, then the 'middle surface' is the line running parallel to AC and bisecting AB and CD, shown in Figure 5.8. Letting $d\phi$ be the angle between the two meridian lines at the north pole, $d\theta$ the angle made by vertex B, the origin and vertex D, θ the angle that the north pole makes with the line through B and the origin, and R the distance B and D are from the origin. Then the distance A and B are from the north pole is $r = R \sin(\theta)$, the length $AB = R \sin(\theta) d\phi$, the length $AD = R d\theta$ and the surface of the area of the section of the shell ABCD is $R^2 \sin(\theta) d\theta d\phi$.

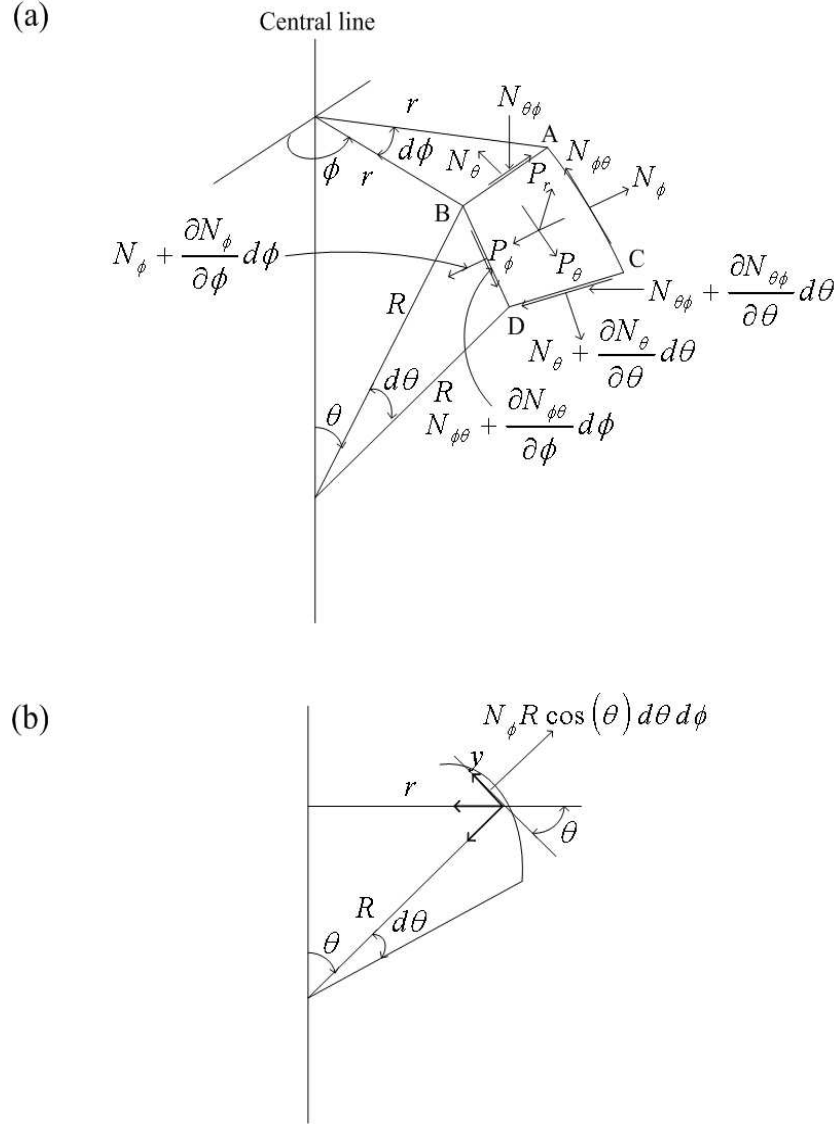


FIGURE 5.9: Stress Resultants in a Spherical Shell Element.

In membrane shell analysis the force actions are usually defined in terms of the resultant stresses: the meridional force, N_θ , the hoop force, N_ϕ , and the shear, $N_{\theta\phi} = N_{\phi\theta}$, are assumed to act at the middle surface of the shell. Consider an infinitesimally small spherical shell element, ABCD with some possible membrane force actions such as shown in Figure 5.9(a). By resolving the forces on the element, ABCD, it will be shown that the three resulting equilibrium force equation consist of three unknown stresses N_θ , N_ϕ and $N_{\theta\phi}$ where these ‘stresses’ are defined as force per unit length.

Now let us start by considering the forces parallel to the tangent to the meridian. The shear acting on one of the meridional edges of the element is

$$N_{\theta\phi} R d\theta. \quad (5.1)$$

The shear acting on the opposite edge is

$$\left(N_{\theta\phi} + \frac{\partial N_{\theta\phi}}{\partial\phi} d\phi \right) R d\theta. \quad (5.2)$$

These two forces (equations (5.1) and (5.2)) are in opposite directions, therefore the difference in these forces is given as

$$R \frac{\partial N_{\theta\phi}}{\partial\phi} d\phi d\theta. \quad (5.3)$$

Next we consider the meridional forces, such that the force on one edge is given by

$$N_\theta r d\phi$$

and on the opposite edge is given by

$$\left(N_\theta + \frac{\partial N_\theta}{\partial\theta} d\theta \right) r d\phi.$$

In the same way, the difference of the two meridional forces is

$$\frac{\partial}{\partial\theta} (r N_\theta) d\theta d\phi. \quad (5.4)$$

We also consider the hoop forces on either side of the element that lies in the plane of a parallel circle where the forces include an angle $d\phi$. Thus the hoop force in the direction of the tangent to the meridian is

$$N_\phi R d\theta \cdot d\phi.$$

The component of the above force in the y direction (see Figure 5.9(b)) is given by

$$N_\phi R d\theta d\phi \cos(\theta) \quad (5.5)$$

Notice that the direction of the force above is opposite to the shear and meridional forces which are parallel to the tangent to the meridian. Therefore this force requires a negative sign. Finally a component of the external force, P_θ will be introduced. P_θ is the product of the load component per unit area of shell surface and the area of the element, $r d\phi \cdot R d\theta$. Thus we have the pressure acting on the element in the θ direction is

$$P_\theta r d\phi \cdot R d\theta. \quad (5.6)$$

By balancing these forces, equations (5.3), (5.4), (5.5) and (5.6), we determine the first equilibrium equation to be

$$R \frac{\partial N_{\theta\phi}}{\partial\phi} d\phi d\theta + \frac{\partial}{\partial\theta} (r N_\theta) d\theta d\phi - R N_\phi d\theta d\phi \cos(\theta) + P_\theta r d\phi \cdot R d\theta = 0.$$

Simplifying the equation above, by dividing the equation by $d\phi d\theta$, we get the partial differential equation

$$R \frac{\partial N_{\theta\phi}}{\partial \phi} + \frac{\partial}{\partial \theta} (r N_\theta) - R N_\phi \cos(\theta) + P_\theta r R = 0. \quad (5.7)$$

By repeating similar steps as before, we obtain an equation for the forces in the direction of a parallel circle. The shear acting on the horizontal edge of the element is

$$N_{\theta\phi} r d\phi$$

and the shear acting on the opposite horizontal edge is

$$\left(N_{\theta\phi} + \frac{\partial N_{\theta\phi}}{\partial \theta} d\theta \right) r d\phi.$$

Thus the difference between the two shearing forces is

$$\frac{\partial}{\partial \theta} (r N_{\theta\phi}) d\theta d\phi. \quad (5.8)$$

In the same way we have the difference between two hoop forces that can be written as

$$R \frac{\partial N_\phi}{\partial \phi} d\phi d\theta. \quad (5.9)$$

In the direction of the parallel circles, there is a shear force acting on the meridional edges. The two forces $N_{\phi\theta} R d\theta$ are not exactly parallel, with the angle between them being $d\phi$, thus the resultant force is given by

$$N_{\phi\theta} R d\theta \cos(\theta) d\phi. \quad (5.10)$$

The force denoted in equation (5.10) is in the direction tangent to a parallel circle. The external force in the direction of a parallel circle is

$$P_\phi r R d\phi d\theta. \quad (5.11)$$

Now we substitute equations (5.8), (5.9), (5.10) and (5.11) into the condition of equilibrium and divide throughout by $d\phi d\theta$, thus we have

$$R \frac{\partial N_\phi}{\partial \phi} + \frac{\partial}{\partial \theta} (r N_{\theta\phi}) - R N_{\phi\theta} \cos(\theta) + P_\phi r R = 0. \quad (5.12)$$

Next we obtain the third equation based on the forces which are perpendicular to the middle surface of the shell. Note that the shear force does not contribute to this. As before we see that the hoop force, $N_\phi R d\theta$ has a horizontal component

$$N_\phi R d\theta d\phi.$$

In this case, the normal component of this force is pointing towards the centre of the sphere. The meridional force and the third load component, P_R also contribute to formulate the third equation. Similar to the two hoop forces, the two meridional forces have the same resultant in the same direction that enters the equilibrium condition, which is

$$N_\theta r d\phi d\theta.$$

The two resultants and together with the component of the load, $P_R r R d\phi d\theta$ may now be written in terms of equilibrium, to give

$$N_\phi R \sin(\theta) + N_\theta r - P_R r R = 0. \quad (5.13)$$

Equations (5.7), (5.12) and (5.13) are the three equilibrium equations of the membrane shell with the three unknown stress resultants being given by the meridional force, N_θ , the hoop force, N_ϕ and the shear, $N_{\theta\phi}$. For a spherical shell with uniform material properties under axisymmetric loading, then the stresses are independent of ϕ , and all derivatives with respect to the spherical coordinate ϕ , are zero. Under these conditions and substituting the relation of the radius of curvature, $r = R \sin(\theta)$ into equations (5.7), (5.12) and (5.13), the equations will reduce to

$$\frac{\partial}{\partial \theta} (R \sin(\theta) N_\theta) - RN_\phi \cos(\theta) + P_\theta R^2 \sin(\theta) = 0, \quad (5.14)$$

$$\frac{N_\phi + N_\theta}{R} = P_R. \quad (5.15)$$

To completely solve the shell problem, we shall now determine the corresponding deformations. The deformation of a shell considers the extensions of line elements $ds_\theta = R d\theta$, on the meridian and $ds_\phi = R \sin(\theta) d\phi$ on the parallel circle by Δds_θ and Δds_ϕ . Let us define the meridional strain to be,

$$\varepsilon_\theta = \frac{\Delta ds_\theta}{ds_\theta},$$

and the hoop strain,

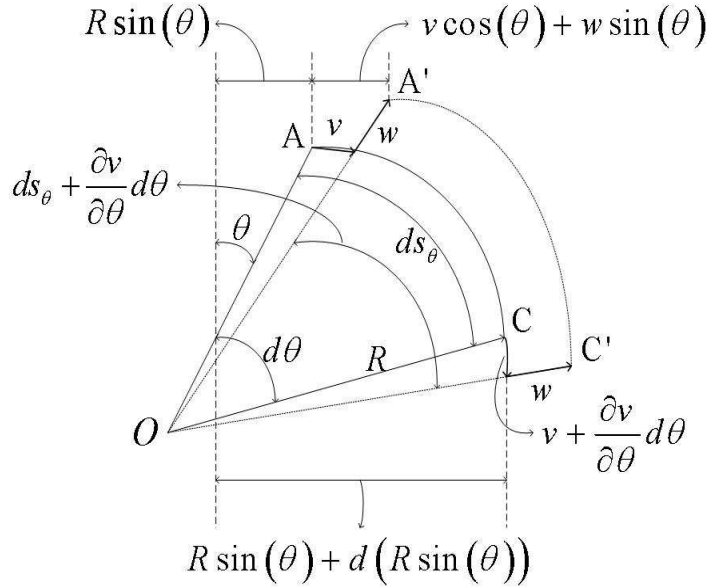
$$\varepsilon_\phi = \frac{\Delta ds_\phi}{ds_\phi}.$$

Note that in this problem we consider an axisymmetric spherical shell. Thus under this condition, there is no displacement, u , in the ϕ direction thus no shearing strains have been produced. The material properties of the shell provide a relationship between these strains and the resultant stresses, this is known as the elastic law.

The elastic law may be written in terms of normal forces, in the form

$$\begin{aligned} \varepsilon_\theta &= \frac{1}{E\alpha} (N_\theta - \nu N_\phi), \\ \varepsilon_\phi &= \frac{1}{E\alpha} (N_\phi - \nu N_\theta), \end{aligned} \quad (5.16)$$

(a)



(b)

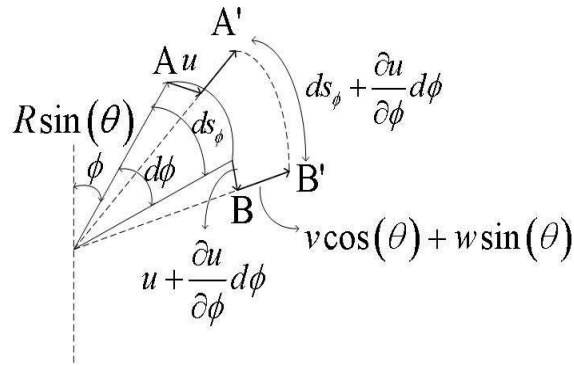


FIGURE 5.10: Line elements before and after deformation (a) meridian (b) parallel circle.

where

$$N_\theta = \frac{E\alpha}{1-\nu^2} (\varepsilon_\theta + \nu\varepsilon_\phi),$$

$$N_\phi = \frac{E\alpha}{1-\nu^2} (\varepsilon_\phi + \nu\varepsilon_\theta).$$

Here E is the Young's modulus, ν denotes the Poisson's ratio and α denotes the wall thickness of the shell. In general, the strains, ε_θ and ε_ϕ , for every point of the shell are not the only quantity important when analysing the deformation. The displacements of each point of the middle surface are also important. The displacement is a vector giving the distance from an initial position to a final position. The displacement may be described by its three components where u is the displacement in the ϕ direction,

v is the displacement in the θ direction and w is the displacement in the R direction. Note that only displacements v and w are of interest in this study.

We shall now determine the equations that relate the displacements (v and w) and the strains, ε_θ and ε_ϕ . Let us start with the meridional strain, ε_θ . Figure 5.10(a) shows that a meridional element AC is equal to ds_θ and A'C' is equal to

$$ds_\theta + \frac{\partial v}{\partial \theta} d\theta.$$

From the centre of curvature, O to A, the distance is given as R and it increases to $R + w$. Therefore the length of the arc increases proportionally to

$$\left(ds_\theta + \frac{\partial v}{\partial \theta} d\theta \right) \frac{R + w}{R}.$$

We calculate the elongation to give

$$\Delta ds_\theta = \left(ds_\theta + \frac{\partial v}{\partial \theta} d\theta \right) \frac{R + w}{R} - ds_\theta \approx \frac{\partial v}{\partial \theta} d\theta + \frac{w}{R} ds_\theta.$$

To determine the meridional strain, ε_θ we divide by $ds_\theta = R d\theta$. Note, we drop all products of two displacements because the elongation that has been produced is very small. Therefore we find

$$\varepsilon_\theta = \frac{\Delta ds_\theta}{ds_\theta} = \frac{1}{R} \left(w + \frac{\partial v}{\partial \theta} \right). \quad (5.17)$$

We shall now determine the equation for the hoop strain, ε_ϕ from Figure 5.10(b). AB is a hoop element with length equal to ds_ϕ . In the same way as before, we determine the line element after deformation, A'B', which is given as $ds_\phi + \frac{\partial u}{\partial \phi} d\phi$. The radial displacement before deformation is equal to $R \sin(\theta)$, after deformation the radial displacement increases from $R \sin(\theta)$ to $R \sin(\theta) + v \cos(\theta) + w \sin(\theta)$. Thus the arc length in the plane of the parallel circle is increased proportionally to

$$\left(ds_\phi + \frac{\partial u}{\partial \phi} d\phi \right) \frac{R \sin(\theta) + v \cos(\theta) + w \sin(\theta)}{R \sin(\theta)}.$$

Therefore the elongation of the line element, Δds_ϕ , is such that

$$\Delta ds_\phi = \left(ds_\phi + \frac{\partial u}{\partial \phi} d\phi \right) \frac{R \sin(\theta) + v \cos(\theta) + w \sin(\theta)}{R \sin(\theta)} - ds_\phi.$$

By similar reasoning to the derivation of equation (5.17) and since there is no displacement, u in the ϕ direction, we rewrite the formula for the elongation of the line element such that

$$\Delta ds_\phi = (v \cos(\theta) + w \sin(\theta)) \frac{ds_\phi}{R \sin(\theta)}.$$

We now determine that the equation of the hoop strain is given by

$$\varepsilon_\phi = \frac{\Delta ds_\phi}{ds_\phi} = \frac{1}{R \sin(\theta)} (v \cos(\theta) + w \sin(\theta)). \quad (5.18)$$

We substitute equations (5.17) and (5.18) into equation (5.16) to derive a set of equations for the displacements v and w . These are

$$\frac{1}{E\alpha} (N_\theta - \nu N_\phi) = \frac{1}{R} \left(w + \frac{\partial v}{\partial \theta} \right), \quad (5.19)$$

$$\frac{1}{E\alpha} (N_\phi - \nu N_\theta) = \frac{1}{R \sin(\theta)} (v \cos(\theta) + w \sin(\theta)). \quad (5.20)$$

Equations (5.14), (5.15), (5.19) and (5.20) are the membrane equations of equilibrium for axisymmetric spherical shells. Notice that the derivations of these equations are based on the studies of direct stresses in shells of revolution by [94] and [96]. Our next objective is to examine these equations in relation to the tonometry and the scleral buckling problems. These equations involve four unknowns (the meridional force, N_θ , the hoop force, N_ϕ , the meridian displacement, v and the radial displacement, w) which we must determine. The quantities P_θ and P_R will be regarded as known, and will reflect the tonometry and/or scleral buckling conditions.

5.6 Mathematical Analysis of the Eyeball Membrane when undergoing Tonometry and Scleral Buckling

Over the last forty years there have been a limited number of studies developing mathematical models of the human eyeball due to tonometry and scleral buckling. [123] proposed a model of the cornea-scleral shell using axisymmetric annular finite elements with a trilinear stress-strain relation. [123] stated that the model is useful in analysing the structural response of tonometry on pathological eyes with lamellar keratectomy. Using the same model, [124] derives the relation between the pressure and the volume of the eyeball by examining the experimental data of the nonlinear elastic material parameters for the cornea and the sclera.

[2] applied linear elastic theory to problems of tonometry and scleral buckling. The author described the external force applied to the eyeball by either the tonometer or the scleral buckle in terms of an infinite series of Legendre polynomials. [2] also considered the plain strain problem over an elastic solid of revolution and expressed the displacements in terms of a biharmonic Love's stress functions. [131] studied changes of the shape of the cornea when undergoing keratoconus and tonometry procedures. These studies were carried out using mathematical shell analysis and nonlinear finite element modelling and also with comparison to laboratory experiments. Using a finite element method a corneal model was presented that simulated the effects of Goldmann

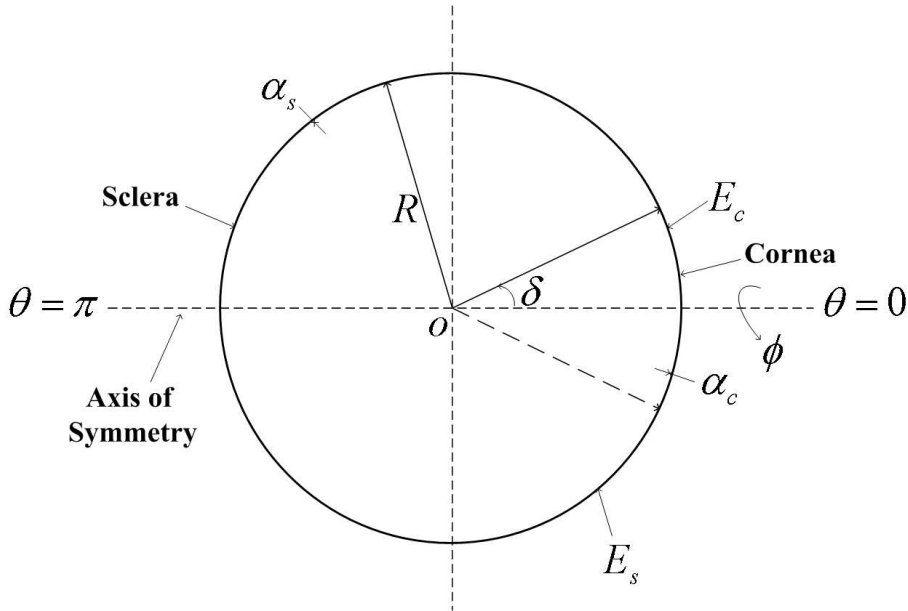


FIGURE 5.11: Schematic diagram of the cross section of the eyeball in the plane $\phi = 0$.

applanation tonometry under various corneal parameters [106]. [106] compared their numerical results with the statistical results of clinical data and showed that clinical data had a similar trend to the numerical results.

The recent study [132] presented a numerical model of the eyeball under several applications; refractive surgery (photorefractive keratectomy) and Goldmann applanation tonometry. [132] concluded that differences between the model and the results of refractive surgery are errors due to simplifications of the model and the rheological material constant parameters. [132] also pointed out the Imbert-Fick principle that has been used in Goldmann applanation tonometry cannot be applied to the real human eyeball, since the principle is based on wrong assumptions. Due to limited studies into these problems, we will attempt to develop a mathematical model of the eyeball based on membrane shell theory and analyse numerically the model under the effect of the tonometer and the scleral buckle.

5.6.1 A Mathematical Model of the Eyeball Membrane

A simplified eyeball model has been developed by considering a sphere at the centre, O , which incorporates the cornea and the sclera, see Figure 5.11. We assume the cornea is directly attached to the sclera at the limbus and the sclera is considered to be continuous at the optic nerve. Figure 5.11 presents the geometry of the cross section of the eyeball model in a spherical coordinate system (ϕ, θ, R) where ϕ is the hoop angle, θ denotes the meridian angle and R is the radius of the sphere. Here the Young's modulus of the sclera and the cornea are denoted by E_s and E_c respectively, δ denotes the angle

of the cornea and $\phi = 0$ is assumed to be the axis of symmetry.

In this eyeball model, we consider the eyeball to be an elastic membrane shell, isotropic in the shell surface and a hollow sphere in which the thickness and Young's modulus both vary. The corneal thickness, α_c is assumed to be thin compared to the thickness of the sclera, α_s . However, both the corneal and scleral thickness are considered to be very small. The vitreous humour is assumed to be an incompressible Newtonian fluid with constant density and viscosity. It is assumed that a pressure P_R is applied to the shell in the direction normal to the surface. This pressure is equal to the pressure difference between the pressure inside the eyeball and the pressure outside the eyeball such that,

$$P_R = \Delta P = P_{IN} - P_{OUT}.$$

The load component tangent to the shell, P_θ is assumed to be zero. The pressure inside the eyeball, P_{IN} , consists of the atmosphere pressure, P_{ATM} and the intraocular pressure, P_{IOP} . The pressure outside the eyeball, P_{OUT} is equal to the atmosphere pressure, P_{ATM} . Thus in the normal human eyeball, under no external outside pressure, it is assumed that the pressure on the eyeball equals the intraocular pressure such that, $\Delta P = P_{IOP}$. In this study we examine the shape of the eyeball under a variation of loading conditions depending on the outside pressure that is exerted from either the tonometer or a scleral buckle.

5.6.2 The Governing Equations

Under the condition of static equilibrium and assuming the sphere is axisymmetric, the general equations of spherical membrane shells have been reduced to the equations (5.14), (5.15), (5.19) and (5.20). These equations have been simplified in order to analyse the elastic membrane of the human eyeball under the effects of external outside pressure which are from the tonometry or the scleral buckling. These are:

$$\frac{d}{d\theta} (R \sin(\theta) N_\theta) - RN_\phi \cos(\theta) = 0, \quad (5.21)$$

$$\frac{N_\phi + N_\theta}{R} = P_R. \quad (5.22)$$

$$\frac{1}{E\alpha} (N_\theta - \nu N_\phi) = \frac{1}{R} \left(w + \frac{dv}{d\theta} \right), \quad (5.23)$$

$$\frac{1}{E\alpha} (N_\phi - \nu N_\theta) = \frac{1}{R \sin(\theta)} (v \cos(\theta) + w \sin(\theta)). \quad (5.24)$$

The governing equations above, contain four unknowns that must be determined. There are the stress resultants, N_ϕ and N_θ , and the displacements, v in the θ direction and w in the R direction. Here ν denotes the Poisson's ratio. The eyeball has radius $R = a$,

Young's modulus $E = E(\theta)$, thickness $\alpha = \alpha(\theta)$ where E and α are defined by

$$E(\theta) = \frac{E_s + E_c}{2} + \frac{E_s - E_c}{2} \tanh(K(\theta - \delta)), \quad (5.25)$$

$$\alpha(\theta) = \alpha_c + (\alpha_s - \alpha_c) \frac{\theta}{\pi}. \quad (5.26)$$

For the Young's modulus we define the equation (5.25) to be the hyperbolic equation because of the different values between the Young's modulus of the sclera and the cornea. K denotes a constant and is assumed to be large. Equation (5.26) defines the thickness distribution of the eyeball and is considered to be a straight line in this problem.

5.6.3 The General Solution Procedures

We now solve the governing equations. Firstly, we rewrite equation (5.22) for N_ϕ to give,

$$N_\phi = aP_R - N_\theta. \quad (5.27)$$

Then we substitute equation (5.27) into equation (5.21) yielding,

$$\frac{d}{d\theta} (\sin(\theta) N_\theta) + N_\theta \cos(\theta) = aP_R \cos(\theta).$$

If we multiply the above equation with the by integrating factor, $\sin(\theta)$, and simplify the equation, we obtain that

$$\frac{d}{d\theta} (\sin^2(\theta) N_\theta) = aP_R \sin(\theta) \cos(\theta). \quad (5.28)$$

We may now solve equation (5.28) for N_θ as such that

$$N_\theta = \frac{a}{\sin^2(\theta)} \left[\int_0^\theta P_R \sin(\theta^*) \cos(\theta^*) d\theta^* + C_1 \right] \quad (5.29)$$

where C_1 is the constant of integration. Rearranging equations (5.23) and (5.24) for w gives,

$$w = \frac{a}{E\alpha} (N_\theta - \nu N_\phi) - \frac{dv}{d\theta}, \quad (5.30)$$

$$w = \frac{a}{E\alpha} (N_\phi - \nu N_\theta) - v \frac{\cos(\theta)}{\sin(\theta)}. \quad (5.31)$$

Equating equation (5.30) and equation (5.31), we get

$$\frac{dv}{d\theta} - \frac{v \cos(\theta)}{\sin(\theta)} = \frac{a(1+\nu)}{E\alpha} (N_\theta - N_\phi). \quad (5.32)$$

By letting $v = u \sin(\theta)$ and substituting into equation (5.32), we can solve to give

$$u = a(1 + \nu) \left[\int_0^\theta \frac{1}{E\alpha} \left(\frac{N_\theta - N_\phi}{\sin(\theta^*)} \right) d\theta^* + C_2 \right] \quad (5.33)$$

where C_2 is a different constant of integration.

5.6.4 Boundary Conditions

Equations (5.21) and (5.23) are first order differential equations and each equation requires one boundary condition. We determine the first boundary condition to calculate C_1 in equation (5.29), by doing an asymptotic expansion as θ tends to zero in the problem where no additional outside pressure is involved except the intraocular pressure, $P_R(\theta) = P_{IOP}$. Here we deduce that,

$$N_\theta(\theta = 0) = \frac{aP_R(\theta = 0)}{2}, \quad (5.34)$$

where N_θ is equal to half of the radius of the eyeball multiplied by the load component normal to the shell, P_R , at θ is equal to zero. The second boundary condition determines C_2 in equation (5.33). We require v to be zero at $\theta = 0$ and $\theta = \pi$, but this is already guaranteed by the definition $v = u \sin(\theta)$ provided u is finite at $\theta = 0$ and $\theta = \pi$. We note further that if we prescribe u to be equal to (say) q at $\theta = 0$, then q corresponds to an arbitrary rigid body translation along the z axis. We therefore set

$$u(\theta = 0) = q. \quad (5.35)$$

In physical circumstances the eyeball remains fixed as it is supported by the eye socket at the back of the eye. Therefore in the modelling assumption, it would be necessary to fix the eyeball from translations by assuming the displacements at the back of the eye to be zero. We shall now solve equations (5.30) and (5.33) numerically subject to the boundary conditions in equations (5.34) and (5.35) to determine solutions for the meridian force, N_θ and the meridian displacement, v . Then we will substitute N_θ into equation (5.30) to derive the hoop force, N_ϕ . Finally, we will determine the radial displacement, w by substituting the solutions for N_ϕ , N_θ and v into equation (5.31).

5.6.5 Numerical Analysis of Tonometry and Scleral Buckling

We now examine and discuss in detail the elastic membrane of the human eyeball under the effect of the tonometer and a scleral buckle.

5.6.5.1 Tonometry

In order to study the effect of tonometry, we consider the load component normal to the shell, P_R to be the pressure difference between the intraocular pressure, P_{IOP} and the pressure exerted by the tonometer, given by

$$P_R(\theta) = \begin{cases} P_{IOP} + P_T \frac{\cos(\eta) - \cos(\theta)}{1 - \cos(\eta)} & \text{if } 0 \leq \theta \leq \eta, \\ P_{IOP} & \text{if } \eta < \theta \leq \delta, \\ P_{IOP} & \text{if } \delta < \theta \leq \pi - \kappa, \\ P_{IOP} + Q (\cos(\pi - \kappa) - \cos(\theta)) & \text{if } \pi - \kappa < \theta \leq \pi, \end{cases} \quad (5.36)$$

where P_T is the tonometer pressure, η is the angle of the tonometer is in contact with the human eye, δ denotes the corneal angle and $(\pi - \kappa, \pi]$ defines as the region of equilibrating pressure. To maintain the static equilibrium condition of the membrane eyeball when we apply the tonometer pressure, we impose the equilibrium pressure, Q in equation (5.36). The condition of equilibrium in this problem is given by the total force per length being zero, stated as

$$\int_0^\pi P_R(\theta) \cdot \cos(\theta) \cdot \sin(\theta) d\theta = 0. \quad (5.37)$$

By using the typical parameter values given in Table 5.2, we let $R = a$, substitute equations (5.25), (5.26) and (5.36) into equations (5.21) - (5.24), and solve the equations numerically in order to examine the effect of the external outside pressure from the tonometer. Figure 5.12 shows the meridian force, N_θ at the outer surface of the eyeball from $\theta = 0$ to $\theta = \pi$. Under the tonometer tip, $\theta = 0$ to $\theta = \eta$, the meridian force increases from zero to 11.5 Nm^{-1} and it stays constant outside the tonometer region. Then under the equilibrating region, $\theta = \pi - \kappa$ to $\theta = \pi$, the meridian force decreases slightly and is approximately equal to 11.0 Nm^{-1} .

We now examine the qualitative behaviour of the shape of the eyeball under several different circumstances. Figure 5.13 presents four different shapes of the eyeball produced by the action of a tonometer, with pressure equal to a range of intraocular pressures, P_{IOP} . The dotted blue line from $\theta = 0$ to $\theta = 2\pi$ represents the original shape of the eyeball when there is no load component normal to the shell, $P_R = 0$. The dashed purple line denotes the corresponding displacement when the load component normal to the shell is equal to the intraocular pressure, $P_R = P_{IOP}$. The solid red line denotes the deformed eyeball due to the effect of tonometer pressure. The distance from the vertical axis to the first solid black line represents the region of contact between the eyeball and the tonometer tip. Meanwhile the distance from the vertical axis to the second solid black line denotes the angle of the cornea. Notice that this problem is symmetric, thus we are only concerned with the displacements from $\theta = 0$ to $\theta = \pi$. When the pressure exerted by the tonometer equals the intraocular pressure, 15mmHg,

Parameter Name	Symbol	Value
Eyeball radius	a	11.5mm
Poisson's ratio	ν	0.5
Tonometer angle	η	$\frac{\pi}{27}$
Corneal angle	δ	$\frac{3\pi}{20}$
Equilibrating angle	κ	$\frac{\pi}{4}$
Constant	K	40
Constant	q	0
Scleral Young's modulus	E_s	15MPa
Corneal Young's modulus	E_c	12MPa
Scleral thickness	α_s	0.7mm
Corneal thickness	α_c	0.5mm

TABLE 5.2: The parameter values of the membrane eyeball model used in numerical calculations.

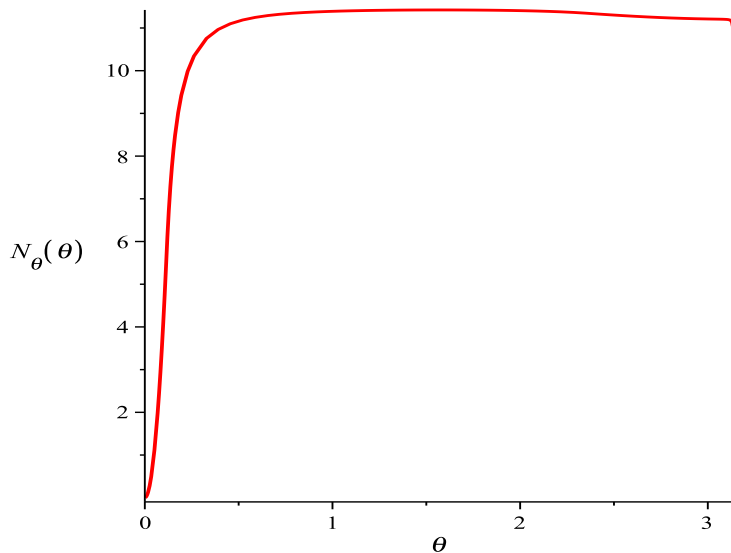


FIGURE 5.12: The axial force, N_θ distribution at the outer surface of the eyeball when the pressure exerted by the tonometer is equal to the intraocular pressure, P_{IOP} , 15mmHg. The remaining parameter values have been established in Table 5.2.

we can see that the solid red line is flat under the region of the tonometer tip. However, the solid red lines indicate excess appplanation when the tonometer pressure and the intraocular pressure are equal to 30mmHg, 45mmHg and 60mmHg. These may be seen clearly from Figure 5.14. Figure 5.14 presents the same results shown in Figure 5.13 for tonometer pressures equal to the intraocular pressure, 15mmHg, 30mmHg, 45mmHg and 60mmHg, in the region from $\theta = 0$ to $\theta = \frac{\pi}{2}$ in order to see the appplanation under the tonometer tip region.

The qualitative results of the displacements suffered by the eyeball under the variation of the intraocular and tonometer pressures shown in Figure 5.13 and Figure 5.14 are useful in order to examine the accuracy of the Imbert-Fick law. The Goldmann appplanation tonometer is fundamentally based on the standard IOP measurement, Imbert-Fick law which states that if the diameter of the appplanation area of contact between the cornea and the tonometer tip is exactly 3.06mm, then 0.1g of force is required to produce the corneal appplanation corresponding to 1mmHg of IOP. This relationship is given as

$$1\text{mmHg} \rightarrow \frac{0.0001 \cdot (9.81)}{\pi \left(\frac{0.00306}{2} \right)^2} = 133.394\text{Pa}.$$

Notice that the kilogram of force is defined as a unit of force that is equal to $9.81N$. The millimetre mercury (mmHg) is a non SI unit of pressure. The standard unit of pressure is Pascal, Pa where 1mmHg is equal to 133.3224Pa. Table 5.3 lists the corresponding values of pressure from 1mmHg to 60mmHg as given by the standard pressure unit conversion. Based on the relationship given by the Imbert-Fick law, we can conclude that under the appplanation area, the pressure exerted from the tonometer, P_T is proportional to the intraocular pressure, P_{IOP} . This may be written as

$$P_T = P_{IOP}. \quad (5.38)$$

According to the Imbert-Fick law, given in equation (5.38) we expect that in our mathematical model if the pressure from the tonometer is exactly the same as the intraocular pressure then the cornea will applanate. However from Figures 5.13 and 5.14, we can see that this does not appear to be exactly correct. In particular for an intraocular pressure greater than 30mmHg, the required amount of pressure exerted from a tonometer, P_T to applanate the cornea is less than the intraocular pressure, P_{IOP} . For the purpose of comparison with the Imbert-Fick law, we then predicted the pressure from the tonometer that flattened the cornea using our present numerical calculation and the parameter values given in Table 5.2. Table 5.4 presents the predicted pressure exerted from the tonometer to applanate the cornea for an intraocular pressure range of 10mmHg and 45mmHg. Table 5.4 also presents the corresponding values of pressure from the Imbert-Fick law. The data in Table 5.4 is now plotted against the corresponding intraocular pressures as shown in Figure 5.15 and the data is fitted using

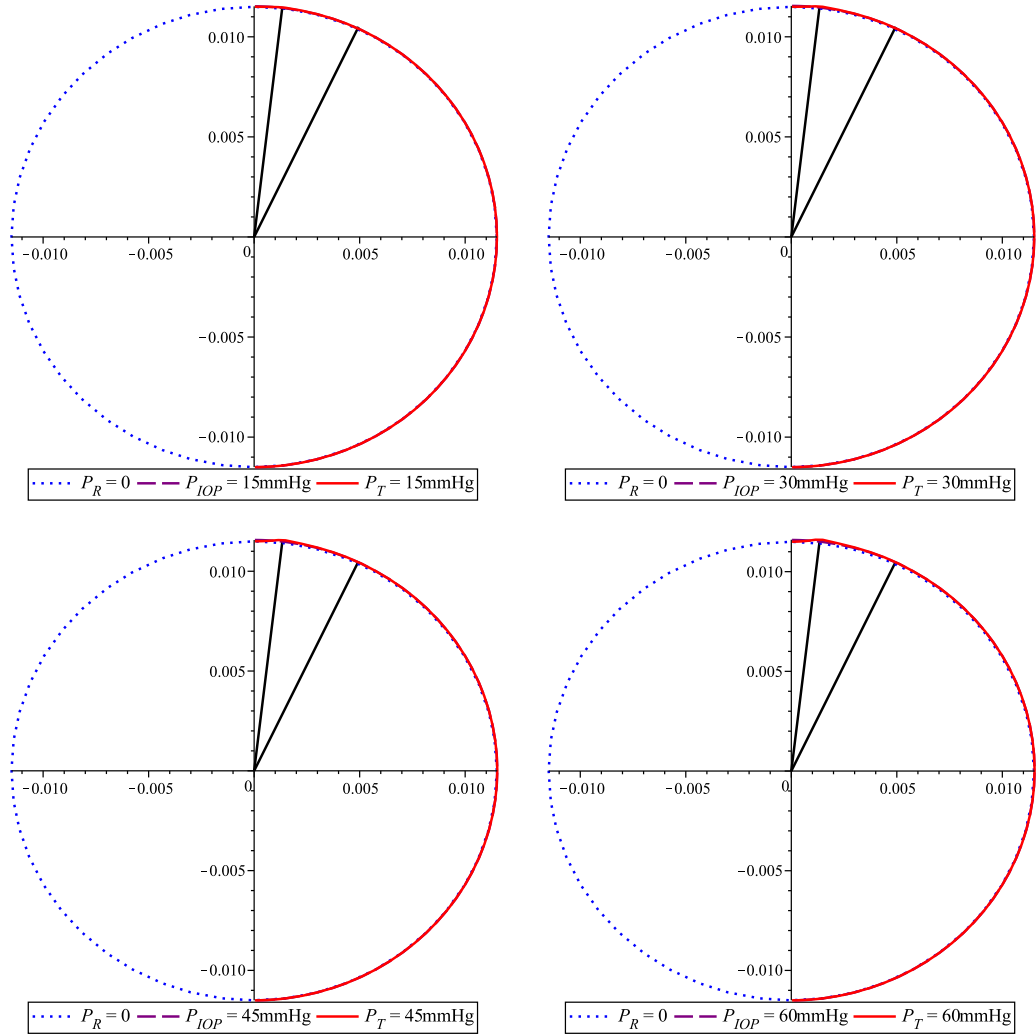


FIGURE 5.13: Qualitative behaviour of the shape of the eyeball presented by the displacements due to the pressure exerted by the tonometer, P_T . The values of the tonometer pressure are taken to be equal to the intraocular pressure, P_{IOP} which are 15mmHg, 30mmHg, 45mmHg and 60mmHg. Standard parameter values required for these numerical calculation are given in Table 5.2.

linear least squares achieved MAPLE, [8]. From the linear trend shown in Figure 5.15, the measurement of the applanation pressure, P_T is not in a good agreement with the results, in particularly between our numerical calculations and those obtained from the Imbert-Fick law. The average slope presented by the Imbert-Fick law is equal to approximately one, however the average slope calculated in this work is 0.28. According to Figure 5.15, our membrane eyeball model under the effect of a tonometer shows that above the healthy intraocular pressure, 15mmHg, the applanation pressure becomes lower than the intraocular pressure. Our model behaves differently to the Imbert-Fick law. This maybe due to a number of reasons which we shall investigate now. We notice that the accuracy of the model depends on the physical parameter values. Thus, to examine and understand the behaviour of our membrane eyeball model, we then analyse the effect of the material values such as the Young modulus, the cornea thickness and

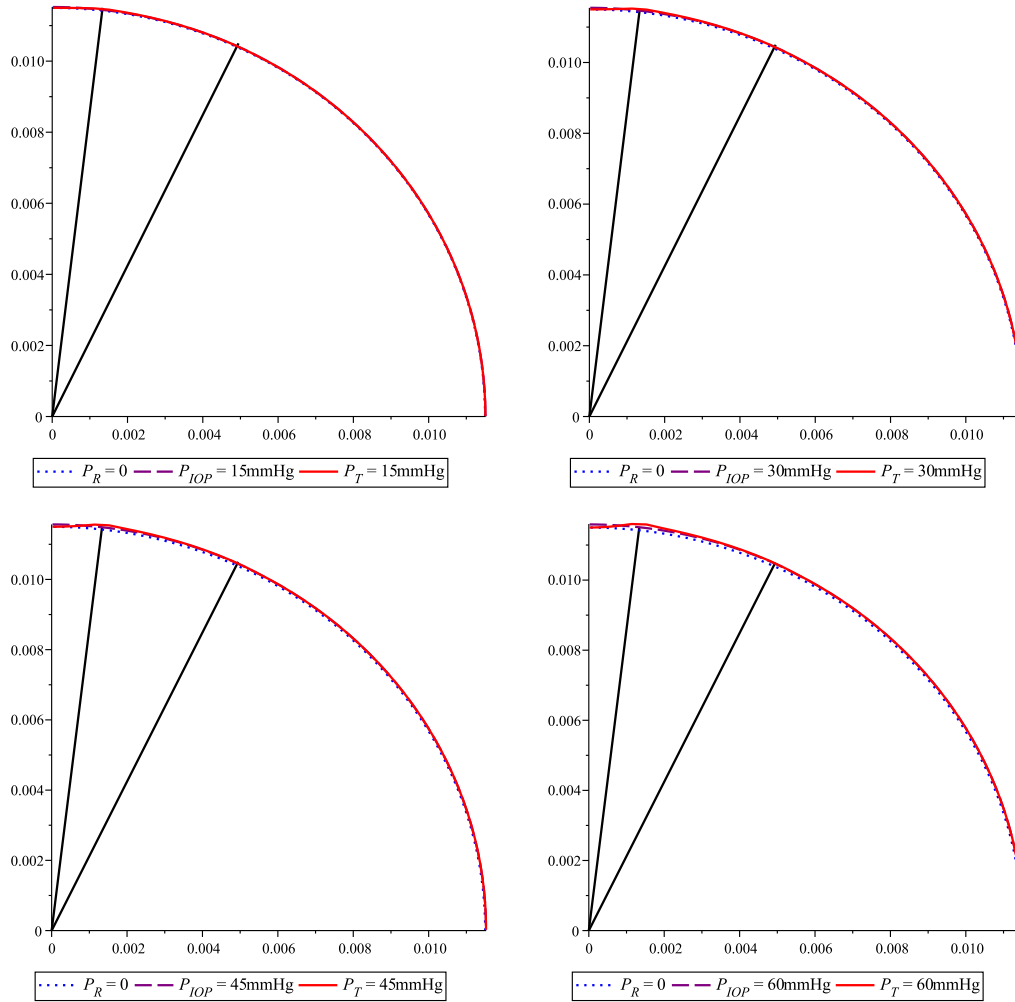


FIGURE 5.14: Qualitative behaviour of the displacements produced by the tonometer when the intraocular pressure, P_{IOP} equals the tonometer pressure, P_T at 15mmHg, 30mHg, 45mmHg and 60mmHg. This figure is the same as Figure 5.13, however these graphs only show the displacements in the quadrant between $\theta \in [0, \frac{\pi}{2}]$

the radius of the eyeball. However these results, which we are not included here, only slightly differed from those presented in Table 5.4. We conclude that above the healthy intraocular pressure, the pressure exerted from the tonometer in order to appenate the cornea is still lower than the any pressure inside the eyeball.

5.6.5.2 Scleral Buckling

We will now examine the elastic membrane of the human eyeball under the effect of the scleral buckling. The scleral buckling is one of the procedures used in treating treat rhegmatogenous retinal detachment (RRD). Usually the scleral buckle stays attached permanently after the treatment and in the long term may cause a risk to changes of the focal length of the eyeball, this has been discussed in Section 3.2.2. Thus, in this study we are interested in examining the deformation of the eyeball and the changes in

mmHg	Standard Pressure Unit (Pa)
1	133.3224
5	666.6120
10	1333.2240
15	1999.8360
20	2666.4480
25	3333.0600
30	3999.6720
35	4666.2840
40	5332.8960
45	5999.5080
50	6666.1200
55	7332.7320
60	7999.3440

TABLE 5.3: Pressure conversion units from 1mmHg to 60mmHg.

P_{IOP} (mmHg)	P_T , Current model (Pa)	P_T , Imbert-Fick law (Pa)
10	30	1333.940
15	35	2000.910
20	41	2667.880
25	47	3334.850
30	53	4001.820
35	59	4668.790
40	65	5335.760
45	71	6002.730

TABLE 5.4: The measurement data of the tonometer pressure, P_T as predicted by the current numerical model and the Imbert-Fick law that corresponds to the given values of the intraocular pressure, P_{IOP} between 10mmHg and 45mmHg.

the focal length due to pressure provoked by the scleral buckle.

Firstly, we examine the case where the scleral buckle is placed around the equator of the eyeball. In this case, we consider the load component, P_R to be the combination of the intraocular pressure, P_{IOP} and the pressure exerted by the scleral buckle, P_S , such

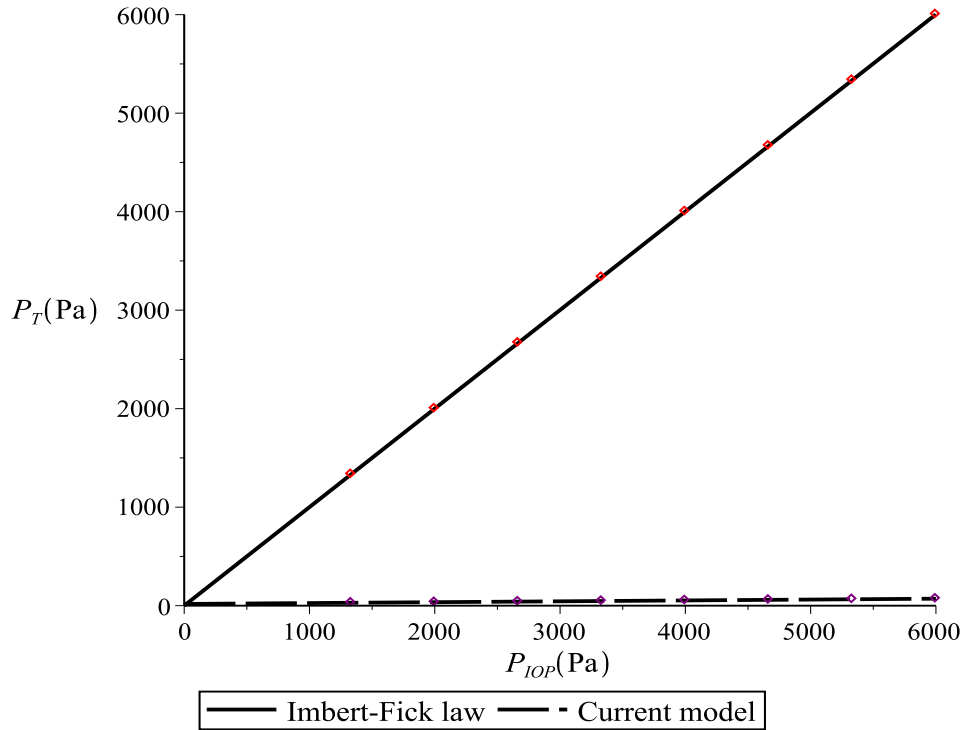


FIGURE 5.15: Numerical calculation of the tonometer pressure, P_T and comparison between the Imbert-Fick law and the current model. The solid black line represents the Imbert-Fick law and the long dashed black line denotes the current numerical model. Both are fitted curves to the data given in Table 5.4.

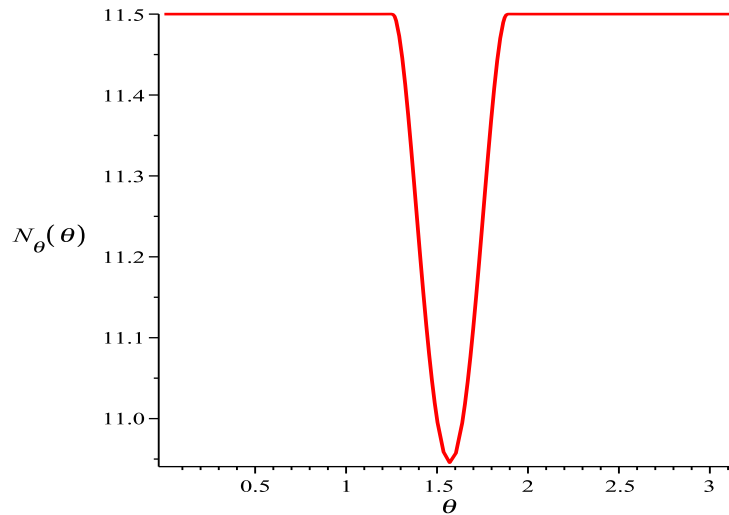


FIGURE 5.16: The axial force, N_θ distribution at the outer surface of the eyeball when the pressure exerted by the scleral buckle around the equator of the eyeball, P_S is equal to the intraocular pressure, P_{IOP} , 15mmHg. Again, the standard parameter values given in Table 5.2 were employed.

that

$$P_R(\theta) = \begin{cases} P_{IOP} & \text{if } 0 \leq \theta \leq \delta, \\ P_{IOP} & \text{if } \delta < \theta < \frac{\pi}{2} - \beta, \\ P_{IOP} + P_S \frac{\cos(\beta) - \sin(\theta)}{1 - \cos(\beta)} & \text{if } \frac{\pi}{2} - \beta \leq \theta \leq \frac{\pi}{2} + \beta, \\ P_{IOP} & \text{if } \frac{\pi}{2} + \beta < \theta \leq \pi, \end{cases} \quad (5.39)$$

where β is the angle that describes the region of contact between the eye and the scleral buckle. The angle has been assumed equal to $\frac{\pi}{10}$, [2]. Notice that this case does not need an equilibrium pressure due to the position of the scleral buckle being around the equator, thus it is self equilibrated. We now examine the first case of the scleral buckling by substituting equations (5.25), (5.26) and (5.39) into equations (5.21) - (5.24), and solve the equations numerically using the parameter values that have been introduced in Table 5.2. Figure 5.16 shows the axial force, N_θ suffered by the eyeball due to the pressure formed by the scleral buckle which is equal to the healthy intraocular pressure, 15mmHg. In Figure 5.16 we can see that the axial force is constant and equal to $11.5Nm^{-1}$ outside the scleral buckle regions, from $\theta = 0$ to $\theta = \frac{\pi}{2} - \beta$ and from $\theta = \frac{\pi}{2} + \beta$ to $\theta = \pi$. While under the scleral buckle, the axial force reduces to the minimum force that is approximately equal to $10.9Nm^{-1}$.

We now look at the deformation of the eyeball described by the displacements of six different values of pressure, exerted by the scleral buckle, at $\theta = \frac{\pi}{2}$, as given in Figure 5.17. In this figure, the dotted blue line represents the original shape of the eyeball without the intraocular pressure and the scleral buckle pressure, thus is given as $P_R = 0$. The dashed green line denotes the half shape of the eyeball where the load component normal to the shell is the intraocular pressure, $P_R = P_{IOP}$ and the solid red line denotes the deformation of the eyeball when the loads component normal to the shell is due to the intraocular pressure and the scleral buckle pressure. The region between the vertical axis and the solid black line represents the region covered by the cornea. Figure 5.17 shows that when the pressure formed by the scleral buckle, P_S is less than the intraocular pressure, P_{IOP} , the deformation of the eyeball is negligible. When we start increasing the pressure exerted by the scleral buckle around the equator, we now see a slight indentation at the equator of the eyeball. However we can do not see a larger indentation because the eyeball is too stiff due to the value of the scleral Young's modulus that has been chosen.

The results from Figure 5.18 show that the indentation under the area of pressure applied by the scleral buckle are getting bigger when we reduce the values of the Young's modulus for the scleral and corneal. When the eyeball becomes less stiff and causes a larger indentation, the shape of the eyeball changes and consequently this will affect the focal length. Due to these changes we are interested in examining the changes in focal length under the influence of the scleral buckle.

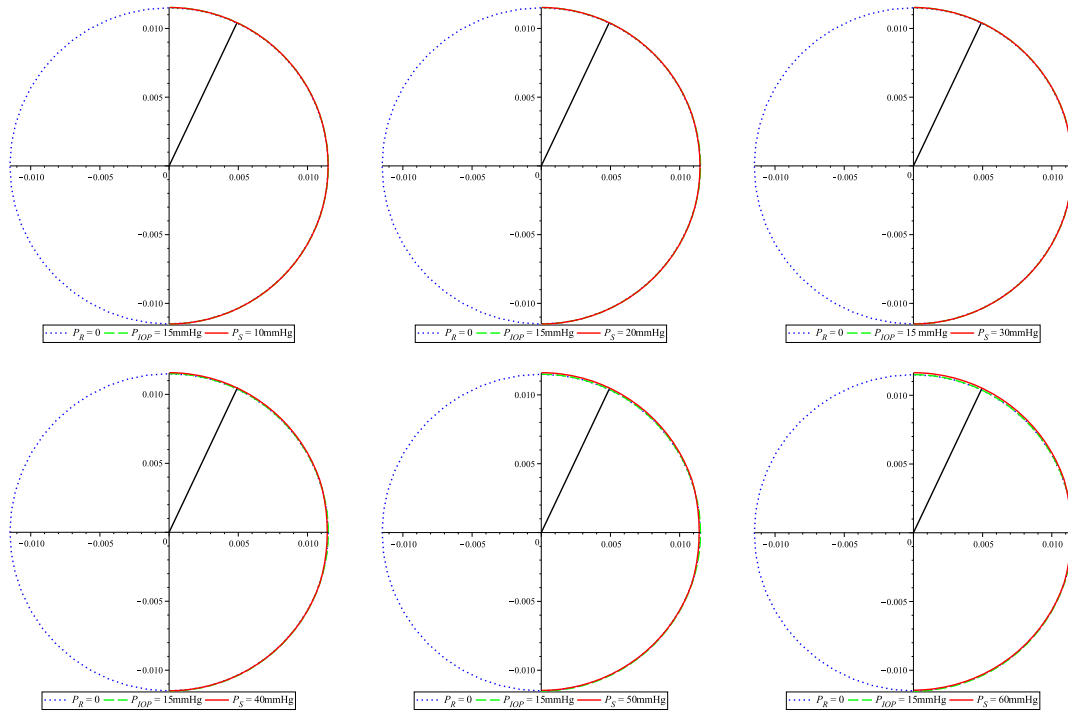


FIGURE 5.17: Qualitative behaviour given by the displacements due to the pressure exerted by the scleral buckle, P_S , at the equator of the eyeball. The values of the scleral buckle pressure are taken to be equal to 10mmHg, 20mmHg, 30mmHg, 40mmHg, 50mmHg and 60mmHg and the intraocular pressure, P_{IOP} is taken to be 15mmHg for each value of P_S . The parameter values required for these numerical calculation are the same as given in Table 5.2.

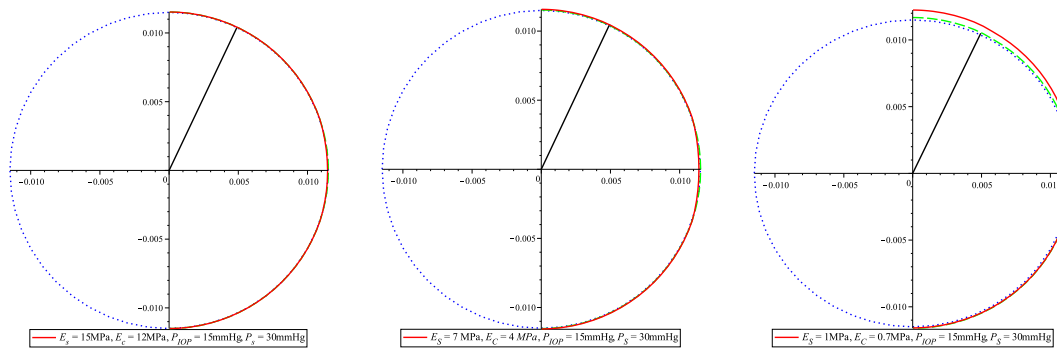


FIGURE 5.18: The deformation of the eyeball given by the displacements under the action of the scleral buckle for different values of the scleral and corneal Young's modulus. The value of the intraocular pressure, P_{IOP} has been taken to be equal to 15mmHg, the pressure provoked by the scleral buckle, P_S is equal to twice the P_{IOP} whereas the rest of the parameter values are given in Table 5.2.

We now plot the predicted focal length against the indentation applied by the scleral buckle using the linear least square fit in MAPLE, [8]. In particular, we take the value of displacements at $\theta = 0$ to be equal to the focal length changes, and double the value of displacements at $\theta = \frac{\pi}{2}$ to account for the full indentation. Figure 5.19 presents the changes in the focal length, FL of the eyeball versus the indentation, I when exerted by the presence of the scleral buckle. The intraocular pressure, P_{IOP} is assumed to be equal to 15mmHg and the pressure associated with the scleral buckle, P_S vary between 10mmHg and 60mmHg. The results in Figure 5.19 shows a constant relation between the changes in focal length for each different values of Young's modulus of the scleral and corneal, and the indentation. The results show that the changes in focal length and the indentation is in linear relation.

Next, we examine the more realistic case where the scleral buckle is placed in general around the eyeball depending on the location of the retinal detachment. In this case we introduce the load component normal to the shell for the general position of the scleral buckle is given as follows:

$$P_R(\theta) = \begin{cases} P_{IOP} & \text{if } 0 \leq \theta \leq \delta, \\ P_{IOP} & \text{if } \delta < \theta < \phi - \beta, \\ P_{IOP} + P_S \frac{\cos(\beta) - \cos(\theta - \phi)}{1 - \cos(\beta)} & \text{if } \phi - \beta \leq \theta \leq \phi + \beta, \\ P_{IOP} & \text{if } \phi + \beta < \theta \leq \pi - \kappa, \\ P_{IOP} + Q (\cos(\pi - \kappa) - \cos(\theta)) & \text{if } \pi - \kappa < \theta \leq \pi, \end{cases} \quad (5.40)$$

where ϕ is the general angle that the scleral buckle is going to be placed around the eyeball and Q is the equilibrium pressure which is needed, in this case, in order to maintain the equilibrium condition. To examine the deformation of the eyeball and the changes of the focal length under the scleral buckle loading condition given in equation (5.40), we then have to repeat the same steps of solving the problems of tonometry and the scleral buckling at the equator. For the purpose of numerical calculations, we are assuming $\phi = \frac{\pi}{3}$, $\beta = \frac{\pi}{10}$ and the remaining parameter values are such as shown in Table 5.2. Figure 5.20 presents the axial forces, N_θ imposed by the outer surface of the eyeball due to the presence of the scleral buckle. The results in Figure 5.20 shows the axial force remains constant at 11.5Nm^{-1} from the north pole to the scleral buckle region. Under the scleral buckle region, the axial force decreases approximately to 7.0Nm^{-1} and then the axial force increased slightly and decreased to -4.0Nm^{-1} due to the equilibrium condition.

We now analyse the deformation of the eyeball under the different pressure exerted by the scleral buckle near the equator when the pressures are between 10mmHg and 60mmHg, see Figure 5.21. The dotted blue line represents no loading applied to the eyeball and this is given by $P_R = 0$, whereas the dashed green line corresponds to the intraocular pressure and the solid red line denotes the deformation of the eyeball due to

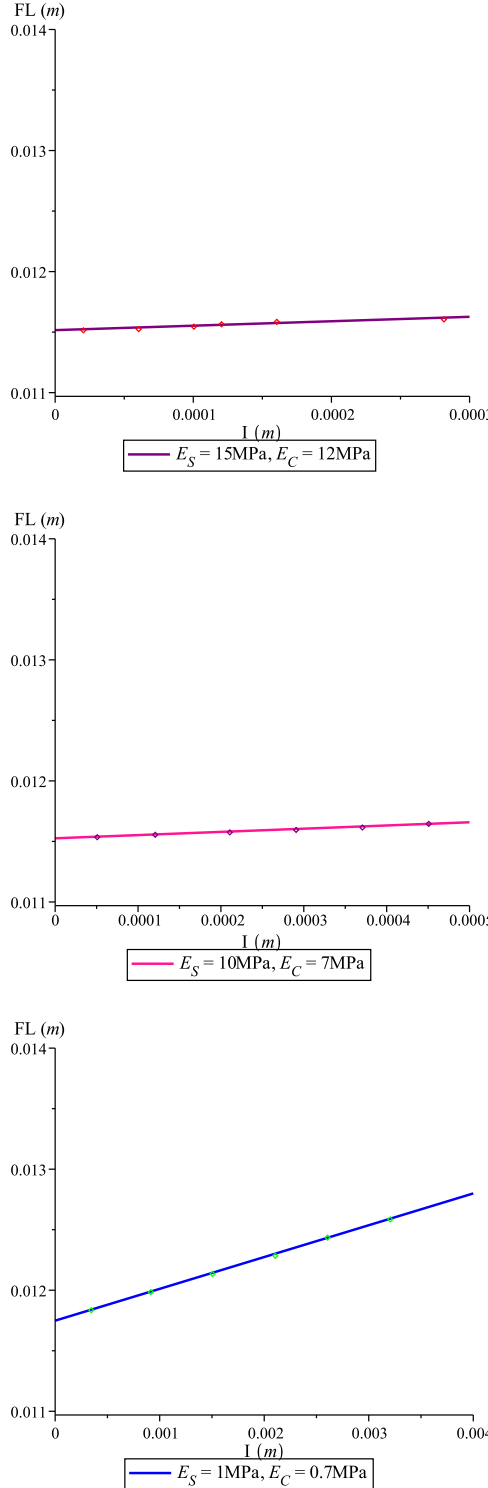


FIGURE 5.19: Numerical calculation of the changes in the focal length around the equator of the eyeball under the pressure exerted by the scleral buckle. The points show the measurement data of the changes in focal length against the indentation whereas the solid lines are fitted curves to the points. The intraocular pressure, P_{IOP} is given by 15mmHg and the pressure exerted by the scleral buckle are taken to be equal to 10mmHg, 20mmHg, 30mmHg, 40mmHg, 50mmHg and 60mmHg. Each graph corresponds to different values of the scleral and corneal Young's modulus, E_s and E_c .

The remaining parameters are given in Table 5.2.

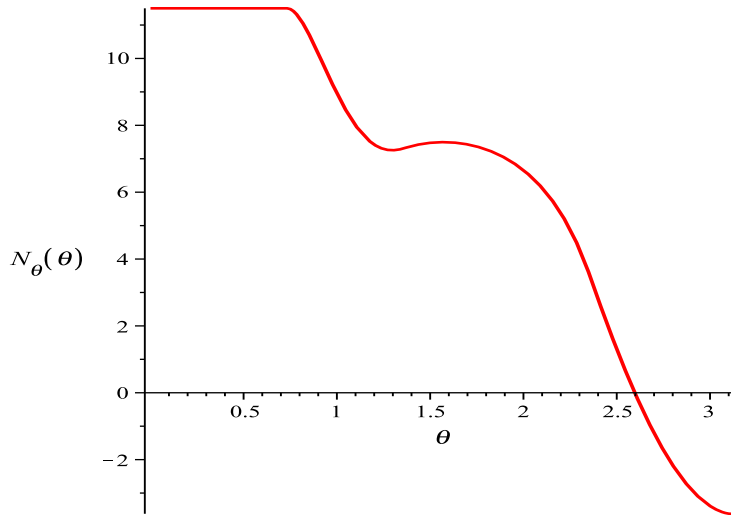


FIGURE 5.20: The axial force, N_θ distribution at the outer surface of the eyeball under the action of the scleral buckle near the equator of the eyeball. The pressure exerted by the scleral buckle, P_S is assumed to be equal to the intraocular pressure, P_{IOP} , 15mmHg, whereas the remaining parameter required for these numerical calculations have been given in Table 5.2.

the effect of the scleral buckle. Figure 5.21 shows the eyeball is not yet deformed when the pressure provoked by the scleral buckle is less than the normal intraocular pressure, 15mmHg. The eyeball starts deforming a little bit when we increase the pressure from the scleral buckle, P_S from 20mmHg to 60mmHg. However, the deformation increases slightly due to the elastic rigidity of the wall of the eyeball. We then carried out an analysis of the shape of the eyeball by reducing the value of the Young's modulus for the sclera and the cornea, and the results of this has been shown in Figure 5.22. The results given in Figure 5.22 show that if the rigidity of the elastic membrane of the eyeball is reduced, then the deformation under the region of contact between the surface of the eyeball and the scleral buckle is increased.

In the study of the scleral buckle near the equator, we also examine the changes in the focal length under the action of the scleral buckle, by predicting the values of the displacements at $\theta = 0$. We then plotted and fitted the changes in the focal length, FL against the indentation, I exerted by the scleral buckle at $\phi = \frac{\pi}{3}$ using the linear least squares method, see Figure 5.23. Figure 5.23 shows the focal length againts the indentation for each different material value of the scleral and the corneal Young's modulus is in linear relation such as the results given in Figure 5.19. Although both results in Figure 5.19 and Figure 5.23 are given the similar linear relations which mean the changes in the focal length are quite small, however the modified focal length seems to be more affected by the indentation suffered by the surface of the eyeball when the scleral buckle is placed near the equator.

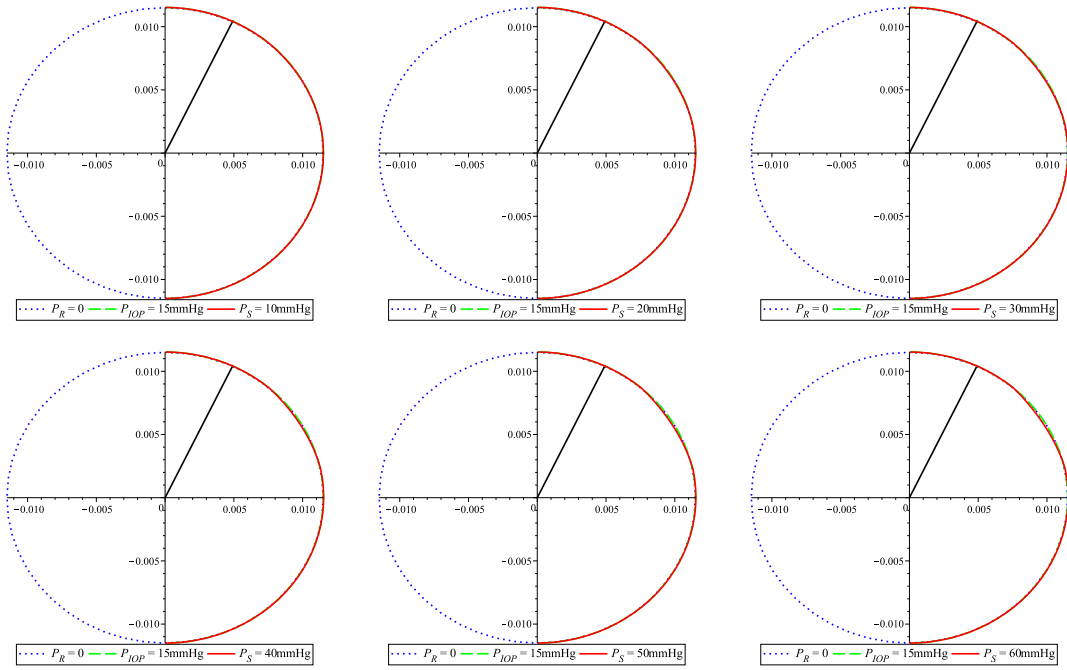


FIGURE 5.21: Qualitative behaviour of the shape of the eyeball presented by the displacements due to the pressure exerted by the scleral buckle, P_S , near the equator. The value of the the intraocular pressure, P_{IOP} is taken to be equal to 15mmHg for each different corresponding values of the pressure exerted by the scleral buckle which are equal to 10mmHg, 20mmHg, 30mmHg, 40mmHg, 50mmHg and 60mmHg. The parameter values inherent to these numerical calculation are given in Table 5.2.

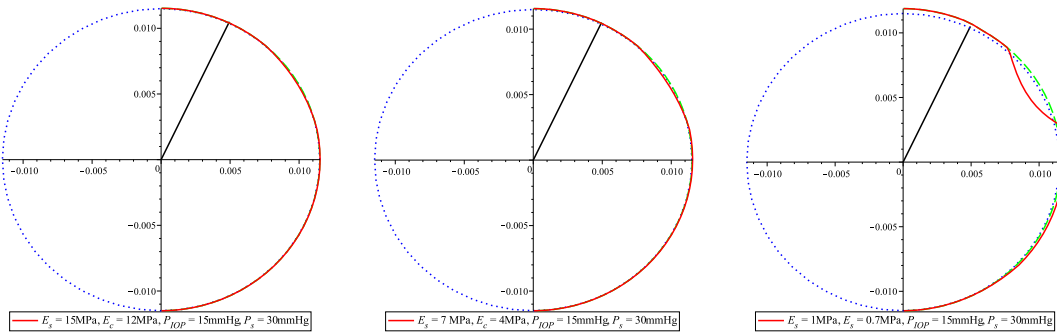


FIGURE 5.22: The deformation of the eyeball near the equator presented by the displacements due to the pressure exerted by the scleral buckle, P_S which is equal to two times the intraocular pressure, P_{IOP} for different values of the Young's modulus of the sclera and the cornea.

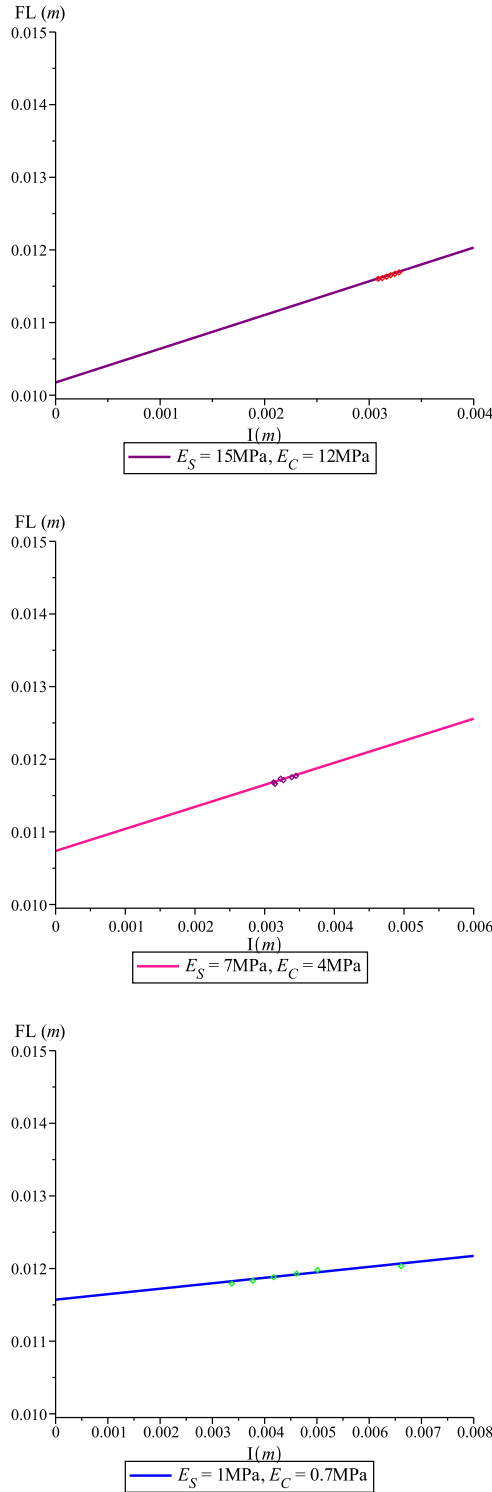


FIGURE 5.23: Numerical calculation of the modified focal length of the eyeball near the equator for different material values of the Young's modulus of the sclera and the cornea. The standard parameters given in Table 5.2 are employed in these graph. The intraocular pressure, P_{IOP} is taken to be 15mmHg and the pressure provoked the indentation at $\phi = \frac{\pi}{3}$ are taken to be varied between 10mmHg to 60mmHg. The points show the measurement data of the modified focal length versus the indentation, whereas the solid lines are fitted curves that coresspond to the measurement data.

5.7 Conclusions and Further Work

In this study, we have developed a mathematical model of the eyeball based on membrane shell theory. This eyeball model has been assumed to be an elastic membrane shell, a hollow sphere in which the thickness and Young's modulus various and isotropic in the shell surface. We have considered the membrane shells in spherical coordinates under the equilibrium and axisymmetric conditions to develop the governing equations and we also have proposed the suitable boundary conditions due to the physical conditions of the eyeball membrane. Then we have examined numerically the resulting stresses, the meridian force and the hoop force, and also the displacements using MAPLE [8] under various loading conditions due to the tonometer and the scleral buckle. These two problems required different function of pressure, P_R , that is applied to the eyeball membrane in the direction normal to the surface according to the pressure difference between the intraocular pressure and the pressure exerted either by the tonometer or the scleral buckle.

Firstly, we proposed a mathematical model of applanation tonometer which we used to study the effect of the tonometer on the shape of the eyeball and to verify the Imbert-Fick law. The numerical results have shown that when the pressure exerted by the tonometer increases from normal eye pressure to the high intraocular pressure, the area under the tonometer tip is over applanate. The behaviour of the results are not corresponding to what we are expected because according to the Imbert-Fick law if the pressure exerted by the tonometer is proportional to the intraocular pressure then the cornea will applanate. The numerical calculations of the measurement of the applanation pressure also have shown that our model not quantitatively agree with the results obtained from the Imbert-Fick law. Even though the results behave differently to the Imbert-Fick law, these results put into whether question the Imbert-Fick law is really true in measuring the intraocular pressure inside an eyeball. The numerical results suggest that our model needs some modification and extension for further work due to the pressure exerted from the tonometer to applanate the cornea is still lower than the intraocular pressure. We think that the major difficulty in this problem is that the collagen fibres that make up the stroma of the sclera and cornea are almost impossible to stretch but may be much easier to compress. Due to this problem we can modify the current eyeball model by considering the eyeball membrane to be a non-isotropic elastic material with a different Young's modulus in each of the directions, θ and ϕ . By considering this we may allow the collagen fibres to be in tension in one direction so the collagen fibres will be stretched and then in compression in the other direction so that the collagen fibres have very low stresses.

Secondly, we developed a mathematical model of a scleral buckle and examined the outer surface of the membrane eyeball when the scleral buckle has been placed either around the equator or anywhere around the eyeball due to the location of the retinal

detachment. We then examined the changes in focal length against the indentation provoked by the scleral buckle. The results presented in this study, show that the modified focal length against the indentation in both the scleral buckle cases are in linear relation. These results have shown that the indentation exerted by the scleral buckle may be affected the changes in focal length. The numerical results also have shown that the indentation affected by the scleral buckle depends on the modulus of rigidity of the membrane eyeball itself. This means that a smaller indentation corresponds to a stiffer eyeball. Notice that when we older the modulus of rigidity of the eyeball increases. This may affect the changes in shape of the eyeball and also reduce vision. However, the bigger indentation might influence in changes in the focal length of the eyeball. Due to this risk, complications such as astigmatism and direct injury to a rectus muscle may occur.

Finally, we note that the work of this chapter seems to show that it is quite difficult to formulate a simple mathematical model for tonometry. Though such a model would undoubtedly be very useful (as it would allow a firm theoretical basis to be established for the Imbert Fick principle), it may be the case that the only hope of carrying out useful predictions is to use a fully three dimensional non linear elastic numerical simulation.

Chapter 6

Conclusions

This research contains four different of the human eye problems, which we examined by understanding the mathematical behaviour of the relevant governing equations. The mathematical models of flow and deformation in the human eye proposed in this research may improved the understanding of the fluid and solid dynamics of the human eye, and how does its influence on eye diseases. These mathematical models can be invaluable help and gave ideas for researchers to improve and implement more realistic physiological conditions by considering the physiological features that have been neglected. Moreover, these models also may answer the questions that arises from doctors and ophthalmologists, and assist them to understand more about the human eye mechanisms and to make the decisions for treatments.

This section contains a summary of the work completed and future possible improvements of the mathematical models for each problem. The main components of the human eye and its functions as well as three common causes of vision loss which are primary open angle glaucoma (POAG), rhegmatogenous retinal detachment (RRD) and descemet membrane detachment (DMD) have been presented in Chapter 1. In this chapter, the contributions of the thesis was also stated.

In Chapter 2, we discussed a problem regarding the progress of POAG. The investigation considered in this problem is focused on the mathematical model of aqueous humour flow through the trabecular meshwork and into the Schlemm canal. This problem has been extended from the work of [23] in order to predict changes in intraocular pressure. The derivation of the governing equations, the appropriate boundary conditions and then the Friedenwald's law were stated. We discussed several different cases relating aqueous humour flow to changes in intraocular pressure including paradigm and complex subcases: (i) the permeability, k in Darcy's law may be either constant or not constant; (ii) the trabecular meshwork is assumed to be deformable; allowing the general theory of beam bending to be applied. We solved these cases analytically and some of the cases we solved by using the regular and singular perturbation method.

For complex cases, higher order equations, we used MAPLE [8] in order to assist the solution process.

Most of the cases that have been examined are shown that we could predict the times and changes in intraocular pressure however only a few subcases cannot be examined because those subcases do not valid and not satisfy the solid boundary conditions. From the results we found that the intraocular pressure rapidly increases due to the fact that the aqueous humour cannot exhaust quickly enough into a collector channel because the trabecular meshwork is not functioning properly. As a result, the intraocular pressure increases rapidly and this may be a strong influence on POAG. In this circumstances, if the high intraocular pressure could not be controlled, then blindness will be an inevitably result. In addition, some cases that have been examined have shown that there is no resistance to the aqueous humour flowing across the trabecular meshwork and exiting a collector channel. Thus, the intraocular pressure remains normal and we can expect that the eye will be healthy.

In this first problem, we conclude that the trabecular meshwork is an important function in predicting the intraocular pressure values because the trabecular meshwork acts as a porous medium and it could be a resistance to the aqueous humour flow from the anterior chamber to the Schlemm canal before exiting at a collector channel. Thus in modelling of the aqueous humour flow through the trabecular meshwork and into the Schlemm canal, we suggest for future work that the trabecular meshwork behaviour cannot be simply ignored but we have to consider the function in order to get closer to a realistic problem and to determine an accurate values of intraocular pressure.

The mathematical modelling of retinal detachment was developed in Chapter 3. In this chapter, we presented a paradigm mathematical model of fluid flow past a detached retina. Specifically we used the lubrication theory limit of the Navier-Stokes equations in order to study the steady two-dimensional incompressible fluid flow problem. Then we analysed the flow between two rigid walls with a thin flap attached to one of the rigid walls and we considered a thin flap to be elastic and deformable so that the general theory of beam bending is applicable. We have discussed the flow behaviour, the deformation of the detached retina, the volume fluxes in two regions and also the bending moment at the end of the detached retina by using the asymptotic analysis. We sought to model the fluid flow driven by pressure gradient through the detached retina in order to analyse the flow behaviour and the deformation of the the detached retina. We modelled the flow between one rigid wall which is a thin flap is attached to the wall and one moving wall and we solved the problem using asymptotic analysis.

In both paradigm mathematical models of retinal detachment, the results have shown that we could examined analytically and numerically the vitreous humour flow through the detached retina. Under these modelling assumption, we found that there is no vitreous humour flow through the space between the tiny tear of retina and the choroid.

Furthermore the results show that whether the deflection of the detached retina becomes either much less or more deformed depends on several physical factors. The physical factors that could be effected the retina deflection such as the length of the retina tear, the pressure difference, the elasticity of the retina and the flow directions. In these paradigm mathematical models, we conclude that even though we could possible examine these two dimensional models, they may still be far away from being realistic models. Therefore for further improvement, we also developed a mathematical model of retinal detachment in three dimensional flow.

We considered the liquefied vitreous humour flow driven by saccadic eye movements through the detached retina. Then we examined several cases in terms of sizes of three dimensionless parameters which are the amplitude oscillations, ε , the Wormesly number, α , and the aspect ratio of the initial height of the detached retina over the eyeball radius, δ , see appendix C. We have solved the Navier-Stokes equations in spherical coordinate system using asymptotic series expansions in various sizes of these three dimensionless parameters. The results in most cases have shown that we could determined the velocity in azimuthal direction at leading and next order. However we could not determine the velocities in radial and zenith directions and also the pressure. Thus in this problem we are not be able to calculate and examine analytically the fluid flow behaviour and the deformation of the retina detachment due to the cases are too complicated and higher order difficulties.

In the problem related to the progression of retinal detachment during saccadic eye motions, we recommend the following cases which are Case (5), Case (6), Case (7) and Case (10) are the realistic cases that could be carried out for future work. The model also could be improved by considering the refinement geometry of the detached retina and the implementation to the boundary conditions to be more realistic. Future alternative for continuing this study is to apply the other mechanisms that drive the flow in the posterior chamber. The nature of flow driven mechanisms is varied, in this study we have considered the flow driven by saccadic eye motions. However the other mechanisms such as phakodenesis driven flow, buoyancy driven fluid motion, flow driven by the pressure differential between the posterior and anterior chambers and many more may be useful in the developing a new mathematical model.

A mathematical model of aqueous humour in the anterior chamber during DMD was been developed in Chapter 4. Buoyancy effects are considered to be the most important mechanism that cause the aqueous humour flow in the anterior chamber, [78]. A fluid mechanical model of buoyancy-driven flow in the anterior chamber of the human eye has been studied by [75]. In this work, the boundary conditions for the temperature at the cornea has been modified. We have also modified the model to include the presence of a detached descemet membrane in the flow in purpose to examine the flow behaviour during DMD that may cause either spontaneous reattachment or worsening of detachment. This model was studied using the lubrication theory limit of the Navier-

Stokes equations. Specifically fluid flow in the anterior chamber is described as a flow driven by buoyancy effects due to the existing temperature difference between the cornea and the pupil. The detached descemet membrane which is kept in contact with the cornea is assumed to be elastic and deformable so the general theory of beams under axial loading has been applied. Using asymptotic analysis the flow behaviour and the deformation of the DMD have been analysed. As a comparison for this simplified model a numerical simulation has been carried out using COMSOL, [72].

There are two models that have been carried out in Chapter 4. Each model has been considered different geometric shaped of the anterior chamber. In the first mathematical model, we considered non realistic shaped of the anterior chamber, *i.e.* the rectangular shaped region. The purpose is to investigate the behaviour of fluid flow and the deformation of the flap under the effect of temperature difference between the top and bottom plates before we could proceed to more realistic model. The analytical results of this simple model showed a qualitative and quantitative agreement with the numerical simulation results and we also could calculate the pressure difference above and below the flap. The results obtained in the first model convinced us to proceed with the more realistic shaped of the anterior chamber. In the second model, we have considered a dome shaped to be the geometry of the anterior chamber. For ease of simplicity and visualising results, we only interested in two dimensional system because it is more straight forward. The results obtained in the second model have shown that we can simply calculate the solutions both analytical and numerical under of reasonable assumptions and we can visualise the progression of a detached Descemet membrane either it leads to spontaneous reattachment or redetachment. In the third problem consists of DMD, we suggest that for further improvement we could extend the study to three dimensional model and improved the shaped of DMD due to the type or severity of DMD is important because it can influence treatment.

Chapter 5 presented mathematical modelling of the eyeball membrane under the effect of the tonometer and the scleral buckle. In this chapter we presented a brief discussion about the anatomy and physiology of the eyeball, the instrument that measuring the intraocular pressure, the derivation of the governing equations and the boundary conditions using the theory of membrane shells in spherical coordinates under the equilibrium and the axisymmetric conditions. We then calculated and examined numerically the outer surface of the eyeball due to the action of the tonometer and the scleral buckle.

In the study of the effect of the tonometer, we examined the shape of the eyeball and we verified the validity of the Imbert-Fick law that has been applied in the measurement of the intraocular pressure by the Goldmann applanation tonometry. The numerical results have shown that our model quantitatively agree with the Imbert-Fick law when the applanation pressure equals the intraocular pressure at less than and equal to 20mmHg. However our model did not quantitatively agree with the Imbert-Fick law when the intraocular pressure increases to more than 20 mmHg to the high intraocular

pressure. The applanation pressure is no longer proportional to the intraocular pressure but lower than any pressure inside the eyeball. The difference between our numerical results and the results obtained from the Imbert-Fick law put into whether question the validity of the Imbert-Fick law. Thus we concluded that neither our model nor the Imbert-Fick law can be trusted in measuring the intraocular pressure. For further refinement to our tonometry problem, we suggest that the eyeball membrane can be modify by assuming the material to be non isotropic in order to make the Young's modulus in the directions θ and ϕ . The modification of this model is required due to the trouble of collagen fibres that make up the cornea and sclera which is cause the eyeball difficult to stretch but easily to compress.

Next we examined the deformation of the outer surface of the eyeball under the pressure exerted by the scleral buckle either at the equator or near the equator. We also predicted the changes in the focal length of the eyeball and the indentation provoked by the scleral buckle. The results have presented the linear relation between the changes in focal length and the indentation provoked by the buckle in both scleral buckle cases. The results also shown that for different values of the Young's modulus of the sclera and cornea, the results in both cases still show the same linear relation. These results may prove useful to predict the modified focal length of the eye under the action of the sclera buckle that place around the eyeball.

A mathematical model of tonometry and scleral buckle may also be carried out for further work. However before we can examine the problem, we have to ensure that the Imbert-Fick law is valid. The purpose of doing this model is to examine whether is there any problem to the intraocular measurement under the action of a scleral buckle. In general, the modelling of the tonometry, the scleral buckling and both could be improved by considering the real geometry shape of the eyeball because in real life the eyeball differs slightly from a sphere.

Appendix A

Linearization of Friedenwald's law

A.1 Introduction

Friedenwald [25] studied the relationship between the volume and the intraocular pressure of a human eye. The resulting Friedenwald's law stated that p_1 and p_2 (two values of intraocular pressure) are related to respective ocular volumes V_1 and V_2 (measured in μl) via

$$K(V_1 - V_2) = \log_{10} p_1 - \log_{10} p_2 \quad (\text{A.1})$$

where $K \sim 0.025/\mu l$ [24] is a constant. Simplifying equation (A.1), thus we get that

$$V_2 = V_1 - \frac{1}{K} \left[\log_{10} \frac{p_1}{p_2} \right]. \quad (\text{A.2})$$

It became clear in Chapter 5 that the nature of material response (linear elastic/non linear elastic) is a crucial matter in any possible model of tonometry or scleral buckling. The only well-accepted model for the deformation of an eye globe seems to be the Friedenwald law. In this appendix, we therefore seek to test how well linear elasticity can approximate the Friedenwald law.

A.2 The Governing Equations

We consider the equation of equilibrium given in [133]; this is,

$$(1 - 2\sigma) [\bar{\nabla} \cdot (\bar{\nabla} \bar{u})] + \bar{\nabla} (\bar{\nabla} \cdot \bar{u}) = 0 \quad (\text{A.3})$$

where the deformation of the body is caused only by forces applied to its surfaces, $\bar{u} = u_r$ denotes a displacement in r direction and $\sigma = 0.49$ represents a Poisson's ratio. If we now simplify equation (A.3), we may find that

$$2\bar{\nabla}(\bar{\nabla} \cdot \bar{u}) - (1 - 2\sigma)(\bar{\nabla} \times (\bar{\nabla} \times \bar{u})) - 2\sigma(\bar{\nabla}(\bar{\nabla} \cdot \bar{u})) = 0$$

Therefore we can write equation (A.3) as

$$2(1 - \sigma)\bar{\nabla}(\bar{\nabla} \cdot \bar{u}) - (1 - 2\sigma)(\bar{\nabla} \times (\bar{\nabla} \times \bar{u})) = 0 \quad (\text{A.4})$$

Since $\bar{\nabla} \times \bar{u} = 0$, equation (A.4) reduces to

$$\begin{aligned} \bar{\nabla}(\bar{\nabla} \cdot \bar{u}) &= 0 \quad ; \quad \bar{\nabla} \cdot \bar{u} = \frac{1}{r^2} \frac{d(r^2 u_r)}{dr} = \text{constant} = 3a \\ \frac{d}{dr}(r^2 u_r) &= 3ar^2. \end{aligned}$$

If we now integrate both sides of the equation above, we may obtain that

$$r^2 u_r = 3a \int r^2 dr = ar^3 + b$$

Thus the radial displacement is

$$u_r = ar + \frac{b}{r^2} \quad (\text{A.5})$$

where a and b are integration constants that should be determined. From the components of the strain tensor in spherical coordinates [133], we only consider

$$\begin{aligned} u_{rr} &= \frac{\partial}{\partial r} \left(ar + \frac{b}{r^2} \right) = a - \frac{2b}{r^3}, \\ u_{\theta\theta} &= \frac{1}{r} \frac{\partial u_\theta}{\partial \theta} + \frac{u_r}{r} = a + \frac{b}{r^3}, \\ u_{\phi\phi} &= \frac{1}{r \sin \theta} \frac{\partial u_\phi}{\partial \phi} + \frac{u_\theta}{r} \cot \theta + \frac{u_r}{r} = a + \frac{b}{r^3}. \end{aligned}$$

We now consider the radial stress (see [133]) and we simplify the equation by substituting the above components of the strain tensor, to get that

$$\sigma_{rr} = \frac{E}{(1 + \sigma)(1 - 2\sigma)} \{(1 - \sigma)u_{rr} + \sigma(u_{\theta\theta} + u_{\phi\phi})\}$$

Since $u_{\theta\theta} = u_{\phi\phi}$, then we may find that

$$\sigma_{rr} = \frac{E}{(1 - 2\sigma)} a - \frac{2E}{(1 + \sigma)} \frac{b}{r^3} \quad (\text{A.6})$$

where E is a modulus of elasticity.

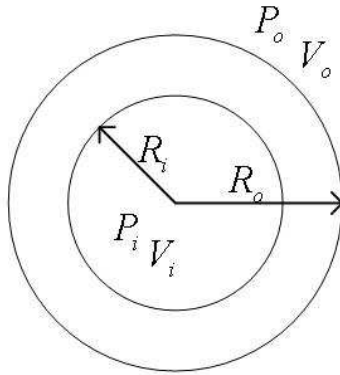


FIGURE A.1: Schematic diagram of the sclera presenting the outer and the inner radius, R , pressure, P and volume, V .

A.3 Boundary Conditions

From Figure A.1, the boundary conditions for this problem are

$$\sigma_{rr}(r = R_i) = -P_i, \quad \sigma_{rr}(r = R_o) = -P_o \quad (\text{A.7})$$

P_i where is a pressure inside the sclera, $\sim 1 \text{ atm} + 15 \text{ mm Hg}$, pressure outside the sclera, $P_o = 1 \text{ atm}$, the inner radius, $R_i = 12 \times 10^{-3} \text{ mm}$, the outer radius, $R_o = 16 \times 10^{-3} \text{ mm}$, the inner volume, V_i and the outer volume, V_o . Then we substitute the boundary conditions (A.7) into equations (A.6) in order to determine the integral constants a and b . From the first boundary conditions, we get

$$\frac{E}{(1 - 2\sigma)}a = \frac{2E}{(1 + \sigma)} \frac{b}{R_i^3} - P_i \quad (\text{A.8})$$

and from the second boundary conditions, we find that

$$\frac{E}{(1 - 2\sigma)}a = \frac{2E}{(1 + \sigma)} \frac{b}{R_o^3} - P_o. \quad (\text{A.9})$$

We now equate equations (A.8) and (A.9), yeilding

$$b = \left(\frac{R_i^3 R_o^3}{R_o^3 - R_i^3} \right) (P_i - P_o) \left(\frac{1 + \sigma}{2E} \right). \quad (\text{A.10})$$

Substituting equation (A.10) into equation (A.8), we obtain

$$a = \frac{P_i R_i^3 - P_o R_o^3}{R_o^3 - R_i^3} \cdot \frac{1 - 2\sigma}{E}. \quad (\text{A.11})$$

Therefore, by substituting equations (A.10) and (A.11), equation (A.5) becomes

$$u_r = \frac{P_i R_i^3 - P_o R_o^3}{R_o^3 - R_i^3} \cdot \frac{1 - 2\sigma}{E} r + \left(\frac{R_i^3 R_o^3}{R_o^3 - R_i^3} \right) (P_i - P_o) \left(\frac{1 + \sigma}{2E} \right) \frac{1}{r^2}. \quad (\text{A.12})$$

In order to compare with Friedenwald's law (A.2), then we define

$$V_i = \frac{4}{3}\pi(u_r + r)^3,$$

which is $r = R_i$. Therefore the inner volume, V_i becomes

$$V_i = \frac{4}{3}\pi \left(\frac{P_i R_i^3 - P_o R_o^3}{R_o^3 - R_i^3} \cdot \frac{1 - 2\sigma}{E} R_i + \left(\frac{R_i^3 R_o^3}{R_o^3 - R_i^3} \right) (P_i - P_o) \left(\frac{1 + \sigma}{2E} \right) \frac{1}{R_i^2} + R_i \right)^3. \quad (\text{A.13})$$

A.4 Linearization

We now reconsider Friedenwald's law given in equation (A.2) in order to do a linearization therefore we assume $V_1 \rightarrow V_1 + \beta\varepsilon = V_2$ and simplify equation (A.2), we obtain

$$p_2 = p_1 [1 + K\beta\varepsilon \ln 10].$$

Let $\bar{\beta} = p_1 K \beta \ln 10$, therefore if $p_1 \rightarrow p_1 + \bar{\beta}\varepsilon$ then we get

$$V_1 \rightarrow V_1 + \frac{\bar{\beta}}{p_1 K \ln 10} \varepsilon.$$

Given that $P_o = 1 \text{ atm}$, $R_o = 16 \times 10^{-3} \text{ mm}$, $\sigma = 0.49$ and $E = 2.7 \times 10^6$, and substituting all into equations (A.10) and (A.11), thus

$$b = \frac{R_i^3 (1.13018 \times 10^{-12})}{4.096 \times 10^{-6} - R_i^3} (P_i - 101325)$$

and

$$a = \frac{P_i R_i^3 - 0.41503}{4.096 \times 10^{-6} - R_i^3} (7.40741 \times 10^{-10}).$$

We rewrite equations (A.12) and (A.13), to obtain

$$\begin{aligned} u_{R_i} &= \frac{P_i R_i^3 - 0.41503}{4.096 \times 10^{-6} - R_i^3} (7.40741 \times 10^{-10}) R_i \\ &+ \frac{R_i^3 (1.13018 \times 10^{-12})}{4.096 \times 10^{-6} - R_i^3} (P_i - 101325) \frac{1}{R_i^2} \end{aligned} \quad (\text{A.14})$$

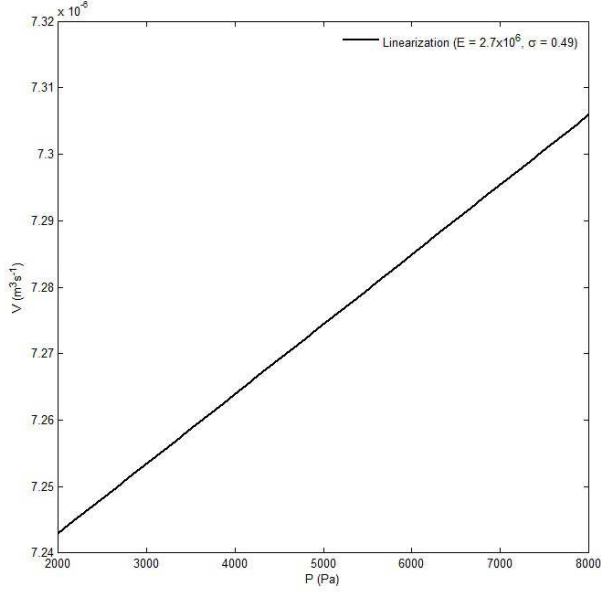


FIGURE A.2: The graph of volume, V versus intraocular pressure, P for linear elastic theory given in equation (A.15). The standard parameter values given in section (A.1 - A.4).

and

$$V_i = \frac{4}{3}\pi \left(\frac{\frac{P_i R_i^3 - 0.41503}{4.096 \times 10^{-6} - R_i^3} (7.40741 \times 10^{-10}) R_i}{+ \frac{R_i^3 (1.13018 \times 10^{-12})}{4.096 \times 10^{-6} - R_i^3} (P_i - 101325) \frac{1}{R_i^2} + R_i} \right)^3. \quad (\text{A.15})$$

When $P_i = 1 \text{ atm} + 15 \text{ mm Hg}$ and $R_i = 12 \times 10^{-3} \text{ mm}$ then substituting into equations (A.14) and (A.15), we find that

$$u_{R_i} = 1.05657 \times 10^{-5}, \quad V_i = 7.25737 \times 10^{-6}.$$

But when $P_i = 1 \text{ atm} + 15 \text{ mm Hg} + \beta\varepsilon$ and $R_i = 12 \times 10^{-3} \text{ mm}$ then substituting into equations (A.14) and (A.15) gives

$$u_{R_i} = 5.7328 \times 10^{-9} \cdot \beta\varepsilon + 1.05638 \times 10^{-5}$$

and

$$V_i = 8.0576 \times 10^{-18} \cdot \beta\varepsilon + 4.9549 \times 10^{-15}.$$

A.5 Numerical Results

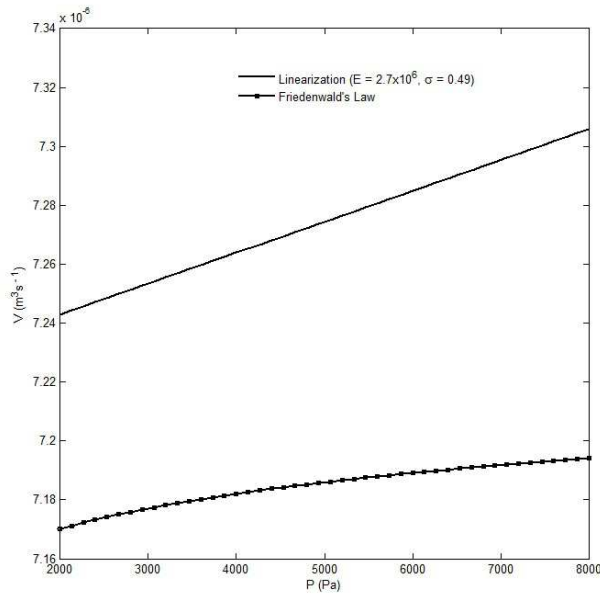


FIGURE A.3: The comparison graph of volume, V versus intraocular pressure, P between linear elastic theory such as given in Figure A.2 and Friedenwald's law given in equation (A.2). The solid line represents the volume changes for linear elastic theory whereas the line with the square marker denotes the Friedenwald's law. The parameter values are given in section (A.1 - A.4) are employed in this calculation.

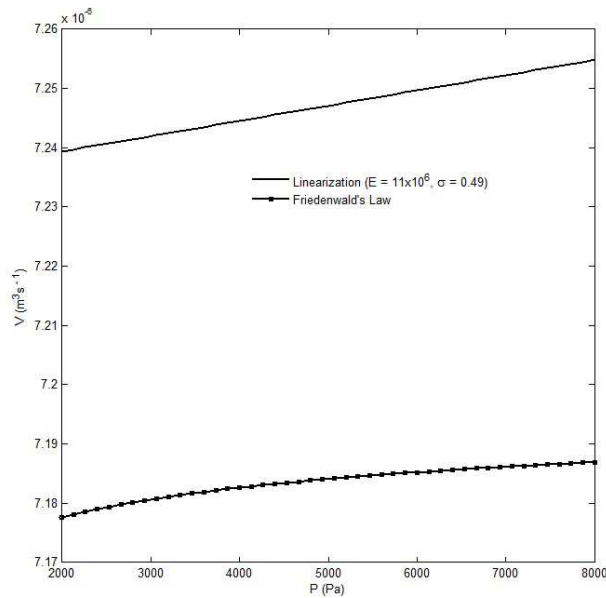


FIGURE A.4: The comparison between linear elastic theory and Friedenwald's law given in equations (A.15) and (A.2). The solid line represents the volume changes for linear elastic theory whereas the line with square marker denotes the volume changes for Friedenwald's law. The modulus of elasticity, E is considered to be 11×10^6 and the other parameter values given in section (A.1 - A.4) are employed in this graph.

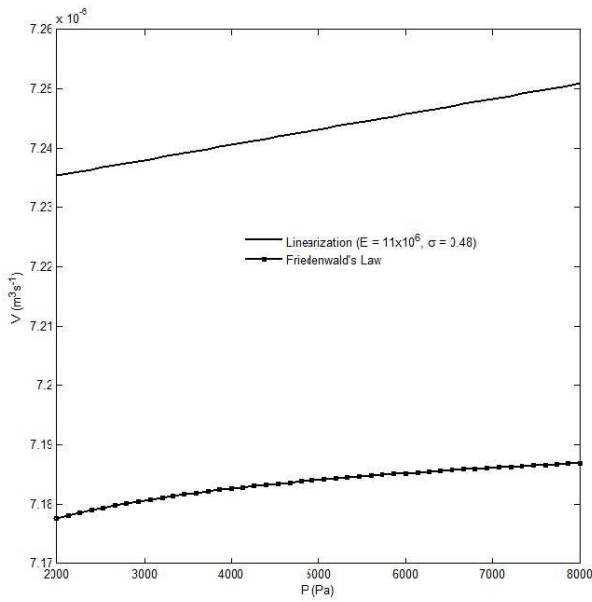


FIGURE A.5: The comparison between linear elastic theory and Friedenwald's law given in equations (A.15) and (A.2). The line with square marker and the solid line represent the corresponding volume, V versus intraocular pressure, P for Friedenwald's law and linear elastic theory. The modulus of elasticity, E and the Poisson's ratio, σ are considered to be 11×10^6 and 0.48. Both curves are plotted using typical values given in section (A.1 - A.4).

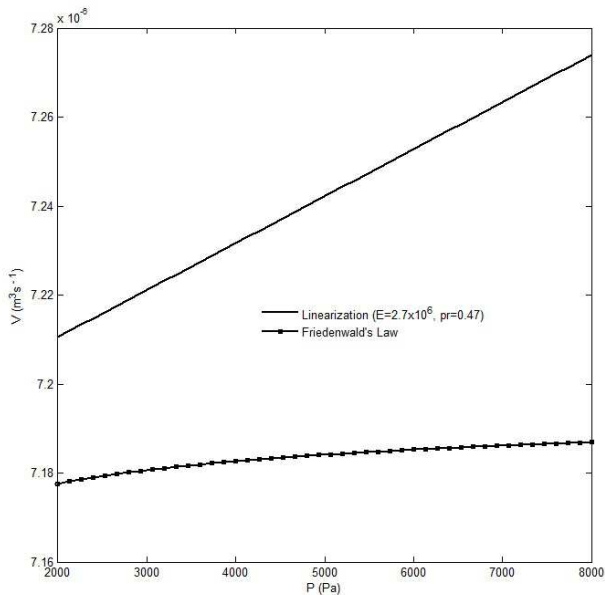


FIGURE A.6: The comparison graph of volume, V versus intraocular pressure, P between linear elastic theory and Friedenwald's law using the typical parameter values given in section (A.1 - A.4) together with the Poisson's ratio, σ which is assumed to be equal to 0.47). The solid line represents the volume, V changes for linear elastic theory whereas the square marker line denotes the volume, V changes for Friedenwald's law.

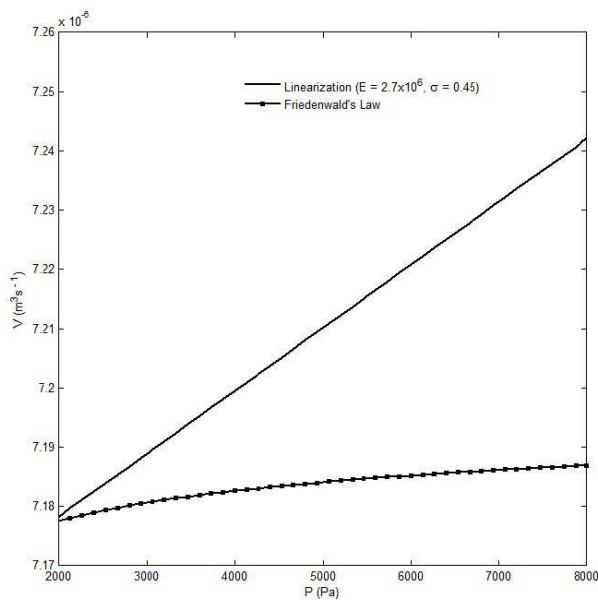


FIGURE A.7: The comparison between linear elastic theory and Friedenwald's law given in equations (A.15) and (A.2). The solid and the square marker lines denote the corresponding volume, V versus intraocular pressure, P for linear elastic theory and Friedenwald's law. The Poisson's ratio, σ is considered to be 0.45 and the rest of parameter values given in section (A.1 - A.4).

Appendix B

Proof of Completeness

This brief argument indicates how the functions introduced in Section 3.8.3 may be shown to be complete.

In general we can write equations (3.121), (3.123), (3.125), (3.127), (3.129), and also equations (3.122), (3.124), (3.126), (3.128) into the following form:

$$\sin \theta (1 + A\cos^2\theta + B\cos^4\theta + \dots)$$

and

$$\sin 2\theta (1 + A\cos^2\theta + B\cos^4\theta + \dots).$$

We may now find $\sin 3\theta$, $\sin 4\theta$, $\sin 5\theta$, $\sin 6\theta$, $\sin 7\theta \dots$ until $\sin n\theta$ and also we write it into the general form of the equations above in order to prove that each series is orthogonal to each other. We have

$$\begin{aligned} \sin 3\theta &= \sin(\theta + 2\theta) = \sin \theta \cos 2\theta + \cos \theta \sin 2\theta \\ &= \sin \theta (2\cos^2\theta - 1) + \cos \theta (2\sin \theta \cos \theta) \\ &= 4\sin \theta \cos^2\theta - \sin \theta = \sin \theta (4\cos^2\theta - 1) \end{aligned}$$

$$\begin{aligned} \sin 4\theta &= \text{Im}(e^{4i\theta}) = \text{Im}(\cos \theta + i \sin \theta)^4 \\ &= \text{Im}(\cos^4\theta + 4i\cos^3\theta \sin \theta - 6\cos^2\theta \sin^2\theta - 4i \cos \theta \sin^3\theta + \sin^4\theta) \\ &= 4\sin \theta \cos^3\theta - 4\sin^3\theta \cos \theta = 2\sin \theta \cos \theta (2\cos^2\theta - 2\sin^2\theta) \\ &= 4\sin \theta (4\cos^2\theta - 2) \end{aligned}$$

$$\begin{aligned} \sin 5\theta &= \text{Im}(e^{5i\theta}) = \text{Im}(\cos \theta + i \sin \theta)^5 \\ &= \text{Im} \left(\cos^5\theta + 5i\cos^4\theta \sin \theta - 10\cos^3\theta \sin^2\theta - 10i\cos^2\theta \sin^3\theta \right. \\ &\quad \left. + 5\cos \theta \sin^4\theta + i \sin^5\theta \right) \\ &= 5\sin \theta \cos^4\theta - 10\sin^3\theta \cos^2\theta + \sin^5\theta \\ &= \sin \theta \left(5\cos^4\theta - 10\cos^2\theta (1 - \cos^2\theta) + (1 - \cos^2\theta)^2 \right) \\ &= \sin \theta (16\cos^4\theta - 12\cos^2\theta + 1) \end{aligned}$$

$$\begin{aligned}
\sin 6\theta &= \operatorname{Im}(e^{6i\theta}) = \operatorname{Im}(\cos \theta + i \sin \theta)^6 \\
&= \operatorname{Im} \left(\cos^6 \theta + 6i \cos^5 \theta \sin \theta - 15 \cos^4 \theta \sin^2 \theta - 20i \cos^3 \theta \sin^3 \theta \right. \\
&\quad \left. + 15 \cos^2 \theta \sin^4 \theta + 6i \cos \theta \sin^5 \theta - \sin^6 \theta \right) \\
&= 6 \sin \theta \cos^5 \theta - 20 \sin^3 \theta \cos^3 \theta + 6 \cos \theta \sin^5 \theta \\
&= \sin 2\theta \left(3 \cos^4 \theta - 10 \cos^2 \theta (1 - \cos^2 \theta) + 3(1 - \cos^2 \theta)^2 \right) \\
&= \sin 2\theta (16 \cos^4 \theta - 16 \cos^2 \theta + 3) \\
&\vdots \\
&\vdots
\end{aligned}$$

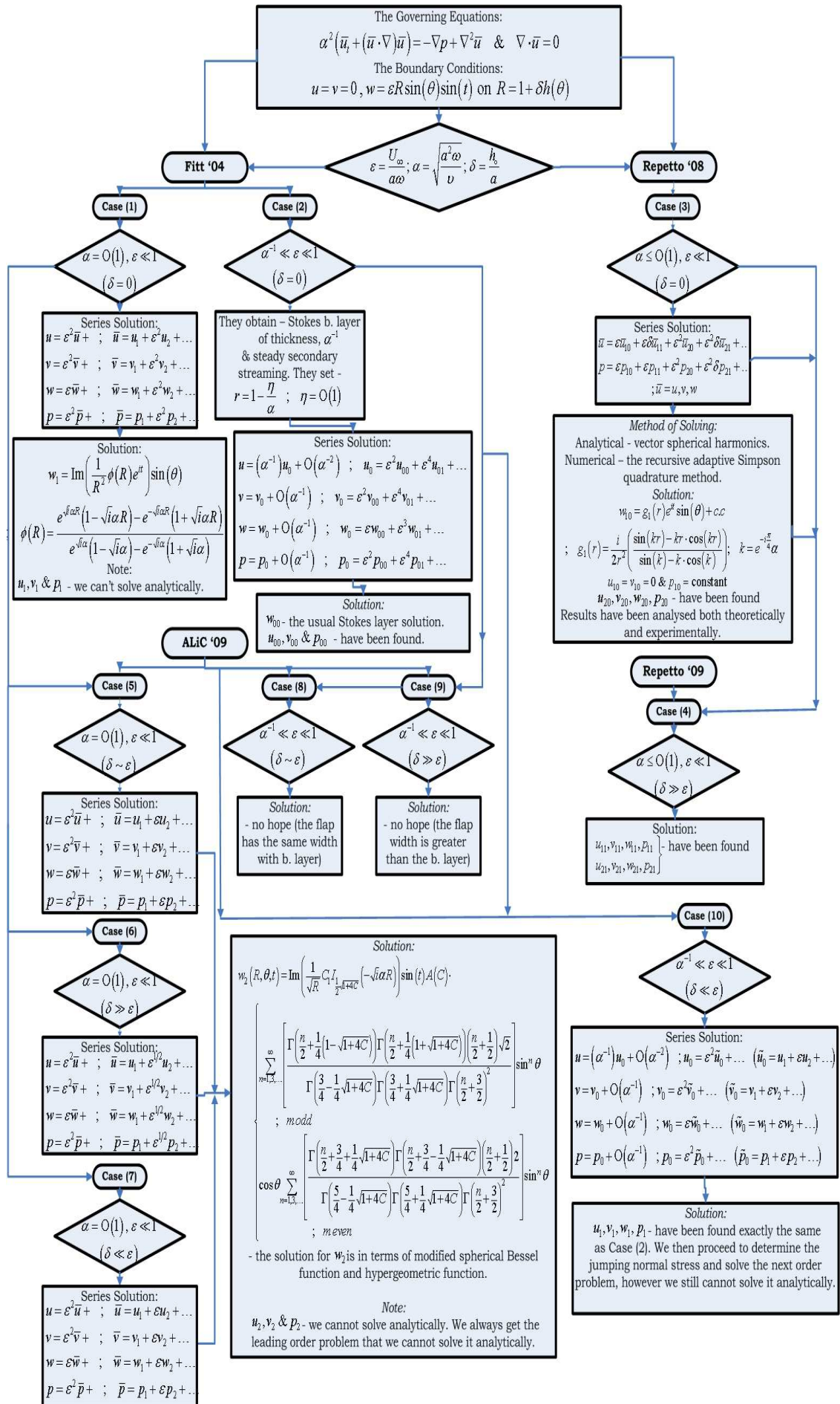
In general

$$\begin{aligned}
\sin n\theta &= \operatorname{Im} \left[\cos^n \theta + n i \cos^{n-1} \theta \sin \theta + \frac{n(n-1)(i)^2}{2!} \cos^{n-2} \theta \sin^2 \theta \right. \\
&\quad \left. + \frac{n(n-1)(n-2)(i)^3}{3!} \cos^{n-3} \theta \sin^3 \theta + \dots + \frac{n(n-1)(i)^{n-2}}{2!} \cos^2 \theta \sin^{n-2} \theta \right. \\
&\quad \left. + n(i)^{n-1} \cos \theta \sin^{n-1} \theta + (i)^n \sin^n \theta \right] \\
\sin n\theta &= \begin{cases} \sin \theta \left[\begin{array}{l} n \cos^{n-1} \theta + \frac{n(n-1)(n-2)(i)^2}{3!} \cos^{n-3} \theta (1 - \cos^2 \theta) \\ + \frac{n(n-1)(n-2)(n-3)(n-4)(i)^4}{5!} \cos^{n-5} \theta (1 - \cos^2 \theta)^2 + \\ \dots + (i)^{n-1} (1 - \cos^2 \theta)^{\frac{n-1}{2}} \end{array} \right]; n \text{ odd} \\ \sin 2\theta \left[\begin{array}{l} \frac{n}{2} \cos^{n-2} \theta + \frac{n(n-1)(n-2)(i)^2}{2 \times 3!} \cos^{n-4} \theta (1 - \cos^2 \theta) \\ + \frac{n(n-1)(n-2)(n-3)(n-4)(i)^4}{2 \times 5!} \cos^{n-6} \theta (1 - \cos^2 \theta)^2 + \\ \dots + \frac{n}{2} (i)^{n-2} (1 - \cos^2 \theta)^{\frac{n-2}{2}} \end{array} \right]; n \text{ even} \end{cases}
\end{aligned}$$

Appendix C

Flow Map

The diagram below is the flow map referred to Section 3.8. This allows easy identification of the different models and flow regimes that have been proposed to analyse the flow of liquefied vitreous humour in the presence of a retinal detachment.



Bibliography

- [1] Saude, T. (1993). "Ocular anatomy and physiology". Blackwell Scientific Publications (Oxford, Boston)
- [2] Gonzalez, G. (2004). "The mathematical modelling of human eyes - a PhD thesis". School of Mathematics, University of Southampton.
- [3] Jackson, T.L., Hillenkamp, J., Williamson, T.H., Clarke, K.W., Almubarak, A.I. and Marshall, J. (2003). "An Experimental Model of Rhegmatogenous Retinal Detachment: Surgical Results and Glial Cell Response". *Investigative Ophthalmology and Visual Science*. **44**. 4026-4034.
- [4] Sodhi, A., Leung, L.S., Do, D.V., Gower, E.W., Schein, O.D. and Handa, J.T. (2008). "Recent Trends in the Management of Rhegmatogeneous Retinal Detachment". *Survey of Ophthalmology*. **53**. 50-67.
- [5] Bourne, W.M. (2003). "Biology of the corneal endothelium in health and disease". *Eye*. **17**. 912-918.
- [6] Danielsen, C.C. (2004). "Tensile mechanical and creep properties of Descemet's membrane and lens capsule". *Experimental Eye Research*. **79**, 343-350.
- [7] Khng, C.Y., Voon, L.W. and Yeo, K.T. (2001). "Causes and management of Descemet's membrane detachment associated with cataract surgery-not always a benign problem". *Annals Academy of Medicine Singapore*. **5**. 532-535.
- [8] Maple 12.0 Maplesoft, Waterloo Maple Inc. 2008.
- [9] Van Dyke, M. D. (1964). "Perturbation Methods in Fluid Mechanics". Academic Press, New York. (Annotated ed. 1975, Parabolic Press, Stanford, CA)
- [10] Newson, T., El-Sheikh, A. and Hamza, O. (2003). "Mathematical modelling of the effect of elevated IOP on the lamina cribrosa". *16th ASCE Engineering Mechanics Conference, July*. 16-18.
- [11] Hazin, R., Hendrick A.M. and Kahook, M.Y. (2009). "Primary Open Angle Glaucoma: diagnostic approaches and management". *Journal of the National Medical Association*. **101**. 46-50.

- [12] Quigley, H.A. (1993). "Open Angle Glaucoma". *The New England Journal of Medicine*. **328**. 1097-1106.
- [13] Quigley, H.A. (1996). "Number of people with glaucoma worldwide". *British Journal of Ophthalmology*. **80**. 389-393.
- [14] Quigley, H.A. and Broman, A.T. (2006). "The number of people with glaucoma worldwide in 2010 and 2020". *British Journal of Ophthalmology*. **90**. 262-267.
- [15] James, S.D. and Grady, M.H. (2003). "Open-Angle Glaucoma". *American Family Physician*. **67**. 1937-1944.
- [16] Gabelt, B.T. and Kaufman, P.L. (2005). "Changes in aqueous humor dynamics with age and glaucoma". *Progress in Retinal and Eye Research*. **24**. 612-637.
- [17] Johnson, M.C. and Kamm, R.D. (1983). "The role of Schlemm's canal in aqueous outflow from the human eye". *Investigative Ophthalmology and Visual Science*. **24**. 320-325.
- [18] Tandon, P.N. and Autar, R. (1989). "Flow of aqueous outflow in the canal of Schlemm". *Mathematical Biosciences*. **93**. 53-78.
- [19] Grundy, R.E. (1990). "On an Equation Modeling the flow in the Canal of Schlemm". *Mathematical Biosciences*. **98**. 243-249.
- [20] Avtar, R. and Srivastava, R. (2006). "Aqueous outflow in Schlemm's canal". *Applied Mathematics and Computation*. **174**. 316-328.
- [21] Moses, R.A. (1979). "Circumferencial flow in Schlemm's canal". *American Journal of Ophthalmology*. **88**. 585-591.
- [22] Ockendon, H. and Ockendon, J.R. (1995). "Viscous flow". Cambridge University Press, Cambridge.
- [23] Fitt, A.D. (2008). "Flow in the Canal of Schlemm and its influence on Primary Open Angle Glaucoma". In Bonilla, L.L., Moscoso, M., Platero, G. and Vega, J.M. (eds). Progress in Industrial Mathematics at ECM 2006, Germany, Springer, 843-847. (Mathematics in Industry, 12).
- [24] Fatt, I. and Weissman, B.A. (1992). "Physiology of the eye". 2nd Edition. Butterworth - Heinemann, Boston.
- [25] Friedenwald, J.S. (1937). "Contribution to the theory and practice of tonometry". *American Journal of Ophthalmology*. **20**. 985-1024.
- [26] Gonzalez, G. and Fitt, A.D. (2003). "The mathematical modelling of human eyes - a PhD study". *Mathematics TODAY, February*. 20-25.

- [27] Ethier, C.R., Read, T.A. and Chan, D. (2004). "Biomechanics of Schlemm's canal endothelial cells: influence on F-Actin architecture". *Biophysical Journal*. **87**. 2828-2837.
- [28] Sluckin, T.J. (2007). "Lecture Notes - Mathematical methods for Civil and Environmental Engineers, part II". School of Mathematics, University of Southampton.
- [29] Ismail, Z. and Fitt, A.D. (2008). "Mathematical Modelling of Flow in Schlemm's Canal and Its Influence on Primary Open Angle Glaucoma". *International Conference on Science and Technology (ICSTIE): Applications in Industry and Education*. 1967 - 1973.
- [30] Llobet, A., Gasull, X., and Gual, A. (2003). "Understanding Trabecular Meshwork Physiology: A Key to the Control of Intraocular Pressure?". *News in Physiological Sciences*. **18**, 205-209.
- [31] Fautsch, M.P., Douglas, D.H. and the Second ARVO/Pfizer Research Institute Working Group. (2006). "Aqueous Humour Outflow: What Do We Know? Where Will It Lead Us?". *Investigative Ophthalmology and Visual Science*. **47**. 4181-4187.
- [32] Johnson, M. (2006). "What controls aqueous humour outflow resistance?". *Experimental Eye Research*. **82**. 545-557.
- [33] Bengtsson, B. (1981). "Manifest Glaucoma in the aged II: Cases detected by Ophthalmoscopy". *Acta Ophthalmologica*, **59**, 332-335.
- [34] Rolim de Moura, C.R., Paranhos Jr.A. and Wormald, R. (2007). "Laser trabeculoplasty for open angle glaucoma". *Cochrane Database of Systematic Reviews 2007*. Issue 4, JohnWiley and Sons, Ltd.
- [35] Burr J, Azuara-Blanco A, Avenell A. (2004). "Medical versus surgical interventions for open angle glaucoma". *Cochrane Database of Systematic Reviews 2004*. Issue 1, JohnWiley and Sons, Ltd.
- [36] Lim, K.S., Allan, B.D.S., Lloyd, A.W., Muir, A., and Khaw, P.T. (1998). "Glaucoma drainage devices; past, present, and future". *British Journal of Ophthalmology*. **82**. 1083-1089.
- [37] Hong, C.H., Arosemena, A., Zurakowski, D. and Ayyala, R.S. (2005). "Glaucoma Drainage Devices: A Systematic Literature Review and Current Controversies". *Survey of Ophthalmology*. **50**. 48-60.
- [38] Broquet, J., Roy, S., Mermoud, A. (2005). "Visualization of the aqueous outflow pathway in the glaucoma surgery by finite element model of the eye". *Computer Methods in Biomechanics and Biomedical Engineering*. **1**. 43-44.
- [39] Coakes, R. (1992). "Laser trabeculoplasty". *British Journal of Ophthalmology*. **76**. 624-626.

- [40] Fankhauser, F. and Kwasniewska, S. (2003). "Laser in ophthalmology: Basic, diagnostic and surgical aspects; A review". Kugler Publications, The Hague, The Netherlands. 171-173.
- [41] Kolb, H. (2003). "How the Retina Works". *American Scientist*. **91**. 28-35.
- [42] Pirenne, M.H. (1967). "Vision and the Eye". 2nd Edition, Chapman and Hall Ltd.
- [43] Lewis, G.P., Charteris, D. G., Sethi, C.S. and Fisher, S.K. (2002). "Animal models of retinal detachment and reattachment: identifying cellular events that may affect visual recovery". *Eye: Cambridge Ophthalmological Symposium*. **16**. 375-387.
- [44] Yin, S., Gardner, T.W., Thomas, T.O. and Kolanda, K. (2003). "Light Scatter Causes the Grayness of Detached Retinas". *Archives of Ophthalmology*. **121**. 1002-1008.
- [45] Wang, S. and Linsenmeier, R.A. (2007). "Hyperoxia Improves Oxygen Consumption in the Detached Feline Retina". *Investigative Ophthalmology and Visual Science*. **48**. 1335-1341.
- [46] Duffy, B.R., Wilson, S.K., Lee, M.E.M. and Taylor, N.H. (2004). "A model of fluid flow in a scraped-surface heat exchange". Published electronically in the Proceedings of the 4th European Thermal Sciences Conference, Birmingham.
- [47] Vaughan, D., Cook, T. and Asbury, R. (1965). "General Ophthalmology". Lange Medical Publications.
- [48] Burkill, J.C. (1962) "The theory of ordinary differential equations". Interscience Publishers, Inc.
- [49] Williams, J.G., Hadavinia, H. and Cotterell, B. (2005). "Anistropic elastic and elastic-plastic bending solutions for edge constrained beams". *International Journal of Solids and Structures*. **42**, 4927-4946.
- [50] Cotterell, B., Hbaieb, K., Williams, J.G., Hadavinia, H. and Tropsa, V. (2006). "The root rotation in double cantilever beam and peel tests". *Mechanics of Materials*. **38**. 571-584.
- [51] Please, C.P. (2007). "Lecture Notes - Mathematics for Electronic and Electrical Engineering, MATH2021". School of Mathematics, University of Southampton.
- [52] Watson, G.N. (1958) "Theory of Bessel Functions". Cambridge University Press, Cambridge.
- [53] Bateman, H. (1953) "Higher Transcendental Functions". McGraw-Hill Book Company, Inc.
- [54] Wang, F., Lee, H.P. and Lu, C. (2007). "Biomechanical effects of segmental scleral buckling surgery". *Current Eye Research*. **32**. 133-142.

- [55] Afrashi, F., Akkin, C., Egrilmez, S., Erakgun, T. and Mentes, J. (2005). "Anatomic outcome of scleral buckling surgery in primary rhegmatogenous retinal detachment". *International Ophthalmology*. **26**. 77-81.
- [56] Dyson, R., Fitt, A.D., Jensen, O., Mottram, N., Miroshnychenko, D., Naire, S., Ocone, R., Siggers, J. and Smith, A. (2004). "Post Re-attachment Retinal Redetachment". UK Mathematics in Medicine Study Group Starthclyde.
- [57] Liversedge, S.P., and Findlay, J.M. (2000). "Saccadic Eye Movements and Cognition". *Trends in Cognitive Sciences*. **4**. 6-14.
- [58] Yang, S.N., and McConkie, G.W. (2001). "Eye Movements during reading: a theory of saccade initiation times". *Vision Research*. **41**. 3567-3585.
- [59] Porte, H.S. (2004). "Slow horizontal eye movement at human sleep onset". *Journal of Sleep Research*. **13**. 239-249.
- [60] Rottach, K.G., Das, V.E., Wohlgemuth, W., Zivotofsky, A.Z. and Leigh, R.J. (1998). "Properties of Horizontal Saccades Accompanied by blinks". *Journal of Neurophysiology*. **79**. 2895-2902.
- [61] David, T., Smye, S., James, T., and Dabbs, T. (1997). "Time-dependent stress and displacement of the eye wall tissue of the human eye". *Medical Engineering and Physics*. **19**. 131-139.
- [62] David, T., Smye, S., James, T., and Dabbs, T. (1998). "A model for the fluid motion of vitreous humour of the human eye during saccadic movement". *Physics in Medicine and Biology*. **43**. 1385-1399.
- [63] Repetto, R., Stocchino, A., and Cafferata, C. (2005). "Experimental investigation of vitreous humour motion within a human eye model". *Physics in Medicine and Biology*. **50**. 4729-4743.
- [64] Riley, N. (1966). "On a sphere oscillating in a viscous fluid". *The Quarterly Journal of Mechanics and Applied Mathematics*. **19**. 461-472.
- [65] Riley, N. (1967). "Oscillatory Viscous Flows: Review and Extension". *IMA Journal of Applied Mathematics*. **3**. 419-434.
- [66] Riley, N. (2001). "Steady Streaming". *Annual Review of Fluid Mechanics*. **33**. 43-65.
- [67] Gophinath, A. (1992). "Steady streaming due to small-amplitude torsional oscillations of a sphere in a viscous fluid". *The Quarterly Journal of Mechanics and Applied Mathematics*. **46**. 501-520.
- [68] Repetto, R. (2006). "An analytical model of the Dynamics of the Liquefied Vitreous Induced by Saccadic Eye Movements". *Meccanica*. **41**. 101-117.

- [69] Repetto, R., Siggers, J.H. and Stocchino, A. (2008). "Steady streaming within a periodically rotating sphere". *The Journal of Fluid Mechanics*. **608**. 71-80.
- [70] Repetto, R., Siggers, J.H. and Stocchino, A. (2009). "Mathematical model of flow in the vitreous humor induced by saccadic eye rotations: effect of geometry". *Biomechanics and Modelling in Mechanobiology*.
- [71] Stocchino, A., Repetto, R., and Cafferata, C. (2007). "Eye rotation induced dynamics of a Newtonian fluid within the vitreous cavity: the effect of the chamber shape". *Physics in Medicine and Biology*. **52**. 2021-2034.
- [72] COMSOL, Inc. COMSOL Multiphysics 3.5a. 2007.
- [73] Assia, E.I., Levkovich-Verbin, H. and Blumenthal, M. (1995). "Management of Descemet's Membrane Detachment". *Journal of Cataract and Refractive Surgery*. **21**. 714-717.
- [74] Avtar, R. and Srivastava, R. (2006). "Modelling the flow of aqueous humour in anterior chamber of the eye". *Applied Mathematics and Computation*. **181**. 1336-1348.
- [75] Canning, C.R., Greaney, M.J., Dewynne, J.N. and Fitt, A.D. (2002). "Fluid flow in the anterior chamber of a human eye". *IMA Journal of Mathematics Applied in Medicine and Biology*. **19**. 31-60.
- [76] Couch, S.M. and Baratz, K.H. (2009). "Delayed, Bilateral Descemet's Membrane Detachments with Spontaneous Resolution: Implications for Nonsurgical Treatment". *Cornea*. **28**. 1160-1163.
- [77] El-Shahed, M. and Elmaboud, Y.A. (2005). "On the fluid flow in the anterior chamber of a human eye with slip velocity". *International Communications in Heat and Mass Transfer*. **32**. 1104-1110.
- [78] Fitt, A.D. and Gonzalez, G. (2006). "Fluid Mechanics of the Human Eye: Aqueous Humour Flow in the Anterior Chamber". *Bulletin of Mathematical Biology*. **68**. 53-71.
- [79] Hirano, K., Sugita, J. and Kobayashi, M. (2002). "Separation of Corneal Stroma and Descemet's Membrane During Deep Lamellar Keratoplasty". *Cornea*. **21**. 196-199.
- [80] Kim, I.S., Shin, J.C., Im, C.H. and Kim, E.K. (2005). "Three Cases of Descemet's Membrane Detachment after Cataract Surgery". *Yonsei Medical Journal*. **5**. 719-723.
- [81] Lagendijk, J.J.W. (1982). "A mathematical model to calculate temperature distributions in human and rabbit eyes during hyperthermic treatment". *Physics in Medicine and Biology*. **27**. 1301-1311.

- [82] Mackool, R.J. and Holtz, S.J. (1977). "Descemet Membrane Detachment". *Archives of Ophthalmology*. **95**. 459-463.
- [83] Monezo, V., Choong, Y.F. and Hawksworth, N.R. (2002). "Reattachment of extensive Descemet's membrane detachment following uneventful phacoemulsification surgery". *Eye*. **16**. 786-788.
- [84] Mulhern, M., Barry, P. and Condon, P.A. (1996). "A case of Descemet's membrane detachment during phacoemulsification surgery". *British Journal of Ophthalmology*. **80**. 185-186.
- [85] Newton, R.H. and Meek, K.M. (1998). "The Integration of the Corneal and Limbal Fibrils in the Human Eye". *Biophysical Journal*. **75**. 2508-2512.
- [86] Nouri, M., Pineda, R.Jr. and Azar, D. (2002). "Descemet membrane tear after cataract surgery". *Seminars in Ophthalmology*. **17**. 115-119.
- [87] Potter, J. and Zalatimo, N. (2005). "Descemet's membrane detachment after cataract extraction". *Optometry*. **76**. 720-724.
- [88] Sevillano, C., Viso, E. and Millan-Rodriguez, A.C. (2008). "Descemet's membrane detachment as a complication of cataract surgery". *Archivos de la Sociedad Espaola de Oftalmologa*. **83**. 549-552.
- [89] Unlu, K., and Aksunger, A. (2000). "Descemet Membrane Detachment After Viscocanalostomy". *American Journal of Ophthalmology*. **130**. 833-834.
- [90] Marcon, A.S., Rapuano, C.J., Jones, M.R., Laibson, P.R. and Cohen, E.J. (2002). "Descemets membrane detachment after cataract surgery: management and outcome". *Ophthalmology*. **109**. 2325-2330.
- [91] Hammel, H.T. (1968). "Regulation of Internal Body Temperature". *Annual Review of Physiology*. **30**. 641-710.
- [92] Moffatt, H.K. (1963). "Viscous and resistive eddies near a sharp corner". *Journal of Fluid Mechanics*. **18**. 1-18.
- [93] Ismail, Z., Fitt, A.D. and Please, C.P. "A Fluid Mechanical Explanation of the Spontaneous Reattachment of a previously Detached Descemet". (Accepted for publication, to appear in IMA Journal of Mathematical Medicine and Biology.)
- [94] Flugge, W. (1960). "Stresses in Shells". Springer-Verlag.
- [95] Turner, C. E. (1965). "Introduction to Plate and Shell Theory". Longmans.
- [96] Timoshenko, S. P. and Woinowsky-Krieger, S. (1959). "Theory of Plates and Shells". 2nd edn. McGraw-Hill.

- [97] Sarkisian, S.R. (2006). "An Update of Tonometry". *Glaucoma Today, November/December*. 31-36.
- [98] Forrester, J.V., Dick, A.D., McMenamin, P.G. and Roberts, F. (2008). "The eye - Basic Sciences in Practice". 3rd Edition, Saunders Elsevier.
- [99] Davson, H. (1980). "Physiology of the Eye". 4th Edition, Churchill Livingstone.
- [100] Kniestedt, C., Punjabi, O., Lin, S. and Stampler, R.L. (2008). "Tonometry through the ages". *Survey of Ophthalmology*. **53**. 568 - 591.
- [101] Ng, T.W., Cheong, T.L. and Sheridan, J. (2007). "Digital read-out manometer using an optical mouse". *European Journal of Physics*. **28**. N11 - N16.
- [102] Moses R. A. (1971) "Theory of the Schiotz tonometer and its empirical calibration". *Transaction of the American Ophthalmological Society*. **69**. 494 -562.
- [103] Dabasia, P. (2006). "Contact Applanation tonometry". *Optician*. **231**. 32 - 39.
- [104] Eklund, A., Hallberg, P., Linden, C. and Lindahl, D.A. (2003). "An Applanation Resonator Sensor for measuring Intraocular Pressure using Combined Continuous Force and Area Measurement". *Investigative Ophthalmology and Visual Science*. **44**. 3017 - 3024.
- [105] Sudesh, S., Moseley, M.J. and Thompson, J.R. (1993). "Accuracy of Goldmann tonometry in clinical practice". *Acta Ophthalmologica*. **71**. 185 - 188.
- [106] ElSheikh, A., Wang, D., Kotecha, A., Brown, M. and Garway-Heath, D. (2006). "Evaluation of Goldmann Applanation Tonometry Using a Nonlinear Finite Element Ocular Model ". *Annals of Biomedical Engineering*. **34**. 1628 - 1640.
- [107] Moses, R.A. (1958). "The Goldmann Applanation Tonometer". *American Journal of Ophthalmology*. **46**. 865 - 869.
- [108] Hamilton, K.E., Dye, D.C., Kao, L., Pam, N. and Tran, A. N. (2008). "The Effect of Corneal Ederma on Dynamic Contour and Goldmann Tonometry". *Optometry and Vision Science*. **85**. 451 - 456.
- [109] Amini, H., Moghimi, S., Golestani, M., Jabbarvand, M., Zarei, R., Esmaili, M., Esfandiarpour, Z. and Moghadam, R.S. (2009). "Prevalence of Calibration Errors in Goldmann Applantion Tonometers". *Journal of Ophthalmic and Vision Research*. **4**. 147 - 150.
- [110] Sandhu, S.S., Chattopadhyay, S., Amariotakis, G.A., Skarmoutsos, F., Birch, M.K., Ray-Chaudhuri, N. (2009). The Accuracy of Continued Clinical Use of Goldmann Applanation Tonometers with Known Calibration Errors. *American Academy of Ophthalmology*. **116**. 9 - 13.

- [111] ElMallah, M.K., and Asrani, G.G. (2008). "News way to measure intraocular pressure". *Current Opinion in Ophthalmology*. **19**. 122 - 126.
- [112] Detry-Morel, M. (2007). "Update in Tonometry. Phosphene and Rebound Tonometries, Self-Tonometry and Technologies for the Future". *Bull Soc Belge Ophthalmol*. **303**. 87 -95.
- [113] Cervino, A. (2006). "Rebound tonometry: new opportunities and limitations of non-invasive determination of intraocular pressure". *British Journal of Ophthalmology*. **90**. 1444 - 1446.
- [114] Fernandes, P. Diaz-Rey, J.A., Queiros, J., Gonzalez-Mejjone, J.M. and Jorge, J. (2005). "Comparison of the ICare rebound tonometer with the Goldmann tonometer in a normal population". *Ophthalmic and Physiological Optics*. **25**. 436 - 440.
- [115] Watson, P.G. and Young, R.D. (2004). "Scleral structure, organisation and disease. A review". *Experimental Eye Research*. **78**. 609 - 623.
- [116] Olsen, T.M. Aaberg, S.Y., Geroski, D.H. and Edelhauser, H.F. (1998). "Human Sclera: Thickness and Surface Area". *American Journal of Ophthalmology*. **125**. 237 - 241.
- [117] Uchio, E., Ohno, S., Joju, K., Aoki, K. and Kisielewicz, L.T. (1999). "Simulation model of an eyeball based on finite element analysis on a supercomputer". *British Journal of Ophthalmology*. **83**. 1106 - 1111.
- [118] Norman, R.E., Flanagan, J.G., Rausch, S.M.K., Sigal, I.A., Tertinegg, I., Eilaghi, A., Portnoy, S., Sled, J.G. and Ethier, C.R. (2010). "Dimensions of the human sclera: Thickness measurement and regional changes with axial length". *Experimental Eye Research*. **90**. 277 - 284.
- [119] Sigal, I.A., Flanagan, J.G. Tertinegg, I. and Ethier, C.R. (2004). "Finite Element Modelling of Optic Nerve Head Biomechanics". *Investigative Ophthalmology and Visual Science*. **45**. 4378 - 4387.
- [120] Liu, J. and Roberts, C.J. (2005). "Influence of corneal biomechanical properties on intraocular pressure measurement: Quantitative analysis". *Journal of Cataract and Refractive Surgery*. **31**. 146 - 155.
- [121] Smerdon, D. (2000). "Anatomy of the Eye and Orbit". *Current Anaesthetic and Critical Care*. **2**. 286 - 293.
- [122] Battaglioli, J.L. and Kamm, R.D. (1984). "Measurements of the compressive properties of scleral tissue". *Investigative Ophthalmology and Visual Science*. **25**. 59 - 65.

- [123] Kobayashi, A.S., Woo, S.L., Lawrence, C. and Schlegel, W.A. (1971). "Analysis of the corneo-scleral shell by the method of direct stiffness". *Journal of Biomechanics*. **4**. 323 - 330.
- [124] Woo, S.L., Kobayashi, A.S., Schlegel, W.A. and Lawrence, C. (1972). "Nonlinear material properties of intact cornea and sclera". *Experimental Eye Research*. **14**. 29 - 39.
- [125] Friberg, T.R. and Lace, J.W. (1988). "A comparison of the elastic properties of human choroid and sclera". *Experimental Eye Research*. **47**. 429 - 436.
- [126] Sjontoft, E. and Edmund, C. (1987). "In vivo determination of Young's modulus for the human cornea". *Bulletin of Mathematical Biology*. **49**. 217 - 232.
- [127] Edmund, C. (1988). "Corneal elasticity and Ocular rigidity in normal and keratoconic eyes". *Acta Ophthalmol*. **66**. 134 - 140.
- [128] Andresson, T.T., Hjorth-Simonsen, A. and Oklund, H. (1980). "Biomechanical properties of keratoconus and normal corneas". *Experimental Eye Research*. **31**. 435 - 441.
- [129] Asejczyk-Widlicka, M., Srodko, D.W., Kasprzak, H. and Pierscionek, B.K. (2007). "Modelling the elastic properties of the anterior eye and their contribution to maintenance of image quality: the role of the limbus". *Eye*. **21**. 1087 - 1094.
- [130] Liessa, A. (1993). "Vibration of Shells". Acoustical Society of America.
- [131] Anderson, K., El-Sheikh, A. and Newson, T. (2004). "Application of structural analysis to the mechanical behaviour of the cornea". *Journal of the Royal Society Interface*. **1**. 3 - 15.
- [132] Srodko, W. (2009). "Biomechanical model of human eyeball and its applications". *Optica Applicata*. **XXXIX**. 401 - 413.
- [133] Landau, L.D. and Lifshitz, E.M. (1959). "Theory of Elasticity". Volume 7 of Course of Theoretical Physics, Pergamon Press, London.
- [134] Schematic Diagram of the Human Eye.
<http://www.larsoneycenter.com/chicago/patient-education/anatomy-of-the-eye.htm> (18 March 2011)
- [135] Primary Open Angle Glaucoma.
<http://www.clarian.org/ADAM/doc/graphics/images/en/9349.jpg>
(18 March 2011)
- [136] Primary Open Angle Glaucoma Process.
<http://www.davidsoneye.com/glaucoma.htm> (18 March 2011)

- [137] Intraocular Pressure.
<http://www.goodtoknow.co.uk/health/133851/What-039-s-the-difference-between-increased-eye-pressure-amp-glaucoma-> (18 March 2011)
- [138] Types of Glaucoma.
<http://www.stlukeseye.com/Conditions/Glaucoma.asp> (18 March 2011)
- [139] Childhood Glaucoma.
<http://www.glaucomafoundation.org/childhoodglaucoma.htm> (18 March 2011)
- [140] Normal Pressure Glaucoma.
<http://www.patient.co.uk/showdoc/23068745/> (18 March 2011)
- [141] Retinal Detachments.
<http://www.bethesdaretina.com/library.htm> (18 March 2011)
- [142] Retinal Detachments.
<http://www.see-your-best.com/webpagesnew/retinaltear.htm> (18 March 2011)
- [143] Types of Retinal Detachment.
<http://www.vrmny.com/pe/rtrd.html> (18 March 2011)
- [144] Posterior Vitreous Detachment.
<http://www.rnib.org.uk/xpedio/groups/public/documents/PublicWebsite/publicrnib003660.hcsp> (18 March 2011)
- [145] Treatment for RRD.
<http://www.revoptom.com/HANDBOOK/SECT5R.HTM> (18 March 2011)
- [146] Cryotherapy.
<http://www.nwkec.org/005rd070.htm> (18 March 2011)
- [147] DMD after cataract surgery.
<http://emedicine.medscape.com/article/1196103-overview> (18 March 2011)
- [148] Darcy Law.
<http://en.wikipedia.org/wiki/Darcy%27slaw> (18 March 2011)
- [149] O'Shea, J.G., Harvey, R.B. and Infield, D.A. (2002). "Diagnosis and management of primary open angle glaucoma". a photo-essay for health professionals.
<http://medweb.bham.ac.uk/easdec/eyetextbook/poag/poag.htm> (18 March 2011)
- [150] Cross section of the eye from above showing aqueous humour flows.
<http://www.thirdeyehealth.com/eye-pressure.html> (18 March 2011)
- [151] Schematic diagram of eye structures involved in aqueous humour dynamics.
http://www.nature.com/nm/journal/v7/n3/figtab/nm0301_94F1.html
(18 March 2011)

- [152] Healthy and Glaucomatous Optic Nerve.
http://www.glaucomaconsultantsmd.com/maryland_eye_care.html
(18 March 2011)
- [153] Retinal Detachment, Rhegmatogenous.
http://emedicine.medscape.com/article/1224737_overview (18 March 2011)
- [154] Scleral Buckling Surgery.
<http://www.britannica.com/bps/media-view/112183/0/0/0> (18 March 2011)
- [155] The Cornea.
<http://www.health.com> (18 March 2011)
- [156] The Structure of the Cornea.
<http://www.ophthobook.com> (18 March 2011)
- [157] Goldmann tonometer.
<http://www.oiic-ca.com/> (18 March 2011)
- [158] The indentation (Schiotz) tonometer.
http://www.rveeh.vic.gov.au/Library/Museum/Intraocular_pressure.htm
(18 March 2011)
- [159] The ICare rebound tonometer.
http://www.dfv.com.au/popup_icare.htm. (18 March 2011)